Dissertation
submitted to the
Combined Faculties for the Natural Sciences and for Mathematics
of the Ruperto–Carola University of Heidelberg, Germany
for the degree of
Doctor of Natural Sciences

Put forward by
Laureata Magistrale in Fisica: Ilaria Rinaldi
Born in: Bra – Italy
Oral examination: October 17, 2011

Investigation of novel imaging methods using therapeutic ion beams

Referees: **PD Dr. Katia Parodi**

Prof. Dr. Oliver Jäkel

Topic in English – Summary in English

Imaging techniques play an increasingly important role for treatment planning and in-situ monitoring in ion beam therapy. In this thesis, two novel methods were studied.

For real-time in-vivo range verification, FLUKA Monte Carlo simulations were performed to address the detection of prompt gammas, emitted during irradiation of homogeneous and heterogeneous targets, using an ideal detector, highlighting main signal and background features relevant for clinical application.

For range monitoring prior to or in-between treatment, a dedicated detector prototype based on a stack of 61 ionization chambers was assembled and its applicability to ion-based transmission imaging was investigated experimentally. Characterization of the set-up in terms of beam parameters and settings of the read-out electronics underlined the potential of heavy ion radiography and tomography as an attractive low dose imaging modality. Possible sources of image artifacts were analyzed and an original method to improve the nominal resolution of the used detector set-up was proposed. The resulting images, expressed directly in water equivalent thickness and path length, of different phantoms of increasing complexity provided a promising proof of principle of ion-based planar and volumetric imaging.

Overall, the findings of this thesis strongly support the large potential of the investigated imaging techniques for future clinical use.

Topic in German – Summary in German

Bildgebende Verfahren spielen eine immer größer werdende Rolle für die Behandlungsplanung und in-situ Überwachung in der Ionenstrahltherapie. Im Rahmen dieser Dissertation wurden zwei neue Methoden untersucht.

Im Hinblick auf Echtzeit in-vivo Reichweitenüberprüfung mit Hilfe von prompt gamma Photonen, die während der Bestrahlung homogener und heterogener Zielobjekte abgestrahlt werden, wurden FLUKA Monte Carlo Simulationen zur Untersuchung der Messbarkeit der Photonen in einem idealen Detektor durchgeführt. Besondere Aufmerksamheit kam den Hauptmerkmalen des Signals sowie des Hintergrundes zu, die für mögliche klinische Anwendungen von Bedeutung sind.

Zur Reichweitenüberprüfung vor und während der Behandlung wurde ein spezieller Detektor-Prototyp auf der Grundlage eines Stapels von 61 Ionisationskammern gebaut und dessen Anwendbarkeit fr die Transmissionsbildgebung mit Ionenstrahlung experimentell untersucht. Die Charakterisierung des Aufbaus bezüglich Strahlparameter und Einstellungen der Ausleseelektronik hob das Potential von Schwerionenradiographie und -tomographie als attraktive bildgebende Techniken bei niedriger Dosisbelastung hervor. Mögliche Quellen von Bildartefakten wurden analysiert und eine originäre Methode zur Verbesserung der nominalen Auflösung des verwendeten Detektoraufbaus vorgeschlagen. Bilder unterschiedlicher Phantome mit zunehmender Komplexität wurden gewonnen und direkt in wasser-äquivalenter Dichte bzw. Weglänge ausgedrückt. Sie lieferten einen ermutigenden Proof of Principle der planaren und volumetrischen Bildgebung mit Ionenstrahlen.

Insgesamt untermauern die Befunde dieser Arbeit deutlich das große Potential der untersuchten bildgebenden Techniken für zukünftige klinische Anwendung.

CONTENTS

Chapter 1

INTRODUCTION

Cancer is a heterogeneous class of diseases in which a group of cells, in the malignant case, grows uncontrolled, intrudes upon and destroys adjacent tissues, and often metastasizes, wherein the tumor cells spread to other locations in the body via the lymphatic system or through the bloodstream. Cancer is primarily an environmental disease (e.g. tobacco use, poor diet and obesity, infection, radiation, lack of physical activity) but it can also have a hereditary genetics cause. Nowadays, cancer is the second most frequent cause of death in developed countries after heart diseases. According to estimates by the World Health Organization (WHO), the number of new cancer patients, worldwide currently at 10 million, will increase by 50% until the year 2020. Cancer will then be the leading cause of death. Despite extensive research, today only one out of two patients is successfully cured.

Although surgery remains the most successful cancer cure, approximately 50% of all patients diagnosed with cancer receive curative or palliative chemotherapy and/or radiation treatments, the latter being most of the time performed with photon or electron beams (Durante and Löffler 2010). All of the radio-therapeutic approaches have in common that they seek to deliver as effectively as possible dose[1] to the tumor in the patient, while sparing the surrounding healthy tissue and the critical structures or organs at risk (OAR) in order to avoid complications and/or induction of secondary tumors. In fact, the radiation applied to the patient causes cell-damages by ionization processes, hitting the Deoxyribonucleic acid (DNA) in the cell nucleus. Single or even more effective double strand-breaks, caused either directly by the radiation or by radiation-induced free radicals, can lead to the death of the cell.

Technological advancements have brought the different radiotherapy techniques closer to the ideal goal of conformal dose delivery. It is important to underline, however, that the physics of the used conventional radiation (e.g., photons and electrons) poses essential intrinsic limitations to the effectiveness of a technique. In this respect, ion beam ther-

[1] The dose deposited in a medium is defined as the mean energy deposited by the ionizing radiation in a mass element as $D = {}^{\mathrm{dE}}/_{\mathrm{dm}}$ and is measured in Gray (Gy).

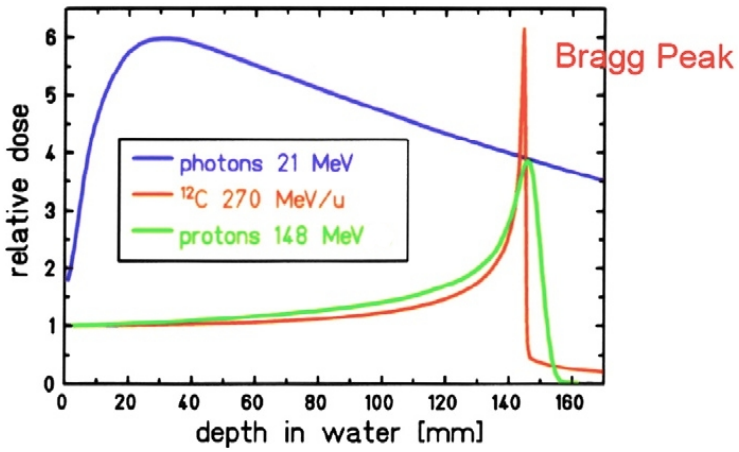

Figure 1.1.: Comparison of depth-dose profiles for photons, protons and carbon ions. The inverse ion depth-dose profile, known as Bragg peak, is favorable to treat deep-seated tumors. Figure adapted from Fokas et al. (2009).

apy has a priori advantages compared to other conventional methods. In particular, ions exhibit a more selective energy deposition in depth, so called Bragg peak as shown in figure 1.1. Moreover, heavier ions like carbon beams show an increase of the radiobiological effectiveness (RBE) in depth, reaching the maximum in the distal region of the tumor in correspondence of the Bragg peak (Kraft 2000).

1.1. Modern high precision external radiotherapy techniques

An ideal radiotherapy treatment would deliver 100% of the prescribed dose precisely to the target volume and zero to the surrounding tissues. For this purpose, in the last decades a lot of effort has been put in the development and constant improvement of external beam radiotherapy using the conventional radiation sources as well as ions.

In the next sections, a brief summary of the most modern techniques for conventional external beam radiation is given. Section 1.1.2 introduces the development of ion beam therapy, explaining its advantages as well as technical and economical challenges. Moreover, an overview over the currently existing ion therapy centers in the world is presented with a special focus on the Heidelberg Ion Therapy center (HIT, c.f section 1.1.2.2).

1.1.1. Conventional external radiotherapy

An example for a conventional external beam radiotherapy that has undergone extensive development is the Intensity Modulated Radiation Therapy (IMRT, Webb 2003). With this technique, a high-dose volume is sculpted around the site of disease with millimetric precision. In modern IMRT, not only the geometrical shape of each irradiation field is spatially modulated via multi-leaf collimators (MLC) throughout the field, but even the

radiation fluence is varied for each beam direction. Moreover, multiplying the number of beam directions (Mackie et al. 1999) from where the irradiation is delivered, it is possible to better spare the healthy tissues tumor surrounding the tumor. In this way, the dose in the entrance regions is diluted over larger volumes while the contribution of each irradiation field sums up in the target. Intuitively, one would expect that using more beams will always help to shape the radiation dose distribution to match the tumor volume. However, a recent theoretical investigation showed that, in realistic cases, nothing will be gained by using more than 10-20 beams (Bortfeld 2010).

More recently, another rotational IMRT approach, called "Single-arc", has been developed (Wang et al. 2008) and has found a lot of interest as a commercial product (RapidArc, VMAT). In the Single-arc approach, there is no intensity modulation within individual beam angles, but the radiation field shape is varied dynamically and rapidly by MLCs as the gantry rotates around the patients. Therefore, in the rotational approaches, the selection of optimal beam angles is not anymore a problem, but the distribution of dose over large healthy tissues has been a concern (Bortfeld and Webb 2009).

Another commercial product which has obtained considerable success and is now installed in more than 150 hospitals is called Cyberknife (Adler Jr. et al. 1997). The two main technological elements of the Cyberknife system are the linear accelerator (LINAC) mounted on a robotic arm that allows more degrees of freedom than an isocentric gantry in choosing the direction of the incoming beam, and a real-time image verification, performed before each beam application, which eliminates the need to use skeletal fixation for positioning.

1.1.2. Introduction to ion beam therapy

The use of charged hadrons in cancer therapy was already proposed by Wilson (Wilson 1946), who investigated the depth-dose characteristics of protons and already envisioned the therapeutic applicability of heavier ions like carbon. The first patients with a deep located tumor were treated with protons in 1954 at the Lawrence Berkely Laboratory (LBL, Tobias 1958).

As already pointed out in Wilson's original proposal, the main argument for particle therapy is the superior physical selectivity compared to conventional radiations. In fact, heavy charged particles, like protons or heavier ions (e.g ^{12}C, ^{16}O), show an inverse depth dose profile as depicted in figure 1.1. The energy deposition, i.e. dose, is relatively low in the entrance channel (plateau) but increases steeply towards the end of the ion path with a rapid fall-off, resulting in a sharp and narrow (few millimetres wide) maximum, commonly called Bragg peak (Bragg and Kleeman 1905). The Bragg peak can be accurately adjusted in depth by proper selection of the initial ion beam energy. Therefore, ions allow a highly conformal dose deposition as can be appreciated from figure 1.2, showing a comparison of two treatment plans, one obtain with carbon ions and the other based on IMRT, for a large tumor of the skull. It can be noticed that only two irradiation fields for carbon ions produce the same dose homogeneity in the target as nine IMRT irradiation fields, and that the use of carbon ions results in a substantial reduction in the integral dose to the normal tissues and an improved sparing of critical structures (Durante and Löffler 2010).

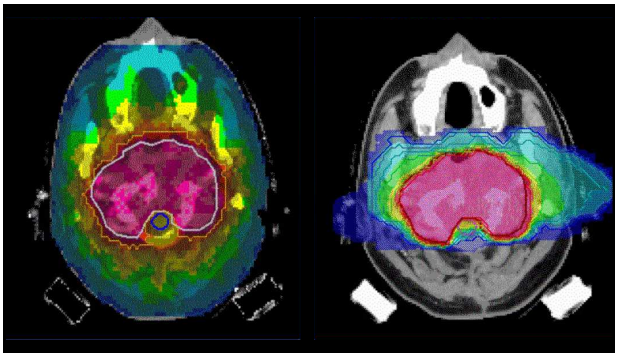

Figure 1.2.: Comparison of treatment plans for large tumor volumes in the base of the skull. Left: plan for IMRT with nine fields of irradiation. Right: plan for carbon ions with two fields of irradiation. The irradiation with carbon ions results in a substantial reduction of the integral dose to normal tissue and better spares critical structures. Figure by courtesy of Oliver Jäkel.

1.1.2.1. Brief overview over ion therapy centers in the world

At LBL, from 1957 to 1992, about 2000 patients have been treated with He ions and from 1975 to 1992, 403 patients have undergone trials with C, Ar, Si and Ne ions (ptcog.web.psi.ch). In 1990, the first hospital-based center for proton therapy, the Loma Linda University Medical Center (LLUMC), opened in the USA and since then, more than 14000 patients have been treated. Afterwards, in 1994, the first patient was treated with carbon ions at the research-based HIMAC facility in Chiba (Japan) and in 1996/1997, the first tumor conform irradiation with scanned (cf. section 1.4) proton beams was performed at the research-based Paul Scherrer Institut (PSI) in Villigen (Switzerland). At the same time, first treatments with carbon ions at the GSI Helmholtz Center for Heavy Ion Research in Darmstadt (Germany) took place. Nowadays, ion beam therapy is becoming more and more available in purely clinical centers, e.g., the Francis H. Burr Proton Therapy Center in Boston, MD Anderson in Houston, Hyogo Ion Beam Medical Center in Japan and HIT in Germany (cf. section 1.1.2.2). Moreover, other new facilities are under construction/commissioning in Europe: CNAO in Italy, MedAustron in Austria, ETOILE in France, PTC Marburg and NroCK Kiel, both in Germany.

1.1.2.2. The Heidelberg Ion Therapy Center

In Germany, after a ten years pilot project at GSI, the first dual proton and carbon synchrotron-based facility with an active beam delivery system (c.f section 1.4) has entered in clinical operation in November 2009 in Heidelberg (HIT, Haberer et al. 2004). At HIT, there are two treatment rooms supplied with a horizontal beam line, where the patient is positioned on a robot-controlled table so that different incident beam directions are accessible. However, the movement of the robot, and so the irradiation directions, are limited to almost coplanar beams. To be able to rotate all around the patient, the worldwide first heavy ion gantry was built. In addition to these three treatment rooms, an experimental room has been installed. A sketch of the most important components of

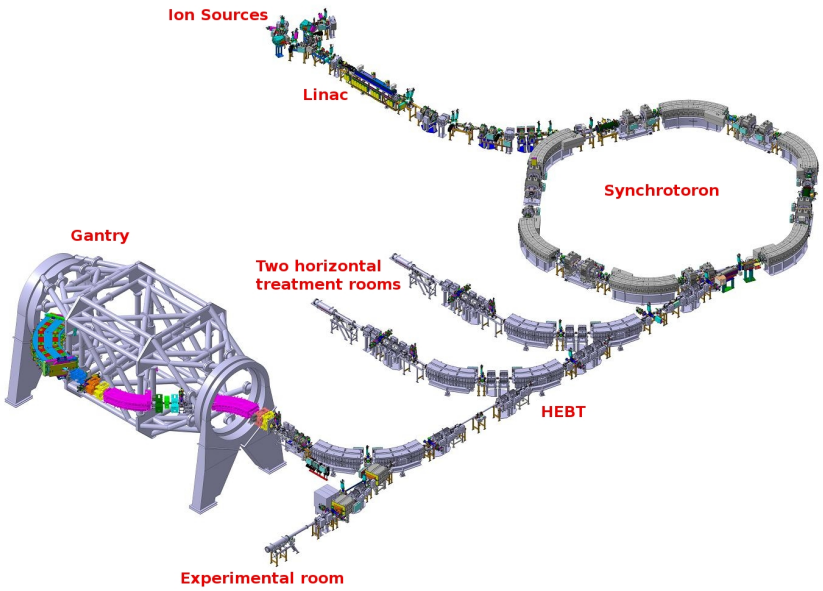

Figure 1.3.: Sketch of HIT. Ions are produced in the sources, then accelerated in a linear accelerator (LINAC) followed by the synchrotron. The High Energy Beam Transfer line (HEBT) guides the ions to the two horizontal treatment places, the gantry and the experimental room. Figure adapted from Kleffner et al. (2009).

HIT is shown in figure 1.3

Up to now, more than 500 patients have been treated in the two horizontal rooms, since the gantry is still in the state of commissioning and will become operational at the end of 2011. At HIT, different ion species are available. So far, patients have been treated with protons and ^{12}C ions. In the future, also irradiation with helium (^{4}He) and oxygen (^{16}O) ions is planned. The accelerator is designed to be able to switch between ion species within seconds (cf. section 1.4.3). The flexible design of the HIT facility offers the possibility to contribute significantly to clinical studies on recommendations regarding which ion species is the superior one for the treatment of certain tumors. In fact, the discussion about which is the best suited ion for therapy is still ongoing (Durante and Löffler 2010). A lot of patients have been treated so far with protons, since they require minor technical effort (e.g., accelerator and beam delivery system) compared to heavier ions, and offer the already mentioned physical advantages (c.f section 1.4) resulting in a lower risk of developing complications/second cancers compared to conventional external radiotherapy. For these reasons, protons can be a particularly attractive treatment option in the case of pediatric tumors. On the other hand, very promising results were achieved at HIMAC and GSI for carbon ion therapy (Hirao 2001). Clinical trials at GSI have shown that carbons are very effective for low-grade and intermediate-grade chondrosarcomas, skull base chordomas and adenocystic carcinomas (Schulz-Ertner et al. 2007). Nevertheless, confirmations with a larger number of patients in randomized clinical trials are still needed.

Another still open debate concerns the cost-benefit of ion beam therapy, since the construction of a combined ion beam therapy facility requires big economical efforts. The total

cost of HIT was € 119 million, financed equally by the Heidelberg University Hospital and the German federal government.

1.2. Physical rationale for ion beam therapy

In ion beam therapy, it is crucial to compose an irradiation plan that delivers the correct dose in the desired region while sparing the surrounding healthy tissues. To this end, it is of central importance to correctly predict the spatial distribution of energy deposit and dose in the patient caused by the incident beam of charged particles. Several physical processes occur and are necessary to be taken into account in order to fully understand the dose distribution observed in the patient. This section is dedicated to briefly review these effects.

In ion beam therapy applications, inelastic Coulomb collisions with atomic electrons are the dominant contribution to the ion energy deposition, and the overall shape of the Bragg curve is the result of the so-called Bethe-Bloch formula, describing the interaction of charged particles at a given energy with matter (cf. section 1.2.1). The absorbed dose and average range are introduced in section 1.2.2 as central concepts in ion beam therapy. In an ensemble of primary beam particles, the depth profile is slightly smeared out, an effect called range straggling (cf. section 1.2.3). Elastic collisions of beam particles with target nuclei lead to lateral spreading (cf. section 1.2.4), and finally, nuclear interactions are responsible for fragmentation effects, which again can significantly alter the depth-dose profile (cf. section 1.2.5).

1.2.1. Inelastic Coulomb scattering and Bethe-Bloch formula

In clinical applications, beam particles typically have a kinetic energy of approximately 70-500 MeV/u. In this range, ions transfer most of their energy to the traversed medium in inelastic Coulomb collisions with the atomic electrons. The Bethe-Bloch formula (Bethe et al. 1938, Bloch 1933) quantifies how much energy a primary beam particle loses on average per unit path length:

$$-\frac{dE}{dx} = 2\pi r_e^2 m_e c^2 N_e \frac{Z^2}{\beta^2}\left[\ln\left(\frac{2m_e c^2 W_{max}\beta^2\gamma^2}{\langle I^2\rangle}\right) - 2\beta^2 - 2\frac{C}{Z_t} - \delta\right] \tag{1.1}$$

where Z and β are the particle charge and velocity (scaled to the speed of light c), respectively, r_e and m_e are the electron classical radius and rest mass, respectively, W_{max} is the largest possible energy loss in a single collision with a free electron, N_e and I are the electron density and ionization potential of the medium of atomic number Z_t, whereas C and δ are the energy and absorber dependent shell and density corrections, respectively. The quantity $^{dE}/_{dx}$ is known as electronic stopping power and equation 1.1 describes the stopping power above $\sim$ 1 MeV/u.

At lower energies, the mean charge redistribution due to the dynamic loss and capture of electrons from the target for ion velocities comparable to the electron orbital velocity ($\simeq 0.008\ c$) has to be taken into account. Therefore, to extend the Bethe-Bloch formula to lower energies, the particle charge Z is replaced by an effective charge Z_{eff}, which depends

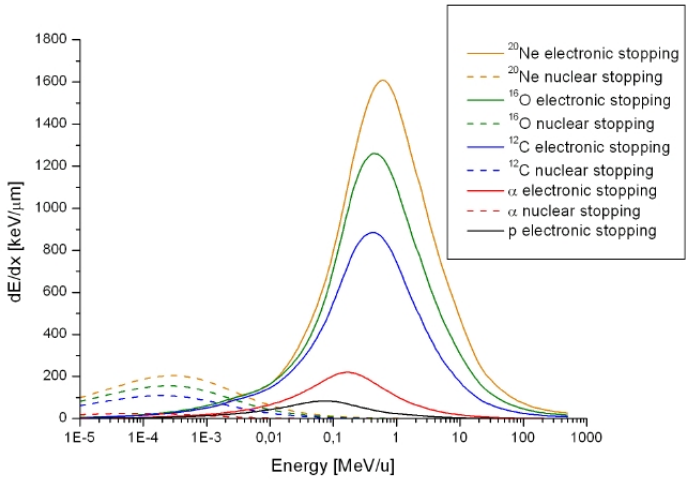

Figure 1.4.: Electronic (full lines) and nuclear (dashed lines) energy loss per unit path length $^{dE}/_{dx}$ for ions of therapeutic interest in water. $^{dE}/_{dx}$ values are calculated with the SRIM code (Ziegler 2004). It can be noticed that the nuclear stopping power is negligible for energy below 10 keV.

on the particle speed. The functional dependence can be well approximated by the Barkas formula (Barkas 1963):

$$Z_{\text{eff}} = Z\left(1 - e^{-a\beta Z^{-\frac{2}{3}}}\right) \tag{1.2}$$

with $a \simeq 125$ in the original proposal.

A graph of the so obtained extended Bethe-Bloch formula, describing the relation between the electronic stopping power and the particle energy, is shown in figure 1.4 for different ions of therapeutic interest.

It is intuitive to understand the typical peak shape of the Bragg curve from equation 1.1: At non-relativistic energies, the equation is dominated by the $1/\beta^2 \simeq 1/E$ energy dependence. In other words, the energy loss rate increases as the kinetic energy of the particle decreases along the penetration depth, resulting in a steep rise at low residual energy values on the last few millimeters of the particle path. At very low energy values, the effective charge Z_{eff} is rapidly reduced according to equation 1.2, causing the stopping power of heavy ions to drop abruptly. Hence, the distribution of the ionization density induced by a heavy charged particle along its path shows a rather constant plateau followed by a sharp maximum towards the end, the Bragg peak (cf. figure 1.1).

1.2.2. Absorbed dose and average range

Two quantities relevant for clinical applications are the absorbed dose and the mean range of the incident ions. The first one (which is to be distinguished from the stopping power, describing the energy loss rate per primary) refers to the spatial pattern of energy deposited

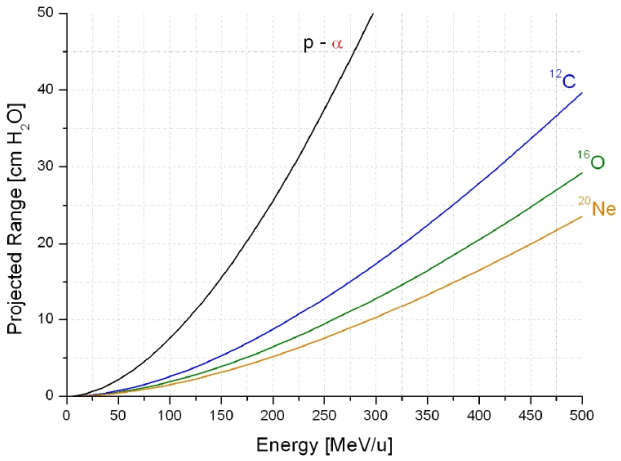

Figure 1.5.: Projected mean range for ions of therapeutic interest calculated in water with SRIM code (Ziegler 2004).

in a medium either directly by the primary ions or by secondary particles. In most practical conditions, the energy carried in and out of a volume of interest by secondary electrons is on average the same. It is then said that the secondary electron equilibrium prevails. Under this assumption, the macroscopic dose D delivered by a fluence Φ of mono-energetic heavy charged particles to a medium of density ρ can be directly linked to the average loss $^{\mathrm{dE}}/_{\mathrm{dx}}$ of the ion:

$$D = \frac{\Phi}{\rho}\frac{dE}{dx} \tag{1.3}$$

The second one is the mean range of the incident ions. The range refers to the length of the finite average path traveled by an ion in a material. Keeping in mind that the stopping power $^{dE}/_{dx}$ describes the loss rate at which heavy charged particles are continuously slowed down, the integral of its inverse allows to calculate a well defined mean range R for a given initial energy E_0.

$$R = \int_{E_0}^{0} \left(\frac{dE}{dx}\right)^{-1} dE \tag{1.4}$$

This is a particularly good approximation in the case of heavier ions since they experience very little scattering and travel almost on a straight line (cf. section 1.2.4). In figure 1.5, the projected ranges in water[2] for ions of therapeutic interest are compared. It should be noted that the range of ions with the same initial velocity scales with a factor of $^{A}/_{Z^2}$ (where A denotes the mass number and Z the atomic number of the particle) and therefore protons and α particles show the same path in water when plotted as a function of their specific initial energy expressed in MeV/u.

[2]Water is typically used as reference medium, as the human body consists to about 70% of it.

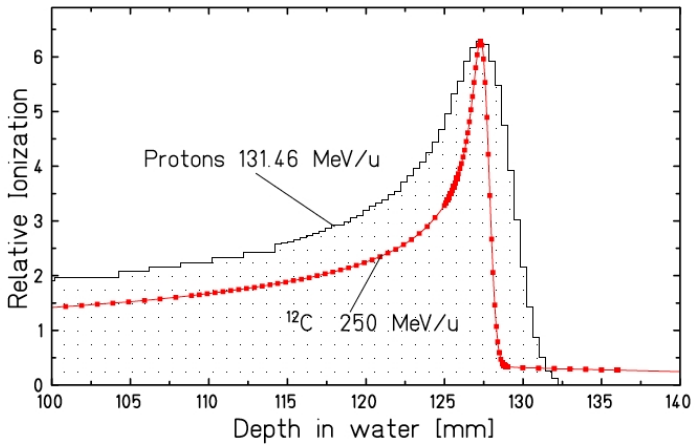

Figure 1.6.: Comparison of measured Bragg curves of proton and carbon ions having the same mean range and initial momentum spread. The measurements are performed in water with two ionization chambers encompassing a variable water column and normalized to the same peak height, from (Schardt et al. 2007).

1.2.3. Range straggling

In principle, there are two different processes that can broaden the Bragg peak, in general at the same order of magnitude . At low energy, the unavoidable momentum dispersion of the beam from the accelerator ($\Delta p/p \approx$ ‰) dominates, while at high energy, the effect of range straggling prevails (Parodi 2004).

Regarding the latter, it is important to bear in mind that the Bethe-Bloch formula (equation 1.1) gives a description of the mean stopping power for a single charged particle. In reality, in an ensemble of charged particles traversing a target, the number of collisions and the energy loss per interaction fluctuate (Bohr 1913, Ahlen 1980). This phenomenon is known as range or energy straggling and results in a broadening of the measured Bragg peak. The range straggling depends on the mass of the projectile. For different ion species, it varies approximately as the inverse of the square root of the particle mass (Schardt et al. 2010). Thus, at the same penetration depth, heavier ions exhibit a narrower Bragg peak with a steeper distal fall-off. The proton Bragg peak, shown in figure 1.6, is therefore broader than the carbon Bragg peak that arises at the same depth in water for comparable initial momentum spread.

Moreover, the range straggling increases with the penetration depth in a given material, resulting in Bragg peaks of larger width and smaller height for higher initial energy of the same ions as represented in figure 1.7.

The effect of straggling is not necessarily a drawback from the treatment point-of-view. In fact, in most practical clinical cases, it is necessary to irradiate extended tumor volumes, so it can be even advantageous to widen the sharp Bragg peak in the longitudinal direction. In fact, for very sharp carbon ion beams, additional broadening in depth is normally obtained via passive energy degraders (e.g., a ripple filter, Weber and Kraft 1999). Moreover, to better cover the tumor longitudinal extension, a proper superposition of several

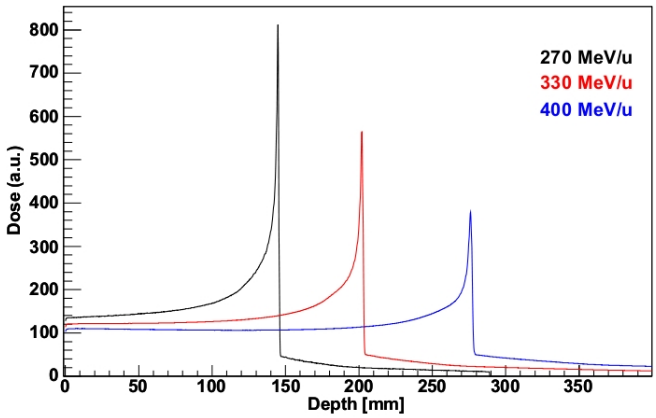

Figure 1.7.: Depth-dose profile in water calculated by means of the FLUKA (Ferrari et al. 2005, Battistoni et al. 2007) code for the same number of primary carbon ions at increasing energies. The energy spread $^{\Delta E}/_{E}$ of the beams is 0.04%. Figure adapted from Mairani (2008).

Bragg peaks at different depth (SOBP, figure 1.8), i.e., different primary ion energy, is accomplished via passive energy degraders or active energy variation of the accelerator. It is evident that the overlap of several Bragg peaks leads to a reduction of the peak to plateau dose ratio with respect to the single mono-energetic case.

1.2.4. Lateral dose profile

The spatial dose distribution is not only given by the depth profile discussed so far, but also by lateral spreading. In fact, charged particles passing through a medium experience not only interactions with target electrons but also multiple elastic collisions with target nuclei. The statistical repetition of these multiple interactions between ions and target nuclei results in a lateral spread of the ion beam. The net angular distribution of the out coming particles after a thick absorber with respect to the incident direction can be interpreted as the result of several highly probable deflections by small angles. It is well approximated by a Gaussian shape with a standard deviation σ_θ given by the empirical formula proposed by (Highland 1975):

$$\sigma_\theta = \frac{14.1MeV}{\beta pc} Z \sqrt{\frac{d}{L_{rad}}} \left(1 + \frac{1}{9} \log_{10} \frac{d}{L_{rad}}\right) \tag{1.5}$$

where p is the momentum of the particle, d the thickness of the absorber, and L_{rad} the radiation length of the traversed medium, respectively. It follows that the angular spread of ions increases as the particle energy decreases due to the βpc term in the denominator of equation 1.5.

In figure 1.9, a comparison of lateral scattering for different ion species of therapeutic interest is presented. Beams of carbon and heavier ions show little lateral scattering ($<$ 1-2 mm), while the angular spread of protons is on average approximately three times larger.

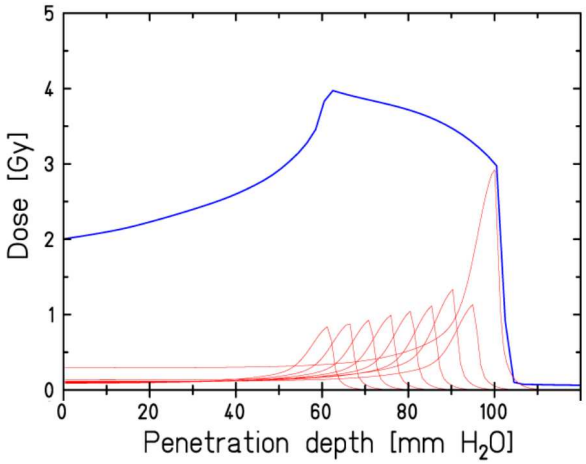

Figure 1.8.: Superposition of several carbon ions Bragg curves with different energies (red lines) to produce a SOBP (blue line). Figure adapted from Mairani (2008).

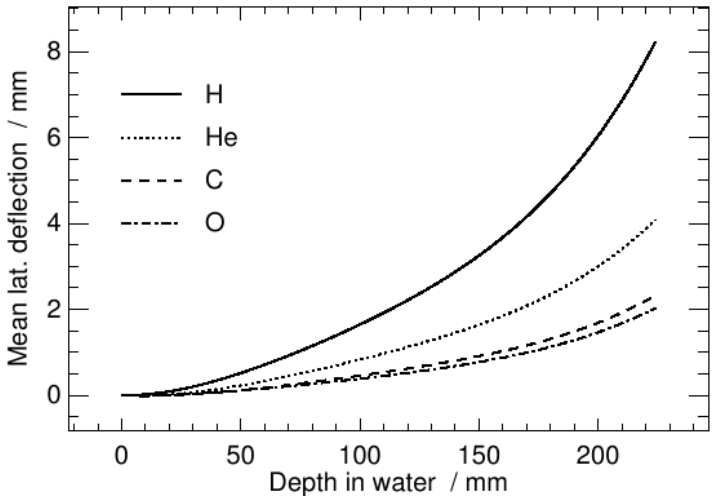

Figure 1.9.: Mean lateral deflection of protons and different heavy ion species as a function of their penetration depth in water. Figure adapted from Parodi (2004).

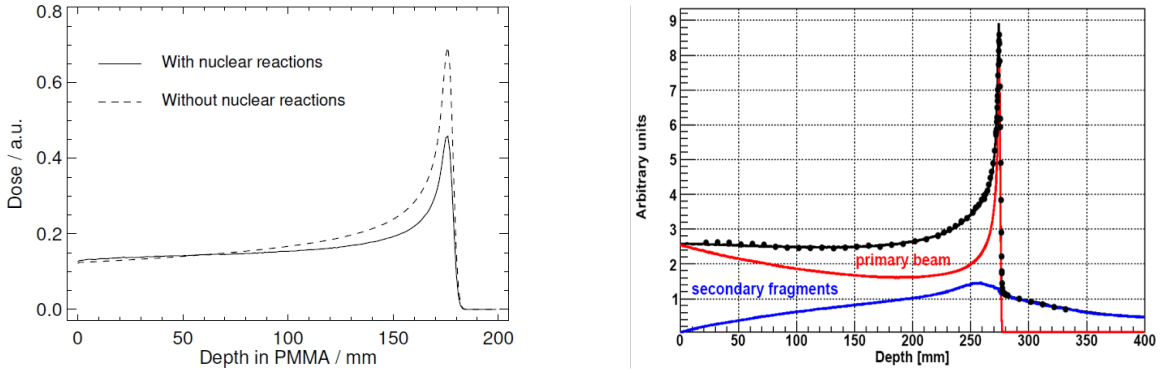

(a) (b)

Figure 1.10.: (a) Depth-dose distribution in Polymethyl methacrylate (PMMA) calculated on the basis of the FLUKA code (Ferrari et al. 2005, Battistoni et al. 2007) for a 175 MeV proton beam including or neglecting nuclear reactions. The reduction of the peak to plateau dose ratio in presence of nuclear reactions is found to be about 35%, in agreement with previous studies (Medin and Andreo 1997). Figure adapted from Parodi (2004). (b) Bragg curve as a function of depth in water for a 400 MeV/u carbon beam. The points (Haettner et al. December 2006) and the solid line (Battistoni et al. 2008) represent the experimental data and the FLUKA calculations, respectively. The dose contribution from primary ^{12}C ions and secondary fragments is also reported. Both the experimental data and the MC results are normalized by the integral of the Bragg curve calculated between the entrance region and the Bragg peak because the experimental data are obtained as relative values.

This scatter behavior of protons is very similar to or even worse than that of photons at large penetration depths. The small lateral deflection penetrating a thick absorber is a particular advantage of heavier ions in comparison to protons since they allow a safer lateral approach to sensitive structures and a further improvement in the dose distribution in the target area (Schardt et al. 2010). The lateral beam scattering is also of clinical relevance for the treatment of tumors in close vicinity to OAR. Indeed, due to uncertainties in the range of the particles in the patient, caused e.g., by tissue inhomogeneities and patient positioning, beams stopping right in front of an OAR are typically avoided. Rather, it is preferred to have the beam passing by it. Hence, the narrower the beam in the lateral direction, the closer the radiation field can get to the adjacent OAR.

1.2.5. Nuclear interactions and fragmentation

The actually observed depth-dose profile differs from the one expected from the extended Bethe-Bloch formula (cf. section 1.2.1), including straggling effects (cf. sections 1.2.3 and 1.2.4), in two regards as illustrated in figure 1.10.
Firstly, the ratio of the dose at the peak and at the entrance is reduced (cf. figure 1.10(a)). Secondly, even behind the steep fall-off after the peak, there is still a small but appreciable dose tail for heavy ions (cf. figure 1.10(b)). These two effects are due to nuclear processes undergone by the primary beam.

High energy ions penetrating a thick absorber not only interact with the target nuclei

via electromagnetic interactions (cf. sections 1.2.1, 1.2.3, and 1.2.5), but they experience as well strong nuclear force interactions mostly resulting in projectile and/or target nuclei fragmentation. The nuclear interactions cause a decrease of the fluence (Φ) of primary ions with increasing depth (z) according to:

$$\Phi(z) = \Phi_0 \cdot e^{-N\sigma_r z} \tag{1.6}$$

where Φ_0 is the initial fluence of primary ions, N the density of nuclei in the target material, and σ_r the total reaction cross section. This exponential attenuation lowers the fluence of primary ions in the Bragg peak with respect to the entrance region. Consequently, the peak to entrance dose ratio is reduced (cf. figure 1.10(b)), since the Bragg peak is produced by a smaller number of primary ions. At low initial energies, the described effect is relatively small. For high energies, the depth-dose distribution shows a decrease of the plateau dose in depth due to the decrease of the primary ion fluence. In addition, there is a build-up of secondary charged particles and nuclear fragments, which can compensated to some extent the mentioned depth-dose decrease due to the depletion of primary ions. The target fragments typically deliver negligible dose contributions, in contrast to the charged secondaries and to the projectile fragments produced for ions heavier than protons. The latter have about the same velocity as the primary ions, but a lower charge Z and thus their range is in general larger than that of the primary ions. Because of this, they deposit dose even behind the Bragg peak, leading to the observed dose tail for heavy ($Z > 1$) ions (cf. figure 1.10(b)).

The lateral distribution of secondary particles is broader compared to that of the primary ions, also due to their stronger lateral scattering. When nuclear reactions are taken into account, the lateral dose profile should thus be described by a superposition of at least two Gaussian distributions with different widths (the narrower being related to the multiple scattering of the primary beam according to equation 1.5) in order to include also the beam halo from nuclear reactions. The broader shape these secondary distributions can lead to non-negligible amounts of dose off the central axis, especially if several ion pencil beams overlap (cf. figure 1.8).

Heavy ion nuclear reactions can be classified according to the value of the impact parameter between the trajectories of the two colliding nuclei. It is therefore possible to distinguish three main classes: central collisions, peripheral collisions and various Coulomb force induced processes (Crespo et al. 2006). For geometrical reasons peripheral collisions, where the beam particle loses one or few nucleons, are the most frequent reactions and they can be well described by the abrasion-ablation model as a two step process (figure 1.11, Serber 1947). In the first step, nucleons are abrated in the overlapping reaction zone ("fireball"), prefragments are produced within $\approx 10^{-22}$ s, while the outer "spectator" nucleons are only slightly affected (Hüfner 1985). In the second step ($\sim 10^{-21}$ s to 10^{-16} s), the excitation energy in the fireball and fragments is released by evaporation (ablation) of nucleons or clusters and by gamma emission. It should be mentioned that the reaction cross section σ_r is nearly constant at higher energies down to about 100 MeV/u. The higher number of fragments for high energetic ion beams, with related larger dose contribution, is a consequence of the longer path length traveled by the primary ions.

As the products of the nuclear reactions can be detected directly or indirectly, they play an important role for imaging purposes. For example, the positrons created as decay

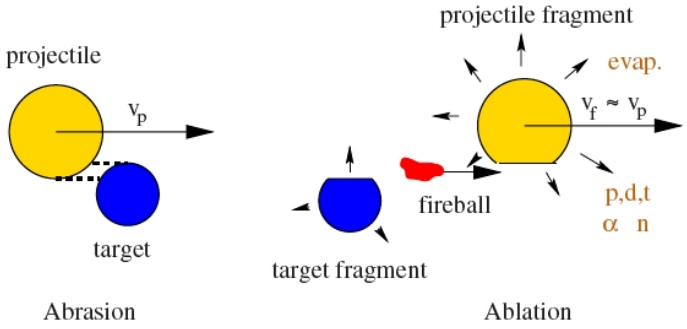

Figure 1.11.: Illustration of the abrasion-ablation model of peripheral collisions at high energies (Gunzert-Marx et al. 2008).

products of unstable nuclei among the fragments are used in the Positron Emission Tomography (PET). Secondary protons are directly revealed in Interaction Vertex Imaging (IVI). So-called prompt γ-rays result from de-excitation of products of the fragmentation process and might possibly be used in imaging applications. These different approaches will be discussed in more detail in section 1.5.2 and chapter 2.

1.3. Radio-biological rationale for ion beam therapy

One of the major rationales for the application of heavy charged particle beams in tumor therapy is their increased biological effectiveness due to the achievable high ionization density at the cell nucleus level. This increased effectiveness is usually expressed in terms of a macroscopically determined quantity, the relative biological effectiveness (RBE). This is defined as the ratio of the photon dose (typically 250 KV X-rays) and the dose of the particle radiation leading to the same biological effect (e.g., cell survival):

$$\mathrm{RBE} = \left.\frac{D_{\mathrm{Photon}}}{D_{\mathrm{Ion}}}\right|_{\mathrm{Isoeffect}} \tag{1.7}$$

The principle of the RBE definition is shown in figure 1.12, where it is also possible to appreciate that the RBE decreases with increasing dose, or equivalently decreasing cell survival.

Besides this relation, the RBE depends, e.g., on the considered cell type and the Local Energy Transfer[3] (LET, cf. figure 1.13). One of the advantages of heavy ions compared to protons originates from this LET dependence. In fact, it was shown that it is sufficient to apply only one single RBE value of 1.1 to the whole treatment field in the case of protons (Paganetti et al. 2002). Heavy ions, on the contrary, reach higher values of LET due to the

[3]The LET of an ion is defined as $LET_\Delta = {}^{dE_\Delta}/_{dx}$. It is the energy dE_Δ locally transferred to charged secondary particles of the medium per path length dx. Secondaries above a certain energy threshold Δ are not taken into account, as they are no longer absorbed locally. The so-called unrestricted LET with $\Delta = \infty$ is equal to the electronic stopping power (cf. equation 1.1 and figure 1.4).

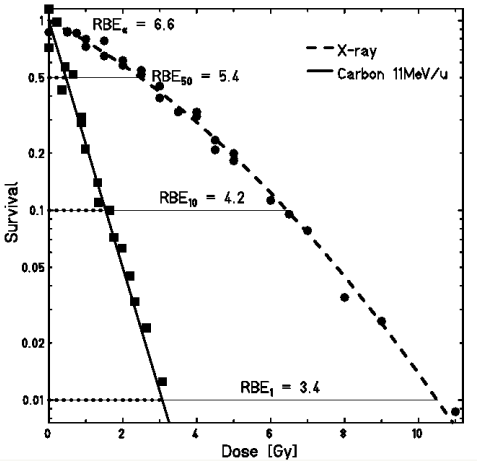

Figure 1.12.: Principle of the RBE definition for the cell survivsl of CHO-K1 cells exposed to different doses of X-ray and 11 MeV/u carbon ions as example of the biological endpoint (Krämer et al. 2003).

Z^2 dependence of the stopping power and therefore can achieve higher values of RBE, in particular around the Bragg peak, where ideally most biological dose should be deposited, as depicted in the right panel of figure 1.13.

The reason for the LET dependence of the RBE is the track structure (cf. figure 1.14) of the stopping ions. The local ion dose deposition is highly inhomogeneous on the scale of the cell nucleus and shows sharp peaks, as can be seen in figure 1.15 (Krämer et al. 2003), causing a dense ionization pattern and leading to complex, clustered DNA damages which are hard to be repaired and thus induce the higher biological effectiveness of high LET radiation. This phenomenon is enhanced for higher LETs (i.e., lower beam energies). On the contrary, a homogeneous X-ray local dose deposition causes only sparse ionization processes and the resulting DNA damages can be repaired easily by the cell.

Besides the increased RBE in the tumor compared to the normal tissue, heavy ions may offer a further biological advantage: The Oxygen Enhancement Ratio (OER), which is defined as the ratio of dose leading to the same effect in hypoxic and oxic cells or tissues, is reduced for heavy ions. This means that they are more effective in damaging the hypoxic cells of radio resistant tumors.

Due to the rather complex dependencies of RBE on various parameters, it can almost impossibly be represented by a single number to be used for converting physical dose to a homogeneous biological dose[4] (cf. figure 1.16). For this reasons, biophysical modeling is needed to help predicting the response to charged particle radiation from the known response of the biological object to photon radiation. Several biophysical models have been proposed for ion beam therapy (Scholz and Elsässer 2007). As an example, a so-called Local Effect Model (LEM) based on track structure (figure 1.15) calculations and cell response to X-rays was developed at GSI for clinical use in the GSI pilot project (Scholz and Kraft 1994). The first version of the LEM is also used at HIT in clinical routine to

[4]The biological effective dose or RBE weighted dose is normally expressed in GyE.

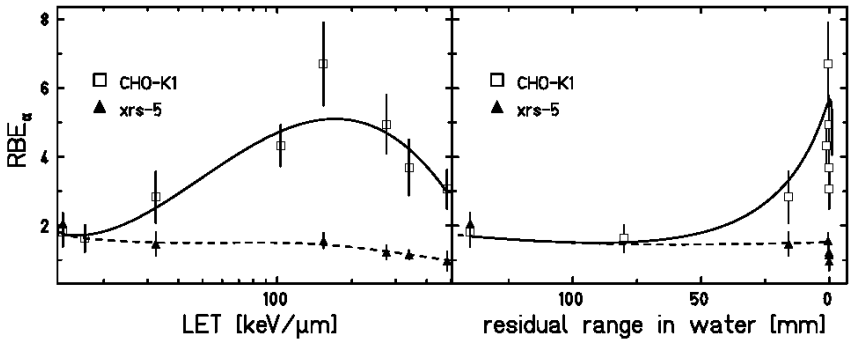

Figure 1.13.: RBE as a function of the LET (left) and of the residual range (right) of ^{12}C for CHO-K1 chinese hamster cells and their repair deficient mutant xrs-5 (Weyrather et al. 1999).

predict the cell response to a heavy ion beam irradiation. This model can also be used to predict the detector response in a mixed radiation field (cf. application for conventional film dosimetry in section 5.1).

1.4. Technical implementation of ion beam therapy

The implementation of heavy ion therapy is demanding due to the more complex dosimetric and radio biological issues related to the mixed radiation fields generated in the patient, but mainly because of the technically challenging requirements of the accelerator and beam delivery system. For this reason, heavy ion therapy has spread much slower than proton therapy.

1.4.1. Accelerator technology

In the last decades, relatively compact (mostly cyclotrons) and commercial solutions able to accelerate proton beams in the therapeutically relevant energy range of 50–250 MeV have become available. This has considerably boosted the worldwide development of facilities for proton therapy, which is nowadays a well-established technique.

Regarding heavy ion therapy, on the other hand, the challenging realization of synchrotron-based combined facilities (e.g. HIT, CNAO) has more recently been promoted by promising clinical results achieved so far with carbon ion beams (Hirao 2001, Schulz-Ertner et al. 2007). Currently, technological development is aiming at making ion beam therapy a compact-designed and commonly affordable treatment modality in the next decades. Novel concepts for the production of energetic proton and heavy ion beams include the use of compact superconducting cyclotrons (Maggiore et al. 2007), laser-based accelerator systems (Bulanov et al. 2004, Schwoerer et al. 2006), or dielectric-wall accelerators (Poole et al. 2007). These approaches have been proposed over the last few years and are being experimentally investigated in several laboratories worldwide (Parodi 2008).

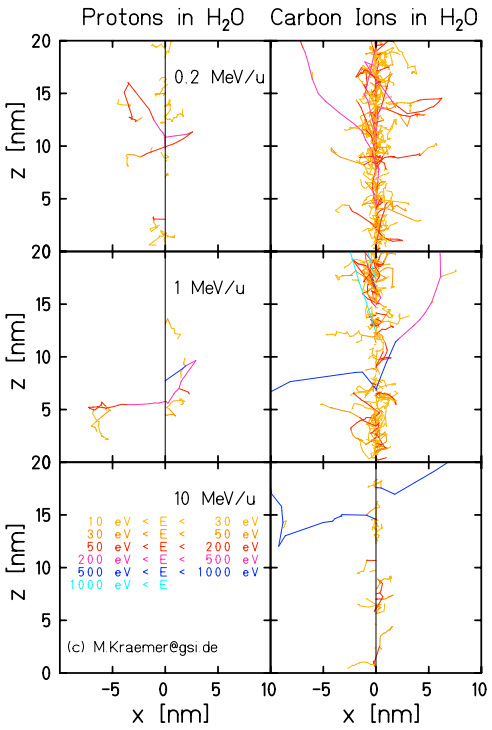

Figure 1.14.: Monte Carlo calculations of track structures of atomic electrons liberated by protons and carbon ions slowing down in water along the z axis (Krämer and Kraft 1994). The left panel shows that protons behave as sparsely ionizing radiation all along their penetration like photons. The right panel illustrates that carbon ions behave as sparsely ionizing radiation only at the higher energies corresponding to the entrance region in the healthy tissue (bottom panel). Differently, for lower energies occurring in the Bragg peak region (middle and top panel) carbon ions induce a much higher ionization density at the nanometer scale, which is responsible for clustered double strand breaks of DNA molecules in the tumor cells.

1.4.2. Beam delivery techniques

In the implementation of ion beam therapy, not only an accelerator system suitable for the desired ions has to be set-up, but it is also necessary to develop techniques to deliver the dose with a proper lateral and longitudinal conformation to the patient.

In the first experimental as well as commercial installations, "passive" techniques using a combination of scattering-foils, energy degraders (e.g., modulation wheels or range shifters) and beam shaping systems (e.g., collimators and boli) were applied to achieve the desired tumor-conformal beam delivery, as schematically illustrated in figures 1.17.

A disadvantage of these well-established methods is that they are intrinsically limited in the achievable distal and proximal dose conformality. Additionally, they lack the capability of a flexible, position-dependent modulation of the ion beam fluence. Moreover, the additional material in the beam path not only causes a physical as well as biological (i.e., in terms of diluted high-LET component for heavy ions) degradation of the primary beam quality. It also leads to the production of secondary radiation like neutrons, which

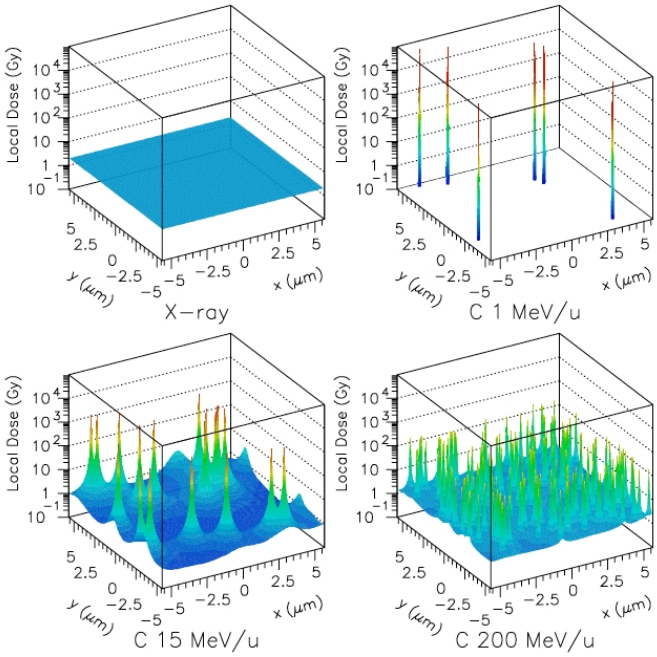

Figure 1.15.: Local dose distributions of X-rays and carbon ions at different specific energies. The average dose is 2 Gy in each case. The size of the area is 10×10 μm^2 and corresponds to the typical size of mammalian cell nuclei (Krämer et al. 2003).

poses an undesired hazard to the patient as well as shielding issues for radio protection of personnel and electronic equipment (Parodi 2008).

As an alternative to these "passive" techniques, "active" steering of the extracted ion beam via magnetic deflection has been proposed. In this approach, the beam is either swept over the target in circular patterns of different diameters ("wobbling", Renner and Chu 1987) to achieve homogeneous lateral broadening, or a pencil-like beam ($\approx$ 4-10 mm diameter) is "painted" laterally over an arbitrary complex tumor surface ("scanning", Renner et al. 1989), as sketched in 1.18, replacing both the scattering system and the transversal beam-shaping devices. In the latter approach, the conformality of the dose delivery in 3D can still be improved by combining 2D lateral scanning with a variation of the beam energy (i.e., penetration depth). This is done either actively at the accelerator level or with the help of a passive energy degrader, together with a significant reduction of the overall material in the beamline (Parodi 2008).

At the pioneering experimental facilities of PSI and GSI, more complex beam scanning technologies for safe and routine clinical operation in proton and carbon ion therapy have been demonstrated to be, both, feasible and reliable. The PSI introduced the so-called "spot scanning" technique (Pedroni et al. 1995) in which the proton beam is magnetically deflected in one dimension while the patient couch is moved in the other direction during treatment. The cyclotron beam is switched off by a fast kicker before moving from a spot in the treatment plan to the next yielding a discrete irradiation field. The longitudinal

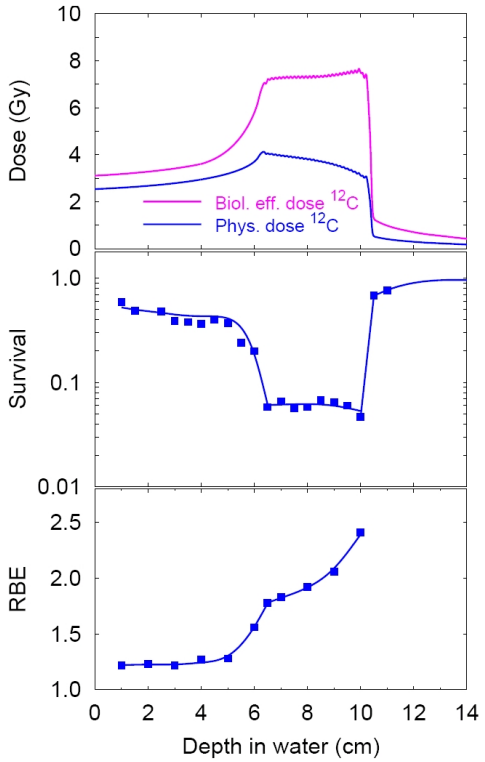

Figure 1.16.: Correlation between physical and biological dose, cell survival and RBE for carbon ion irradiation. The top picture shows the physical and biological dose for a SOBP ranging from 6 to 10 centimeter. The corresponding calculated (solid lines) and measured (squares) cell survival is shown in the middle picture and the corresponding RBE in the bottom picture (Crespo et al. 2006).

---

variation in depth is achieved by means of a passive range shifter. Fully 3D active "raster scanning" with continuous (i.e., beam always on during movement) 2D steering of a mono energetic pencil beam within each extraction cycle and variable adjustment of the beam energy, focus (i.e., lateral dimension) and intensity from pulse to pulse at the accelerator level has been first realized for carbon ion therapy at the SIS heavy ion synchrotron of GSI (Haberer et al. 1993).

Both techniques require that the desired amount of ions to be applied to each "spot" or "scan" position within the iso-energy (i.e., iso-depth) slices (IES), in which the target volume is virtually dissected, is monitored on-line and fed back to the beam steering unit. They therefore intrinsically offer the possibility to modulate the intensity, which allows to compensate partial irradiation of the more proximal slices when delivering the highest energy beams. Additionally, sharp dose gradients can be achieved yielding optimal coverage of the tumor volume with excellent sparing of the surrounding radio-sensitive OAR (Parodi 2008).

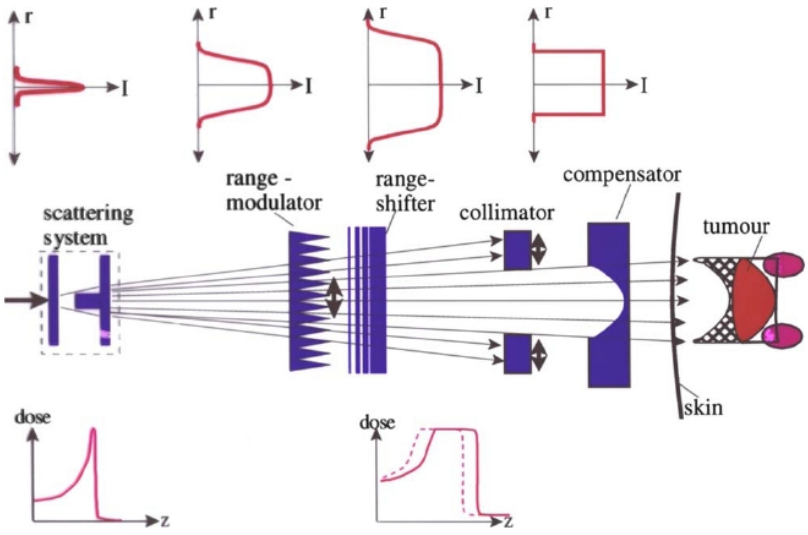

Figure 1.17.: Sketch of a fully "passive" beam shaping system. The initially narrow beam is broadened by a scattering system and adapted to the target volume by various passive beam shaping devices. Adaptation of the dose field to the distal contour of the target volume is achieved by a compensator, but results in unwanted normal tissue dose in the proximal part indicated by the doubly hatched area (Schardt et al. 2010).

1.4.3. Scanned ion beam at HIT

This section briefly outlines the beam delivery system used at HIT (Haberer et al. 1993), since it plays a fundamental role for the imaging investigations addressed in this thesis. A more detailed description of some aspects related to the experimental measurements carried out in this work are in reported in section 5.2.2.

At HIT, a synchrotron is used to accelerate the particles to the requested energy and to extract them into the subsequent high energy beam transport lines until the treatment/experimental rooms. A synchrotron demands a sequential procedure of particle injection, acceleration and extraction functions, in contrast to a cyclotron, in which these phases can be performed continuously. When the extraction is finished, the settings of the synchrotron components have to be changed in order to be ready for a new injection. The total time from one injection to the next is called "cycle time". The extracted beam is named "spill". Right now at HIT, its pulse length is about 5 s (∼5 s is also the average time to complete one IES during a patient treatment) and the time interval between two spills is of about 4-5 s. Once the extracted beam leaves the vacuum pipe line, it passes through a stack of independent detectors mainly consisting of ionization chambers (IC) and multi-wire proportional chambers (MWPC) within the Beam Applications Monitoring System (BAMS, Voss et al. 2005), as sketched in figure 1.19. This detector arrangement is required for the on-line control of the beam position, the beam dimension, the fluence, and for a feedback to the raster scan position control system.

In the raster scan technique, the delivery of an optimized 3D dose distribution into a predefined treatment volume is performed through series of 2D fluence distributions, i.e.,

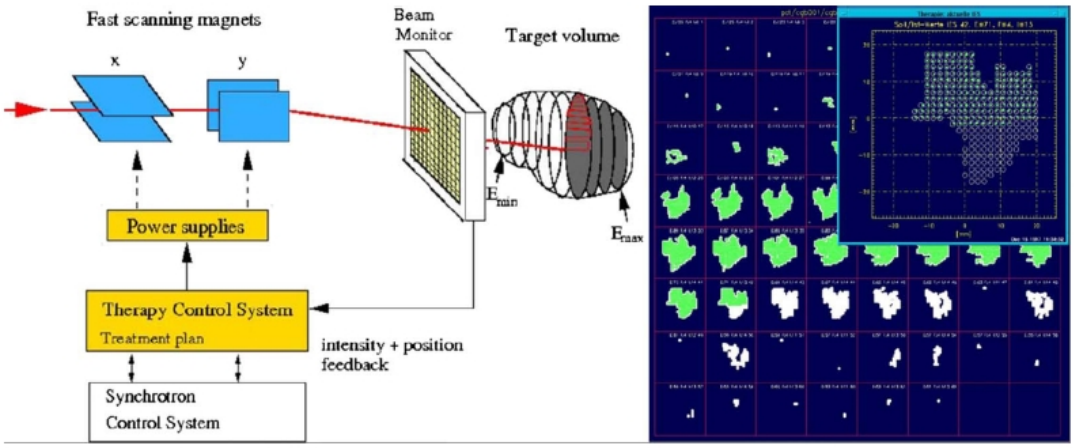

Figure 1.18.: Principle of the intensity-controlled magnetic scanning system. Left: The target volume is irradiated by moving a pencil-like ion beam with fast magnets over thin slices in depth. The required beam parameters are supplied on a pulse-to-pulse operation by the synchrotron control system. From (Haberer et al. 1993). Right: Beam's eye view of slices for a typical patient treatment plan. In each panel one slice is shown. The actually irradiated slice is seen in the magnified panel with the raster point positions indicated as open circles. The superimposed dots show the beam center positions measured on-line by a multiwire proportional chamber. The spot size of the beam is larger than the circles and overlaps many positions (Schardt et al. 2010).

varying number of stopping particles per mm^2 from one lateral scan position to another, at fixed initial energy. In this way, the treatment volume is virtually divided in series of isoenergy slices IES, corresponding to a fixed (water equivalent) depth. The selection of an IES is achieved by varying the beam energy at the accelerator level. The irradiation of each IES is performed with two fast scanning magnets (cf. figure 1.18), deflecting the beam in the transversal horizontal and vertical direction at steps Δx and Δy, respectively, to cover all the define raster points. The whole sequence of raster points for every IES necessary to cover the desired irradiation volume defines a plan/scan.

Typically, a tumor volume is divided into 20000 to 50000 raster points. At each raster point, one pencil beam of ions is applied, but an algorithm is needed to solve the complex task of overlapping the single pencil beams of each raster point. This algorithm has to optimize the dose delivered to the patient, taking into account the physical (e.g. Bragg peak shape, lateral scattering, cf. section 1.2) and biological properties of the ion beam (cf. section 1.3), as well as the fact that the dose of each raster point contributes to many different volume elements (i.e. voxel[5]). This task is performed by the Treatment Planning System (TPS) that, using an iterative optimization process, yields the number of particles to be delivered at each raster point.

[5]The dose in each volume elements comes from many different raster points. The dose in a voxel can, e.g. , be influenced by the dose delivered in two raster points of two subsequent IES.

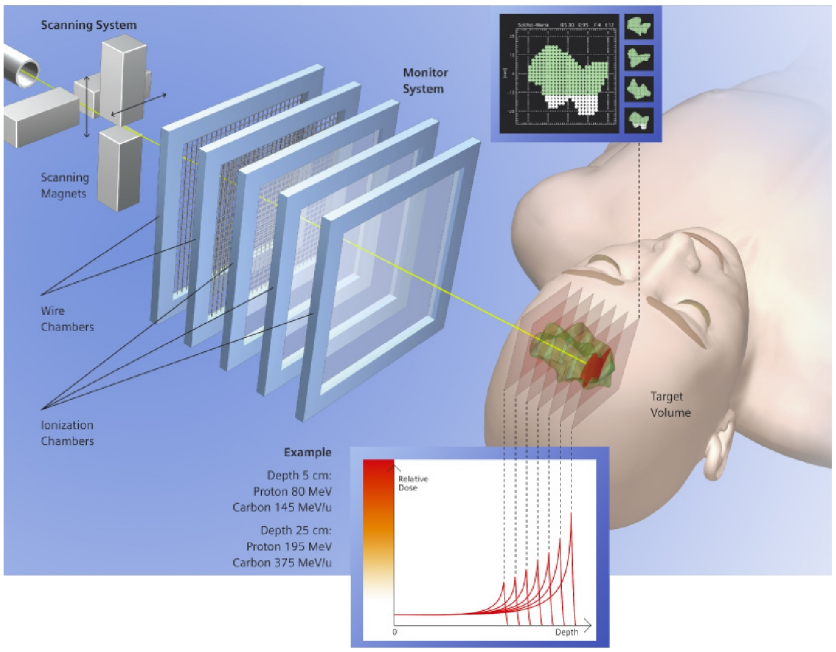

Figure 1.19.: Illustration of the 3D raster scanning technique at HIT. Lateral deflection is accomplished by the scanning magnets, the penetration depth is actively varied by adapting the synchrotron energy. The Beam Application Monitoring System (BAMS), consisting of three ionization chambers (IC) and two multi-wire proportional chambers (MWPC) in front of the patient is also shown. Figured adapted from Siemens Particle Therapy Technology (www.siemens.com).

At the GSI pilot project, the challenging task of treatment planning was accomplished by the dedicated TRiP (TReatment plannIng for Particles) software (Krämer et al. 2000, Krämer and Scholz 2000). At HIT, a commercial TPS from Siemens is used, which is however largely based on TRiP. To further optimize the treatment, at HIT the beam settings (e.g., energies, spot sizes and intensities, cf. section 5.2.2) are stored in corresponding libraries (Haberer et al. 2004), which are used by the TPS to generate the patient plans. These libraries were calculated with Monte Carlo (MC) simulations, performed with the FLUKA code (Ferrari et al. 2005, Battistoni et al. 2007, cf. section 3.1). Moreover, to set up the database, only some dedicated depth-dose distributions were measured accurately. These data were used to tune the FLUKA code to match the experimental results. The whole database was then generated by simulating the remaining depth-dose distributions for all other energies (Parodi et al. 2009).

1.5. The role of imaging techniques in ion beam therapy

This section briefly introduces the role of imaging at the different stages in the course of a heavy ion treatment.

The main physical advantages of ion beam therapy (cf. section 1.2) are due to the finite range of ions in tissue, determined by the position of the Bragg peak, which allows a precise dose delivery. The improvements in the achievable selectivity of the dose delivery have been accompanied over the last few years by an increasing role of imaging techniques to support precise diagnosis and identification of the target volume at the planning stage (Parodi 2008).

However, the ion selectivity can also cause adverse therapeutic results in case of tumor miss and/or accidental exposure of OAR due to incorrect delivery of the intended dose during the fractionated treatment course, provoked by uncertainties related to the accuracy of the patient set-up and immobilization, to the issue of organ motion for specific anatomical sites like the lung, the liver, the rectum and the prostate as well as to anatomical modifications (e.g., tumor shrinkage) and displacements (e.g., due to rectum or bladder filling). To account for these uncertainties, safety margins are typically added around the identified tumor volume when designing the treatment plan on the basis of X-ray Computed Tomography (CT) data of the patient anatomy (i.e. "planning CT"). In addition, imaging techniques can come to use to ensure the correspondence between the planning and treatment situation during the actual irradiation (Parodi 2008).

1.5.1. The planning CT

The ion treatment planning always starts with an imaging application (e.g. Magnetic Resonance Imaging (MRI), CT, PET) and in particular with the already mentioned "planning CT", which measures the photon attenuation coefficient μ without any contrast agent administrated to the patient. In a specific tissue x, μ_x is then converted to the Hounsfield Unit (HU) scale using the attenuation coefficient in water μ_{H_2O} as described by the following equation:

$$\mathrm{HU}_x = 1000 \cdot \frac{\mu_x - \mu_{H_2O}}{\mu_{H_2O}} \tag{1.8}$$

HU_x is a normalized value of the measured μ_x for a specific tissue. Normally in a CT, HU_{H_2O} is calibrated to be zero, while, e.g., $\mathrm{HU}_{air} \approx$ -1000. The ion beam range expressed in water equivalent (WE) thickness is then typically obtained using experimentally validated calibration curves of the water equivalent path length (WEPL), as shown in figure 1.20.

The theoretical background for this relationship is that the ratio between the ion stopping power in the considered material and in water is proportional to the relative electron density and thus correlated with the photon attenuation measured by the CT scanner. In practical applications, the HU-WEPL calibration curve is obtained from a piecewise linear fit to the measured differences (Δ) of Bragg peak shifts after the traversal of samples of known thickness (d) and experimentally determined HU values in comparison to water (i.e.,

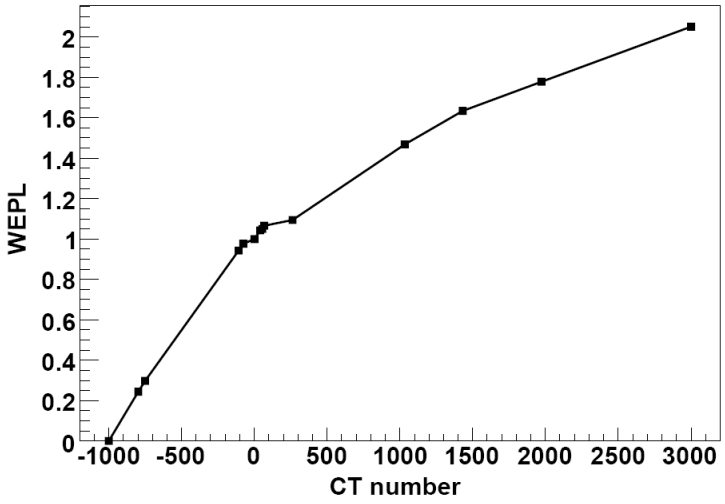

Figure 1.20.: HU-WEPL calibration curve used for carbon ion treatment planning at GSI (Rietzel et al. 2007). The straight line connects measured data points (circles) of WEPL (cf. equation 1.9), which have been acquired using the experimental set-up of figure 1.21(a) with different samples of tissue equivalent materials (Jäkel et al. 2001, Geiß et al. 1997).

$\mathrm{WEPL}_{H_2O} = 1$ and $\Delta = 0$, Rietzel et al. 2007, Jäkel et al. 2001, Schaffner and Pedroni 1998) as illustrated in figure 1.21 and described by:

$$\mathrm{WEPL(HU)} = 1 + \frac{\Delta}{d} \tag{1.9}$$

Due to the non-unique correspondence between HU numbers and materials in addition to unavoidable experimental uncertainties of the CT image (Rietzel et al. 2007) and of the HU-WEPL calibration curve, the accuracy of the ion range calculation in the patient is estimated to be within 1-3%. This corresponds to approximately 1-3 mm uncertainty in a patient at typical depths of 10 cm. A method to directly obtain the distribution of WEPL in the target volume would circumvent some of these uncertainties (cf. chapter 5). Besides that, HU values can be improperly assigned along the actual ion beam path due to artifacts (e.g., because of metallic implants, Jäkel and Reiss 2007) in the planning CT, or modifications of the patient position and/or anatomy in the treatment situation, introducing deviations up to $\approx$ 5-20% from the planned range (Parodi 2008).

Because of these intrinsic sources of range uncertainties, as well as the higher sensitivity of ion beam therapy to discrepancies between the planned and actual treatment situation (cf. figure 1.22, Enghardt 2005), cautious safety margins, which can hopefully be reduced in the future, are still used in routine ion treatment planning.

In the course of fractionated therapy, additional unpredictable range deviations can occur because of minor inaccuracies in the positioning of the patient or local anatomical changes with respect to the information of the planning CT, typically acquired several days before starting the therapy.

For all these reasons, tools for the visualization and monitoring of the particle distribution within the patient during the irradiation are strongly desirable (cf. chapters 2, 5, and 5).

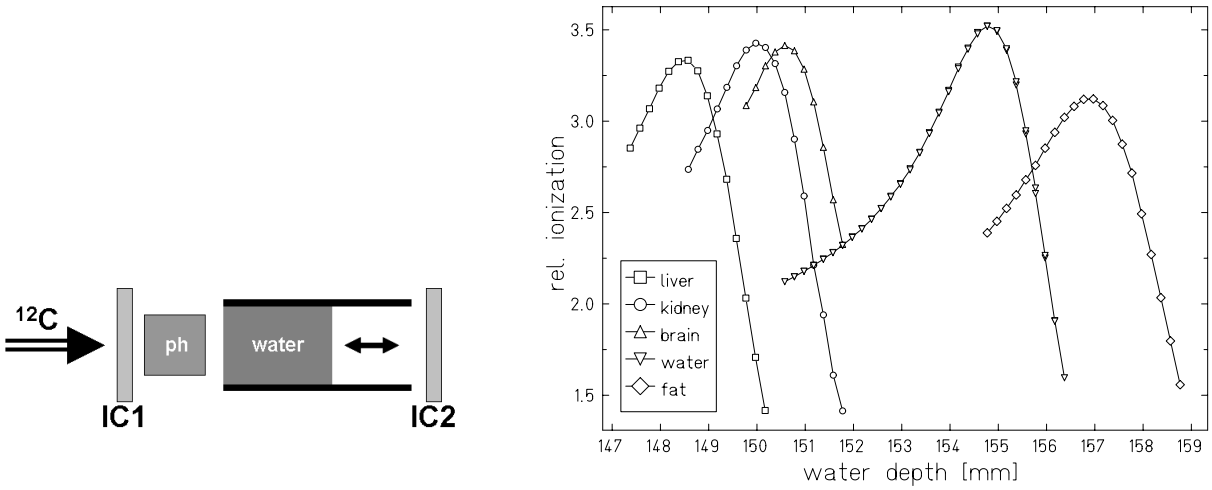

(a) Measurement set-up for carbon ion radiography

(b) Measurement results for WEPL

Figure 1.21.: (a) Schematic representation of the experimental set-up used at GSI to acquire residual carbon ion ranges behind the sample (ph) by varying the thickness of a water absorber. The relative measurement is performed using two parallel plate ionization chambers (IC1, IC2) (Rietzel et al. 2007, Jäkel et al. 2001, Schaffner and Pedroni 1998). (b) Examples of relative ionization curves acquired for different tissues and the water reference (Rietzel et al. 2007). According to equation 1.9, it follows that only the sample of fat tissue exhibits a lower WEPL (i.e., $\Delta < 0$) than that of water.

1.5.2. Brief overview of ion beam imaging techniques

Nowadays, the only technically feasible method fulfilling the requirement for a 3D, non-invasive, in-vivo monitoring of the delivered ion treatment and, in particular, of the beam range in the patient is the PET. However, various alternative or complementary techniques are currently being explored. Some of them try to exploit the emerging secondary radiation (e.g., photons as well as light fragments, cf. section 1.2.5), produced during nuclear interactions, while others make use of primary ions at higher energy than used in a treatment for obtaining low dose transmitted planar (radiographic) or volumetric (tomographic) images of the patient.

These novel imaging techniques can come to use in different phases of a patient treatment. In fact, PET (cf. section 2.1) is carried out during or after the irradiation, the techniques based on the detection of prompt photon radiation (cf. section 2.3) and IVI (cf. section 2.2) are performed simultaneously to the beam delivery, and the Heavy Ion Computed Tomography (HICT, cf. section 2.4) can be applied before or in-between the treatment.

A more detailed description of the current and proposed imaging modalities in ion beam therapy is presented in chapter 2.

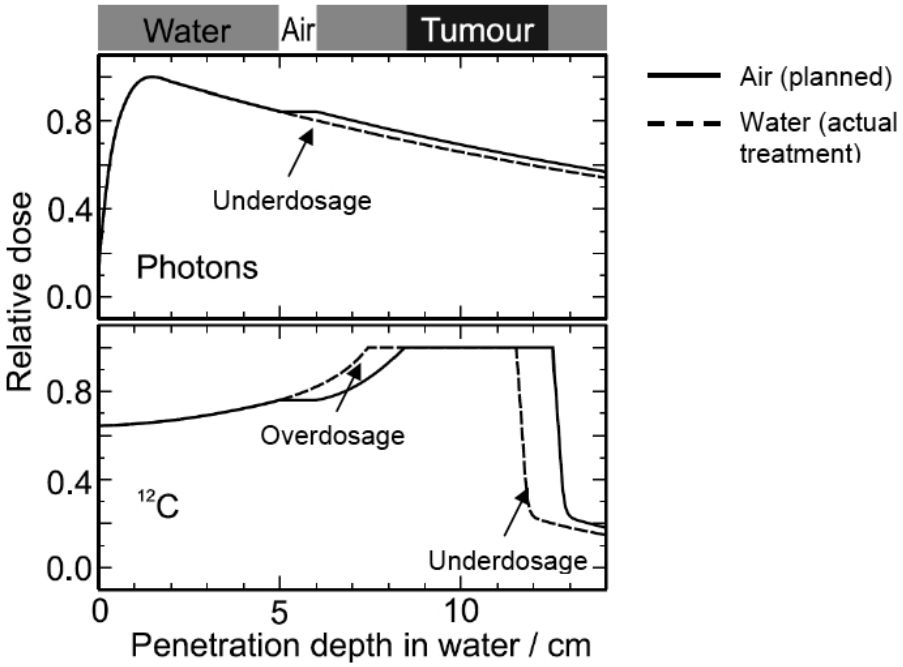

Figure 1.22.: Depth-dose deposition in water by a 6 MV photon beam (top) and a carbon ion extended treatment field (bottom) in the reference condition with a 1 cm air gap in the beam path (solid line) as well as in the case of an unexpected filling of the cavity with water (dashed line, e.g., simulating the presence of mucus in a nasal cavity, Enghardt 2005). Whereas the anatomical change has only a marginal influence on the photon depth dose deposition, a substantial overdosage in the healthy tissue proximal to the tumor as well as a drastic underdosage in the distal part of the tumor is introduced in the case of carbon ion irradiation.

1.6. Aim and outline of this thesis

The aim of this thesis was to investigate two possible novel imaging techniques for future application at HIT. In fact, at HIT a PET/CT device has recently been installed nearby the treatment rooms for post-treatment verification. However, it would be desirable to complement off-line PET with additional novel in-situ imaging techniques. For this purpose, within this thesis, emission imaging techniques were investigated principally using MC calculations based on the FLUKA code, while experimental studies were carried out to address the feasibility of ion-based radiographic or tomographic transmission. These novel imaging techniques could be performed, as shown in figure 1.23, using:

1. **emerging secondaries**, in particular gammas, from the therapeutic beams (E_T) to verify simultaneously and in-vivo the treatment delivery (cf. chapter 4)

2. **transmitted** high energy (E_H) **primary particles** for low dose 2D and 3D imaging

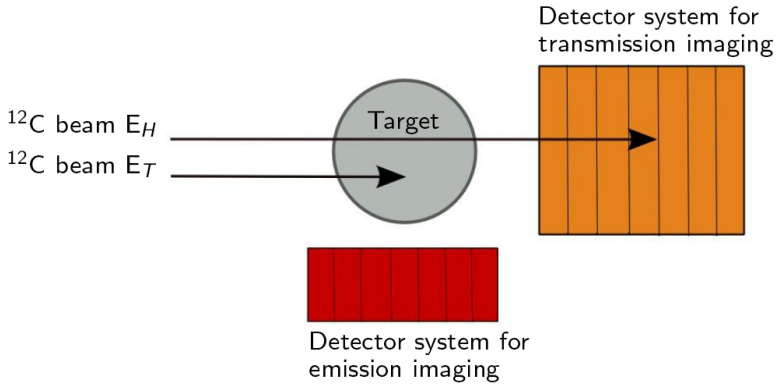

Figure 1.23.: Schematic representation of the alternative or complementary techniques to PET investigated in this thesis performed using: **transmitted** high energy (E_H) **primary particles** or **emerging secondaries** from the therapeutic beams (E_T).

---

to evaluate the correct patient positioning and verify the ion range before or in between the treatment, especially to reveal morphological modification and motion. Ideally, HICT also aims at substituting the use of the planning CT and HU-WEPL calibration curve, providing directly a map of the WEPL in a patient (cf. chapter 5).

The investigations presented in this work regarding HICT have been so far concentrated on carbon ion beam due to the mentioned advantage of reduced lateral beam scattering in comparison to protons. Moreover, HIT offers the unique clinical availability of the worldwide first heavy ion beam gantry, as well as scanned carbon ion beams accelerated with a synchrotron which is able to provide the initial energies needed to perform HICT.

The thesis is organized in the following way: In the second chapter, the state of the art of imaging modalities in ion beam therapy is reviewed. Starting from PET, the only nowadays already clinically used technique, the chapter then gives an overview of new methods based on the detection of prompt gamma radiation. Moreover, ion-based imaging techniques are presented. Some of them use heavier fragments (e.g., protons) produced during ion irradiation, while others consider the primary beam particles directly (e.g., protons, carbon ions), yet with a higher initial energy (still in the therapeutic range) than used for treatment.

The third chapter introduces the MC method as useful tool to simulate the complex process of interactions with matter, especially for ion beam therapy applications. In particular, the FLUKA MC code is presented as a reliable tool to support and validate experimental investigations for ion beam therapy. Moreover, a specific benchmark of the FLUKA code against experimental data in the case of a proton beam using Multi Layer Faraday Cups is reported.

Chapter four presents investigations regarding the prompt gamma imaging. The studies were performed with the help of the FLUKA MC code in the framework of the FLUKA collaboration, using a dedicated development version, kindly provided by the FLUKA developer team. In particular, results are shown for the comparison between FLUKA

calculations and experimental data using carbon ion beams. Moreover, MC studies for different target complexity scenarios using proton beams are reported. These were carried out to investigate main features of the prompt gamma detected signal ultimately aiming at setting up a detector properly designed in order to obtain an optimum signal.

In the fifth chapter, the most extensive part of the thesis, experimental investigations carried out at HIT to address the feasibility of low dose 2D and 3D imaging with transmitted high energy carbon ions are presented. First of all, the clinical feasibility of HICT at HIT is demonstrated. Then, following the encouraging results of the first experimental proof of principle, the chapter reports in detail experimental characterizations and results obtained with a dedicated experimental set-up. The detector has been composed in collaboration with colleagues from GSI and consists of 61 parallel-plate ionization chambers interleaved with 3 mm Polymethyl methacrylate (PMMA) absorbers.

Finally, general conclusions and an outlook are given in the last chapter.

Chapter 2

CURRENT AND PROPOSED IMAGING TECHNIQUES IN ION BEAM THERAPY

In this chapter, a brief overview of the current and proposed imaging modalities in ion beam therapy is given. In particular, the review starts describing the work already done in the field of Positron Emission Tomography (PET), underlying its potentiality and limiting factors (cf. section 2.1). Afterwards, the techniques under investigation using the detection of fragments produced during nuclear interactions are presented. The attention is concentrated on the Interaction Vertex Imaging based on the detection of charged particles (e.g., protons in case of carbon ion beams) emerging from a patient (cf. section 2.2). Moreover, techniques based on the detection of prompt gammas originated from de-excitation of nuclear fragments are reviewed in more detail since they are linked to the studies carried out within this thesis, reported in chapter 4. Finally, section 2.4 introduces the approach of the heavy ion CT (HICT), which has been extensively investigated within this thesis from the experimental point of view (cf. chapter 5).

2.1. Positron Emission Tomography

Presently, PET is the only clinically investigated method for in-vivo and in-situ monitoring in charged particle therapy (Enghardt et al. 1992). The physical principle of PET-based verification of ion beam therapy is that during therapeutic irradiation, positron emitters, such as ^{11}C, ^{15}O and ^{10}C, are produced inside the patient by nuclear fragmentation reactions between the projectiles and the target nuclei of the traversed tissue (cf. section 1.2.5). PET scanners can detect the photon pairs resulting from the annihilation of the positrons in a patient either during (on-line) or after (shortly after: in-room, with greater delay: off-line) treatment. These measured activities are successively compared with MC simulations based on the prescribed beam plan providing a non-invasive validation method of

the whole treatment planning and delivery chain (Parodi et al. 2008).

Promising results were achieved so far for ion-based PET imaging for in-vivo verification of ion treatment and beam range. The first clinical activities showed the usefulness but also the limitations of in-vivo PET range verification. The pioneering investigations were performed at GSI during the pilot project using a dedicated in-beam double-head detector integrated into the experimental treatment room for carbon ion therapy (Enghardt et al. 2004a, Parodi 2004). Afterwards, at Massachusetts General Hospital (MGH) in Boston, a commercial PET/CT scanner was also used for post-treatment imaging in proton therapy (Parodi et al. 2007, 2008).

The differences of these two technical implementations of PET are summarized in the following. At GSI, the acquisition was performed in between the spill extraction pauses with a data acquisition system synchronized with the beam delivery and for approximately 40 s after each irradiation with a limited angle detector (Enghardt et al. 2004a). It is evident that in-beam solutions are technically very demanding but, on the other hand, offer the possibility of monitoring individual fields in the treatment position without losing the significant activity contribution from the short-lived ^{15}O emitter. At MGH, the patient is moved, shortly after the irradiation, to a commercial PET/CT scanner in close proximity to the treatment site (Parodi et al. 2008). The off-line solution is used nowadays also at HIT. It has been also investigated at the HIMAC facility, although it is not yet used in clinical routine for carbon ion dose verification (Schardt et al. 2010). An advantage of the off-line PET is the use of commercially available full-ring PET scanners that typically offer better imaging performance with respect to in-beam limited angle detectors. The main drawbacks are patient re-positioning issues as well as the loss of signal from short-lived positron emitters and the larger influence of metabolic processes in the time elapsed between irradiation and imaging. Moreover, post-treatment imaging only detects the integral beam delivery, with a loss of range information in the case of multiple treatment fields (Parodi et al. 2008).

The characteristics of PET imaging depends on the primary beam used in the treatment. In figure 2.1, the differences between PET monitoring performed for an irradiation with proton and carbon ion beams are depicted. For irradiation with carbon ions (left panel of figure 2.1), a peak in the β^+-activity is formed in close proximity to the Bragg peak since the main contributions to the PET signal are given by the positron emitters ^{10}C and ^{11}C projectile fragments. In fact, carbon isotope projectile fragments keep approximately the same velocity as the primary carbon ions and therefore have almost the same range due to the A/z^2 dependence (cf. section 1.2.2). Consequently, the maximum of positron radioactivity is formed at the end of the β^+-activity profile not far away from the Bragg peak position in the primary depth-dose distribution. On the contrary, the correlation between the proton depth-dose curve and the β^+-activity profile (right panel of figure 2.1) is poorer due to the lack of projectile fragmentation which implies that no maximum of positron radioactivity is formed at the end of the primary proton range (Parodi et al. 2002). Nevertheless, this lack of peak structure in the activity profile for proton beams is balanced to some extent by the three times higher total induced activity for the same range and dose delivery (Parodi et al. 2002), which is due to the about 20 times higher number of protons compared to carbon ions necessary to deliver the same physical dose (Kraft 2000). The ratio could further increase in favor of protons when comparing the

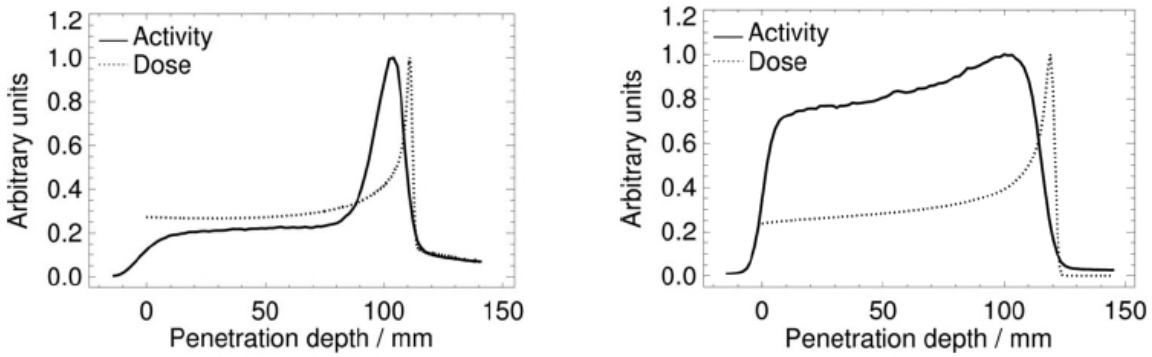

Figure 2.1.: Measured autoactivation of thick PMMA targets by means of 260 MeV/u carbon ions (left) and 140 MeV protons (right). The solid lines show the depth profiles of the measured β^+-activity. For comparison the depth-dose profile of the primary beam is shown as dotted line. Figure from (Parodi 2004).

same biological effective dose.

Applications of proton off-line PET for range monitoring were feasible for head and neck cases in well co-registered low perfused bony structures, however challenges for millimeter accurate range verification were encountered especially in extra-cranial anatomical locations due to limiting factors such as physiological washout, co-registration, and motion (Knopf et al. 2011).

In any case, the main drawback of PET imaging applied to particle therapy is the low β^+-activity[1] induced by fragmentation: about 200 Bq Gy^{-1} cm^{-3} for ^{12}C and about 600 Bq Gy^{-1} cm^{-3} for protons (Enghardt et al. 2004b). Moreover, the positron activity is correlated but not directly proportional to the spatial pattern of the delivered dose (Schardt et al. 2010).

In clinical routine, the therapy control is achieved by visually comparing the measured β^+-activity distribution with a MC prediction based on the treatment plan and the specific time course of the irradiation (cf. figure 2.2). In case of observed discrepancies between the measured and expected PET images, the radio-oncologist is provided with a quantitative estimation of the deviation between the planned and actually applied physical dose (Parodi 2004). Before the next irradiation fraction, the radiotherapist can, e.g., expose the patient to a new X-ray CT for further investigation of possible anatomical changes and, in case of significant deviation between the planned and applied dose, a new treatment plan can be elaborated.

To summarize, the PET monitoring technique, especially in the on-line implementation, allows to monitor the maximum ion range, to verify the field position, and to detect deviations in the patient positioning or local changes of the patient anatomy in the course of the fractionated treatment (Schardt et al. 2010). On the other hand, unfortunately, 3D tomographic in-beam PET solutions are, nowadays, not commercially available, but

[1] The irradiation-induced activity is 2-3 orders of magnitude lower than in conventional tracer imaging in nuclear medicine PET.

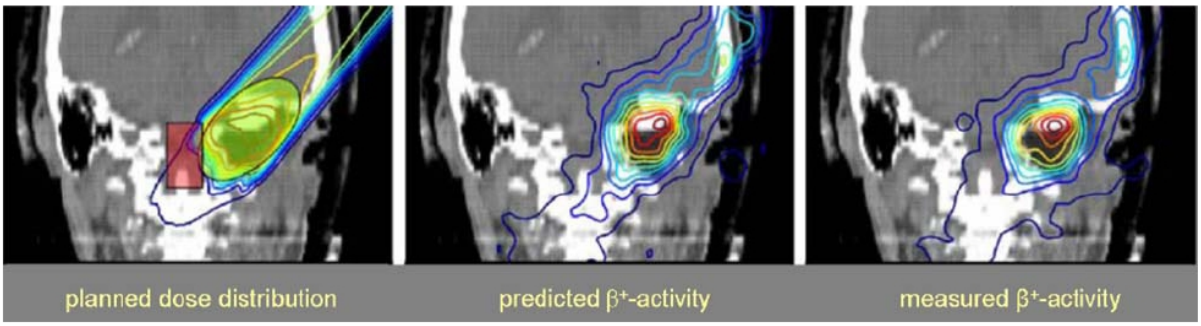

Figure 2.2.: Example of in-beam PET monitoring showing the irradiation of a skull base tumor at GSI. Left: Planned dose distribution superimposed on the CT image. The target volume and the brain stem as an OAR are highlighted. Middle: Predicted β^+-activity distribution calculated from the treatment plan and time course of the irradiation. Right: Measured β^+-activity distribution. By comparison with the prediction it was verified that the carbon ions were correctly stopped before the brain stem (Crespo et al. 2006).

research is ongoing in several groups to realize new generation dedicated detector solutions.

2.1.1. Ion range verification with in-beam PET at GSI

The systematic deviations observed between measured and calculated PET images in the early therapy sessions at GSI in 1998 indicated a lack of accuracy in the planned carbon ion range, especially in the soft tissue region (Parodi 2004). These deviations were attributed to the non-optimal calibration of the correlation curve between HU-WEPL[2] (cf. section 1.5.1 and figure 1.20) that was therefore successively corrected (Enghardt et al. 1999, Rietzel et al. 2007). Consequently, the in-vivo verified improvement in the reliability of the TPS ion range calculation in tissue allowed extending treatment plans to more critical irradiation fields, like the cranio-lateral portal of figure 2.2 in which the beam has to be stopped precisely in the tumor in front of the brain stem, that in this case represents the OAR.

The analysis of in-beam PET images for 205 patients treated at GSI until 2003 led to new X-ray CT re-exposure for six of them. In five cases the investigation confirmed a local anatomical change and for one patient a new treatment plan was elaborated. For the sake of objectivity, it has to be pointed out that, in practice, proper safety margins and careful selection of the beam portals help avoid too delicate irradiation fields. Therefore, in all the observed cases of ion range deviation, no serious clinical consequences were encountered (Parodi 2004).

More recently, Fiedler et al. (2010) performed a first quantitative study on the accuracy of the in-beam PET method to detect range deviations between the planned and applied treatment in clinically relevant situations using MC simulations based on clinical data obtained with 81 patients treated at GSI. For each patient, a range difference of ±6 mm in water was virtually applied to produce simulated PET images which were then blindly

[2]It has to be remarked that the PET calculations and the TPS used the same HU-WEPL calibration curve.

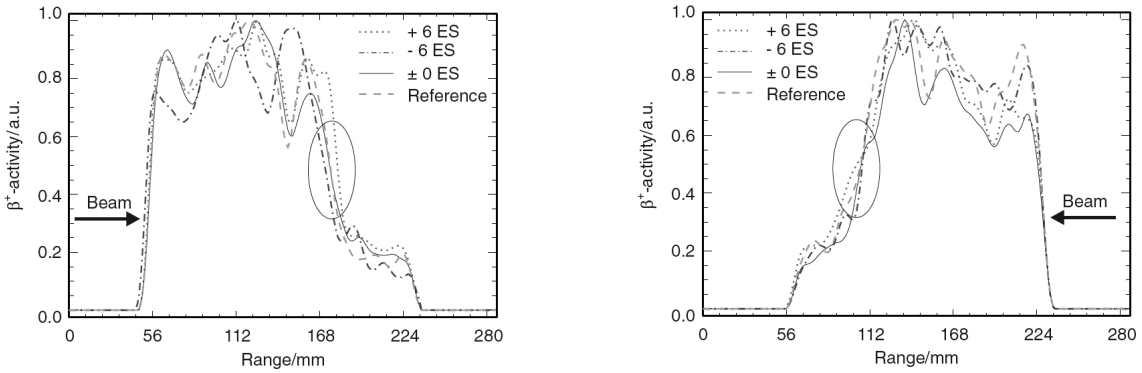

(a) Correct recognition of differences in ranges

(b) Incorrect recognition of differences in ranges

Figure 2.3.: Profiles of reconstructed β^+-activity distribution taken in a beam direction crossing the isocenter of the treatment room, coinciding with the center of the field of view of the PET camera. The different activity distributions are drawn for range variations of ±6 energy steps (ES) corresponding to projected range variation in water of ±6 mm. The 0 ES curve differs from the reference distribution only by statistical fluctuations during the simulation. The region where the range difference is expected is marked as an ellipse. In (a) it is shown a case of a patient in which the larger and smaller ranges have been correctly recognized while in (b) it is shown an example of patient in which the majority of the evaluators failed to detect the differences in ranges. Figure adapted from (Fiedler et al. 2010).

visually compared by six experienced evaluators, together with the reference PET images without any change. The results indicate that larger and smaller ranges have been recognized by the evaluators in about 90% of the cases. Nevertheless, there is strong evidence that specific effects may impede the visibility of range deviations, such as beam passing through highly inhomogeneous tissues, large irradiation volumes as well as low doses. As an example, figure 2.3 illustrates the profiles of the reconstructed β^+-activity distribution taken in a beam direction crossing the isocenter of the treatment room, which coincides with the center of the field of view of the PET camera. In figure 2.3(a), a case of a patient is represented in which the larger and smaller ranges on the PET images have been correctly recognized while in figure 2.3(b), the majority of the evaluators failed to detect the range differences.

2.2. Interaction Vertex Imaging

An alternative technique for ion therapy monitoring and range verification is the IVI (c.f figure 2.4), especially attractive in the case of pencil beam scanned delivery. The IVI is based on the detection of secondary charged particles emerging from the patient, that were generated in nuclear interactions between the incoming ions and target nuclei (cf. section 1.2.5). This technique is currently under investigation, e.g., by a collaboration between

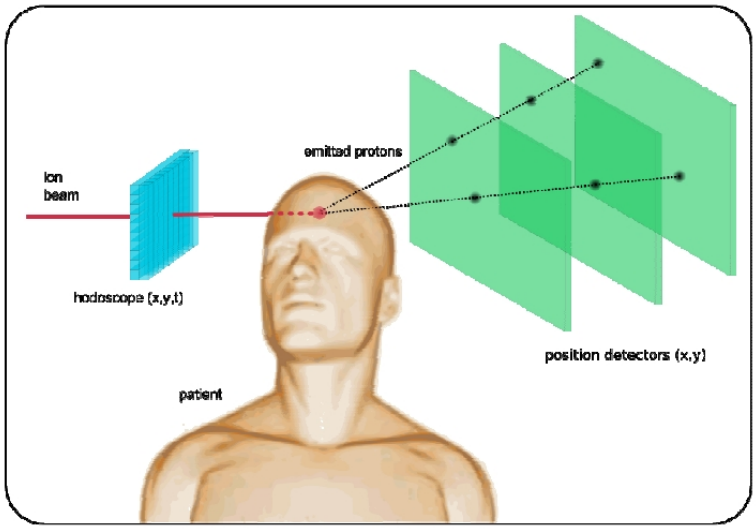

Figure 2.4.: Artistic scheme of the IVI system. The hodoscope tags the ions in time and space coordinates. In single-track vertexing, the vertex is reconstructed as the intersection of the emerging particle trajectory and the beam direction provided by the hodoscope. In multi-track vertexing, the vertex is reconstructed by the intersection of two or more emerging particle trajectories arising from the same fragmentation point. Figure adapted from Dauvergne et al. (2009).

---

the groups of Lyon (Institut de Physique Nucléaire de Lyon and CNDRI-INSA, working on the Regional Research Program for Hadron Therapy (ETOILE)) and the TERA (Therapy with Hadronic Radiations) foundation (Henriquet 2010) and also in the framework of the Advanced Quality Assurance project (AQUA, `http://project-aqua.web.cern.ch/project-aqua`) for CNAO. There are two main advantages which make IVI a potentially attractive technique: The detection of charged particles is easier and the counting statistic potentially achievable is larger (i.e., 2-3 orders of magnitude, Henriquet 2010) compared to systems that detect, e.g., photons (Braunn et al. 2010, Gunzert-Marx et al. 2008, Testa et al. 2010). This possible new technique is based on the reconstruction of the trajectories of the emerging particles which are then extrapolated back to their production point (Dauvergne et al. 2009). Indeed, the position of the fragmentation points are expected to be correlated with the ion range, and the amount of emerging charged particles could be, in principle, correlated to the dose. Figure 2.5 illustrates the possible correlations of proton interaction vertex profiles and the Bragg peak position obtained with a GEANT4 (Agostinelli et al. 2003, Allison et al. 2006) MC simulation of 400 MeV/u carbon ion beams hitting a PMMA target.

The vertex reconstruction can be done with two different techniques based on the particle multiplicity arising from each fragmentation vertex. In the simplest form, also named single-track vertexing, the vertex is reconstructed as the intersection of the emerging particle trajectory and the beam direction provided by the hodoscope. While in the more complex so-called multi-track vertexing, the vertex is reconstructed by the intersection of two or more emerging particle trajectories arising from the same fragmentation point (cf.

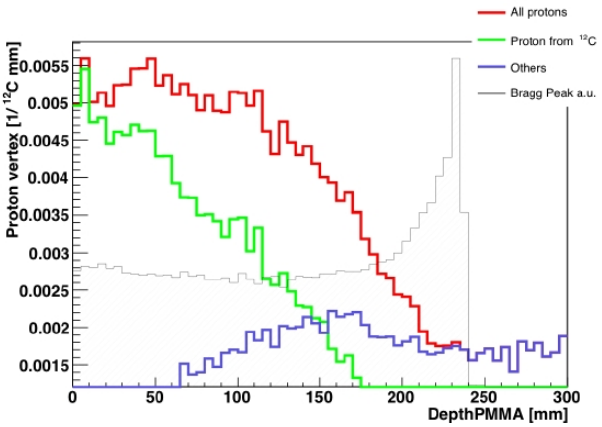

Figure 2.5.: Vertex distribution of emerging primary, secondary and total protons created by 400 MeV/u carbon ions impinging onto a PMMA target simulated with the GEANT4 MC code. The respective Bragg curve is also illustrated in arbitrary units. While not directly representing the dose distribution, a measurement of the interaction vertex distribution is somewhat correlated with the Bragg peak position. Figure adapted from the AQUA project website (`http://project-aqua.web.cern.ch/project-aqua`).

figure 2.4 and Henriquet 2010).

2.3. Prompt gamma radiation

Prompt gammas are mainly produced in de-excitation processes during nuclear interactions (cf. section 1.2.5). The detection of prompt gamma profiles can be, in principle, correlated to the Bragg peak position providing one dimensional information on the ion range in a patient, especially suitable for pencil beam scanning.

In the case of protons, the measurement of the emitted prompt photons, detected at an angle of 90° with respect to the incident direction of a 100 MeV proton beam, has verified the correlation with the Bragg peak position with an accuracy of 1-2 mm (cf. figure 2.6, Min et al. 2006).

More recently, the discussion about the potential use of prompt gamma emission as a method to verify the accuracy and efficacy of doses delivered with proton radiotherapy was raised by Polf et al. (2009a,b). In a first work based on MC simulations (Polf et al. 2009a), the results of a preliminary study on secondary prompt gamma emission produced within tissue during proton irradiation are presented. A second work (Polf et al. 2009b) presents the results of comparisons between measured and simulated prompt gamma spectra using a detector, shielded either with lead (passive shielding) or a Compton suppression system (active shielding). Although in both studies the analysis focused mainly on the characteristics of gamma spectra emitted during proton irradiation of elemental and tissue targets, a correlation was found between the delivered SOBP dose distribution and the characteristic prompt gamma production (cf. figure 2.7).

The first proof of principle for carbon ion beams was performed by the Lyon groups at the

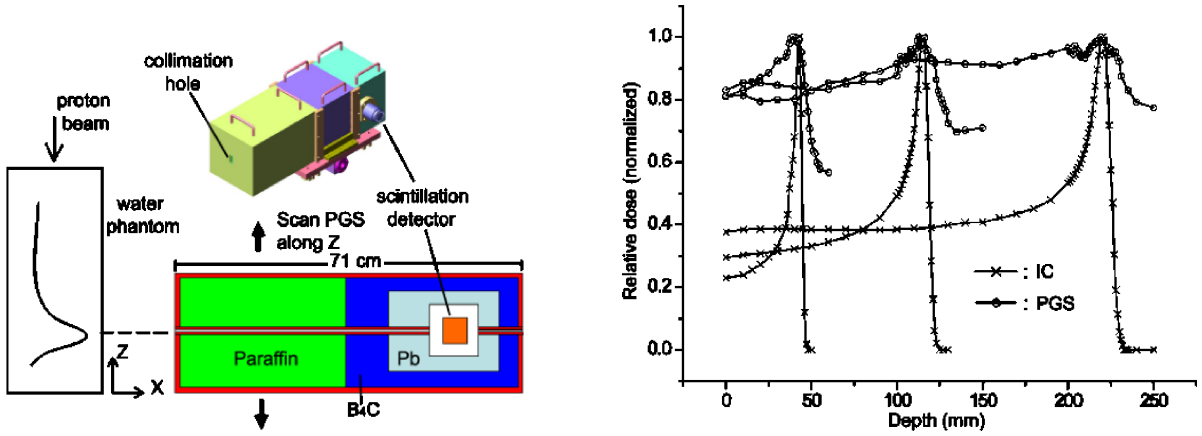

(a) Experimental set-up

(b) Correlation between the Bragg peak locations and prompt gamma scans along the beam penetration in water

Figure 2.6.: (a) Experimental set-up used by Min et al. (2006) for right-angled measurement of prompt gamma induced by proton beams slowing down in water. A collimator system consisting of lead, paraffin and B_4C powder is used to suppress the considerable background from scattered photons and neutrons, respectively. The gamma detector is a CsI(Tl) scintillator. (b) The resulting prompt gamma scans (PGS) along the beam penetration in water are compared in the 2.6(b) to depth dose measurements taken with an ionization chamber (IC) to illustrate the correlation with the Bragg peak location.

GANIL facility (Caen, France) in 2007 with 73 MeV/u $^{13}C^{6+}$ ions impinging on a PMMA target. The correlation between 90° angled prompt photon profiles and the Bragg peak position, obtained for a carbon ion beam in which both, target nuclei and primary ions, undergo nuclear fragmentation (Testa et al. 2008), is shown in figure 2.8, when properly discriminating the photon signal.

Other experimental investigations with carbon beams were performed in the following years at GANIL and GSI (Testa et al. 2009, 2010) and details of some of these experiments will be presented and discussed in chapter 4. The main feature of these experiments is the introduction of time of flight (TOF) discrimination between prompt photons and background radiation, especially neutrons, avoiding the use of bulky neutron shielding like in the case of the work presented by Min et al. (2006). This feature is of particular importance since it allows the use, in case of scanned ion beam delivery, of a stacked multi-detector set-up that, in principle, can be employed clinically for real-time in-situ ion range monitoring.

The major drawback of this technique, on the other hand, is the low achievable counting statistic of measured gammas, also related to the detector efficiency. The Lyon groups have measured the net gamma count rate along the primary ion path per incident carbon ion, unit solid angle, and unit path length for a primary beam of 95 MeV/u ^{12}C impinging onto a PMMA target and using a single scintillator (e.g., BaF_2) for gamma detection. The value was found to be $\approx 1 \cdot 10^{-7}$ gammas ion^{-1} msr^{-1} mm^{-1} (Testa et al. 2010). A patient treatment plan in which, e.g., $7 \cdot 10^8$ carbon ions are required to deliver an absorbed dose

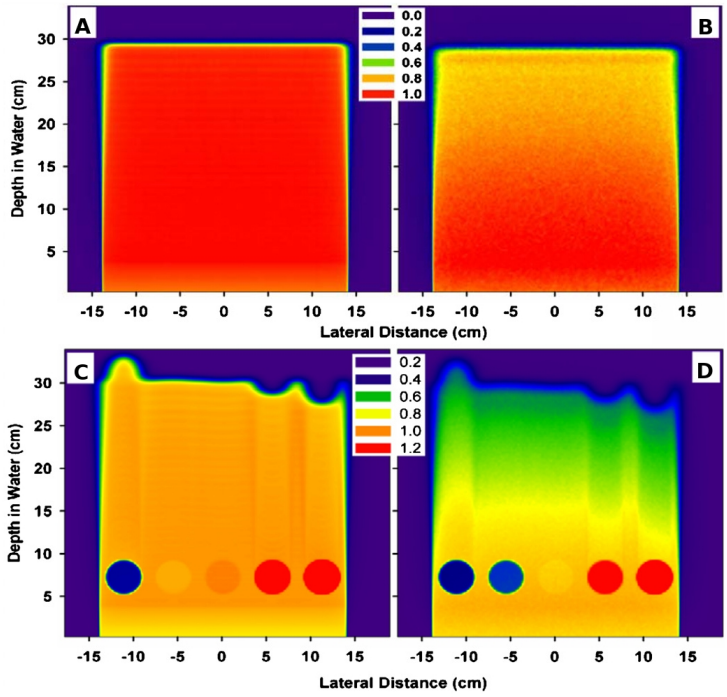

Figure 2.7.: Two-dimensional profiles for (A) a proton SOBP in a homogeneous water phantom and (B) the corresponding gamma production as well as (C) a proton SOBP in a water phantom with cylindrical compact bone (12 cm), rib (6 cm), muscle (0 cm), fat (-6 cm) and lung tissue (-12 cm) inserts and (D) the corresponding gamma production. Each graph is normalized to a point along the beam central axis (x=0 cm) at the proximal edge of the SOBP at a depth of 5 cm. The color scale located between panels (A) and (B) refers to the homogeneous phantom and the color scale located between panels (C) and (D) refers to the phantom with the tissue inserts. Figure adapted from Polf et al. (2009b).

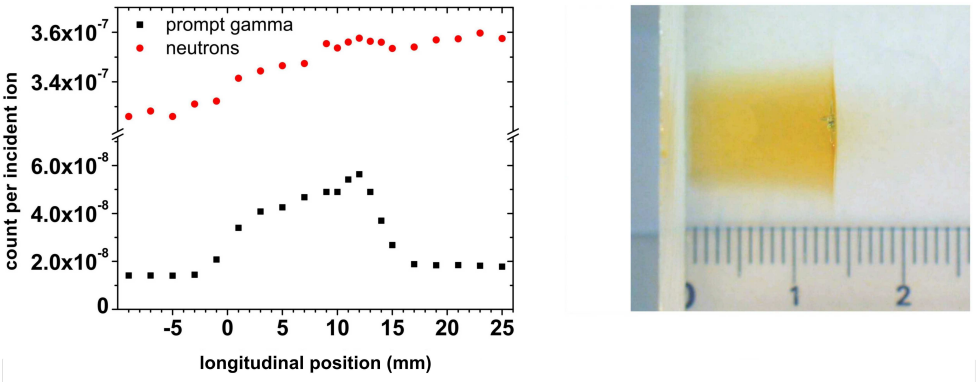

Figure 2.8.: Details of the experiment performed at the GANIL facility in 2007 by the Lyon groups with 73 MeV/u $^{13}C^{6+}$ ions impinging onto a PMMA target. Left: 90° angled prompt gamma detection rates as a function of the longitudinal position of target applying a TOF selection. The neutron (round symbols) background is also shown. Right: scaled photograph of the irradiated PMMA sample. Figure adapted from Testa et al. (2008).

of 1 GyE to a tumor volume of 120 cm^3, divided in 39 slices of 3 mm width (Krämer et al. 2000) corresponds on average to $1.8 \cdot 10^7$ delivered carbon ions per slice. Therefore, according to the above mentioned value of $1 \cdot 10^{-7}$ photons ion^{-1} msr^{-1} mm^{-1}, about 7 gamma counts per slice within the ion path would be obtained for the considered set-up.

Detector developments will allow to improve the counting statistic of measured gammas and thus determine the prompt gammas applicability to 3D total delivery or IES/pencil beam based imaging. To obtain 3D information, not only prompt gamma profiles have to be detected but also precise information on the transverse position of the beam is required (e.g., from a hodoscope). Prompt gamma based imaging techniques for ion beam therapy have recently gained remarkable interest and several groups are working on developing an optimized experimental set-up (e.g., Compton camera, collimated prompt gamma camera).

2.4. Heavy Ion Computed Tomography

The use of energetic ion beams to obtain low dose transmitted planar (radiographic) or volumetric (tomographic) images of the patient prior to or in between the treatment could be one alternative method to improve the accuracy of the calculated ion ranges in tissue and to avoid range uncertainties correlated to the usage of X-ray-based calibration curves (c.f. section 1.5.1 and figure 1.20). Primary ions lose their energy in matter mostly in inelastic Coulomb collisions with atomic electrons (cf. section 1.2.1). This transfered energy is characterized by the stopping power, which depends on the properties of the traversed material (i.e., electron density, atomic number and atomic weight). Due to the weak energy dependence of the stopping power ratio in a traversed material relative to water, the radiographic images obtained at higher energies than used for therapeutic purposes could serve for verification of the HU-WEPL calibration curve used in the treatment planning. In addition, ion radiographic images could be made at the treatment site and employed to monitor the patient positioning and to check the primary ion range in the target volume, which is important especially in case of morphological modifications and motions.

In the extension to tomographic imaging, the distribution of relative WEPL in the patient could be reconstructed directly based on the knowledge of the Bethe-Bloch formula (c.f. equation 1.1) and by irradiating the patient from several different angles with an energetic ion beam and measuring the corresponding residual energy or range behind the traversed volume. A so obtained 3D WEPL map could then be directly used by the TPS, without resorting to the use of the X-ray planning CT and HU-WEPL calibration curve (c.f. section 1.5.1 and figure 1.20).

The history of heavy charged particle radiography began already in 1968 with the pioneering work of Koehler. In Koehler (1968) it is shown that images obtained on a radiographic film irradiating objects with a thickness slightly smaller than the range of the incident 160 MeV proton beam had a much greater contrast than images produced with X-rays under the same conditions. In the following years, publications about proton radiography (Koehler and Steward 1974) and tomography (pCT, Cormack and Koehler 1976) addressed proton imaging as a diagnostic tool (Hanson et al. 1981, 1982).

In those decades, however, most of the technological effort was put forward to improve X-ray CT, so that the interest in developing medical pCT stagnated until the advent of the

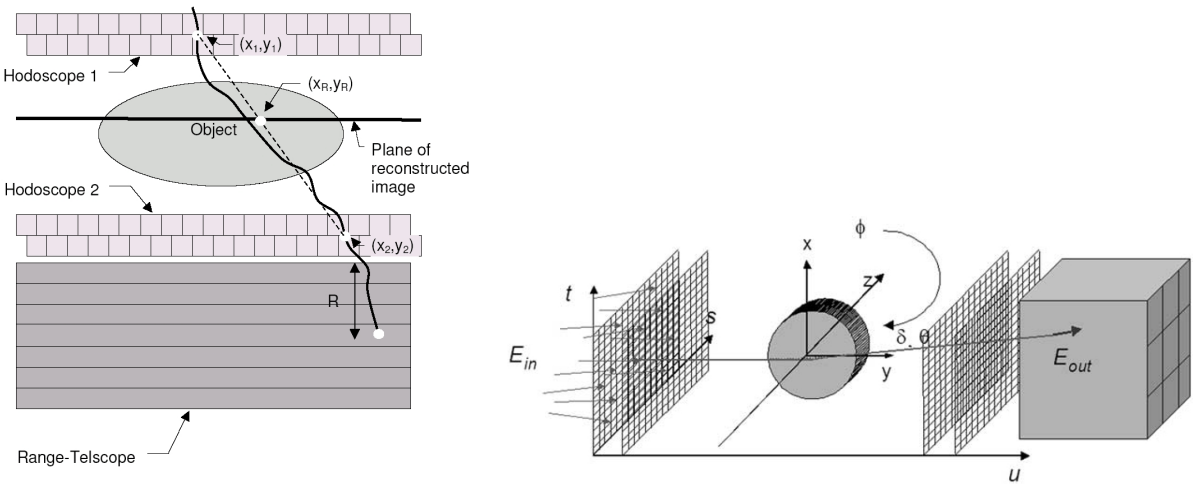

(a) PSI experimental set-up

(b) LLUMC experimental set-up

Figure 2.9.: (a) Schematic view of the PSI radiographic experimental apparatus. The hodoscopes for the measurement of the proton coordinates in front (Hodoscope 1) and behind the object (Hodoscope 2) are shown as well as the range telescope for the range measurement (R). A proton trajectory is delineated. The white dots mark the measured coordinates (x_1,y_1,x_2,y_2) in the hodoscopes and the reconstructed coordinate (x_R,y_R) on a straight line for the plane of image reconstruction Schneider et al. (2004). (b) Schematic representation of the LLUMC approach. Primaries with known entry energy (E_{in}) are recorded one-by-one in the detector reference system (s; t; u) as they traverse the image object from many different projection angles θ. The recorded data can include entry and exit positions and entry and exit angles as well as initial and exit energy prior to and after the imaged object as well as in the detector (E_{out}) (Reinhard W. et al. 2005).

---

first medical proton gantries at LLUMC. With the worldwide installation of proton gantries and the increased number of patients treated with proton therapy, the need of an accurate prediction of the proton range and verification of the patient position increased. Therefore, the development of accurate imaging techniques led to the construction of a first radiographic system at PSI (Schneider and Pedroni 1995, Schneider et al. 1996, 2004), shown in figure 2.9(a). In the same year, within the LLUMC project, a design study concluded that a pCT scanner, depicted in figure 2.9(b), should utilize instrumentation developed for high-energy physics such as silicon track detectors and crystal calorimeters equipped with fast read-out electronics, allowing one-by-one registration of protons traversing the body during a full revolution of the proton gantry (Schulte et al. 2004).

One technical challenge of pCT is due to the fact that the range/energy measurements are strongly dependent on the precise knowledge of the most probable trajectories of the protons through the patient, since protons are affected by multiple Coulomb scattering (cf. section 1.2.3). To develop algorithms to accurately reconstruct their path through matter, it is a very complex task (Li et al. 2006). To improve the spatial resolution of proton radiography or tomography to meet clinical standards, each incident proton has to be labeled and the range (PSI approach) or the energy (LLUMC approach) for the

corresponding proton exiting the target has to be revealed (cf. figure 2.9). PCT also requires fast data taking methods in order to scan the patient in a tolerable time (Pemler et al. 1999). The dose received by the patient during a proton radiographic exposure was found to be smaller than during the acquisition of a comparable X-ray CT image by approximately a factor of 50-100 (Schneider et al. 2004).

Although the proven advantages of proton-based imaging techniques such as superior density resolution at lower dose exposure have been experimentally demonstrated (Schneider et al. 2005, Reinhard W. et al. 2005), this technique is not yet used in the clinical routine.

In 2006 in Japan at HIMAC, the first attempt was made to implement HICT, using broad carbon ion beams and measuring the residual energy behind the targets (Shinoda et al. 2006, Ohno et al. 2004). Since both, primary and fragmented secondary ions, add to the residual energy, revealed e.g., by a calorimeter, the discrimination of their contributions to the signal is difficult. On the other hand, the Bragg peak position is determined only by primary ions, suggesting the use of a range telescope as alternative detector in HICT applications (cf. chapter 5). Contrarily to protons, the trajectories of high energy carbon ions can be assumed to be straight in first approximation (cf. section 1.2.4), thus simplifying a lot the path reconstruction problem.

Difficulties related to HICT concern the financial and technical effort needed to accelerate therapeutic ion beams to sufficiently high initial energy (e.g. ≈ 400 MeV/u) and to deliver heavy ions with a suitable isocentric system, e.g., with a gantry for carbon ions. At HIT (cf. sections 1.1.2.2 and 1.4.3), carbon ion beams of initial energy up to ≈ 430 MeV/u, a 3D fast and precise active raster scanning beam delivery system as well as the worldwide first heavy ion gantry are available and offer the ideal scenario to develop HICT (cf. chapter 5).

Chapter 3

FLUKA SIMULATIONS AND FIRST VALIDATION IN MULTI LAYER FARADAY CUPS

Monte Carlo (MC) codes are useful tools in ion beam therapy to simulate the complex processes of ion interactions with matter. Moreover, they can handle geometries containing the detailed descriptions of the patient anatomy (e.g., obtained from CT data) and provide accurate multi-dimensional transport in the volume of interest. Nowadays, MC methods play an increasingly important role in the field of radiation therapy with ions, where they are used for different purposes. These for example include shielding calculations, beamline modeling, generation of TPS input data (cf. section 1.4.3), validation of TPS physical and biological dose calculations, treatment verification, estimation of neutron dose to the patient, support to the test and the development of quality assurance and imaging modalities (Medin and Andreo 1997, Carlsson et al. 1997, Paganetti 2002, Parodi et al. 2007, Mairani et al. 2008, Parodi and Enghardt 2000). The precise determination of ion ranges and ionization losses is of utmost importance in dosimetry and in therapeutic applications (cf. section 1.2.1 and 1.2.2). Moreover, ion beams, while penetrating tissues, undergo inelastic nuclear reactions producing significant secondary fragments (cf. section 1.2.5) and influencing the dose distribution. Therefore, the validation of electromagnetic and nuclear models adopted in MC codes is a critical requisite for their use in this field. Nowadays, different general purpose MC codes are available for application to ion beam therapy, e.g., FLUKA (Ferrari et al. 2005, Battistoni et al. 2007), GEANT4 (Agostinelli et al. 2003, Allison et al. 2006), MCNPx (Hughes et al. 1997, LANL 2002), PHITS (Niita et al. 2006), SHIELD-HIT (Dementyev and Sobolevsky 1999, Gudowska et al. 2004).

At HIT (cf. sections 1.1.2.2 and 1.4.3), the FLUKA MC code was chosen as common computational platform. Several recent studies have reported comparisons between the FLUKA models and experimental data of interest for ion therapy, especially for carbon ion beams (Sommerer et al. 2006, Mairani 2008, Sommerer et al. 2009, Mairani et al. 2010, Böhlen et al. 2010). The results provide evidence that the agreement between FLUKA

predictions and experimental data is very satisfactory, although there is still room for improvement, which is especially due to the lack of available experimental data and their limited precision. Further investigations and validations are especially needed for protons in the energy range of therapeutic relevance. To this regard, within this thesis, an integral test of FLUKA models has been performed for proton beams. The validation of the FLUKA code in Multi Layer Faraday Cups (MLFC) is reported in section 3.2 (Rinaldi et al. 2011), after a brief introduction to the FLUKA code (cf. section 3.1) and to its models relevant for ion beam therapy (cf. section 3.1.1).

Moreover, the FLUKA MC code was used to support and to validate the experimental investigations within this thesis, mainly for carbon ion beams (cf. sections 4.2.2 and 5.1) and as a sound tool to investigate prompt gamma based imaging techniques, especially for proton beams (cf. sections 4.3 and 4.4).

Due to the continuous evolution and upgrade of the FLUKA code, the used version will be specified in the respective section.

3.1. The FLUKA code

FLUKA (FLUktuierende KAskade, www.fluka.org, Ferrari et al. 2005, Battistoni et al. 2007) is a general purpose particle and heavy ion transport and interaction code which is developed and maintained in the framework of an agreement between the European Laboratory for Particle Physics (CERN) and the Italian National Institute for Nuclear Physics (INFN). It is capable of handling the transport and interactions of hadrons, heavy ions, and electromagnetic particles from a few keV (or from thermal energies for neutrons) up to cosmic ray energies in whichever solid, gas or liquid material. FLUKA is used for a vast variety of applications like proton and electron accelerator shielding applications, target design, calorimetry, activation, dosimetry, detector design, accelerator driven systems, space radiation and cosmic ray showers, neutrino physics, and ion beam therapy. Particles can be transported in arbitrary complex geometries, which can also include magnetic fields. For therapeutic applications, a module which handles voxel geometries like CT scans is available. FLUKA is constantly updated and extended.

An overview of the main physical models relevant for ion beam therapy is given in section 3.1.1. A description of recent developments can be found in the FLUKA manual and in the materials of the 1^{st} FLUKA Advanced Course and Workshop (October 2010, Portugal) on the official FLUKA website.

To work with FLUKA, the user has to write an input file and, for special problems, to customize some FORTRAN routines (user routines). A graphical user interface is not part of the standard FLUKA distribution. However, recently a front-end interface called FLAIR (FLUKA Advanced Interface) was developed and can be separately downloaded from the FLUKA website (www.fluka.org/Flair/). It offers features like easier creation of input files, debugging, compiling, running and monitoring the status of the simulation during its execution.

FLUKA has defaults for specific problems to support the user in the choice of the physics options to use. Defaults exist for calorimetry, electromagnetic cascades, low energies neutron experiments, shielding calculations hadrontherapy, and for many other kinds of prob-

lems. In particular, the DEFAULTS HADROTHE card provides a default configuration for ion beam therapy applications. This enables the use of pre-defined settings for different options (e.g., production threshold of δ-rays, energy thresholds for the transport of charged hadrons, neutrons and, photons, and electrons) suiting best the needs of ion beam therapy simulations. Moreover, FLUKA gives the possibility to adjust few settings of the available physical models (cf. section 3.1.1) using the PHYSICS card, allowing to overwrite default settings for certain physical processes.

Standard scoring is done in binnings which are uniform spatial meshes independent of the geometry. In such binnings, energy deposition, star density (i.e., inelastic hadron reactions) or particle fluence distributions can be scored. FLUKA has also boundary crossing and track length estimators as well as estimators to score double-differential quantities. However, in some cases, the standard scoring options are not sufficient, and user-specific applications need to be implemented for the simulation of dedicated problems. For this purpose, the user routines have to be customized.

In this thesis, typically the DEFAULTS HADROTHERAPY card was used, adjusted as needed by modifying the production and energy thresholds of the transported radiation, adding specific PHYSICS cards and customizing user routines. Especially, two routines were extensively used within this thesis: The `source.f` and `mgdraw.f`. A user defined source routine is used at HIT to better characterize the available ion beams. The mgdraw routine offers a complete interface to the whole FLUKA transport, allowing, e.g., an event by event output and scoring.

3.1.1. FLUKA models relevant for ion beam therapy

In the following, some of the most important models of the FLUKA code relevant for ion beam therapy applications are briefly outlined. More information and details on the implemented FLUKA models can be found in the manual and in the material and publications provided on the FLUKA website.

In FLUKA, the transport of charged particles is performed through an original Multiple Coulomb scattering algorithm (Ferrari et al. 1992), supplemented by an optional single scattering method. Multiple scattering with inclusion of nuclear form factors is applied also to heavy ion transport. The treatment of ionization energy loss is based on a statistical approach, alternative to the standard Landau and Valivov one, that provides a very good reproduction of average ionization and fluctuations (Fassò et al. 1997). Up-to-date effective charge parametrizations are employed, and straggling of ion energy loss is described in "normal" first Born approximation with inclusion of charge exchange effects.

In terms of the more complex nuclear processes, hadron-nucleus interactions up to 5 GeV and, therefore, relevant for ion therapy application, especially in the case of proton beams, are handled by PEANUT (Pre-Equilibrium Approach to NUclear Thermalization). Presently, PEANUT, which has been thoroughly validated against experimental data, handles interactions of nucleons, pions, kaons, and γ-rays. The reaction mechanism, depicted in figure 3.1(a), is modeled in PEANUT by explicit Generalized IntraNuclear Cascade (GINC) smoothly joined to statistical (exciton) pre-equilibrium emission (Gadioli and Hodgson 1992, Griffin 1967). At the end of the GINC and exciton chain, the evaporation of nucleons and light fragments is performed, following the Weisskopf (Weisskopf and

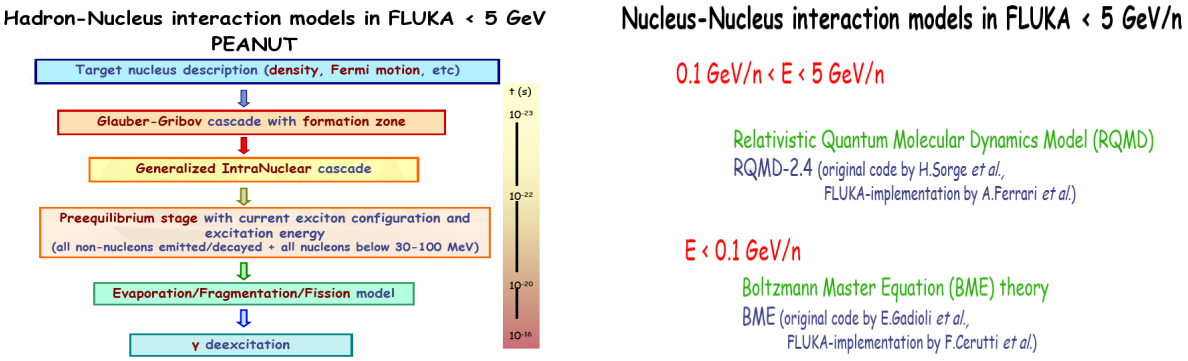

(a) (b)

Figure 3.1.: Overview of the most important nuclear models in FLUKA below 5 GeV/u, which are relevant for ion beam therapy applications. (a) PEANUT for hadron-nucleus interactions. (b) RQMD and BME event generators for nucleus-nucleus interactions. Figure adapted from the FLUKA website (www.fluka.org).

Ewing 1940) treatment. Competition of fission with evaporation is taken into account, again with a statistical approach. Since the statistical evaporation model becomes less sound in light nuclei, the so-called Fermi Break-up model (Epherre and Gradsztajn 1967, Fermi 1950) is used instead. The excitation energy still remaining after evaporation is dissipated via emission of γ-rays (Ferrari et al. 1996a,b). A description of PEANUT at low-intermediate energies can be found in Ferrari and Sala (1997).

Nucleus-nucleus interactions generated by heavy ions (Z>1) are treated through interfaces to external event generators. Two of them are relevant for ion beam therapy applications. For energies between 0.1 GeV and 5 GeV per nucleon, an interface to a suitably modified RQMD (Relativistic Quantum Molecular Dynamics Model) is used. For energies below 0.1 GeV per nucleon down to the Coulomb barrier, a relatively new event generator based on the Boltzmann-Master-Equation (BME) theory has been developed (Cerutti et al. 2006, Cavinato et al. 1998, 2001). The excited pre-fragments resulting from these interactions can then undergo several additional steps, like evaporation, Fermi-Break-Up, fission or γ-emission, until they are completely de-excited and transported further by FLUKA. A sketch of the FLUKA workflow is given in figure 3.2.

Secondary radiations like, e.g., neutrons, electrons, gammas are also produced and transported by FLUKA.

3.2. Validation of the FLUKA code in MLFCs

A simple integral method to test the global effect of nuclear reaction models of a MC code can be performed using a MLFC. This method allows separation of the nuclear and atomic interaction processes, which are responsible for secondary particle emission and the finite primary range, respectively. Previous comparisons of MLFC results with other MC simulation codes were performed to test GEANT3 and GEANT4 (Gottschalk et al.

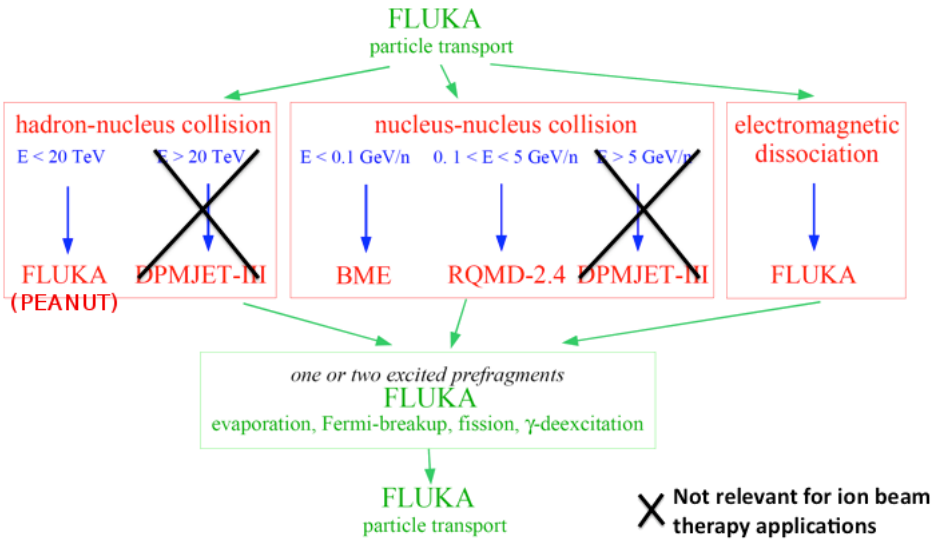

Figure 3.2.: Sketch of the FLUKA workflow. Figure adapted from the FLUKA website (www.fluka.org).

1999, Paganetti and Gottschalk 2003, Jarlskog and Paganetti 2008), MCNPx (Mascia et al. 2004) and SHIELD-HIT (Henkner et al. 2009).

Simulations with the FLUKA MC code of a 160 MeV proton beam stopping in two MLFCs, made of polyethylene (CH_2) and copper (Cu), were performed within this thesis and are presented in the following.

3.2.1. Experimental set-ups

This study relies upon the experimental measurements described in Gottschalk et al. (1999) and Paganetti and Gottschalk (2003) performed at the Harvard Cyclotron Laboratory (HCL) using MLFCs (figure 3.3).

Any MLFC is composed of insulating or conducting materials. If a proton stops in an insulator, it creates an image charge in the neighboring conducting plates (cf. figure 3.4(a)). This image charge attracts an electron from the ground as if the proton had actually stopped in the conductor (Gottschalk et al. 1999, Paganetti and Gottschalk 2003). If a proton stops in a conductor, the added charge attracts an electron from ground through the current integrator electronics (cf. figure 3.4(b)).

In the experiments two different MLFCs were used. One MLFC is a stack of 66 brass collector sheets (15 cm × 15 cm × 0.00254 cm) separated by high density ($\rho = 0.98$ g/cm^3) CH_2 sheets (15 cm × 15 cm × 0.317 cm), while the second one is a stack of 66 Cu sheets (7.6 cm × 7.6 cm × 0.0529 cm) separated by insulator (kapton) sheets (7.6 cm × 7.6 cm × 0.00254 cm). In both cases the number of active channels connected to current integrators is 64, while the collector 65 is grounded. Since the beam diameter (FWHM ∼ 1 cm) is much smaller than the dimension of the MLFC, all the primaries entering the detector will

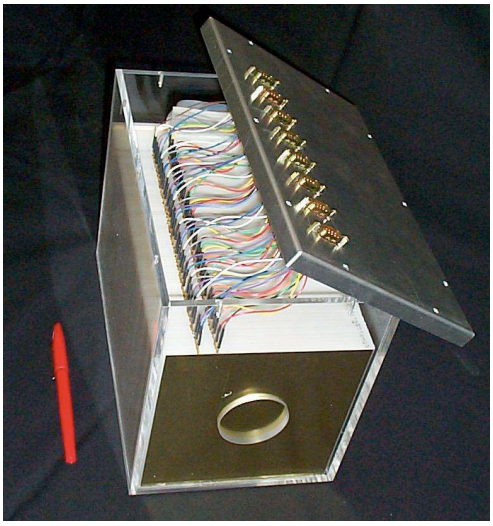

Figure 3.3.: CH_2 MLFC with its lid open. There are 65 brass collector sheets, nominally 0.00254 cm thick. The one visible is connected to an aluminum foil wrapping applied during measurements to form a grounded shield. Active collectors 1-64, connected to current integrators, are separated by high density (0.98 g/cm^3) polyethylene sheets, nominally 0.3175 cm thick. Collector 65 is grounded. (Paganetti and Gottschalk 2003).

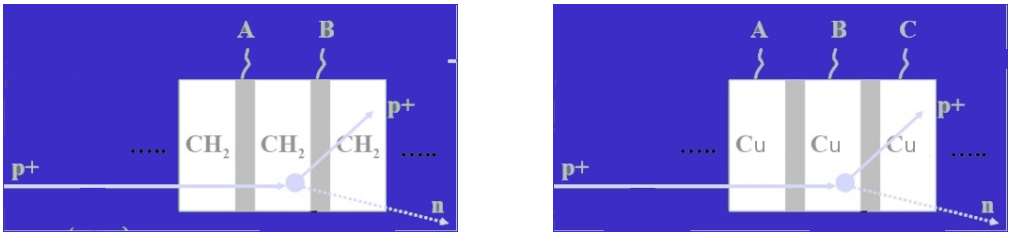

(a) CH_2 MLFC (b) Cu MLFC

Figure 3.4.: Sketch of the charge collection in two different MLFCs. In the CH_2 MLFC (3.4(a)), the charge is measured in the brass sheets (gray area), while in the Cu MLFC (3.4(b)), the charge is measured in the copper sheets (white area). In the illustrated case of a (p, pn) reaction, for example, the charge measured in B is 0 since there is +1 charge from the incoming proton and -1 charge from the recoil proton, while in C the charge measured is +1 due to the stopping proton. Figure by courtesy of Harald Paganetti.

stop within the volume. The longitudinal charge distribution along the beam penetration (cf. measured data points in figure 3.5) exhibits the two expected distinct regions: a build-up due to nuclear reactions and a sharp peak due to primaries stopping by electromagnetic interaction.

3.2.2. FLUKA simulations of the MLFC experiments using proton beams

In this study, the FLUKA MC code version 2008.3 (Ferrari et al. 2005, Battistoni et al. 2007) was used. MC results were used to evaluate the charge distribution. The experimental geometry was simulated exactly as described in Gottschalk et al. (1999), in Paganetti and Gottschalk (2003), and in section 3.2.1.

Two approaches were adopted to estimate the charge deposited in each channel. In the first one, equal to all previous works (Gottschalk et al. 1999, Paganetti and Gottschalk 2003, Mascia et al. 2004, Henkner et al. 2009), the charge produced by primaries and charged nuclear secondaries (i.e., without accounting for ionization electrons) was scored, using two customized FLUKA user routines (i.e., `mgdraw.f` and `comscw.f`). The charge amount of the recoil nucleus at each nuclear interaction point was calculated subtracting the charge of the final state from that of the initial state at each interaction point. Moreover, for any transported primary or charged nuclear secondary stopped at a certain position, the appropriate charge amount was added. In the case of more nuclear interactions, for one primary history, the procedure was repeated. Since it is a relatively rare event for the total charge to appear close to the primary reaction site, the appearance of negative or zero charge at the nuclear interaction point and of positive charge downstream is more frequent. Moreover, since the MLFC should stop all charged particles, the net charge deposit by any event, nuclear or EM, should be +1 proton charge per incident proton.

The same approach was followed also in the second method accounting for secondary electron emission. A charge +1 was scored at the production point, and a charge -1 at the point where the electron was coming at rest. For both processes, if the scoring point was in a metallic electrode, the charge was attributed to the corresponding channel. When the scoring point was inside a dielectric, the charge was shared between the two neighboring channels inversely proportional to the distance from the corresponding electrodes. In practice, assuming that a dielectric layer has a thickness d, a net charge generated in a depth z in a channel n, where $0 < z < d$, contributes z/d to the $(n+1)^{th}$ electrode and $(d-z)/d$ to the n^{th} electrode (as follows from electrostatics). Due to the relatively short range of secondary electrons, the effect of their transport on the simulated charge collection is expected to be relatively small, unless the electron energy is large enough (45 keV or more for the Cu MLFC) to cross the dielectric layer between two electrodes. When electrons are produced and stopped inside the same insulation layer, the effect on the charge collection is proportional to the ratio of the electron projected path along the longitudinal direction to the electrode separation. Unless in areas of strong gradient in the deposited charge profile, the dielectric charge sharing is expected on average to be well approximated by attributing all the charge to the closest channel. Under the same

assumptions and taking into consideration the energy spectrum of secondary electrons emitted by 160 MeV protons, the influence of secondary electron transport is expected to be small.

In the following, results obtained without and with electron transport and charge sharing will be presented and referred to as method 1 and method 2, respectively. For every set of simulations, short test runs were performed to adjust the MC input parameters for beam energy and beam energy spread to obtain the same position of the EM peak of the proton beam as in the experimental data. In fact, in the absence of precisely calibrated beam energy (E) and spread (σ), these are the quantities that can be varied in order to reproduce the experimental condition. Moreover, the purpose of this investigation is to assess the relative importance of EM and nuclear models but not the absolute validation of the FLUKA range calculation in the considered MLFC detectors at the nominal initial beam parameters. The final MC calculations with the chosen optimal input values were then performed using 10 million protons for 5 independent runs.

3.2.3. Results and discussion

The selected values of the input parameters for reproduction of the two separate experiments and for the two different approaches explained in section 3.2.2 are: $E_1 = 160.1$ MeV and $\sigma_1 = 0.5$ MeV (method 1) and $E_2 = 160.4$ MeV and $\sigma_2 = 0.35$ MeV (method 2) for the CH_2 MLFC, while $E_{1,2} = 159.5$ MeV and $\sigma_1 = 0.5$ MeV and $\sigma_2 = 0.35$ MeV for the Cu MLFC. These values are rather consistent with the previous studies using other MC codes (Gottschalk et al. 1999, Paganetti and Gottschalk 2003, Mascia et al. 2004, Henkner et al. 2009).

The results of method 1, scoring the charge produced by primaries and charged nuclear secondaries, are shown in figure 3.5A and 3.5B for the CH_2 MLFC and in figure 3.5C and 3.5D for the Cu MLFC. This is done for both in a linear representation, where the electromagnetic peak is suppressed by a factor of 0.04, as well as in a semilogarithmic one to emphasize the EM peak and the tail. The vertical scale in the figures, pC per incident Giga-Proton (10^9), is absolute for both, the experiment and the simulation.

The results of method 2, which takes into account the effect of secondary electrons on the simulated charge and the charge sharing in the dielectric layers, are shown in figure 3.6A and 3.6B for the CH_2 MLFC and in figure 3.6C and 3.6D for the Cu MLFC.

Finally, the comparisons of experimental data and FLUKA MC calculations, performed by including or excluding the more detailed physics handling, but keeping the same input beam energy parameters of method 2 for consistency, are reported in figure 3.7 to appreciate the impact of the electron (figure 3.7(a)) and charge sharing contributions (figure 3.7(b)).

Apparently no big difference is visible between the two investigated methods when looking at figures 3.5A and 3.5C. This is because method 1 implicitly accounted for the missing correct handling of the physics via an arbitrary tuning of the beam momentum spread. However, the differences can be appreciated in figure 3.7, where the same input beam parameters were used, thus suggesting that if the momentum spread in the experiment was accurately known, only method 2, which comprises a more correct treatment of physics, would correctly reproduce the data.

Since the nuclear secondaries from inelastic interactions should stop before reaching the

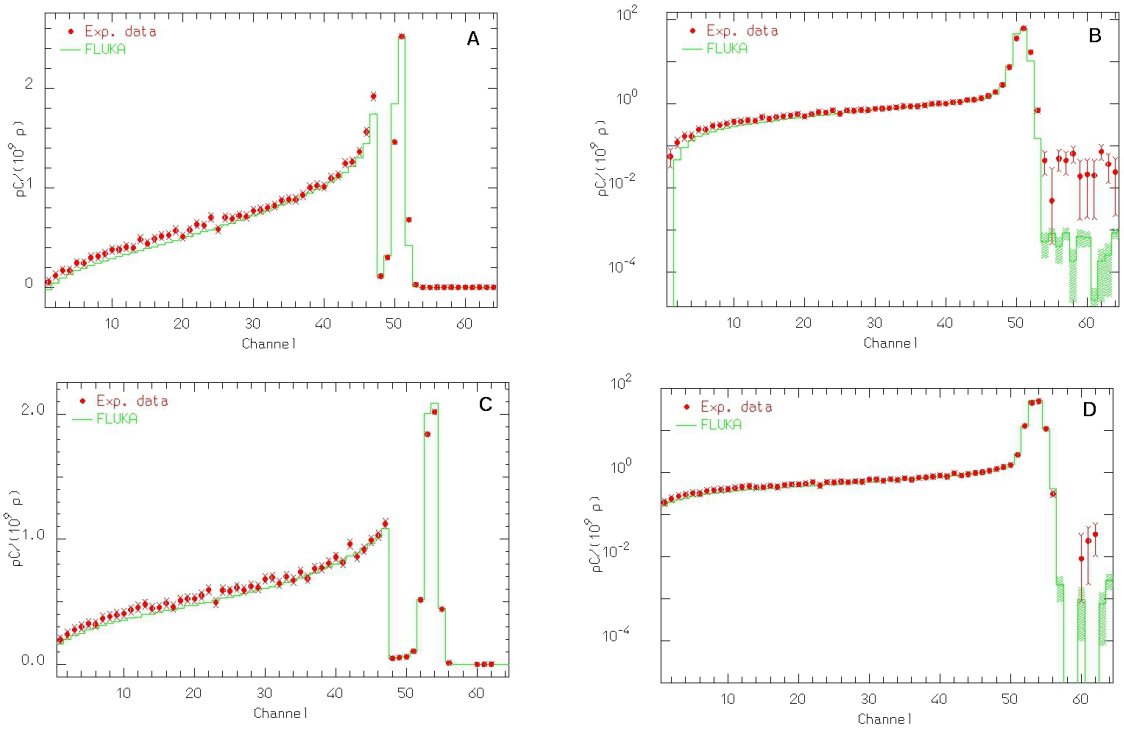

Figure 3.5.: Experimental data (circles) and FLUKA MC calculations (line) of the CH_2 (A, B) and Cu (C, D) MLFC set-up for method 1. The ordinate is absolute (no arbitrary normalization). The abscissa shows the channel number. Left panel: linear scale (electromagnetic peak suppressed by a factor of 0.04), right panel: logarithmic scale. Figure from (Rinaldi et al. 2011).

EM peak, the ratio of total charge in the build-up region to the charge deposited in the entire spectrum from primary and nuclear secondaries can equal the probability of the primary beam to undergo an inelastic nuclear reaction. The value of this ratio for the simulation is about (17 ± 1 %) for the CH_2 MLFC and about (19 ± 1 %) for the Cu MLFC, considering as separation between the two regions the channel 48. These values are in good agreement with the measured ones reported in Paganetti and Gottschalk (2003). However, the arbitrary choice of the channel which divides the two regions can influence the separation between the two processes. In tables 3.1, 3.2 and 3.3 some detailed results of the simulations for both MLFCs are summarized, where all the interactions are individually counted for the primaries and all the descendant particles. Table 3.1 displays the percentages of different interactions per primary proton, table 3.2 shows the number of secondaries generated in inelastic reactions per primary proton and table 3.3 lists the number of secondary interactions, including the elastic ones, created by low energy neutrons per primary proton. These values agree substantially with Paganetti and Gottschalk (2003) and ICRU (2000).

On the whole, FLUKA predicts the overall shape of deposited charge and agrees with the data quite well. Nevertheless, although the more accurate implementation of method 2 improves the signal in the first channel, all the simulated approaches show a consistent

Table 3.1.: Percentages of different interaction channels per primary proton

	CH_2 MLFC	Cu MLFC
`inelastic interactions`	18.6 %	20.4 %
`elastic interactions`	27.4 %	27.7 %
`low energy neutron interactions (including the elastic ones)`	307.04 %	42.3 %

Table 3.2.: Number of secondaries generated in inelastic reactions

	CH_2 MLFC	Cu MLFC
`proton`	0.231	0.261
`deuteron`	0.044	0.033
`tritium`	0.008	0.004
`helium-4`	0.217	0.062
`helium-3`	0.018	0.002
`neutron`	0.102	0.384

Table 3.3.: Number of secondary interactions (including the elastic ones) created by low energy neutron per primary proton

	CH_2 MLFC	Cu MLFC
`proton`	0.195	0.011
`neutron`	3.058	0.421

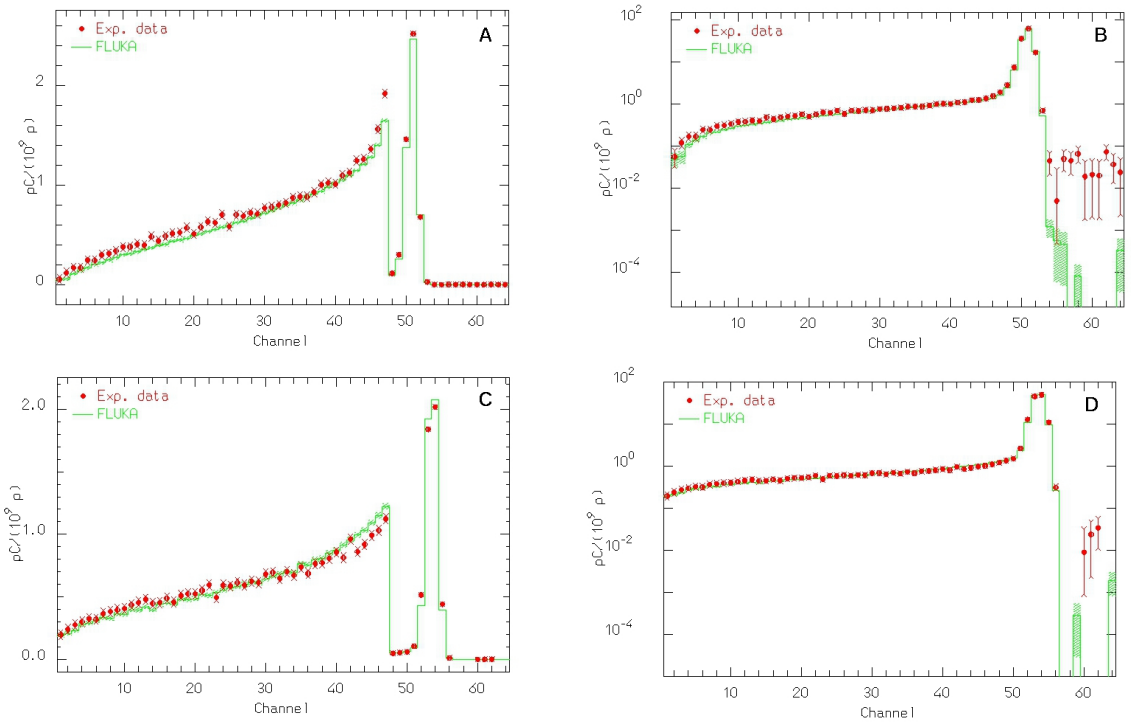

Figure 3.6.: Experimental data (circles) and FLUKA MC calculations (line) of the CH_2 (A, B) and Cu (C, D) MLFC set-up for method 2. The ordinate is absolute (no arbitrary normalization). The abscissa shows the channel number. Left panel: linear scale (electromagnetic peak suppressed by a factor of 0.04), right panel: logarithmic scale.

underestimation of the signal measured in the tail after the EM peak. The possible reasons of these underestimations especially for the signal in the high channel numbers of the CH_2 MLFC (cf. figures 3.5 and 3.6) were analyzed in detail. In Paganetti and Gottschalk (2003) it has been suggested that the measured signal beyond the Bragg peak in the CH_2 MLFC is not just noise but due to neutron-induced knock-on protons resulting in a +1 charge for the proton and a -1 for the recoil. In general if the knock-on protons are generated and then stop in the same channel the internal charge would be rearranged so that there is no net charge registered. However a positive signal was claimed to be created beyond the Bragg peak due to an imbalance between knock-on protons entering and leaving each sheet because of the neutron fluence attenuation, resulting in a reduction of knock-on proton yield in depth.

In the FLUKA calculations, this hypothesis was investigated, but a significant imbalance was not found as shown in figure 3.8, where the charge difference between the knock-on protons stopping and the ones leaving a recoil behind is shown for each channel. The explanation is that, even if the neutron fluence decreases with depth and the maximum energy and range of the recoil protons can reach values up to 90 MeV and 6 cm, respectively, (cf. figure 3.9), the average energy value is always below 26 MeV, which is the minimum energy value that these protons need to cross one channel. The average range

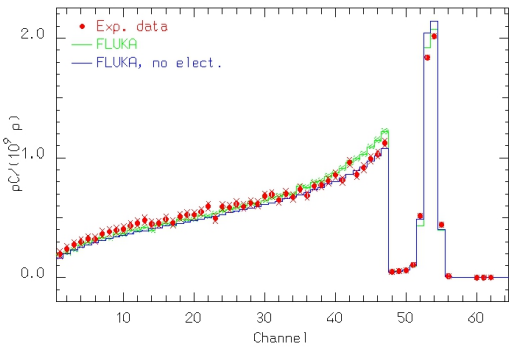

(a) FLUKA results with (green line) and without (blue line) the secondary electrons contribution for the Cu MLFC set-up.

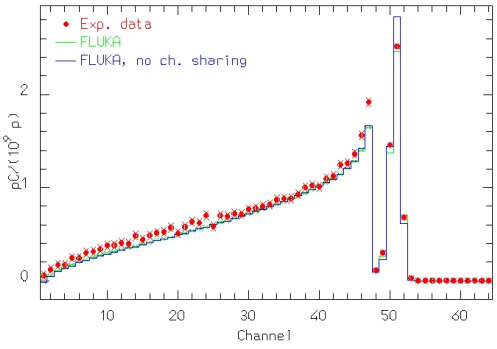

(b) FLUKA results with (green line) and without (blue line) the charge sharing in the dielectric layers for the CH_2 MLFC set-up.

Figure 3.7.: Comparisons of experimental data (circles) and FLUKA MC calculations (line) to appreciate the impact of the electron transport (especially evident for the Cu MLFC, left) and charge sharing effects (important for the CH_2 MLFC, right), when using the same beam energy and momentum spread for consistency. The ordinate is absolute (no arbitrary normalization) and in linear scale (electromagnetic peak suppressed by a factor of 0.04). The abscissa shows the channel number.

is therefore always below the dimension of one channel (about 0.6 cm) in the CH_2 MLFC. This conclusion is independent of the accuracy of the used MC code. In fact, in order to reproduce the experimental data in the tail, a two orders of magnitude higher neutron flux would be necessary, which is beyond the MC uncertainties. Moreover, a good agreement between the MC nuclear interactions reproduced by FLUKA and the experimental ones were already observed (cf. tables 3.1, 3.2 and 3.3), thus assuring the consistency of the presented analysis.

Moreover, figure 3.10 illustrates the major contributions of the different interaction channels to the simulated total charge in comparison with the experimental data. The positive charge is due to protons and alpha particles stopping in electromagnetic interactions, including those generated in the build-up region via nuclear interactions as well as the EM peak of the primary beam. The negative charge, on the other hand, is due to the recoils left behind in inelastic, elastic and low energy neutron interaction processes for each channel.

Thus, even if a small positive signal is predicted (roughly up to 0.3 pC/Incident Gigaproton) beyond the EM range owing to the total stopping protons (cf. figure 3.10), only a net charge of about 0.001 pC/Incident Gigaproton remains due to the imbalance between stopping and leaving neutron-induced knock-on protons, as estimated from figure 3.8 for the channels after the Bragg peak. Moreover, to this net charge additional charge signals from other reaction channels has to be added, resulting in the significantly lower total charge detected in the last channels beyond the EM peak (cf. figures 3.5, 3.6, and 3.10).

Although the validity of these investigations depend on the reliability of the FLUKA models and deserve deeper investigations resolved for each specific reaction channel, the underestimation may more realistically be due to the effect of a background. This back-

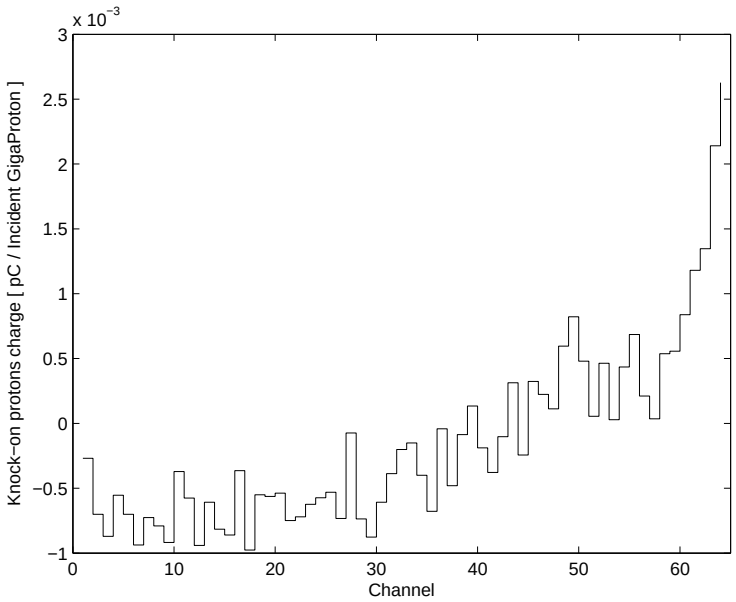

Figure 3.8.: Resulting charge imbalance due to knock-on protons as a function of channel in the CH_2 MLFC, i.e. difference between positive charges of stopping protons and negative ones due to leaving protons or corresponding recoils left behind. Figure from (Rinaldi et al. 2011).

ground, that must not necessarily be identical in the two MLFC experiments since they were performed in different years and with different detector arrangement, can derive from the electronic noise (Henkner et al. 2009). In figure 3.11, the comparisons between the experimental data and the MC calculations using method 2 are reported (left panel: CH_2 MLFC, right panel: Cu MLFC), where a total charge integral background of 1.6%, meaning 0.04 pC/GigaProton for each channel, has been added to the FLUKA values to illustrate the effect of a background addition. Considering this background estimation anyhow reasonable, since also the integral charge is still conserved within 1%, it can be concluded that the FLUKA results, after background addition, are in very good agreement with the experimental data even in the first channels and in the tail region.

3.3. Conclusion

Investigations with the FLUKA MC code have been presented aiming to reproduce experiments which measured the distribution of projected ranges of charged nuclear secondaries of proton beams stopped in MLFCs. Since MLFC detectors measure charge rather than dose, they give the possibility to distinguish between EM and nuclear interactions. As test case, FLUKA was used to simulate data on 160 MeV protons stopping in CH_2 and Cu MLFCs. From the results shown, it can be concluded that the FLUKA MC code achieves reliable results against experimental data. The MLFC provides a simple test of the overall range distribution of charged nuclear secondaries predicted by a MC code, but it does not

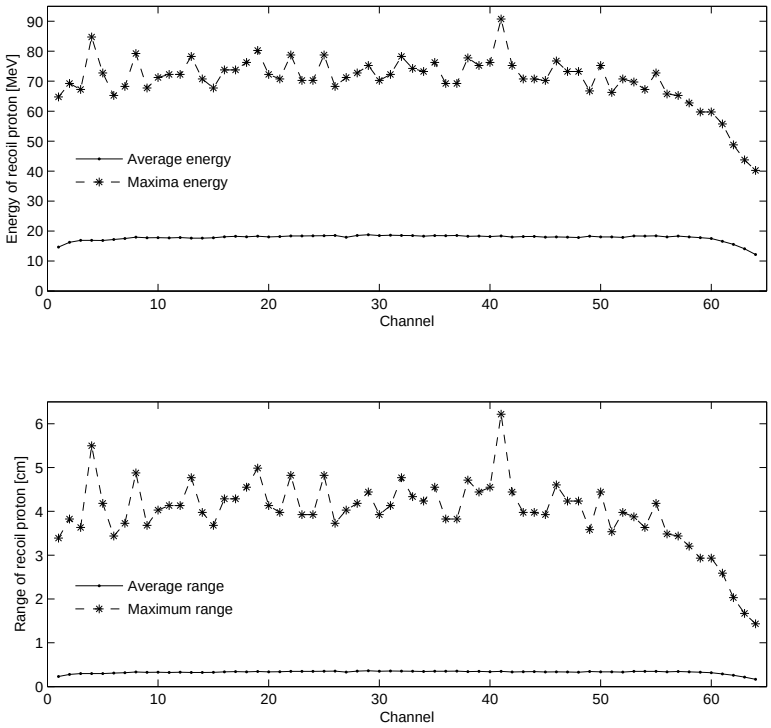

Figure 3.9.: Maximum and average energies [MeV] and ranges [cm] of recoil protons in the CH_2 MLFC. Figure from (Rinaldi et al. 2011).

check any particular reaction channel. Therefore, any event generator suitable for therapeutic applications should pass this test, which is necessary but not sufficient to guarantee its correctness in every aspect.

Moreover, the results obtained with method 2 (i.e., including electron transport and charge sharing in dielectric) also suggest that while the approach traditionally used in the literature for other codes (method 1) is indeed sufficient for testing of the nuclear models, it can be insufficient to fully characterize the electromagnetic charge deposition in the region of the Bragg peak for absolute settings of the initial beam parameters (i.e., energy and momentum spread).

Further works could look at separate channels for processes of interest, e.g., β^+ production, and also implement the two different kinds of MLFCs (i.e., CH_2 and Cu) for similar tests using a different ion beam (e.g., carbon), where for the latter experimental data are still unavailable.

Anyhow, this work, performed for therapeutic proton beams, nicely complements the already done detailed benchmarking of the FLUKA nuclear models in carbon ion therapy, further supporting the reliability of the code and thus justifying its usage in the thesis as addressed in chapter 4.

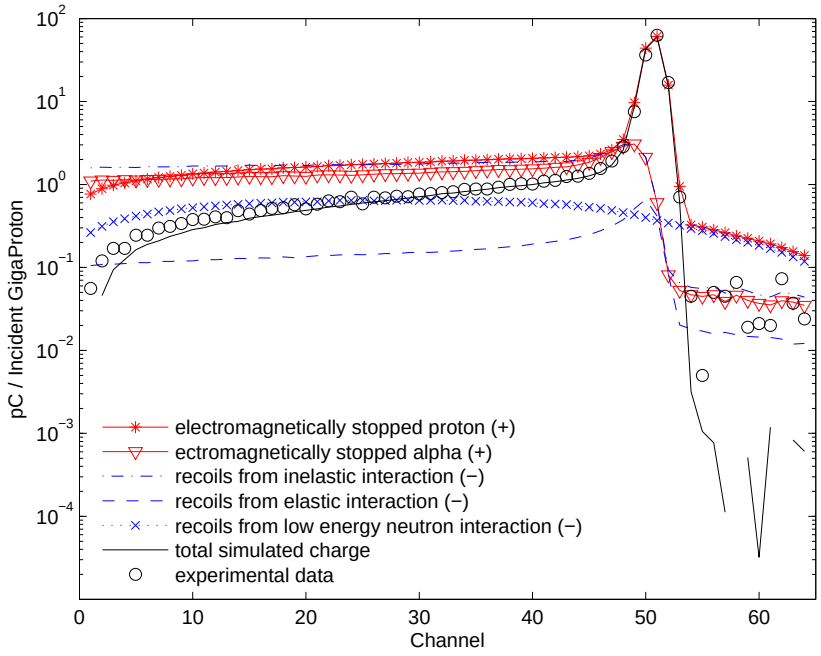

Figure 3.10.: Contributions of the different interaction channels to the total charge. The symbols (+) and (-) distinguish between the positive and negative charge contributions to the total charge, respectively. (Rinaldi et al. 2011)

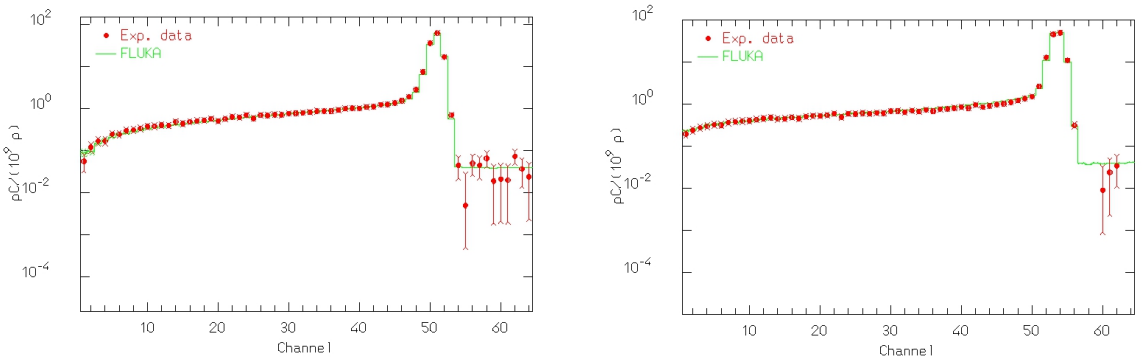

Figure 3.11.: Experimental data (circles) and FLUKA MC calculations (line) for method 2 of the CH_2 (left panel) and Cu (right panel) MLFC set-ups when adding to the MC data a total charge integral background of 1.6%. The ordinate is absolute (no arbitrary normalization) in a logarithmic scale. The abscissa shows the channel number. Figure from (Rinaldi et al. 2011).

Chapter 4

PROMPT GAMMAS

In order to test the reliability of the FLUKA MC code for investigations on prompt gamma imaging, comparisons against the currently only available experimental data for which detailed description of the experimental set-up is given, were performed within this thesis (cf. sections 4.1 and 4.2). Based on the promising results obtained for carbon ions, the FLUKA MC code was then used as a sound tool to investigate specific physical effects for proton beams, in view of future experimental validation when measured data will be available. The simulations were performed for homogeneous and heterogeneous phantom configurations to study the main features of the emerging prompt gammas and to understand how to set up a detector system to obtain an optimum measured signal (cf. section 4.3). Finally, first results for a real patient case are presented (cf. section 4.4).

4.1. Single-detector experiments at GANIL and GSI

This section presents the two series of experiments for the measurement of prompt photons produced during ^{12}C ion fragmentation which have been performed by the Lyon groups at GANIL and GSI facilities (Testa et al. 2008, 2009, 2010, Le Foulher et al. 2010). These experiments have been simulated with the FLUKA MC code within this thesis.

4.1.1. Experimental set-ups

The first experiment was performed with 95 MeV/u ^{12}C ions at GANIL. The primary beam directly hit a PMMA target ($\rho = 1.2$ g/cm^3, $50 \times 50 \times 50$ mm^3). In the second experiment at GSI, higher energy ions of 310 MeV/u bombarded a water target ($12 \times 25 \times 20$ cm^3). In figure 4.1, the schemes of the two experimental set-ups are shown. In both experiments, the targets were placed on a table which could be remotely moved along the beam axis (cf. figure 4.2). A BaF_2 scintillator was used as detector. This scintillator was chosen for its excellent time response and its high efficiency for photon detection. In fact, BaF_2 has a time-resolution which is 4-5 times better than NaI(Tl) and an efficiency rather constant

Table 4.1.: Characteristics of the experimental set-ups.

	GANIL (2008)	**GSI (2009)**
Primary beam	^{12}C 95 MeV/u	^{12}C 310 MeV/u
Target	5×5×5 cm PMMA phantom	21×20×12 cm water flasks
Collimator	(5×20×20)×2 cm Pb blocks	(5×20×20)×2 cm Pb blocks
Neutron collimator	–	(15×20×40)×2 cm water phantom
Shielding	(7.5×10×5)×2 cm Pb blocks	(15×20×30)×2 cm Pb blocks
		(3×20×10)×2 cm Pb blocks
Scintillator	cyl BAF_2 r=4.5 cm h=16 cm	cyl BAF_2 r=4.5 cm h=16 cm
Slit collimator	2 mm	4 mm
Slit schielding	1 cm	5 cm
Slit neutron collimator	–	6 cm
Target-Scint distance*	68 cm	135 cm
Target-Coll distance	25 cm	20 cm
Target-Shielding distance	50 cm	–
Target-NeuColl distance	–	70 cm

*All the following distance are intended between the center of each volume.

in the photon energy range from 0.1 to 10 MeV. To optimize the collimation of the photon component for the BaF_2 detector, lead bricks were used. The set-up configuration for both experiments is shown in figure 4.2. The characteristics of the experimental set-ups are summarized in table 4.1.

The main difference between GANIL and GSI experiments is related to time pick-up measurements where the beam structure plays a major role. In fact, the investigated ion range verification technique based on prompt gammas rests upon the measurement of the time interval between the impact of the ions on the target and the photon detection by the scintillators. This is done by means of a Time to Amplitude Converter module (TAC).

At GANIL, where the beam is sharply pulsed (beam pulse of 1 ns every 80 ns), the cyclotron high frequency signal (suitably delayed) could be used as stop signal. The start signal was provided by the BaF_2 detection of a photon or neutron in an event by event acquisition mode. The choice of taking the start signal from the detector was adopted to minimize the number of void events for which a start signal does not have a corresponding stop signal. An example of the time of flight (TOF)-energy spectrum measured with the BaF_2 scintillator at the GANIL facility with a 95 MeV/u ^{12}C ion beam is shown in figure 4.3. The beam intensity was monitored by the NaI(Tl) "3 inches" detector placed at a large distance from the target, in order to obtain a counting rate proportional to the beam intensity but nearly independent of target position and collimation. The NaI(Tl) detector was calibrated with a Faraday cup at higher intensities. The beam intensity was

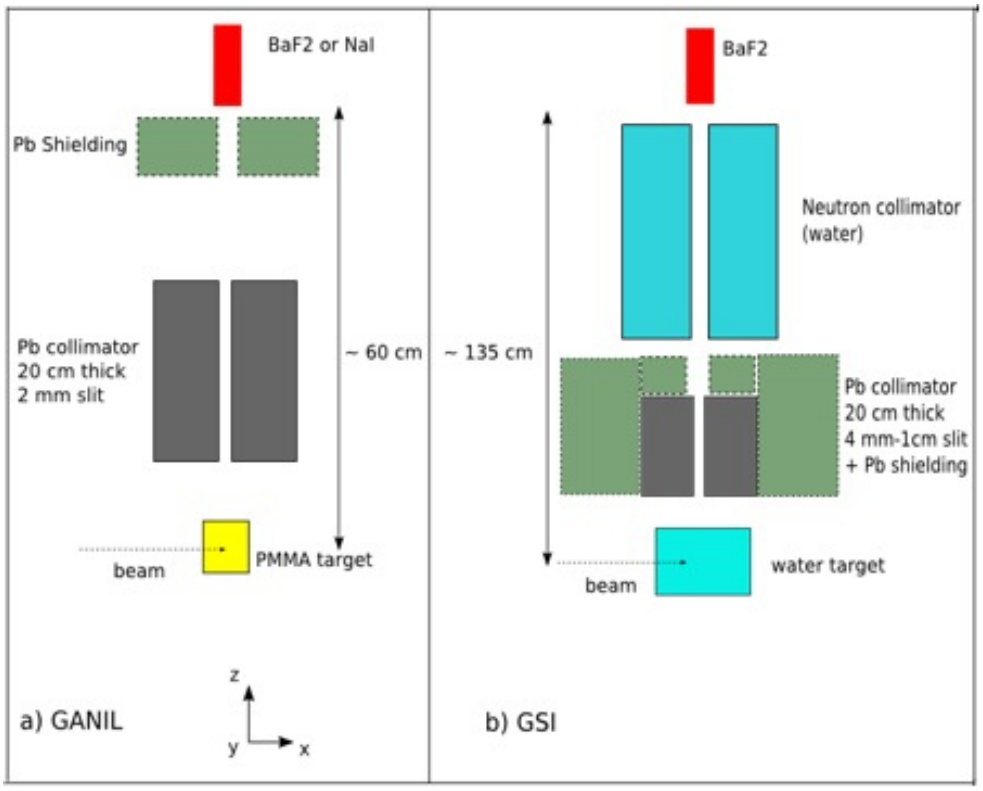

Figure 4.1.: Scheme of the GANIL (left) and GSI (right) experimental set-up. Figure adapted from Le Foulher et al. (2010)

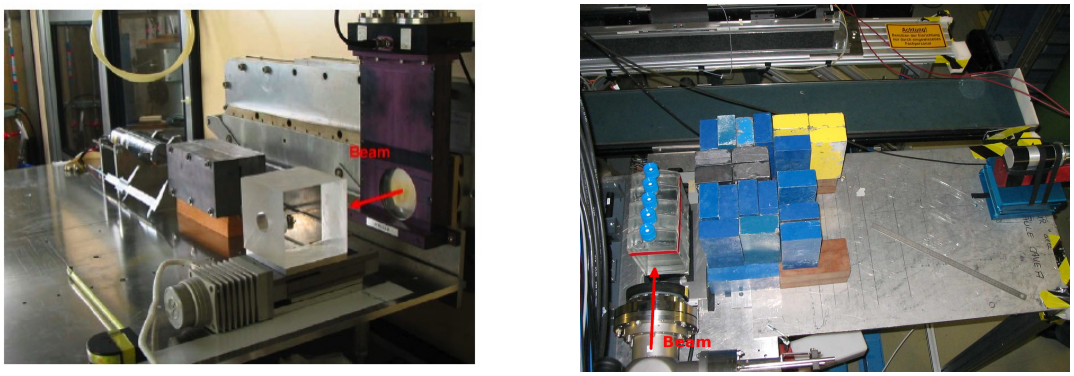

Figure 4.2.: Left: picture of GANIL experimental set-up. The target-detector distance is set to 68 cm and a detection angle h = 90° (with respect to the beam direction). Figure adapted from Testa et al. (2009). Right: picture of GSI experimental set-up. This figure illustrates the beam line exit window in front of the water filled flasks (target), the lead collimator (gray) with additional lead bricks shielding (blue and yellow), the BaF_2 detector. Two thin plastic trigger-scintillators (not present in this picture) were placed between the vacuum window and the water target. Figure courtesy of the Lyon groups.

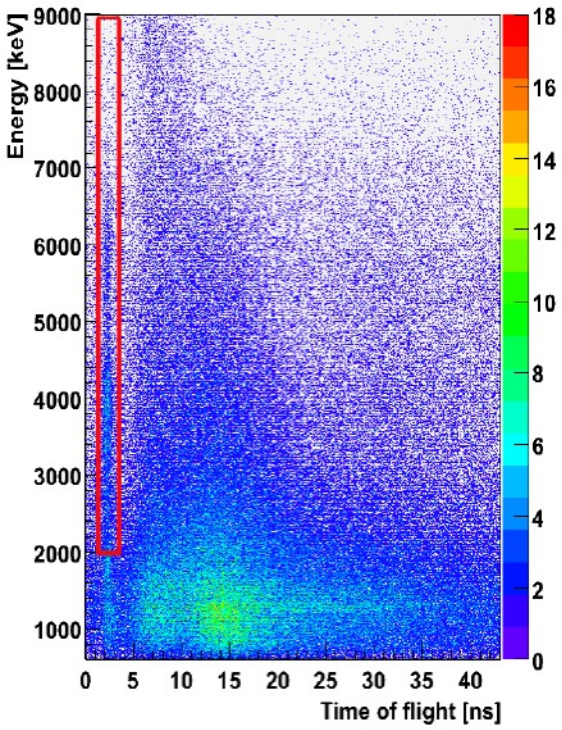

Figure 4.3.: TOF-energy spectrum measured with the BaF_2 scintillator at the GANIL facility with a 95 MeV/u ^{12}C ion beam. The red box marks data points attributed to prompt gamma detections. Figure adapted from Testa et al. (2008).

set to about 1 nA (10^9 ions/s), in order to optimize the detector counting rates while avoiding pile-up and dead-time effects.

Differently, at the SIS-GSI synchrotron, where an almost continuum[1] extraction mode is used (≈8 s extraction every ≈10 s), the TOF stop signal was provided by two thin plastic scintillators intercepting the beam. During the carbon ion extraction, the intensity was kept at a quite low value (≈ 10^5 ions/s) to allow an ion per ion triggering by the plastic scintillators (their efficiency was checked by comparing single and coincidence detection modes). The scintillators were also used to measure the integrated number of ions hitting the target. For both experiments, the detector readout (time and energy distributions) was performed with conventional NIM electronics and a VME data acquisition system.

4.1.2. Prompt gamma scan profiles

The more interesting and relevant results related to the GANIL and GSI single-detector experimental set-ups are the scan profiles reported in the upper part of figure 4.4. Fragmentation occurs almost all along the ion path till 2-3 mm before the Bragg peak, where nuclear reaction cross sections start dropping as the available energy in the projectile-target

[1] The beam of GSI has micropulsed structures of approximately Gaussian shape with FWHM of ≈20-60 ns for periods of ≈250-450 ns (Parodi 2004).

nuclei center of mass approaches the Coulomb barrier. This implies that the measurement of the emitted prompt gammas could bring valuable information on the dose distribution and the Bragg peak position. The prompt photon scan profiles were obtained by integrating the counts detected by the BaF_2 scintillator in the prompt photon peak of the TOF spectra (cf. red box in figure 4.3) at various longitudinal positions (position zero corresponds to the target entrance). The time integration interval was 1.5 ns centered on the prompt photon peak.

The importance of the TOF discrimination technique is evident from the scan profiles in figure 4.5. A photon energy threshold of 2 MeV was chosen to optimize the statistics and the signal to background ratio. In the case of the scan obtained by integrating only the prompt photon component of the TOF spectrum (red points), a correlation is observed between the ion range (the Bragg peak position is marked by a dashed line) and the detected photons. The increase of the gamma yield at the end of the ion path can be attributed to an increase of the fragmentation cross section and photon emission multiplicity, when the ion energy decreases. On the contrary, the scan profile obtained by integrating the entire TOF spectrum (black points) is completely flat and therefore uncorrelated to the ion range. This demonstrates the absolute need of TOF selection of the prompt gammas to obtain photon scan profiles correlated with the ion range when using the chosen BaF_2 detector. Indeed, it has to be noted that the signal to background ratio measured in the present set-up was not yet optimized: more than 90% of the 1 liter volume of BaF_2 detected only background, which required a large quantity of lead shielding to be used, which in turn created a high background (cf. figure 4.3).

4.2. Monte Carlo simulations of the GANIL and GSI experiments

4.2.1. GEANT4 simulations

Parallel to the experiments presented so far, MC simulations have been performed by the Lyon groups in order to reproduce the measurements and to perform a benchmark of the GEANT4 (version 9.1) code with measured data of prompt gammas created during nuclear fragment de-excitation. The details of all these simulations can be found in Le Foulher et al. (2010). The shape of the experimental profile is not perfectly reproduced by the GEANT4 simulations as shown in the bottom of figure 4.4. In fact, for the GANIL experiment (cf. left panel in figure 4.1), the measured counting rates increase with the ion penetration depth, while the simulated counting rates decrease. GEANT4 fails also to reproduce the Bragg peak enhancement in the prompt gamma profile. Moreover, with the physics list used in Le Foulher et al. (2010) (i.e., Shen formula, binary cascade model, Weisskopf-Ewing model, photon evaporation channel and standard electromagnetic physics package), the gamma evaporation models overestimate the total emission yield by a factor up to $\sim$12, as consistently observed in several experiments. Further developments of the models handling the hadronic interactions in GEANT4 are highly desirable and currently ongoing to finally make GEANT4 a fully reliable simulation code. Nevertheless, comparisons of the experimental data and GEANT4 toolkit results with other MC codes are of crucial

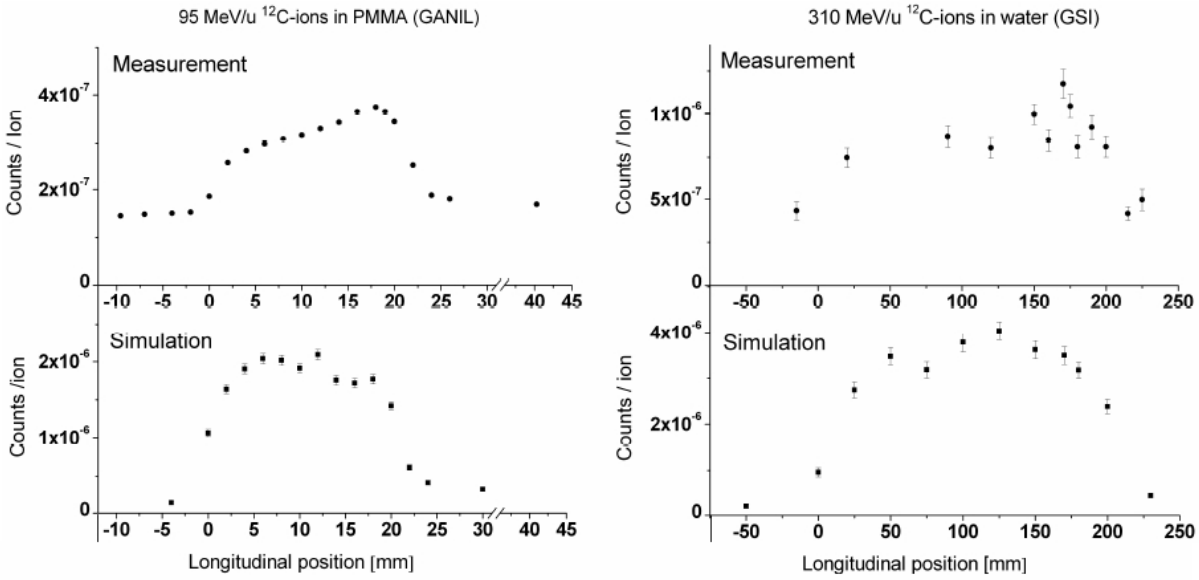

Figure 4.4.: Longitudinal prompt photon scan profile obtained for the GANIL experiment with 95 MeV/u ^{12}C ions (left) and for the GSI set-up with 310 MeV/u ^{12}C ions (right). Comparison between the measured gamma profiles at GANIL and GSI (top) and simulated with GEANT4 (bottom). Figure adapted from Le Foulher et al. (2010).

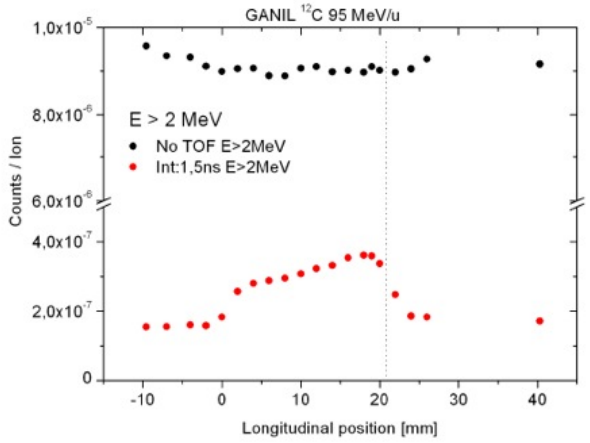

Figure 4.5.: Example of TOF selection. Longitudinal scan profile obtained for GANIL experiment with 95 MeV/u ^{12}C ions. The origin of the longitudinal axis corresponds to the target entrance position. The prompt gamma yield obtained with TOF selection (red points) is strongly correlated to the ion path in the target, whereas the counting rate profile without TOF selection (black points) is almost flat. The calculated Bragg peak position is given by the dashed vertical line. Figure adapted from Testa et al. (2010).

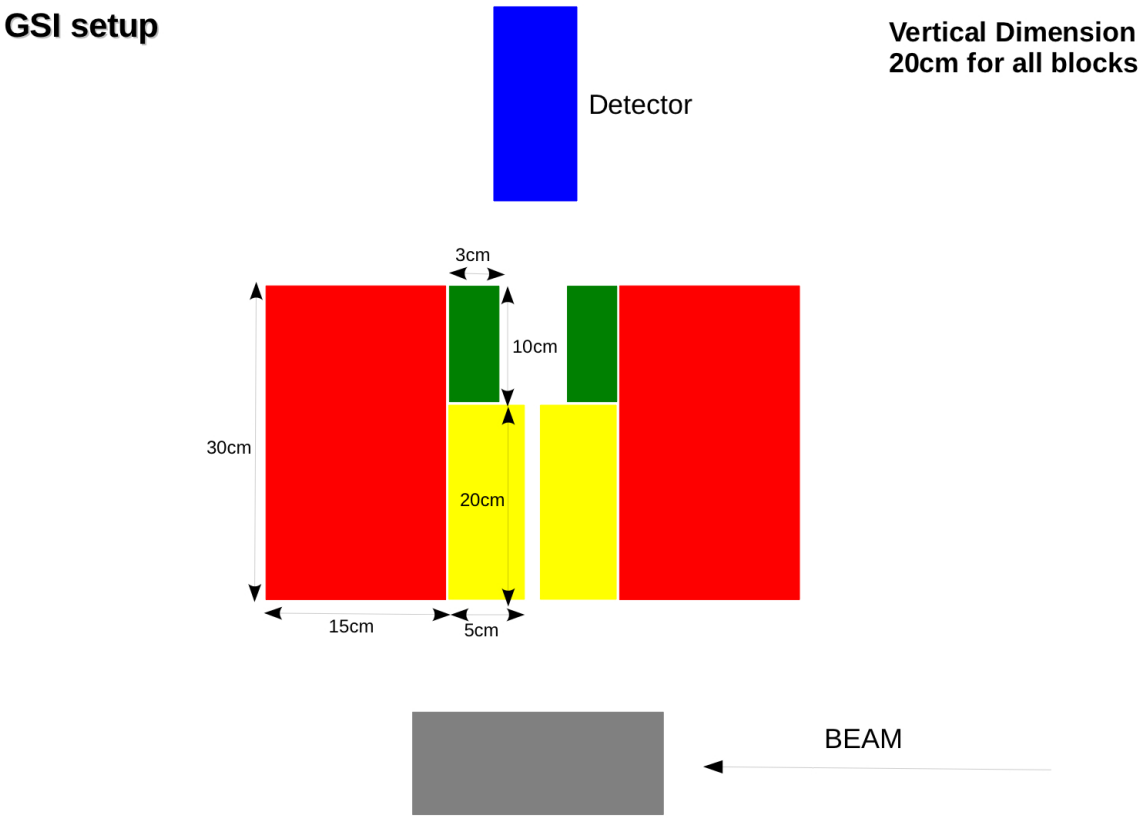

Figure 4.6.: Details of the GSI experimental set-up implemented in FLUKA. The colored regions indicate collimators (yellow), shielding blocks (green and red), target (gray), detector (blue), as listed in table 4.1.

importance. For this reason, within this thesis, simulations using the FLUKA MC code were performed to reproduce the two experiments. The results are presented in section 4.2.2.

Lately, these investigations on prompt gammas for imaging applications have been reinforced in the framework of the ENVISION (European NoVel Imaging Systems for ION therapy, http://envision.web.cern.ch/ENVISION/) European project.

4.2.2. FLUKA results

The geometries shown in figure 4.1 and described in table 4.1 were implemented in the FLUKA simulations in order to reproduce the experimental set-ups. In particular, the details of the GSI geometry as implemented in FLUKA are displayed in figure 4.6.

For this work and all the following investigations on prompt gammas, the FLUKA development version, kindly made available by the FLUKA collaboration, was used in a joint

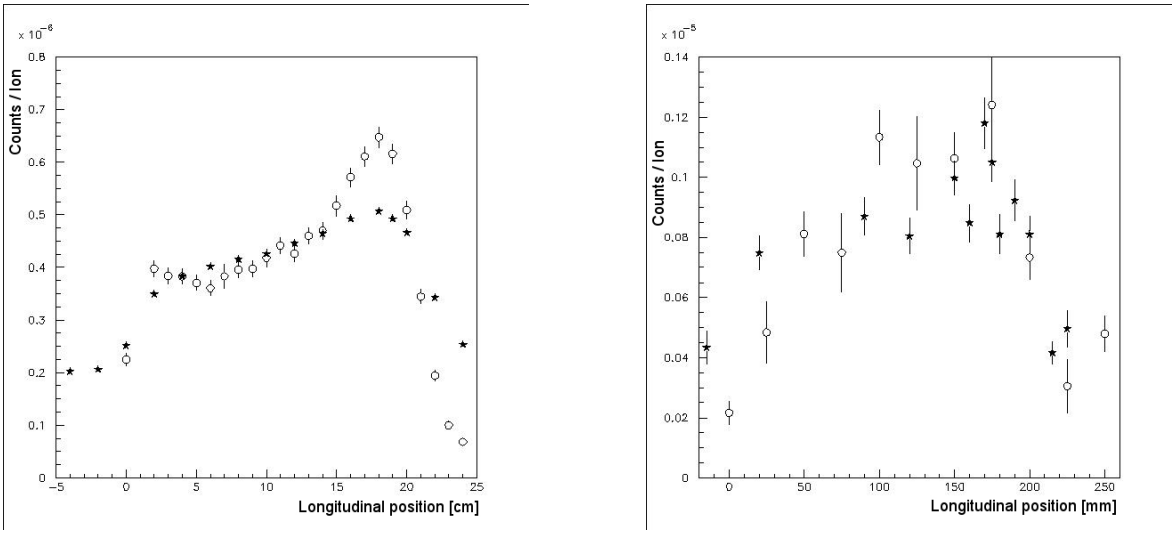

(a) GANIL set-up

(b) GSI set-up

Figure 4.7.: (a) Comparison between experimental data (stars) and FLUKA results (open circles) for the GANIL set-up with a beam of 95 MeV/n ^{12}C ions onto a PMMA target. The experimental data are multiplied by a factor of 1.35. (b) Comparison between experimental data (stars) and FLUKA results (open circles) for the GSI set-up with a beam of 310 MeV/n ^{12}C ions onto a water target. No normalization was applied here due to larger fluctuations.

research activity together with the code developer team at CERN. This version contains recent developments relevant for the physics of prompt gammas emitted in the de-excitation phase following nuclear fragmentation (cf. section 1.2.5). The new features are already partially inserted in the released FLUKA version 2011.2.

The results of the comparison between experimental data and FLUKA simulations for the GANIL and GSI set-ups are presented in figures 4.7(a) and 4.7(b), respectively. These plots show that simulations performed with FLUKA reproduce quite well the enhancement of the prompt photon detection towards the end of the ^{12}C ion range and more generally the entire photon scan profiles. Moreover, it has to be noticed that the GANIL experimental data are effected by background noise visible in the first two data points. These have been taken in the air just in front of the PMMA phantom where theoretically almost no gammas are expected. The read-out signal can therefore only be attributed to noise. The real detector efficiency has not been taken into account in the simulations and the GANIL experimental data are multiplied by a factor 1.35 to make them overlap.

In regard to the GSI set-up, it has to be remarked that the experimental results include fewer data points compared to the GANIL experiment and show larger fluctuations due to the low beam intensity and higher neutron background because of the increased beam energy. The peak position can be roughly estimated although identifying an accurate profile is difficult. Therefore, limited conclusions can be drawn from comparison of these data and the FLUKA results.

Overall, there is a reasonable correspondence between experimental and simulated data

and it is thus concluded that, thanks to the recent improvements in the modeling carried out by the developers, the FLUKA MC code already provides a sound tool to investigate more detailed aspects of prompt gamma detection.

4.3. Prompt gammas to monitor range and density variation

Some of the following investigations (Biegun et al. 2011) are being pursued within the framework of a scientific collaboration between the RD&M, Delft University of Technology (The Netherlands), the Maastro Clinic in Maastricht (The Netherlands), the LIP-Laboratório de Instrumentação e Física Experimental de Partículas of Coimbra (Portugal), the ISEC-Instituto Superior de Engenharia de Coimbra (Portugal) and HIT. The aim of this collaboration is to study the physics related to prompt gamma experiments and in particular its implications for the use in imaging applications. The interest is to understand how to set up a detector system and to tune its parameters to obtain an optimum signal of the gammas. To this end, use has been made of different MC codes (FLUKA, GEANT4, MCNPx) as independent tools to support the design of detectors and experiments. The simulations using the development version of the FLUKA MC code, kindly made available by the FLUKA collaboration, were performed within this thesis and, in the following, the results are presented.

In these virtual experiments, proton pencil beams of different initial energies impinging onto PMMA phantoms were simulated. The complexity of the phantoms was successively increased by adding various internal regions of different materials. In all simulations, gammas and neutrons were scored in a very thin (1 mm) perfect cylindric detector (i.e., having 100% detection efficiency as well as perfect position and time resolution) as depicted in figure 4.8. The calculations were done with $20 \cdot 10^6$ primaries.

4.3.1. Investigations in a homogeneous phantom

In a first step, the most simple phantom geometry consisting of homogeneous PMMA was adopted. This way, the influence of the gamma detection angle (cf. section 4.3.1.1), the primary energy (cf. section 4.3.1.2), and the phantom density (cf. section 4.3.1.3) on the gamma profiles and the TOF and energy spectra was studied.

4.3.1.1. Angle of detection

In this section, the dependence of the measurable gamma and neutron yields on the angle of detection is presented.

A 200 MeV proton pencil beam impinging on a homogeneous PMMA phantom (cf. figure 4.8) was simulated and the prompt gamma profiles were detected with different collimation angles θ. The results are shown in figure 4.9 for five different detection angles of $\pm 1°$ centered around $\theta = 30°$, 60°, 90°, 120° and 150°. The collimation of photons is done taking into account the angle of the gammas entering the ideal detector. The neutrons remain uncollimated and are counted entirely in the simulations. From these figures it is

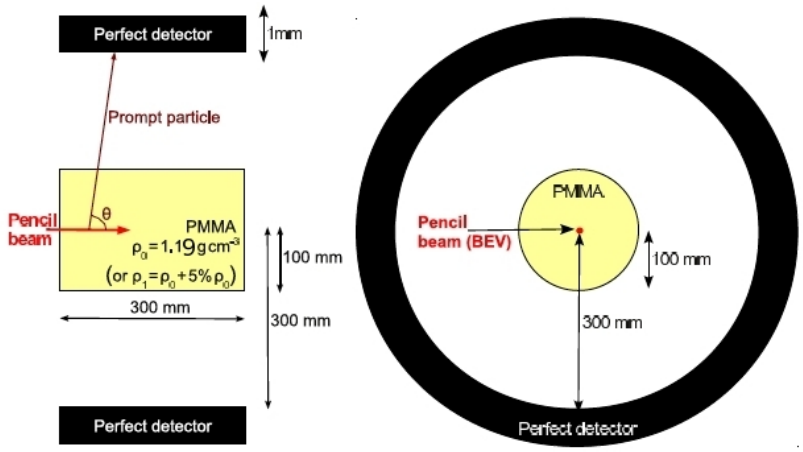

Figure 4.8.: Side view (left) and the Beam's Eye View (BEV, right) of the first set-up simulated for the prompt gamma investigations. The incoming protons are assumed to be monoenergetic and the beam shape is pencil-like. The cylinder PMMA target phantom has a radius of 10 cm and a height of 30 cm. Figure adapted from Biegun et al. (2011).

clear that the dose profiles match with a sharp and steep fall-off of the prompt gamma profiles only in the case of a collimation angle around 90°. Alternatively, figure 4.10 shows the angular distribution of both, gammas and neutrons, underlining that the former are detected mostly around 90°, while the latter occur mostly in the forward direction.

From the physics point of view, this correlation at 90° is justified by the spatial relationship between collimated detection and angular emission, the latter being isotropic in the center of mass.

Moreover, collimation angles centered at 90° with different apertures ($89.9° < \theta < 90.1$, $89.8° < \theta < 90.2$, $89.7° < \theta < 90.3°$, $89.5° < \theta < 90.5°$, $89.3° < \theta < 90.7°$, $87.0° < \theta < 93.0°$) are depicted in figures 4.11 and 4.9(c).

The distal edges of the prompt gamma profiles correspond remarkably well to those of the proton delivered doses for narrow collimation angles until $\theta \simeq (90° \pm 1°)$. Enlarging the acceptance angle to $\theta = (90° \pm 3°)$ (cf. figure 4.11(f)), there is an increase in the prompt gamma yields, but the correlation between the Bragg peak position and the fall-off of the prompt gamma profiles is not so pronounced anymore. Indeed, this is not surprising since a larger opening angle implies stronger spatial smoothing of the gamma profile. In all following simulations, a detection aperture of $(90° \pm 1°)$ was used.

Despite the observed spatial correlation, these graphs also reveal a very large neutron background. Consequently, some form of neutron discrimination must be implemented to obtain a measurable signal. Techniques like TOF tagging (Testa et al. 2008, Parodi et al. 2005, Crespo et al. 2007), pulse shape discrimination (Testa et al. 2008) or neutron shielding (Min et al. 2006) could be a solution, at the expense of increased detector complexity.

It has to be taken into account that the total signal to noise (S/N) ratio is also determined by statistical fluctuations in the photon signal, which improves with increasing photon counts. Opening up the collimation angle increases the number of detected photons (improving S/N) but results in a shallower fall-off of the measured prompt gamma

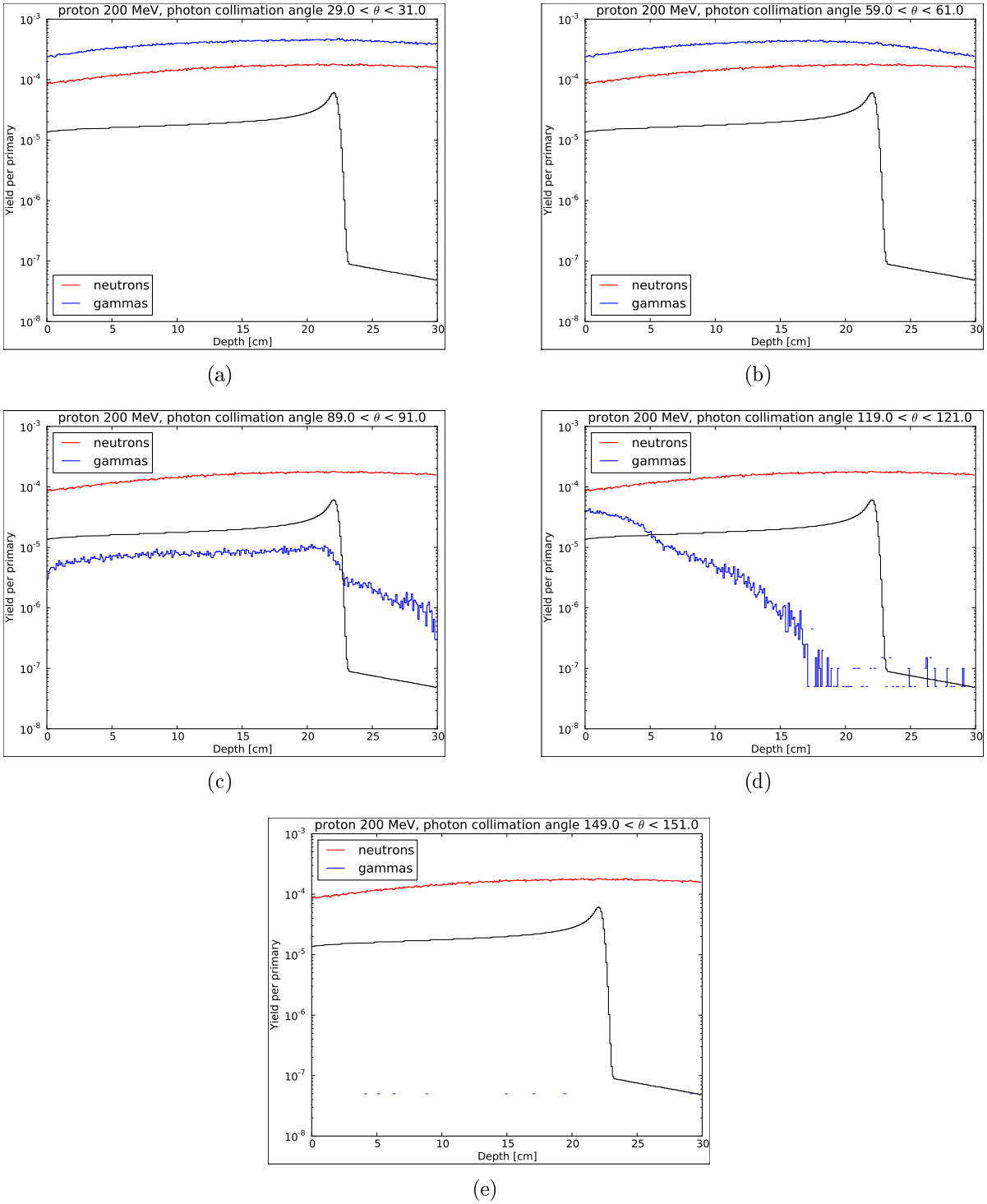

(a) (b) (c) (d) (e)

Figure 4.9.: Correlation between the depth-dose distribution of a 200 MeV proton beam impinging on a homogeneous PMMA phantom and the detected prompt gamma profiles using different collimation angles θ for the photon detection: (a) $29.0° < \theta < 31.0°$, (b) $59.0° < \theta < 61.0°$, (c) $89.0° < \theta < 91.0°$, (d) $119.0° < \theta < 121.0°$, (e) $149.0° < \theta < 151.0°$. Neutrons remain uncollimated and are counted entirely in the simulations.

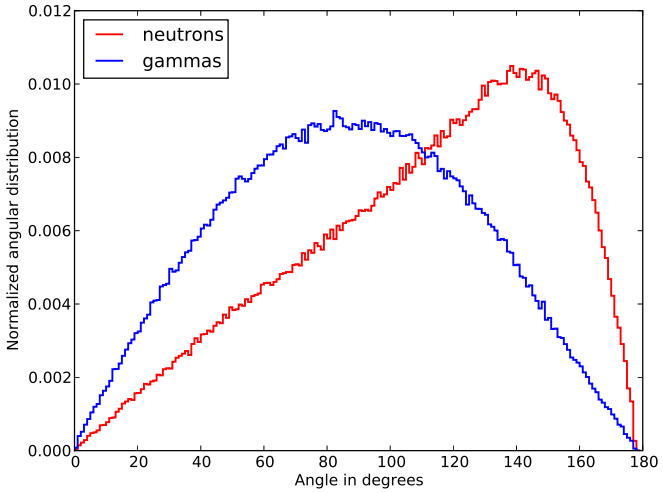

Figure 4.10.: Angular distribution of the detected gammas and neutrons.

profile. In fact, the accuracy by which the Bragg peak can be localized depends both on the S/N and the slope of the gamma profile in the fall-off region. During the design of a detector and/or an experiment, a trade off has to be made between signal strength and profile shape.

4.3.1.2. Influence of primary energy

To analyze the influence of the primary energy on the prompt gamma profiles and the TOF-energy spectra, proton pencil beams of 100, 150, and 200 MeV impinging onto PMMA phantom were simulated according to the geometry reported in figure 4.8. Following the analysis presented in section 4.3.1.1, a collimation angle of $89° \leq \theta \leq 91°$ for the prompt gammas was used, while all neutrons impinging onto the annulus detector were accepted.

In figure 4.12, the depth-dose distributions and the profiles of the collimated prompt gammas and uncollimated neutrons scored in the ideal detector are shown. It can be seen that the photon yield per primary is around $5 \cdot 10^{-6}$ and quite unchanged by the increase in primary energy. The number of detected neutrons, on the other hand, increases with higher beam energy. Regarding the profile shape, it can be observed that the distal edge of the prompt gamma profiles shifts in depth as the Bragg peak position according to the primary beam energy

Moreover, the TOF spectra of prompt gammas and neutrons resulting from this set-up are shown in figure 4.13. The TOF is the total elapsed time between the generation of the primary beam and the detection of the gamma (or neutron) in the detector. It is therefore obtained summing two time components which depend on the distance traveled by the primary beam particles in the stopping medium and by the gamma itself from the point of emission to the place of detection. The figure illustrates that for low proton beam energy (e.g., figure 4.13(a)), the gamma and neutron TOF spectra are clearly separated. In fact,

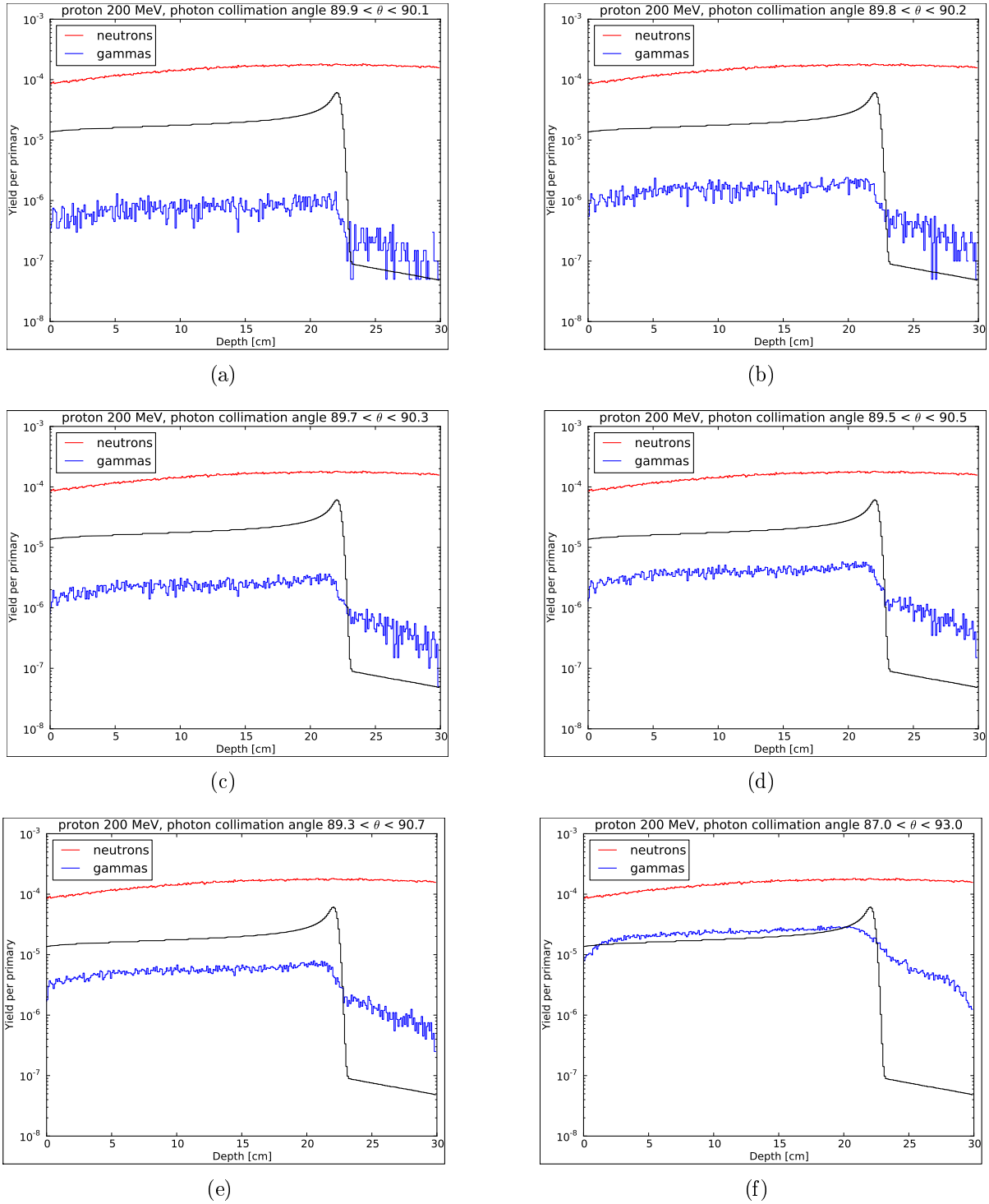

Figure 4.11.: Investigation of the correlation between the depth-dose distribution of a 200 MeV proton beam on a homogeneous PMMA phantom and the detected prompt gamma profiles using different collimation angle θ centered at 90° of the photons: (a) $89.9° < \theta < 90.1$, (b) $89.8° < \theta < 90.2$, (c) $89.7° < \theta < 90.3°$, (d) $89.5° < \theta < 90.5°$, (e) $89.3° < \theta < 90.7°$, (f) $87.0° < \theta < 93.0°$. Neutrons remain uncollimated and are counted entirely in the simulations.

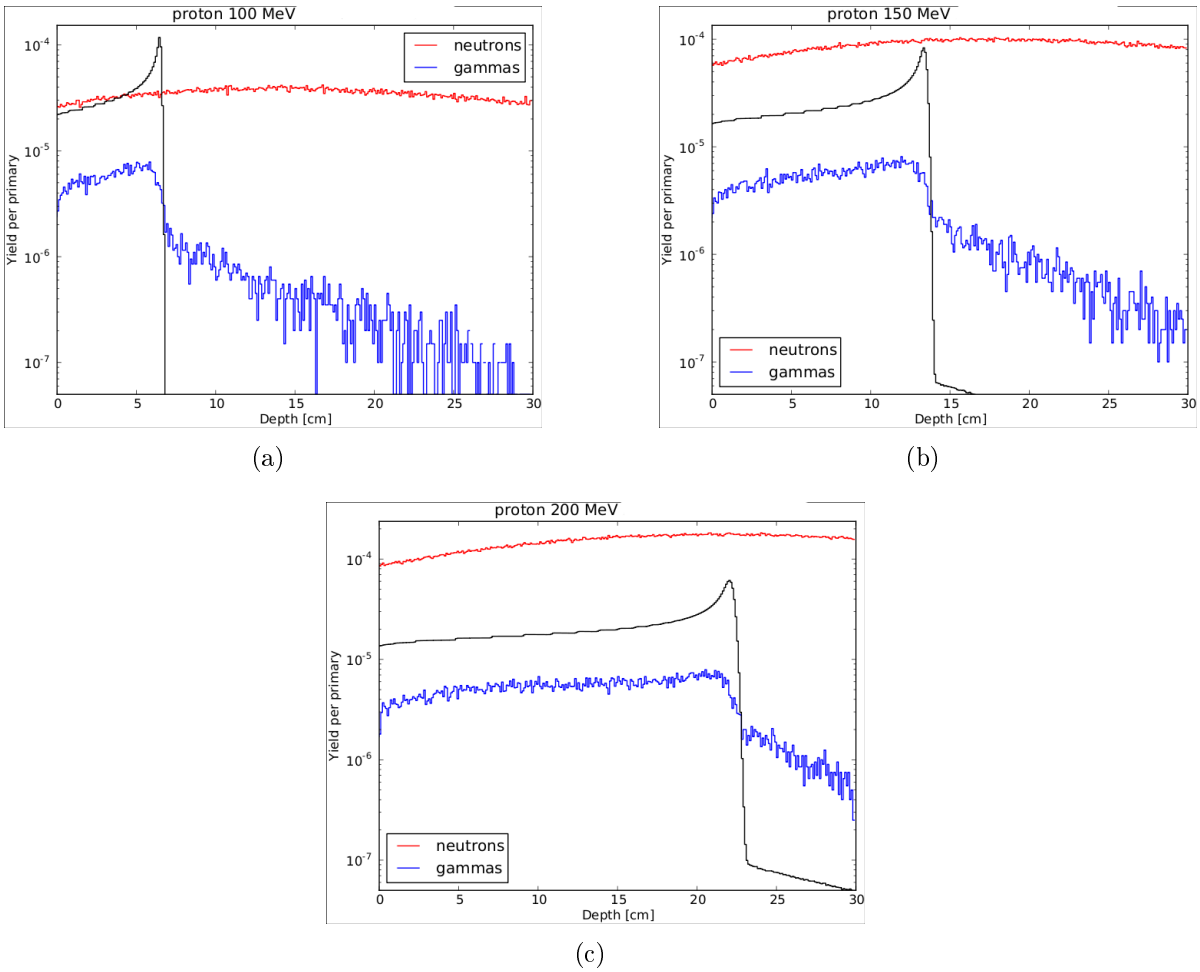

Figure 4.12.: Depth-dose distributions in the PMMA phantom and the profiles of the collimated prompt gammas and uncollimated neutrons scored in the ideal detector of figure 4.8 for three different initial energies of the proton pencil beam: 100, 150, and 200 MeV.

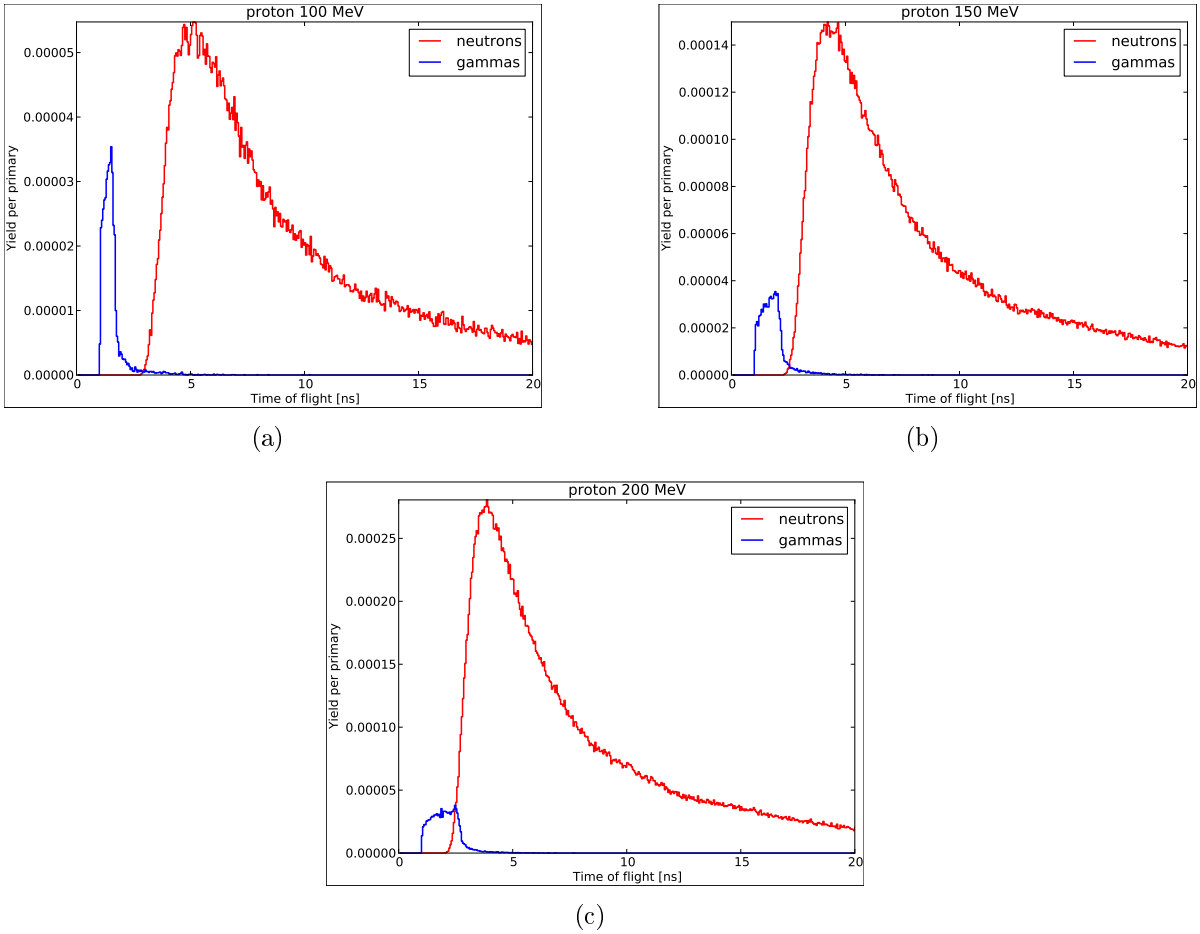

Figure 4.13.: TOF spectra of the collimated gammas and uncollimated neutrons escaping the PMMA phantom and impinging onto the detector for proton beam at three different initial energies: 100, 150, and 200 MeV.

the TOF spectrum of the gammas is confined between 1 and 2 ns, while the TOF spectrum of neutrons starts around 3 ns.

In the case of a pencil beam in a homogeneous phantom, the TOF dispersion of the gammas is due only to the different depths of the points of production of the gammas. Counting only gammas emitted in a short depth interval would produce a much narrower TOF distribution. If the beam energy is increased, both, the total yield and the overlap of the neutron and gamma TOF spectra grow (cf. figures 4.13(b) and 4.13(c) for 150 and 200 MeV proton beam, respectively). These plots underline the importance of detectors with a high time resolution (on the order of 1.0 ns or less) for the TOF technique, in particular at higher energies. Moreover, detectors enabling the use of pulse shape discrimination for gamma/neutron separation could be utilized.

Additionally, in figure 4.14, the TOF-energy spectra of the collimated gammas and uncollimated neutrons scored in the detector are visualized. These scatter plots show that there is a maximum energy of the detected prompt gammas at around 10 MeV. The prompt

photon peak, arising at a few ns, broadens with the increase of the proton beam energy. Moreover, the difference to the experimental TOF-energy spectra (cf. figure 4.3) is evident, where a huge background is present due to the shielding and the experimental environment (e.g., walls of the treatment room).

4.3.1.3. Density changes

The further simulations and analyses concern density changes due to morphological modifications in the target possible in real radiotherapy scenarios (e.g., tumor or normal tissue swelling, breathing). In fact, during patient treatment for example the occurrence of edematous swelling of the tumor is possible typically within the first three days of treatment (Cameron et al. 1969, Biegun et al. 2011), with consequent accumulation of additional material in the beam path producing potential distal tumor underdosage.

For this purpose, the density of the PMMA phantom depicted in figure 4.8 has been increased ($\rho_1 = \rho_0 + 5\%\rho_0$) and decreased ($\rho_2 = \rho_0 - 5\%\rho_0$) by a factor of 5% ($\rho_0 = 1.19$ g/cm^3). The resulting shift of the Bragg peak is clearly observed and the prompt photon profiles are found to change accordingly, as presented in figure 4.15.

4.3.2. Investigations in heterogeneous phantoms

The next step was to study the potential of this method under the influence of local morphological changes. In fact, another possible biological mechanism that might disturb the dose distribution are empty cavities in the head filled with mucus and/or inflamed tissue (edema). This may arise as a response of healthy and tumor tissues to the consecutive and fractionated irradiations (Denham and Hauer-Jensen 2002, Biegun et al. 2011). All these potential morphological modifications may change the range of the ion beam.

For this purpose, a bone-tumor-like geometry before (cf. upper panel of figure 4.16) and after (cf. lower panel of figure 4.16) the formation of an edema (treated as water) in an air cavity was simulated.

Depth-dose distributions and the profiles of the collimated prompt gammas and uncollimated neutrons scored in the ideal detector for two different energies (i.e., 150 and 200 MeV) of the proton pencil beam are shown in figure 4.17. Within the limitations given by statistical noise, the profiles of the collimated prompt gammas are observed to follow reasonably well the depth-dose distributions of the primary protons.

More interesting for these two geometries (cf. figure 4.16) are the TOF spectra presented in figure 4.18 for two different primary energies (i.e., 150 and 200 MeV). In addition to the considerations presented in section 4.3.1.2 for the homogeneous phantom, in a heterogeneous phantom the total TOF distribution of the gammas is not only due to the different depths of the points of production of the gammas but also due to the different densities of the traversed materials. This phenomenon is well visible in figure 4.18 for the considered phantom with discrete zones of different densities. In fact, the total TOF spectra are composed of several peaks centered around different points on the time axis each showing some dispersion. The different positions of the peaks are due to the characteristic times needed by the collimated gammas to traverse the different materials on their way to the detector, while, as stated above, the dispersion of the peak is due to the different

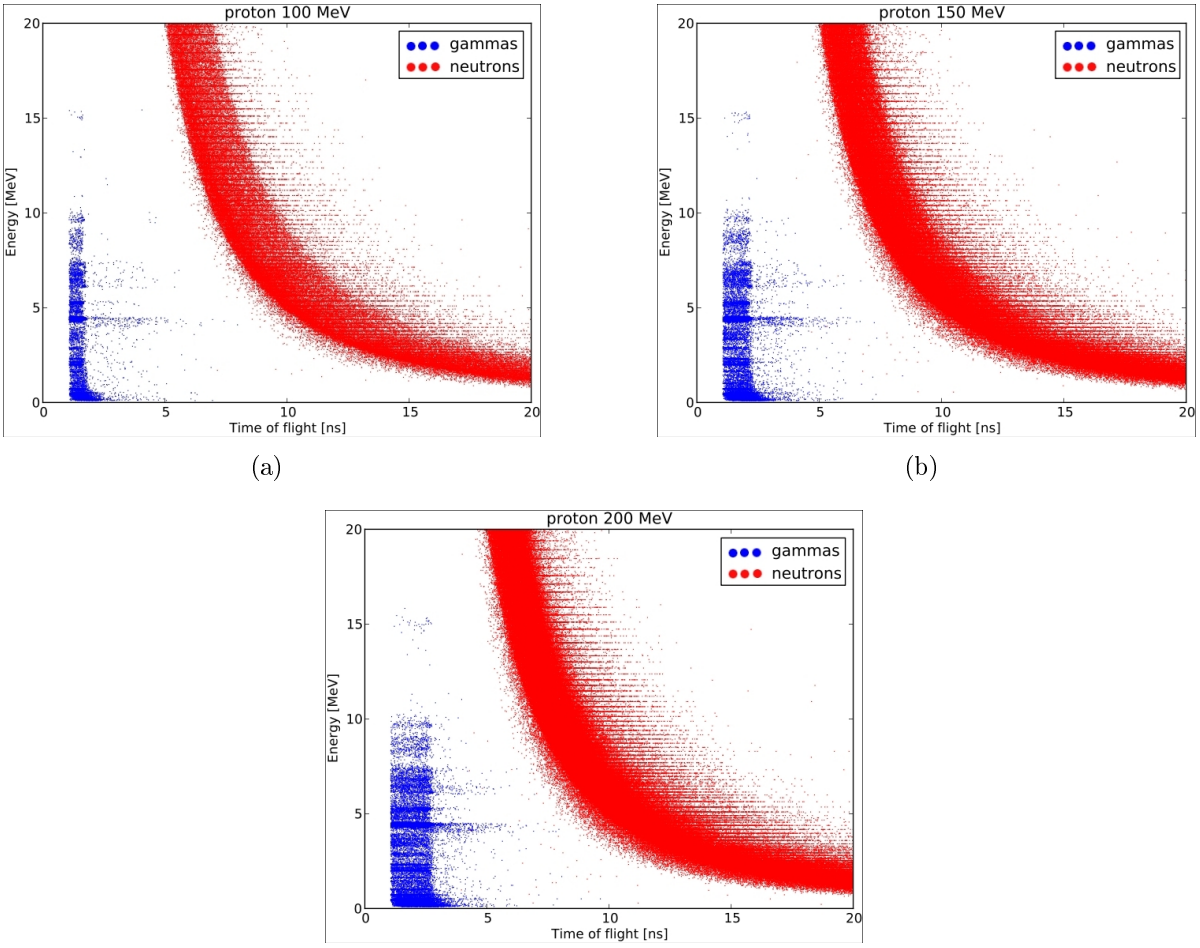

Figure 4.14.: Two-dimensional spectra of the energy deposited in the detector as function of TOF of the collimated gammas and uncollimated neutrons escaping the PMMA phantom and impinging onto the detector for proton beam at three different energies: 100, 150, and 200 MeV.

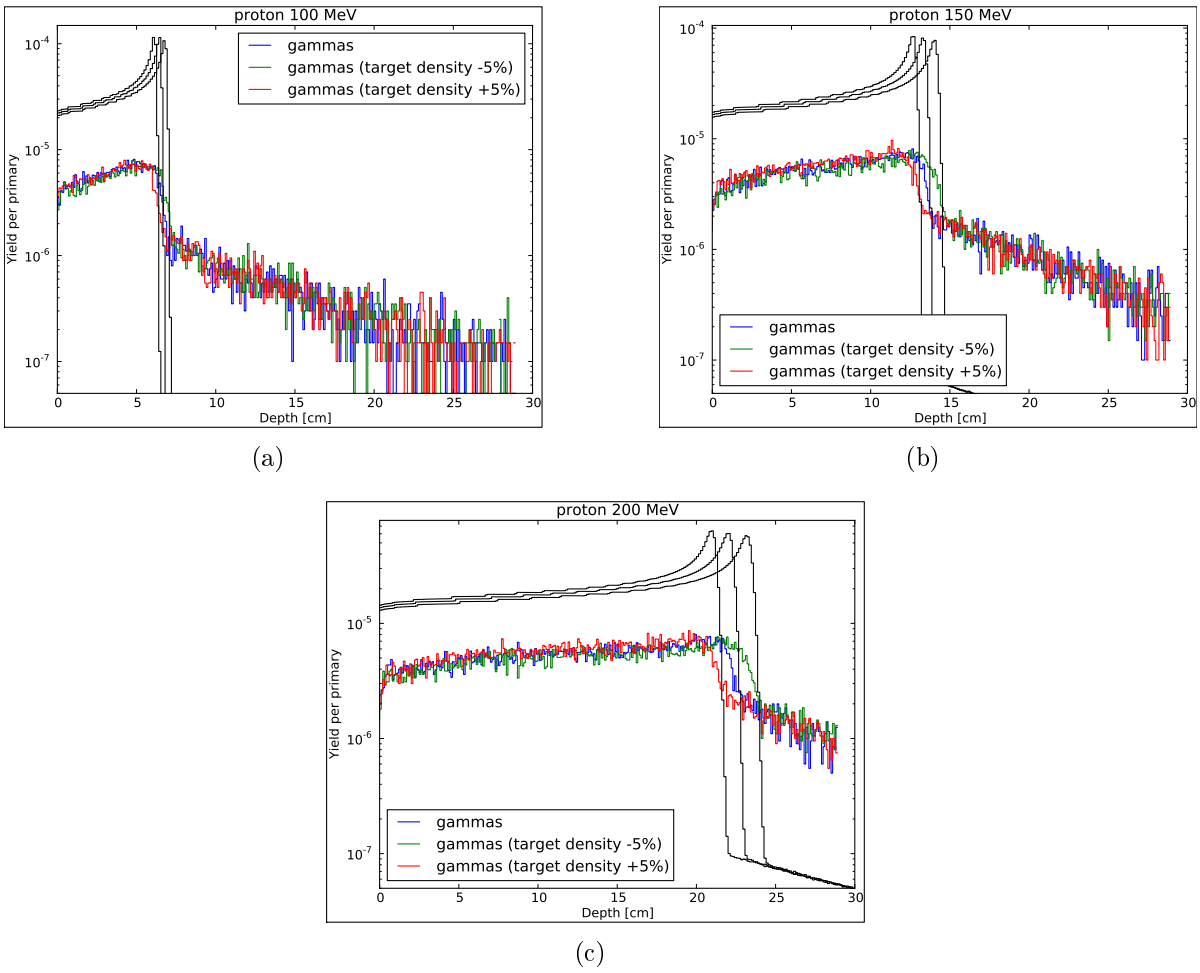

Figure 4.15.: Depth-dose distribution (black) and the profiles of the collimated prompt gammas scored in the ideal detector for three different energies of the proton pencil beam: 100, 150, and 200 MeV. Prompt gammas profiles of PMMA phantom with density $\rho_0 = 1.19\ g/cm^3$ in blue, 5% higher density $\rho_1 = \rho_0 + 5\%\rho_0$ in red and 5% lower density $\rho_2 = \rho_0 - 5\%\rho_0$ in green.

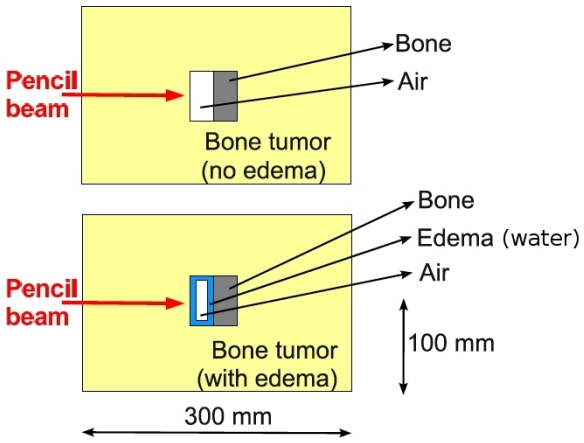

Figure 4.16.: Set-ups simulated for the investigations in heterogeneous phantoms. The incoming protons are assumed to be monoenergetic and the beam shape is pencil-like. The cylinder PMMA target phantom has a radius of 10 cm and a height of 30 cm. Additionally, the simulated geometries include a bone tumor before (upper panel) and after (lower panel) the formation of an edema, treated as water, in an air cavity. Figure adapted from Biegun et al. (2011).

depths of the points of production of the gammas.

Summarizing, it can be stated that the prompt gamma scan profiles are sensitive to density and morphological changes in phantoms. The detection of collimated gammas can be potentially used as indicators for these morphological parameters. Further studies will be needed to assess the feasibility of TOF discrimination techniques.

Moreover, in all of the presented simulations, the neutrons impinging onto the detector were collected with 100% efficiency and without considering any angular collimation. Therefore, the neutron profiles obtained in this simulation study represent the worst case scenario. In fact, for example, large scintillator detectors (e.g., BaF_2 with approximately 5 dm^3 active volume) have a measured detection efficiency lower or equal to 20% for fast neutrons (E $\geq$ 100 MeV). This efficiency drops down in the case of neutrons with inferior energy (Gunzert-Marx et al. 2005). Finally, it must also be stated that no detector response was simulated at this stage.

4.4. Simulations in a real patient

The investigations presented in section 4.3 were performed for pencil beams impinging onto phantoms of different complexities. In this section, first results for a real patient case treated in the last months at HIT are presented.

One objective is to check the validity of the conclusions drawn from the previous simulations of relatively simple geometries concerning collimated gamma profiles (cf. section 4.4.1) and TOF spectra (cf. section 4.4.2). In particular, an interesting aspect is to compare cumulative gamma profiles to the dose delivered by an extended treatment

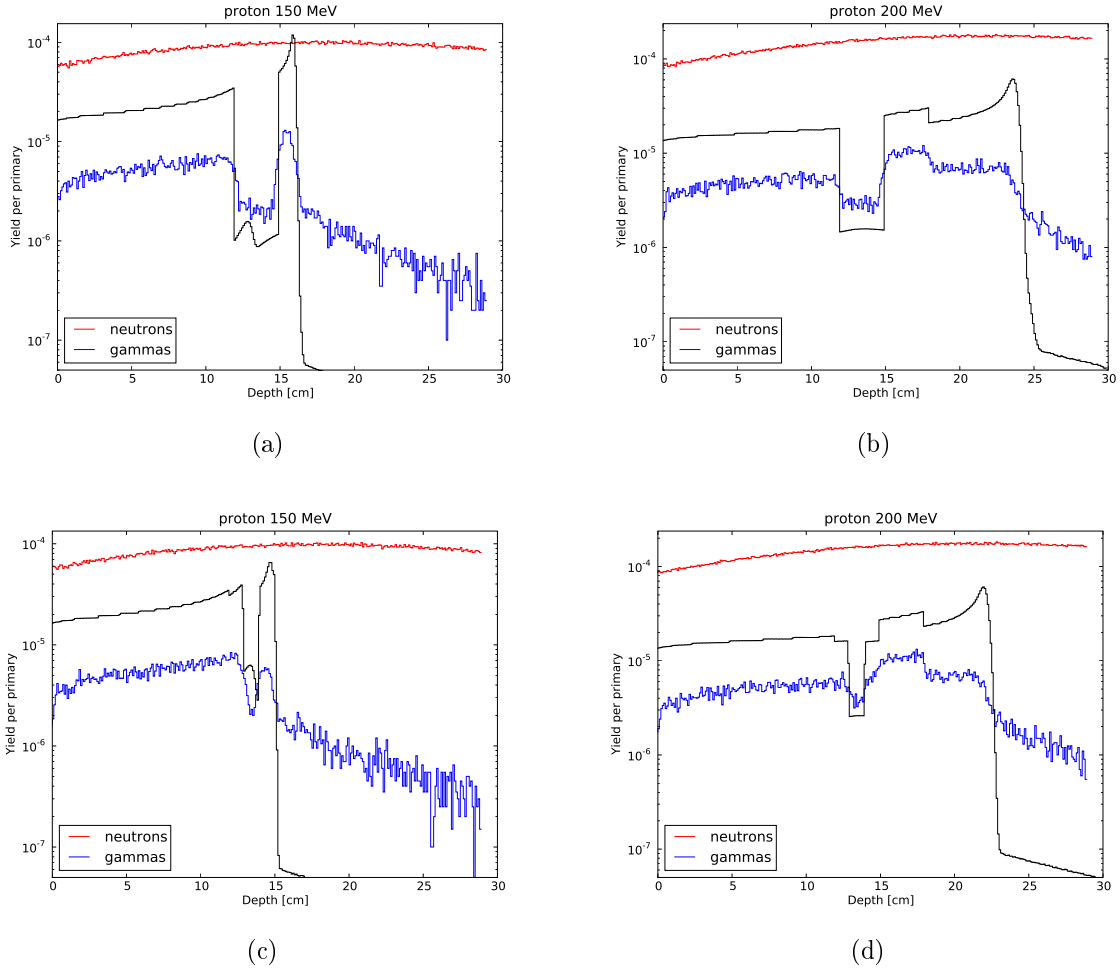

Figure 4.17.: Depth-dose distribution and the profiles of the collimated prompt gammas and uncollimated neutrons scored in the ideal detector for two different energies of the proton pencil beam: 150 and 200 MeV. A bone-tumor-like geometry before (a,b) and after (c,d) the formation of an edema in an air cavity were simulated.

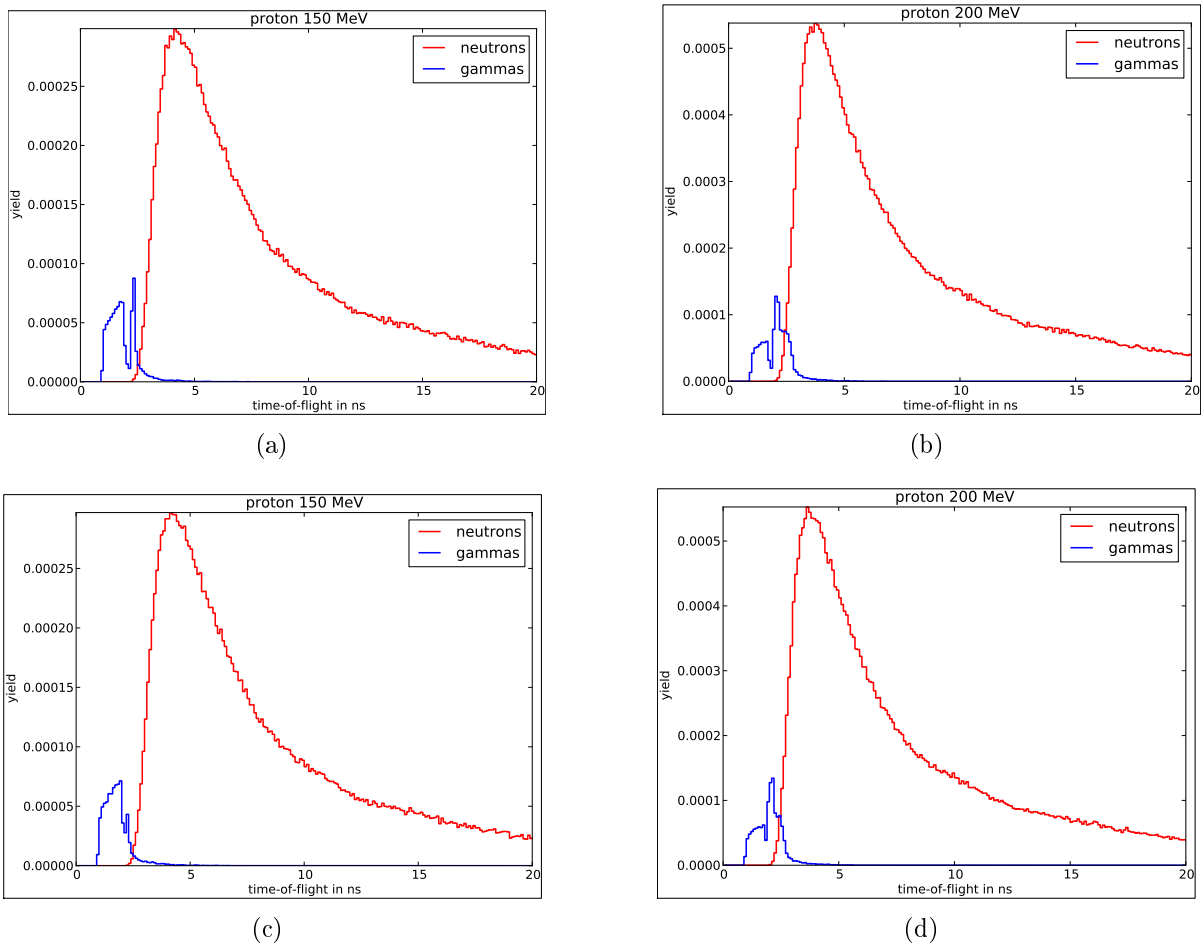

Figure 4.18.: TOF spectra of the collimated gammas and uncollimated neutrons escaping the PMMA phantom with a bone-tumor-like geometry before (a,b) and after (c,d) the formation of an edema in an air cavity and impinging onto the detector for proton beam at two different energies: 150 and 200 MeV.

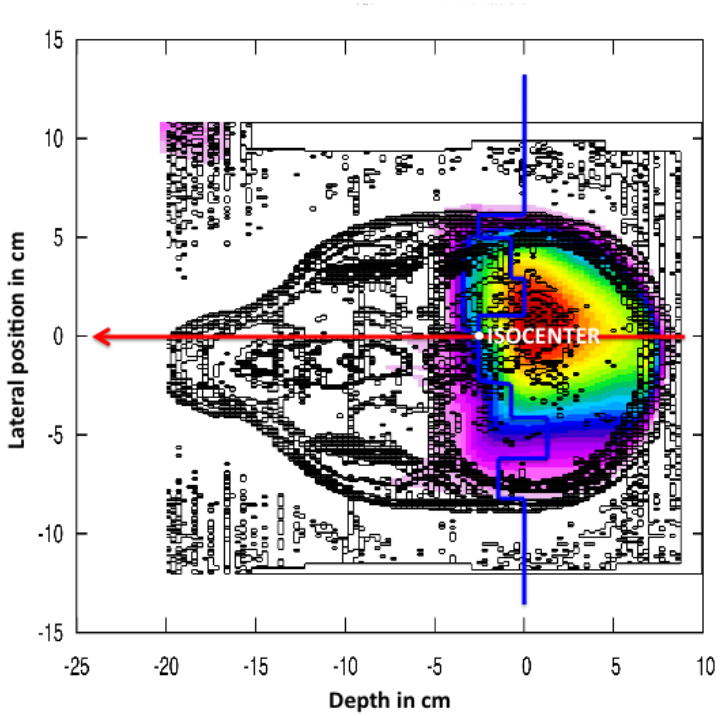

Figure 4.19.: 2D projection of the patient head with a sketch of the delivered treatment plan superimposed as color wash display for a cranial field. The red arrow and blue line indicate the two subsets of the treatment plan that were used for the simulations.

field (SOBP). Finally, a first approach is introduced to quantitatively correlate the gamma profile and the Bragg peak position (cf. section 4.4.3).

For these studies, patient CT information was imported into the FLUKA MC code and also the active ion beam delivery scanning of HIT (cf. section 1.4.3), was simulated (Parodi et al. 2007, 2010). As in the earlier calculations, the ideal cylindric detector set-up was employed. Figure 4.19 shows a 2D projection of the patient head with a sketch of the delivered treatment plan superimposed as color wash display. To obtain sufficient gamma statistics, approximately 10^7 primary particles are needed for each raster point and IES. For the sake of reasonable computational time, two simpler subsets of the treatment plan were used. The first contains the central positions of all IESs, spanning a range of 34 proton beam energies from 69.06 MeV to 139.37 MeV, corresponding to the beam passing through the isocenter. This is indicated by the red arrow in figure 4.19. The second subset includes 11 laterally displaced beams belonging to one single IES of 134.04 MeV proton beam energy, as schematically indicated by the blue line in figure 4.19.

4.4.1. Prompt gamma profiles

For illustrative purpose, figure 4.20 shows the depth profiles for three selected IESs out of the first subset of the treatment plan corresponding to three different energies of the proton beam along the red arrow in figure 4.19, one at the beginning (69.06 MeV), one in

the middle (105.43 MeV), and one near the end (134.06 MeV) of the energy range. As in all the following profiles, the beam is delivered from the right, thus moves towards negative depth, and enters into the patient head at around z = 8 cm. As expected, the profile of collimated gammas follows the depth-dose distribution, slightly increasing near the Bragg peak. Also, the yield of uncollimated neutrons rises with increasing beam energy.

To observe the correspondence of the SOBP from the considered subset of the treatment plan and the corresponding cumulative gamma and neutron profiles, all single gamma and neutron profiles were summed up and normalized by the number of primaries. This is presented in figure 4.21. It should be noted that the fall-off of collimated gammas in the tail of the SOBP is about one order of magnitude weaker than the fall-off of the SOBP itself.

4.4.2. TOF spectra

The TOF spectra for three selected IESs out of the first subset of the treatment plan, corresponding to three different energies (i.e., 69.06, 105.43, and 134.06 MeV) of the proton beam along the red arrow in figure 4.19, are shown in figure 4.22. It can be observed that even in the case of a highly heterogeneous head the gamma peak is still well separated from the neutron signal, especially for lower beam energies. While the height of the gamma peak changes only slightly, the neutron spectrum increases by about one order of magnitude between the lowest and highest energy. Interestingly, the gamma peak is shifted by about 15 ns comparing the lowest and highest beam energy, while its width remains relatively constant. This is explained by the fact that the real beam simulated here traverses some distance in air before entering the patient. The resulting additional time causes a shift in the TOF spectra depending on the beam energy. Since the distance outside the patient is comparatively larger than the distance traveled in the head, the shift is much larger compared to the width of the gamma TOF peak.

This effect becomes clearer in figure 4.23 where a scatter plot indicates the TOF and depth of all detected collimated gammas and uncollimated neutrons. The gammas appear on the leftmost edge which corresponds to the gamma peak found to the left of the neutron signal in the TOF spectra (cf. figure 4.22). Moreover, the edge is slightly tilted to the left illustrating the depth dependence of the gamma TOF in the patient head. These considerations are summarized in figure 4.24, where the mean gamma TOF and the width of its peak in the spectrum are given as a function of the proton beam energy.

To estimate the contribution to the TOF by the prompt gammas traveling from the point of production to the detector, the mean gamma TOF was determined for the 11 different lateral positions (i.e., different distances to the detector) of the second subset of the treatment plan (i.e., all within the same IES along the blue line in figure 4.19). The results are depicted in figure 4.25 and demonstrate that the photons contribution to the TOF is negligible compared to that of the primary particles as described above.

4.4.3. Correlation of gamma profile and Bragg peak position

While figure 4.21 showed a comparison of the SOBP and the cumulative gamma yield, it might be desirable to deduce quantitative information about the longitudinal Bragg peak

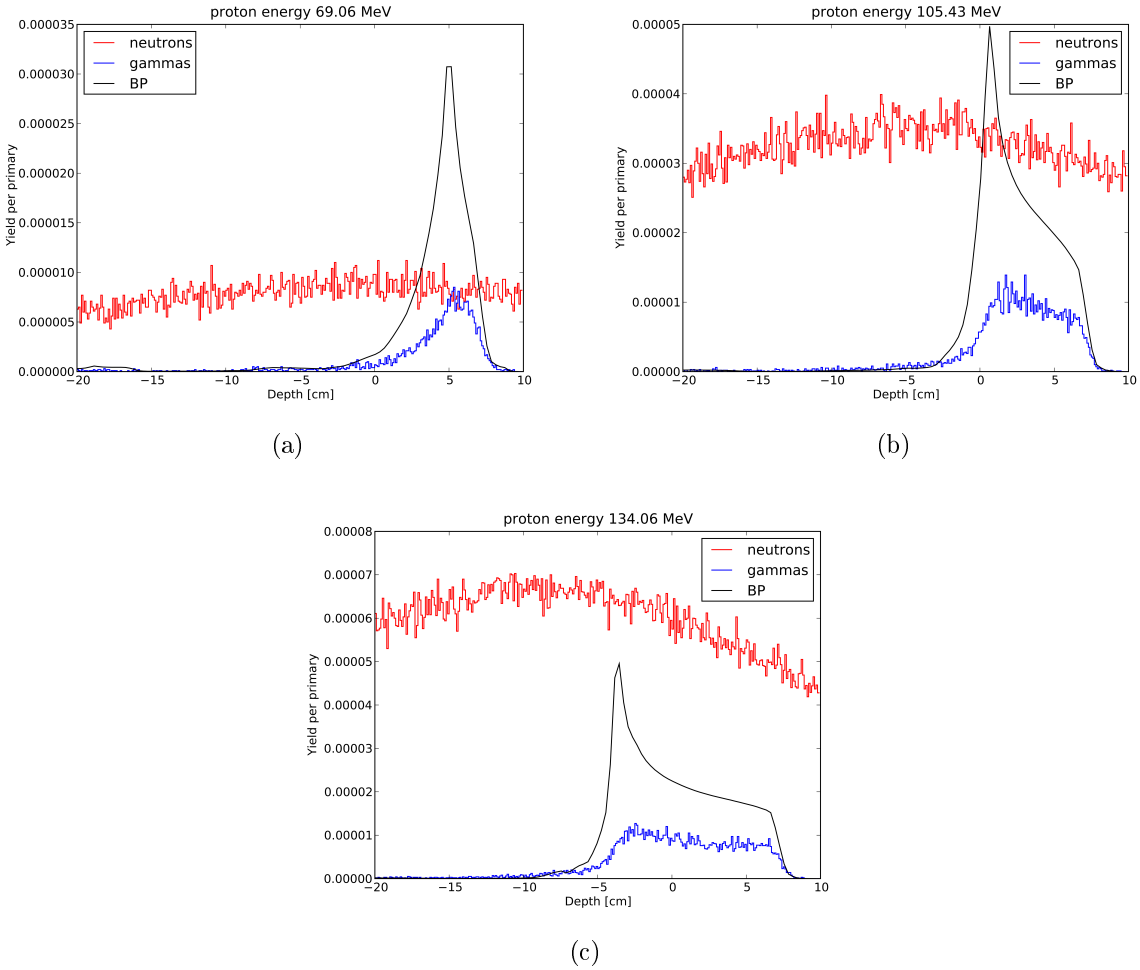

Figure 4.20.: Depth-dose distribution and the profiles of the collimated prompt gammas and uncollimated neutrons scored in the ideal detector for three different energies of the proton beam (i.e., 69.06, 105.43 and 134.06 MeV), confined to the central beam axis in the patient head (cf. red arrow in figure 4.19).

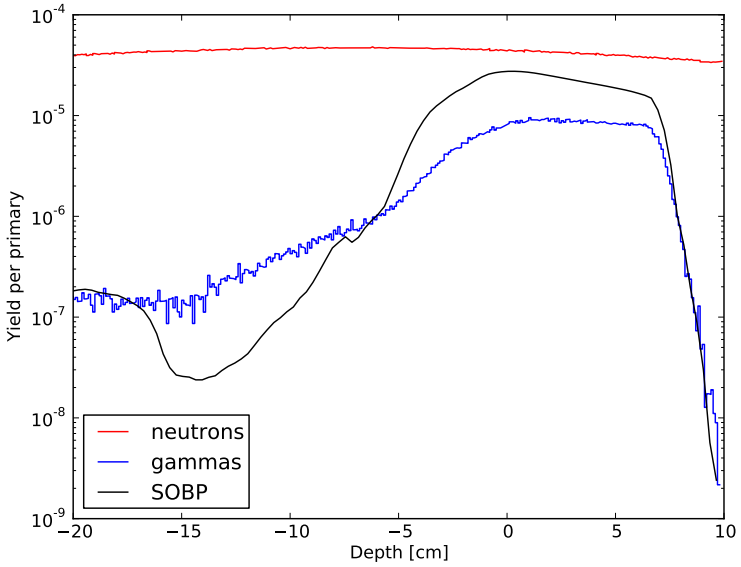

Figure 4.21.: SOBP of the first subset of the treatment plan (cf. red arrow in figure 4.19) in arbitrary units and the corresponding cumulative profiles of collimated gammas and uncollimated neutrons in yield per primary.

positions from the single pencil beam resolved gamma profiles. One characteristic feature of the gamma profile is its fall-off near the Bragg peak. An intuitive way to quantify its position is to calculate the spatial derivative of the gamma profile. Since the profile data are affected by small scale statistical noise, smoothing was necessary before performing such an operation. The smoothing is done by calculating for each point of the gamma profiles the mean value within its twenty (ten to the right and ten to the left) neighboring points. As expected, this approach diminishes the statistical noise but also alters the shape of the curve[2]. One simple criterion was then to determine the position of the maximum of the derivative profile which was again smoothed, using the already described approach, to avoid mis-detections due to noise. Figure 4.26 shows these derivative profiles for three selected beam energies (i.e., 69.06, 105.43 and 134.06 MeV) out of the first subset of the treatment plan (cf. red arrow in figure 4.19). For comparison, the gradient profiles were normalized to the height of the Bragg peak.

To obtain an impression on how well the gamma fall-off correlates with the Bragg peak position, both are depicted as a function of the 34 beam energies (i.e., from 69.06 to 139.37 MeV) of the first subset of the treatment plan in figure 4.27. Clearly, the two positions do not exactly match, yet heuristically they do show a quite good spatial correlation. However, to use the gamma profile for tracing the Bragg peak position, more detailed and quantitative analyses are needed. In particular, since the smoothing operation alters the profile shape, the position of maximum gradient will potentially depend on the specific convolution approach used for the smoothing. Moreover, it should be noted that the

[2]The damping effect of the smoothing operation on a curve depends on its second derivatives. Regions of large curvature are altered in shape more strongly.

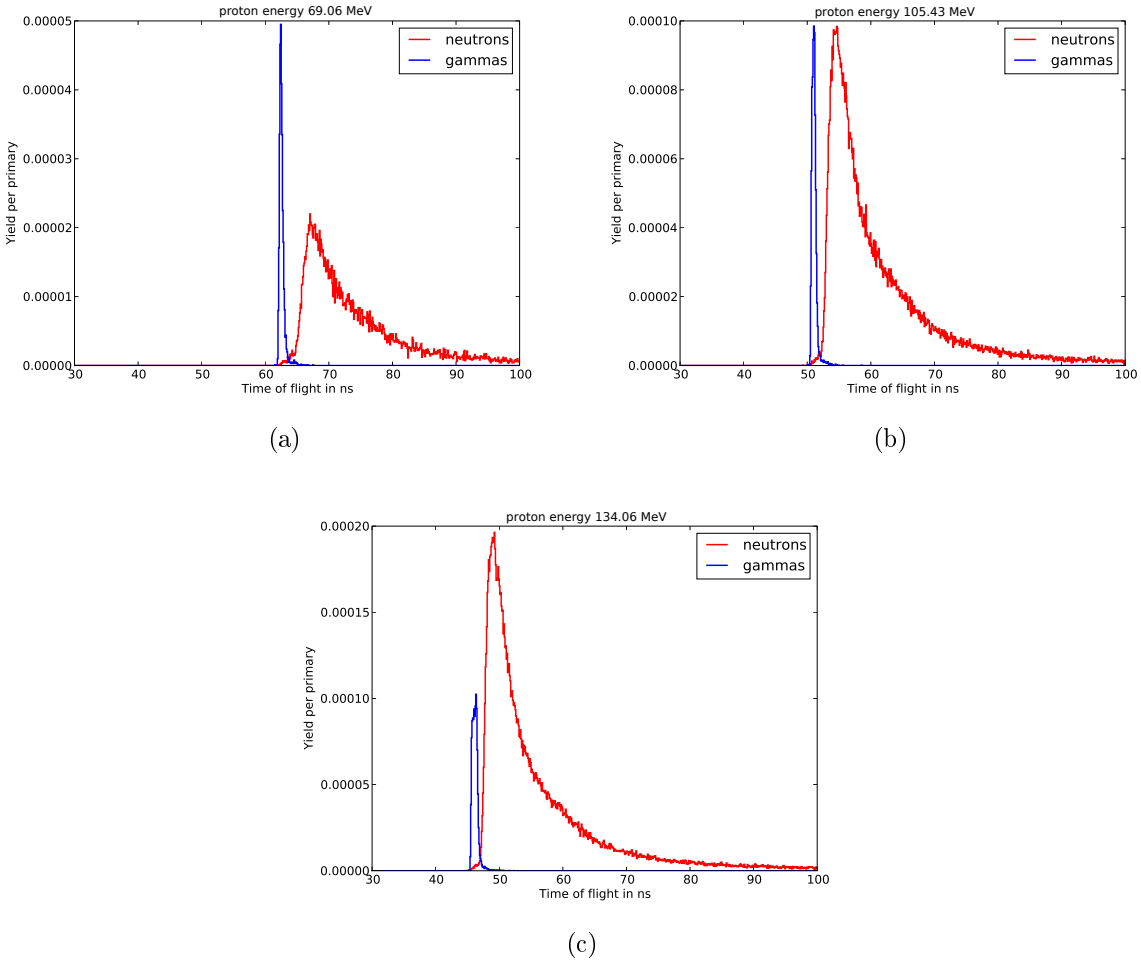

Figure 4.22.: TOF spectra of the collimated prompt gammas and uncollimated neutrons scored in the ideal detector for three different energies of the proton beam (i.e., 69.06, 105.43 and 134.06 MeV) along the central beam axis in the patient head (cf. red arrow in figure 4.19).

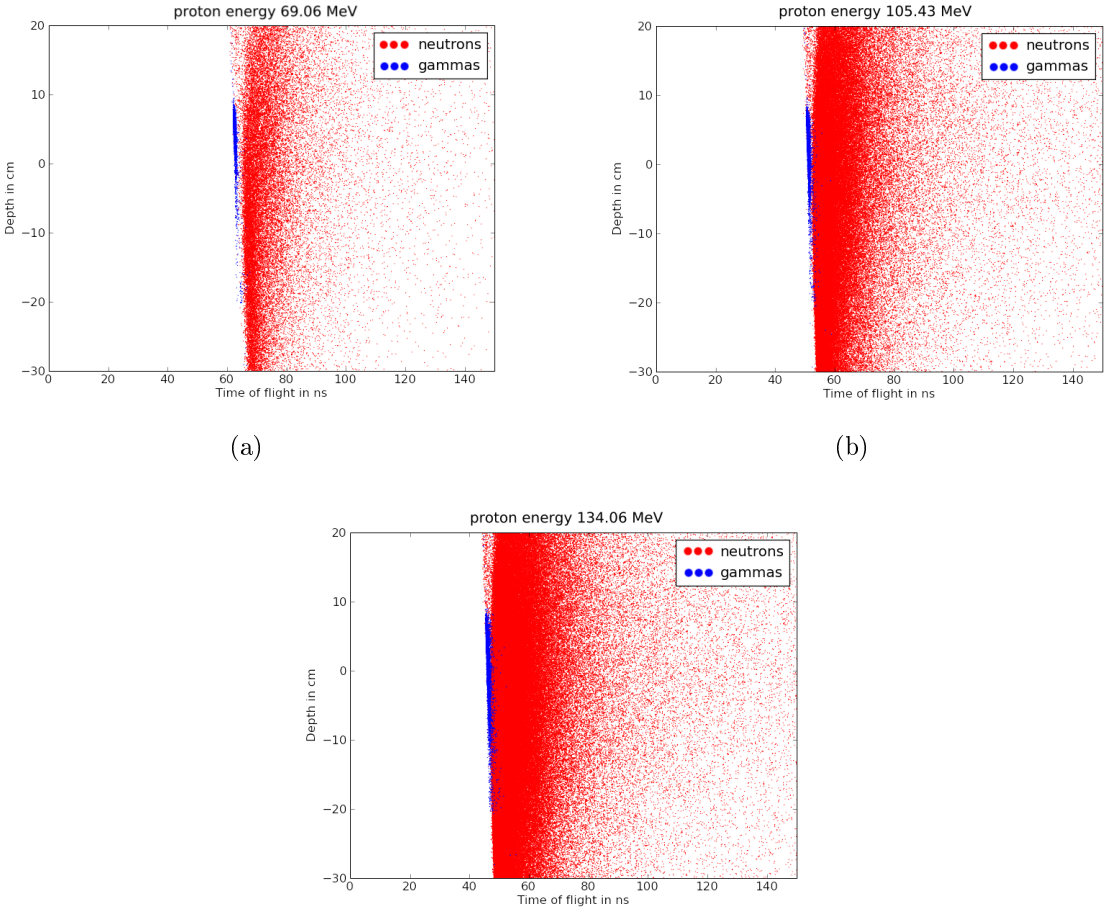

Figure 4.23.: Depth-TOF scatter plots of the collimated prompt gammas and uncollimated neutrons scored in the ideal detector for three different energies of the proton beam (i.e., 69.06, 105.43 and 134.06 MeV) along the central beam axis in the patient head (cf. red arrow in figure 4.19). Note that the depth on the y-axis indicates the longitudinal position in the detector.

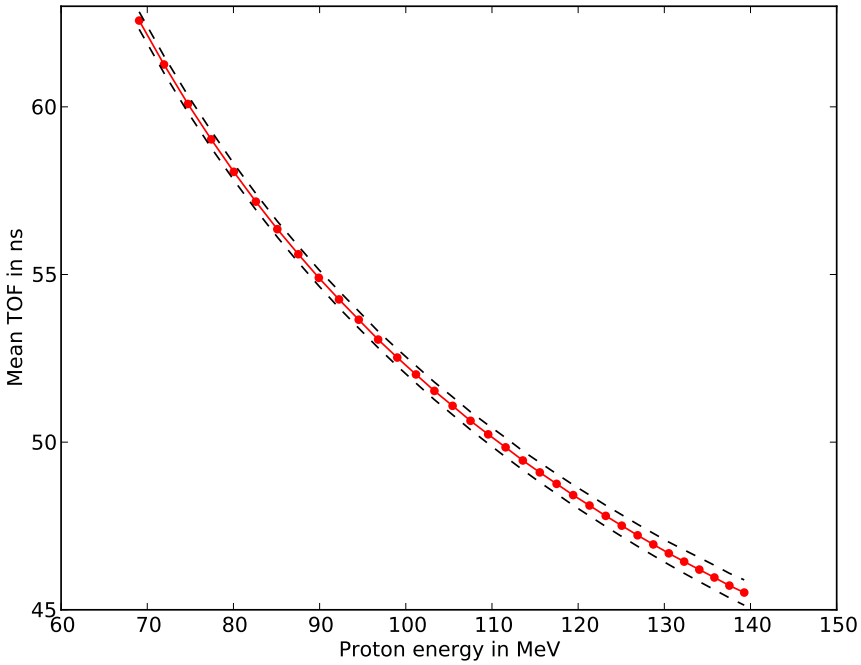

Figure 4.24.: Mean gamma TOF as a function of beam energy (red line) along the central axis in the patient head (cf. red arrow in figure 4.19). The dashed lines indicate the width of the gamma peak in the TOF spectrum and were calculated as standard deviation of the peak centered around its mean value.

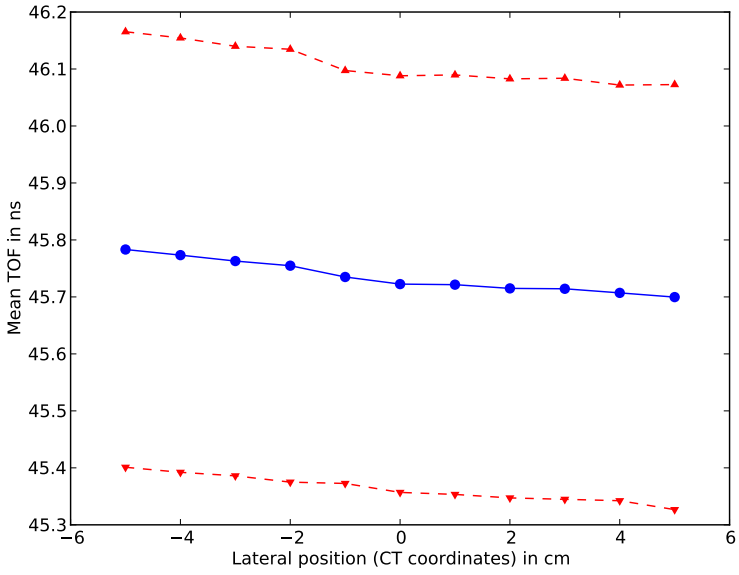

Figure 4.25.: Mean gamma TOF (blue circles), plus (red upward triangles) and minus (red downward triangles) the width of its peak in the spectrum, calculated as standard deviation of the peak, as functions of the lateral position in the patient head (i.e., all within the same IES along the blue line in figure 4.19).

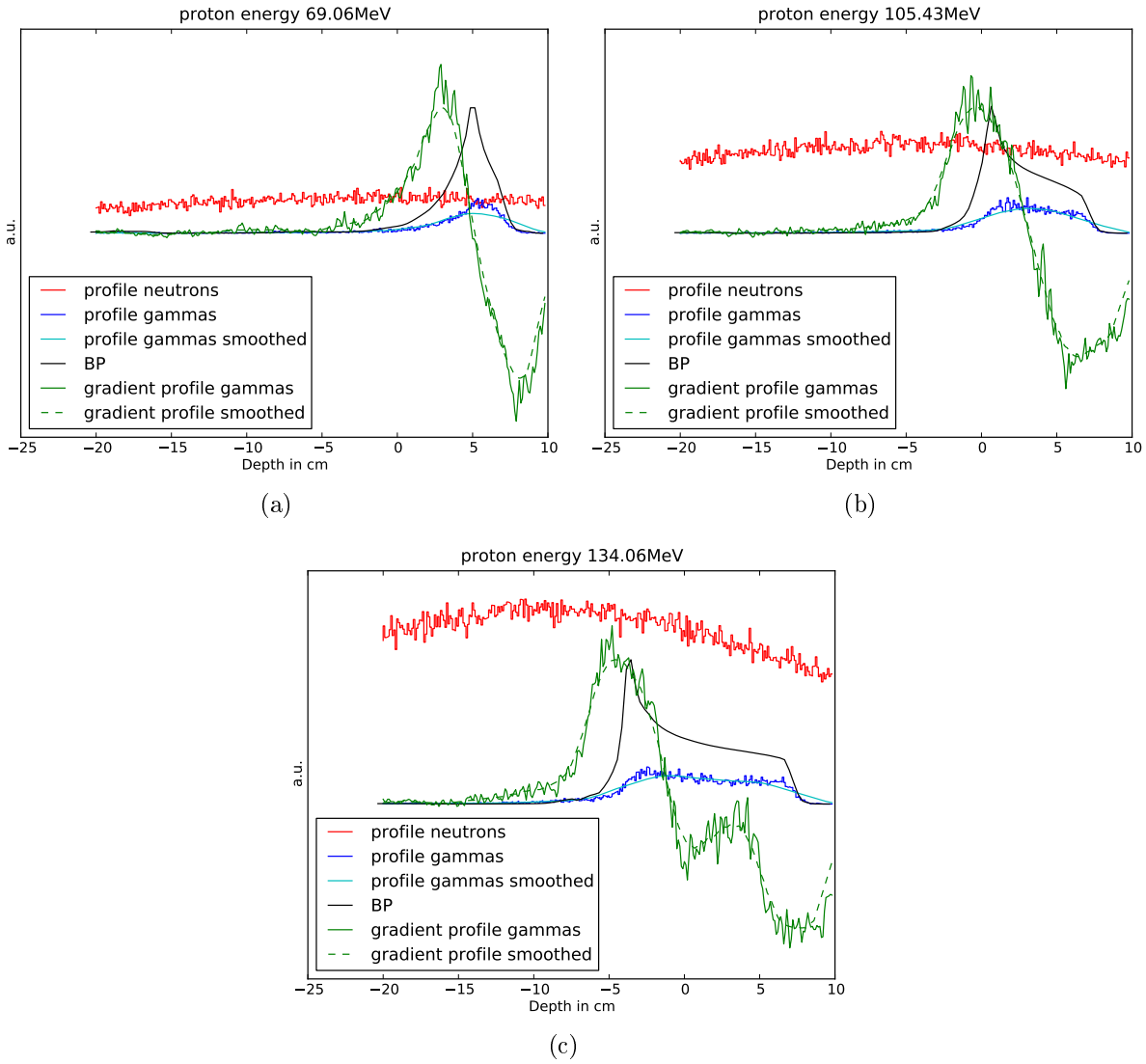

Figure 4.26.: Depth-dose distribution, profiles of the collimated prompt gammas and uncollimated neutrons, and derivative profiles obtained from smoothed gamma profiles scored in the ideal detector for three different energies of the proton beam (i.e., 69.06, 105.43 and 134.06 MeV) in the first subset of the treatment plan (cf. red arrow in figure 4.19). It should be kept in mind that the profiles were rescaled to arbitrary units for illustrative purpose.

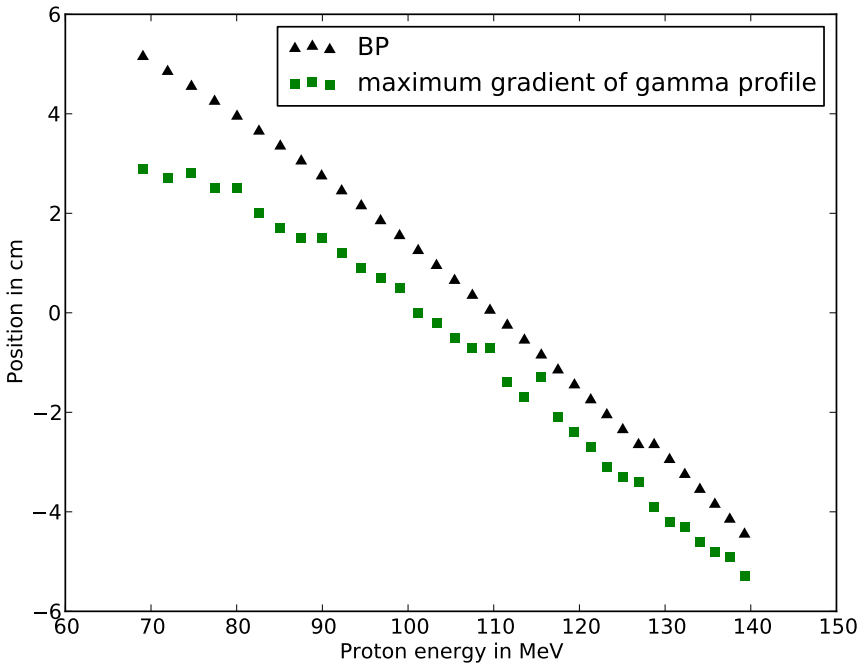

Figure 4.27.: Position of fall-off in gamma profile determined from the maximum of the derivative profile (green squares) and position of the maximum of the Bragg curve (black triangles) as a function of beam energy for the 34 energies in the first subset of the treatment plan (cf. red arrow in figure 4.19).

---

derivative is very sensitive to small scale noise and, therefore, more research on robust de-noising methods is needed once experimental data will be available.

Chapter 5

HEAVY ION COMPUTED TOMOGRAPHY

This chapter presents the experimental investigations carried out to address the feasibility of transmitted high energy ^{12}C ions for low dose 2D and 3D imaging (cf. section 2.4). Ion radiography and its extension to Heavy Ion Computed Tomography (HICT) implies that the patient has to be irradiated before or in between (in this case only radiography) the treatment with a small flux of ions of initial energy higher than the one used for therapy, such that the exit range or energy can be measured. This technique aims at evaluating the correct patient positioning and verifying the ion range before or in between the treatment. In particular, the distribution of WEPL in the patient reconstructed from the measurement of the residual range of an energetic ion beam traversing the target could be directly used for ion treatment planning without resorting to the usage of external X-ray radiation and semi-empirical HU-WEPL calibration curves (cf. section 1.5.1 and figure 1.20 therein). Moreover, a radiographic check of the range uncertanties in between the treatment becomes crucial in the presence of organ motion (e.g., due to respiratory breathing).

Initially, the clinical feasibility of HICT at HIT was addressed (cf. section 5.1.1). Then, experimental data were taken with radiographic films at different angles and reconstructed using a backprojection algorithm, supporting the feasibility of HICT at HIT (cf. section 5.1.2). Following these encouraging results, a first prototype of a dedicated detector system, a stack of ionization chambers with newly acquired electronics, has been assembled and characterized for experimental investigations (cf. sections 5.2 and 5.3). Details and results are shown in the following (cf. sections 5.4, 5.5, and 5.6).

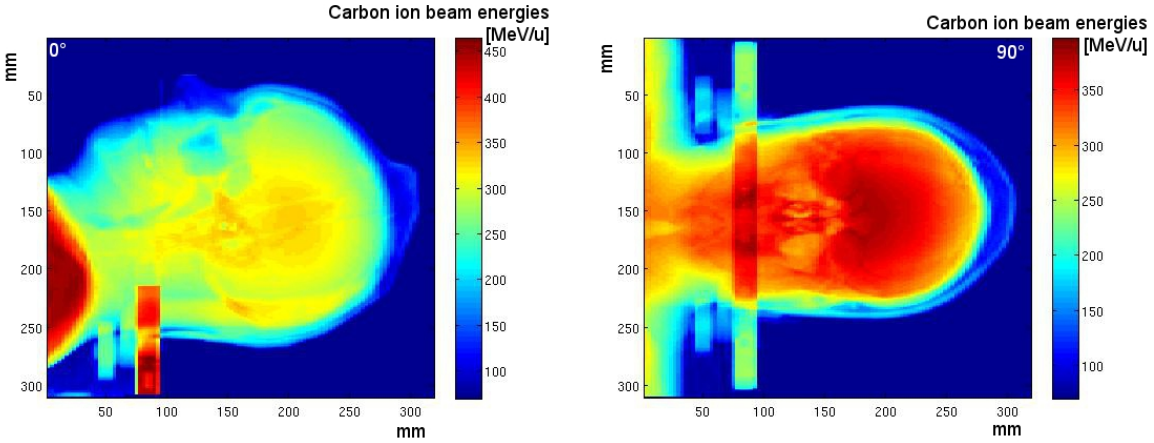

Figure 5.1.: Calculated initial carbon ion beam energies, displayed in MeV/u in the rainbow color bars, needed to perform transmission imaging in the head case for two different projection angles of 0° on the left and of 90° on the right. (Rinaldi et al. 2010)

5.1. Proof of principle of HICT

5.1.1. The clinical feasibility

In a first step, the clinical potential of the HICT was studied starting from CT data of patients that were treated with carbon ions at GSI during the pilot project. Calculations of the Water Equivalent (WE) thicknesses and beam energies needed to perform the HICT for head, prostate, and sacral cases were done using an own-written MATLAB routine. This algorithm, first of all, converts the HU map of a patient into a WE map using the semi-empirical HU-WEPL calibration curve (cf. figure 1.20 in section 1.5.1). Additionally, it derives the initial energy of the primary ion necessary to completely traverse the patient thickness expressed in WE limiting the patient exposure to the plateau region of the Bragg peak in order to minimize the delivered dose.

The resulting carbon ion beam energies calculated to be needed for transmission imaging in the head cases are shown in figure 5.1 for two different projection angles of 0°and 90°. In these cases, the energy values required are in a range between 250 and 400 MeV/u. Therefore, using the HIT accelerator, which is able to accelerate carbon ions up to 430.10 MeV/u, it is possible to perform the HICT for head cases.

For the prostate and sacral cases, carbon ion beams of up to 500 MeV/u are needed (cf. upper-left panel in figure 5.2) for the lateral beam directions, which are normally used for treatment (i.e., projection angle of 0°), due to the high density bone structures in the beam path. However, it is possible to decrease the energy values by roughly 100 MeV/u via a proper reduction of the beam projections trying to skip the pelvic bone structures, for example avoiding beam angles in the [0°, 25°] interval. Examples for more feasible projections with angles of 90°and 60°are also depicted in figure 5.2.

These results confirmed that, using the HIT accelerator, it is possible to perform HICT for head cases, and even for prostate and sacral cases via a proper reduction of the beam projections trying to skip the dense bony structures in the hips (Rinaldi et al. 2010).

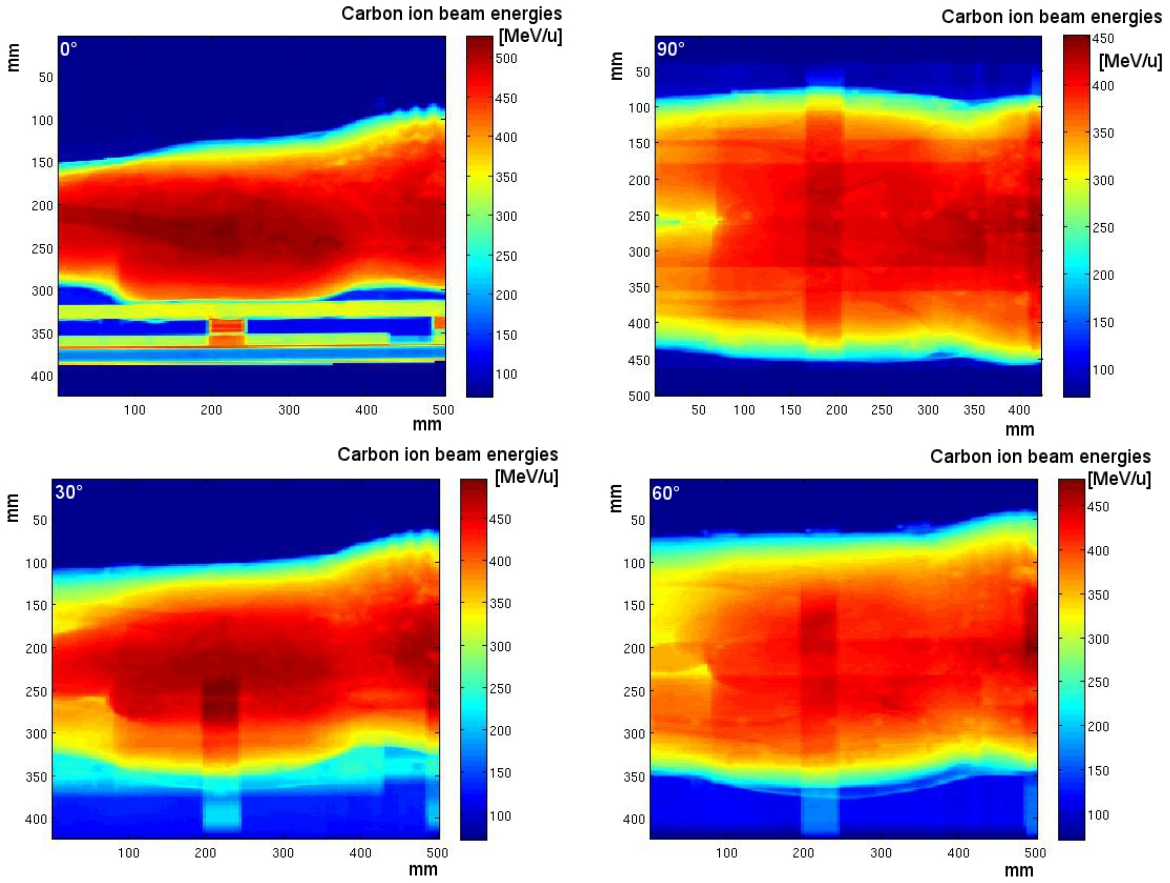

Figure 5.2.: Calculated initial carbon ion beam energies, displayed in MeV/u in the rainbow color bars, needed to perform transmission imaging in the prostate/sacral case for different projection angles of 0° (left) and 90° (right) on the top and 30° (left) and 60° (right) on the bottom. (Rinaldi et al. 2010)

5.1.2. The experimental proof of principle

The experimental feasibility of the HICT technique was first investigated via measurements acquired using standard radiographic films at HIT. The experiment was performed using a laterally extended field (200×30 mm^2) of monoenergetic ^{12}C ions with an initial energy of 396.29 MeV/u and a beam spot with a full width at half maximum (FWHM) of 3.5 mm delivered with a lateral (Δx) and vertical (Δy) step of 1 mm. The irradiated phantom was a PMMA cylinder of 80 mm radius R, as depicted in figure 5.3, with five tissue equivalent rods (one Gammex insert of PMMA, two of Air, one of Lung and one of Cortical Bone) with a radius r of 14 mm. The phantom has been centrally positioned in the isocenter of the treatment unit. The data were acquired with Kodak X-Omat V film (Spielberger et al. 2001), a classical silver bromide emulsion commonly used in conventional radiation therapy. The films were arranged perpendicular to the ion beam just after the phantom. Prior to the experiment, a calibration irradiation at different dose levels was performed to deduce a dose-response curve. The radiographic projections were acquired by rotating the

Figure 5.3.: The PMMA cylindrical ($R = 80$ mm) phantom with five tissue equivalent rods ($r = 14$ mm) of PMMA (1 rod), Air (2 rods), Lung (1 rod) and one Cortical Bone (1 rod). The values written on the Gammex inserts indicate the electron density relative to water (ρ_e^w).

Figure 5.4.: Examples of data acquired under different projection angles (left: 0°, right: 90°) using standard radiographic films measured at HIT.

phantom from 0° to 180° in steps of 7.5°. Examples of the acquired experimental data for different angles of the phantom position are shown in figure 5.4.

After irradiation, the films were developed with a KodakM35 processing machine, using DX31 as developer and FX31 as fixer components. A simple backprojection algorithm without any filters in Fourier space was used for the tomographic reconstruction.

The experimental results were also compared with FLUKA MC (cf. section 3.1) calculations. However, in order to perform this comparison, it was nececessary to include in the simulations the complex dependence of the film response on particle type and energy (Spielberger et al. 2001, 2002) through the film efficiency.

In fact, as discussed in Geiß et al. (1997), on the macroscopic scale films saturate at high doses because of the finite number of sensitive grains in the emulsion, while on the microscopic scale saturation effects do occur at high local doses. Therefore, due to the different spatial distribution of ionization events, films respond differently to irradiation with photons or ions, showing also dependence on the ion charge and energy. This behaviour becomes relevant in heavy ion therapy, where dose distributions are composed by the superposition of different beam energies. In addition, fragmentation processes of the primary beam in the absorbing material producing lighter ions of different atomic numbers and energies have to be taken into account (cf. section 1.2.5).

For these reasons, the approach described in Spielberger et al. (2001) was adopted. First

of all, this method proved experimentally that, in general, the shape of the dose-response curves for heavy ions and high-energy photon radiation follows a purely exponential function, which is comparable to a single-target single-hit Poisson distribution:

$$OD(D) = OD_{\max}[1 - e^{-mD}]$$

where $OD_{\max}$ is the saturation optical density and m the exponential slope (James and Mees 1977). Additionally, this approach expresses the response of films to particle irradiation depending on ion charge Z and energy E ($m_{HI}(Z,E)$) relative to the response to Co-60 photon radiation (m_{Co-60}), yielding the relative film efficiency $\eta(Z,E)$ independent of the dose level as:

$$\eta(Z,E) = \frac{m_{HI}(Z,E)}{m_{Co-60}}$$

This change in the film efficiency depending on ion type and energy is due to a variation of the spatial energy distribution pattern, which can be explained by the particle track structure, as outlined in section 1.3.

Following this approach, therefore, the dose scored in the simulations was weighted using the relative film efficiency factor, used by TRiP (cf. section 1.4.3, Krämer et al. 2000), for every particle type and energy to correctly estimate the dose-response.

The reconstructed image from the measurements with radiographic films shown in figure 5.5(a), reflecting the response from the entire mixed radiation field without the discrimination of primary and secondary particles, could be well reproduced by the MC simulation of the experiment (cf. figure 5.5(b)), accounting for the particle and energy dependent film efficiency based on a particle track-structure model (Spielberger et al. 2002).

Moreover, the MC study of the calculated reconstructed image for an ideal detector response taking into account only the contribution due to primary carbon ions showed very encouraging results for HICT (figure 5.6). Thus, this first proof of principle experiment motivated new efforts for the investigation of improved detection systems (cf. section 5.2).

5.2. Dedicated experimental set-up

The dedicated set-up used for HICT experiments is described in the following and depicted in figure 5.7. The detector, consisting of a stack of 61 parallel-plate ionisation chambers (PPICs), is presented in section 5.2.1. It has been equipped with newly acquired electronics (cf. section 5.2.4) for a real-time data acquisition during the scanned beam delivery. The experiments have been carried out at the HIT facility. A short summary of elements relevant to this work is given in sections 5.2.2, 5.2.3 and 5.2.5.

5.2.1. ICs stack

Advantages of revealing the range rather than the residual energy in HICT applications motivated the choice of an ICs stack as detector (cf. section 2.4). The prototype has been set-up in collaboration with colleagues from GSI (Voss et al. 2010) and is based on a detector system using a gaseous active volume. This helps to minimize effects which

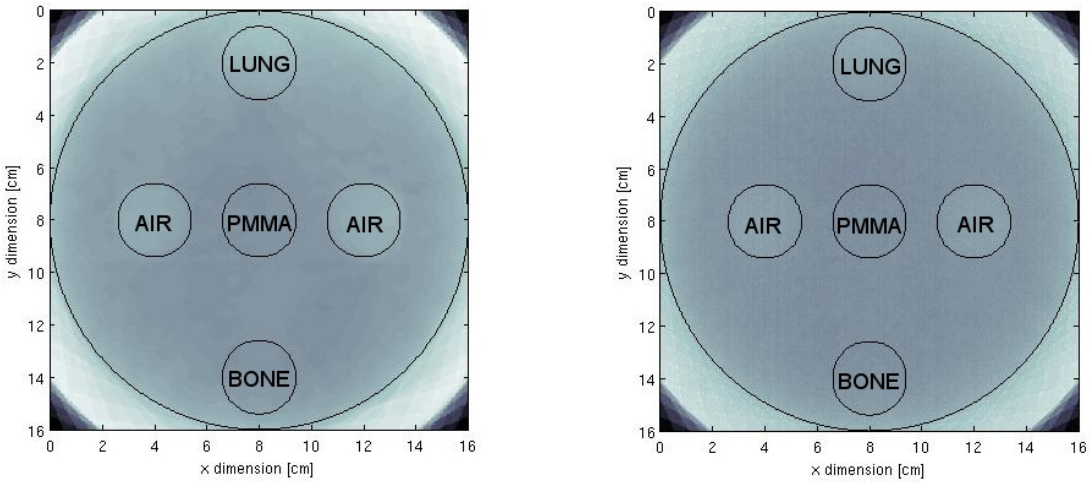

(a) (b)

Figure 5.5.: (a) Reconstructed image from the measurements with radiographic films at HIT reflecting the response from the entire mixed radiation field without the discrimination of primary and secondary particles. (b) Calculated reconstructed image from the MC simulation of the experiment reproducing the film efficiency depending on particle type and energy based on the particle track structure.

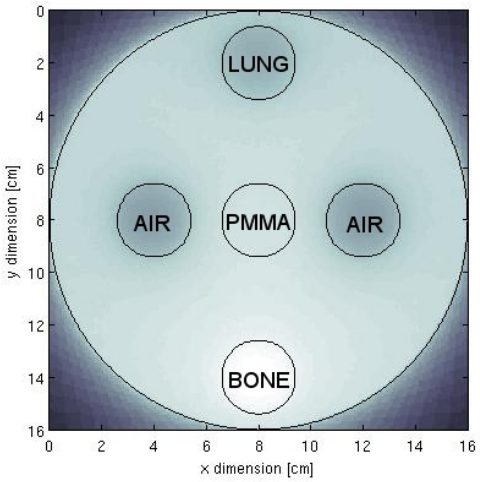

Figure 5.6.: Calculated reconstructed image for an ideal detector response taking into account only the contribution due to primary carbon ions.

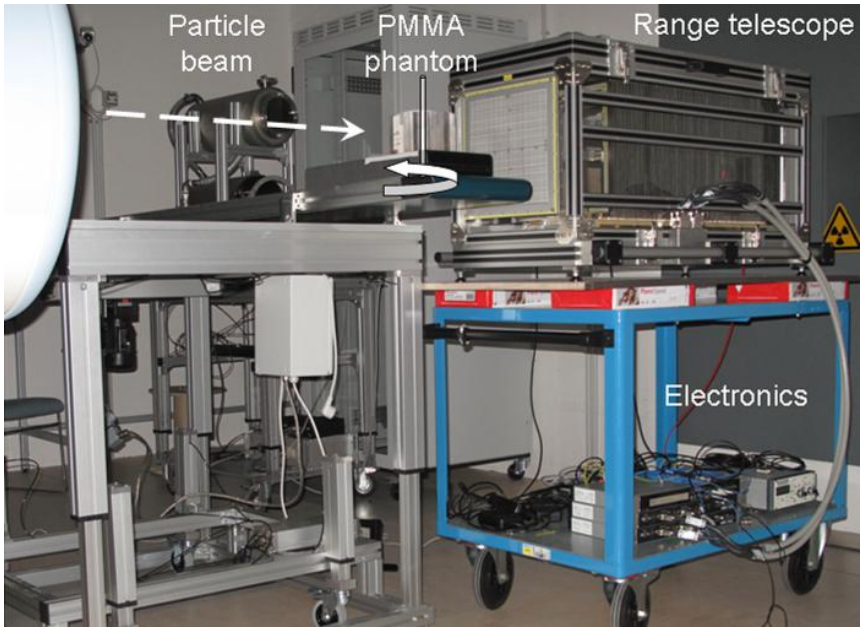

Figure 5.7.: Experimental set-up: stack of parallel-plate ICs with newly acquired electronics in the experimental room at HIT.

---

are strongly linked to the nature and the linear energy transfer of the traversing particles. Examples are the impact of recombination losses on the achievable detector signals and the composition of the mixed radiation field with respect to the dosimetrically relevant energy loss. Both effects are minimized using interaction volumes composed of low-density material if compared to high-density solid state detector material (e.g., silicon).

Considerable preparatory work has been done in the framework of the GSI pilot project looking closely into the feasibility of such a system for 3D dosimetry (Brusasco et al. 2000). Whereas the stack of PPICs can serve to measure the depth-dose profile of a single or spread-out Bragg peak in steady (Voss et al. 2006) or scanned-mode (Brusasco et al. 2000), the combination with appropriate low-mass position detectors (Voss et al. 2007) allows to do at least a 2 ½ - D analysis by projecting the initial position into the active volumes of the ICs downstream.

ICs give an output resulting from the collection of the charge created in a gas volume crossed by ionizing radiations. In the simplest configuration, the gas volume is included in a pair of electrodes that create an electric field in the gas by application of an external voltage. When ionizing radiation traverses the detector, it excites and ionizes the gas molecules. The created ions and electrons drift along the electric field towards the electrodes where they are collected. In the absence of an applied voltage, no net current should flow and the ions and the electrons which are created by ionization in the gas disappear by recombination or diffusion. As the voltage increased, the resulting electric field begins to separate the ion pairs and the recombination diminishes. The measured current thus increases with the voltage, approaching a flat plateau corresponding to the region of ion saturation in which an almost complete collection of the produced charge would be achieved. The current

collected by the chambers is proportional to the number of ionization interactions per unit time that took place in the gas, each resulting in the creation of an ion-electron pair. The mean value of the energy necessary to create an ion-electron pair in the gas, called W value (Brusasco et al. 2000), is approximately a constant characteristic of the gas with variation of only a few percent depending on the interacting particle and its energy (if larger than a few MeV/u). By definition, the W value takes into account also the percentage of energy that, for each created ion pair, goes into electronic excitation of the gas atoms or molecules, without resulting in ionizations. With the W value as division factor, the collected charge in the chamber (Q) is directly proportional to the energy deposited in the gas that is related to a modification in the electronic structure of the gas atoms and it can be calculated from the following formula:

$$Q = N \cdot \left.\frac{dE}{dx}\right|_{gas} \cdot \frac{\Delta x_{gas}}{\frac{W_{gas}}{e}} \tag{5.1}$$

where N is the number of particles contributing to the signal registered by the electronics, $^{dE}/_{dx}|_{gas}$ and Δx_{gas} are respectively the energy loss and the thickness of the considered gas.

The detector system investigated in this work is based on a stack of subsequent large-area PPICs interleaved with removable absorber plates of homogeneous thickness serving as high-voltage electrodes and range degrader at the same time. The active cross section of each IC has been chosen to be 300 × 300 mm^2 in order to allow for a scanned carbon ion beam field size of at least 250 × 250 mm^2. The collecting gas gap has a thickness of 6 mm and it is, for easier operation, filled with air, yielding almost equal performances (Brusasco et al. 2000) in comparison to other gas (e.g., N_2). The collecting electrodes are aluminized kapton foils of 20 nm. The absorber plates consist of 3 mm slabs of PMMA, since it consists of elements with a low atomic/mass number, similar to tissue. The thickness of the absorbers gives the nominal resolution in depth of the ICs stack and the overall sum (3 mm times 61 ICs) defines the maximum range covered ($\simeq$ 21 cm in WE) by the detector. Moreover, the electrodes are supplied with a high voltage of 1000 V and each IC section has a capacitance of 80 pF. This value is quite large and it has to be taken into account when choosing the right electronics. The system is kept modular and can be easily upgraded with respect to the sequence, composition and thickness of the active layers of the detector units, as well as the absorber plates.

In the use of an ICs stack for absolute dosimetry applications, as done in Brusasco et al. (2000), it is crucial to precisely relate the measured charge to the delivered dose. In a HICT application, the ICs stack functions as a range telescope. The relevant information is encoded in the position of the Bragg peak estimated from the channel number of the maximum ICs current. In this sense, the signal of 61 ICs gives a discretized approximation of the theoretical Bragg curve. The absolute level of the ICs current is insignificant as long as the maximum signal position can be precisely determined.

5.2.2. Details of the scanned ion beam at HIT

This section resumes what has already been outlined in section 1.4.3 and clarifies more details about the beam delivery system used at HIT for ions accelerated with a synchrotron since it plays a fundamental role for the HICT technique.

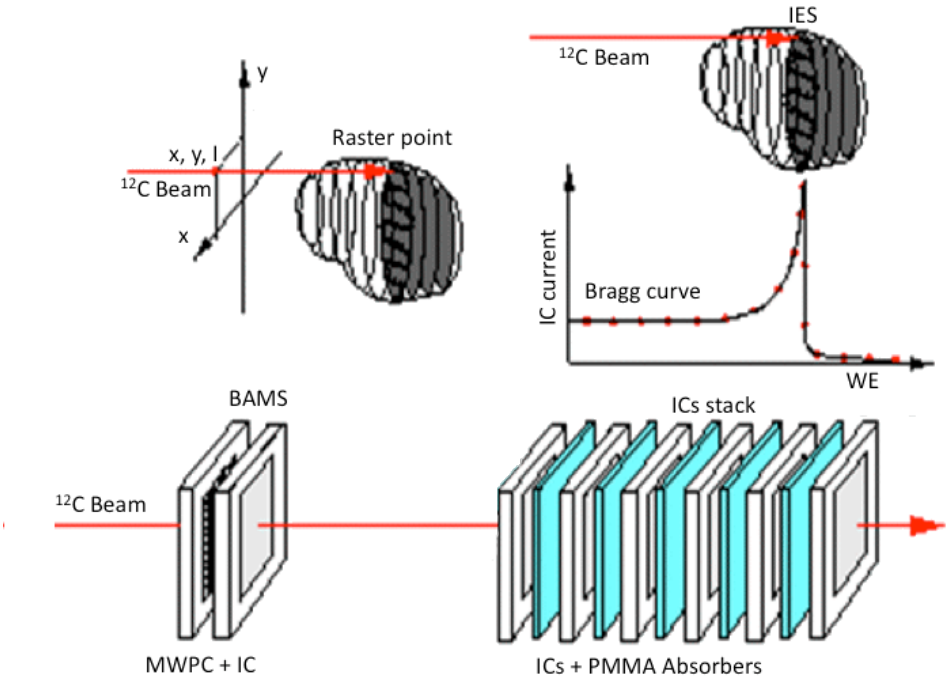

Figure 5.8.: Sketch of the raster scan beam delivery system (top) and the on-line control of the beam delivery via the BAMS in the beamline (bottom). Moreover, the red points on the Bragg curve (top right) show the digitalized signal detected by the ICs stack (bottom right).

In the raster scan technique (Haberer et al. 1993), the beam resides at a given raster point (RP) for a certain time and then slews to the next one. The residence time at a given raster point (t_{RP}) is not known in advance and can vary depending on the number of particles delivered in a raster point, N_{RP}, and the beam intensity (I). In fact, $t_{RP} = {}^{N_{RP}}/_{I}$. Moreover, for the principle of the raster scanning, the beam is not turned off between two raster points if they are close enough, requiring fast scanning magnets (i.e., having a maximum speed of about 2 cm/ms at HIT) to keep the dose applied between two raster points at an acceptable level. When the target dose at the raster point is reached, as measured by a set of transmission ICs within the BAMS, the beam is moved on. The whole process is illustrated in figure 5.8.

The dose for each delivered raster point can be calculated as:

$$D = \frac{N_{RP}}{\Delta x \Delta y} \cdot \left.\frac{dE}{dx}\right|_{material} \tag{5.2}$$

where Δx and Δy are the lateral steps of the raster scanning system in x and y, and ${}^{dE}/_{dx}|_{material}$ is the mass stopping power in the considered material.

The Accelerator Control System (ACS) at HIT allows selection of intensity, energy and spot size (i.e., focus) of the beam from one synchrotron cycle to the next. In the case of a ^{12}C ion beam, the available intensity values can be set in a range from 10^5 to 10^8 ions/s.

The beam profile is approximately symmetric and nominal Gaussian shaped. Different foci sizes in a range of ≈ 3-10 mm FWHM are available depending on the beam energy. A list of 255 energies has been set-up, ranging from 89 MeV/u to 430 MeV/u, in order to achieve a millimeter spacing of the corresponding ranges in water from 20 mm to 330 mm, respectively.

5.2.3. Trigger

At HIT, at the moment, there are different trigger modalities available. Some of them use information given by the Siemens Therapy Control System (TCS) which also handles the delivery of treatment/experimental plan, i.e., the sequence of raster points per IES. Two of the implemented trigger modalities can be interesting for this work. In one case, the TCS signal reaches the TWINCAT Ether-CAT system, which generates a pulse of a minimum width of 50 μs every time a new raster point is selected. For this reason, this kind of trigger is called Next Point. It should be remarked that the Next Point trigger detects the delivery of a new raster point but not any real-time information related to the irradiation status (e.g., actual presence of the beam). The other one is related to the delivery of a new spill and therefore named Beam On. This trigger starts when a new spill is created, but it remains always active also during a spill pause (e.g., irradiation pause during beam acceleration).

Since for all HICT related experiments data points recorded by the electronics had to be attributed to raster points, the Next Point trigger was used. A sketch of the data acquisition technique is reported in figure 5.9.

5.2.4. Electronics

The electronics must be able to collect the currents measured by the individual ionization chambers. A discretized Bragg curve has to be acquired for each raster point of the beam.

The ideal read-out system suitable for this purpose should integrate each of the chamber signals for the duration of the trigger, without any deadtime, and store the resulting Bragg curve. The integration process should start and stop synchronously across all channels. The process should be repeated for each raster point irradiated during a beam spill, and for each beam spill. The total number of Bragg curves measurable in an experimental session could be up to some ten-thousand.

For this purpose, two I3200 Thirty-Two Channel Digital Electrometers[1], synchronized and buffered by an A500 module as real-time controller, were chosen as read-out electronics. The electrometer system is intended to measure 64 low-current signals in synchronization in the dynamic range of 1 pA to 50 μA per channel. The charge integration period can in principle be varied in the range of 20 μs to 65 s, which is necessary to accomodate for different signal levels and time resolution requirements. All analog circuitry, digitization, and communication of measured data to a host computer system is integrated in the system. Flexible triggering options allow various data acquisition sequences to be initiated by external synchronization signals. A host software system is included. To turn the incoming

[1]Pyramid Technical Consultants, Lexington USA Models A500 I3200 PS455 (http://www.ptcusa.com).

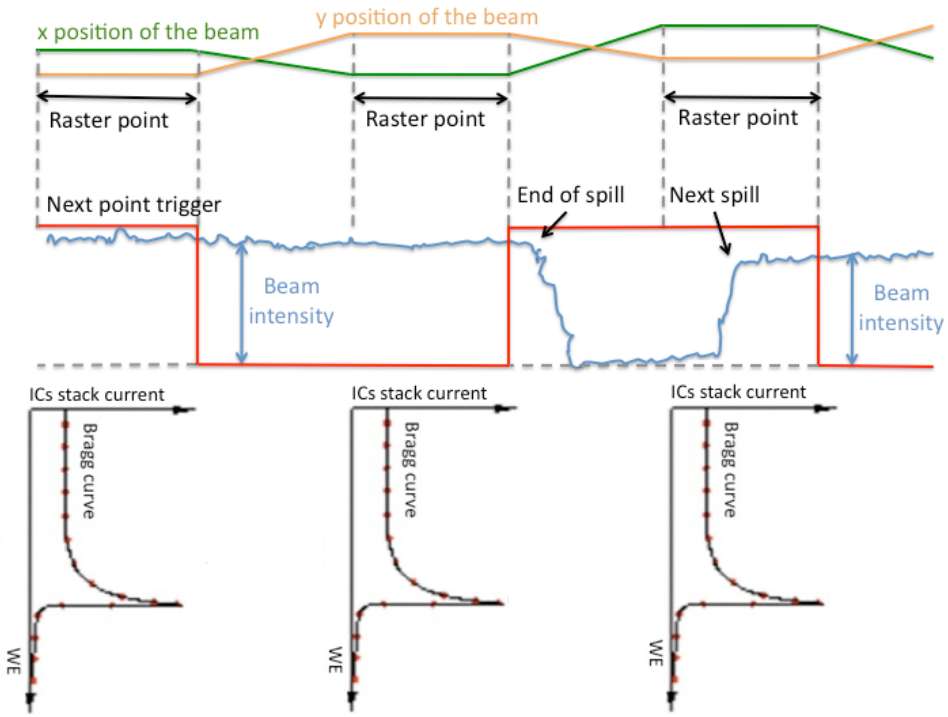

Figure 5.9.: Sketch of the data acquisition technique with the most important parameters: x and y position of the raster scan, the Next Point Trigger and the beam spill. Moreover, the red points on the Bragg curve show the digitalized signal detected by the ICs stack.

current signal into readings, the I3200 uses a method called gated integration. In fact, each single channel of the I3200 at some point in time starts accumulating (i.e., integrating) the current on a capacitor. The capacitor charges up and an increasing voltage, therefore, appears across the capacitor. Measuring this voltage with an analog-to-digital converter (ADC) gives the charge on the capacitor at the time of conversion. The increase in charge over a known time interval is determined by measuring the voltage at the beginning and the end of the interval. In this way, the average current during that time interval, called integration period (t_{IP}), is known since current is simply charge divided by time. The ADC has a specified input voltage range. Therefore, the capacitor must be periodically discharged (typical duration of 20 μs) before the cycle can be restarted. The process of charging the capacitor and discharging to reset is called gated integration. The length of the integration can be controlled in the recommended working range of 100 μs up to 100 ms. Notice that the first ADC conversion does not take place immediately when the integration starts. This is because the signal is unreliable just after the reset, so it has to be waited a time, called settle time, before making the first conversion. This time is normally set to 25 μs. To avoid the opening reset switch to spoil the integrated signal, an additional set-up time is waited between integration and the following reset. Every measurement made by the I3200 is a response to a trigger. The measurement only starts, however, when an initiating event is detected. There are several initiation sources and modes.

In this work, the minimum available value for (t_{IP}) of 100 μs was selected as well as the default values for the reset time (t_{reset}) of 20 μs, the settle time (t_{settle}) of 25 μs, and the set-up time (t_{setup}) of 20 μs. Moreover, the External Start Hold mode was used because it works properly in combination with the Next Point trigger as sketched in the top of figure 5.10. In fact, a high (low) level on the gate input causes the first integration of the predefined sequence, then the I3200 waits in reset for the next high (low) to cause the second integration. This process continues until the defined number of triggers/raster points is reached, or the "abort" message is received.

5.2.5. Implications for the HICT

In the light of a possible future clinical application of the HICT method at HIT, two critical factors are particularly relevant. Firstly, for practical reasons, the duration of an entire scan must be as short as possible. This in turn implies that the acquisition time for each single data point must be kept at a minimum. Secondly, the dose delivered to the patient during a scan must be as low as possible, which depends primarily on the number of beam particles per raster point. Consequently, this parameter has to be minimized as well.

Keeping these clinical requirements and the discussions in the previous sections in mind, the following conclusions can be drawn regarding the present set-up.

As explained in section 5.2.2 and sketched in figure 5.10, the beam moves in about tens of μs from one raster point prescribed by the treatment plan to the next. Because of the settle and reset time of the electronics, t_{IP} has to be kept shorter than the time interval between two raster points (t_{RP}). Otherwise, the electronics would still be idle on successive points and thus lose those data. Therefore, the signal registered by the electronics is recording only a portion of the actually delivered particles. The ratio of measured to delivered particles is given by the live time proportion:

$$\frac{N_{\mathrm{measured}}}{N_{\mathrm{delivered}}} = \frac{t_{\mathrm{IP}}}{t_{\mathrm{RP}}} = \frac{t_{\mathrm{IP}}}{t_{\mathrm{IP}} + t_{\mathrm{reset}} + t_{\mathrm{settle}} + t_{\mathrm{setup}} + t_{\mathrm{lost}}} \tag{5.3}$$

In an ideal set-up, t_{IP} would be adjustable depending on the expected t_{RP} as calculated from the planned $N_{\mathrm{delivered}}$ and the actual intensity of the extracted beam reducing t_{reset}, t_{settle}, t_{setup} and t_{lost} as much as possible. Since the default settings of the settle, reset, and set-up time are recommended by the manufacturer as lower limits, these values were used for this work (cf. section 5.2.4). Anyhow for this reason, for future set-ups, it will be desirable to optimize the live-time proportion of the electronics.

Additionally, the beam delivery time per raster point slightly fluctuates during one treatment plan, since it is given by the number of particles per raster point and the ion beam intensity, where the latter fluctuates. Specifically, the beam intensity expressed in $^{\mathrm{ion}}/_{\mathrm{s}}$ can vary by up to 30-40%, causing t_{RP} to vary accordingly, while the number of particles delivered in a raster point, i.e., the particle fluence, is constantly checked by the BAMS with a tolerance of 5%. Again, in order not to lose data points, t_{IP} has to be set low to accommodate for the smallest values of t_{RP} due to intensity fluctuations. On a raster point, where the irradiation takes a longer time with respect to another raster point at the same beam intensity, relatively fewer particles contribute to the signal registered by the electronics. The mean ratio of effectively seen particles over an entire laterally extended

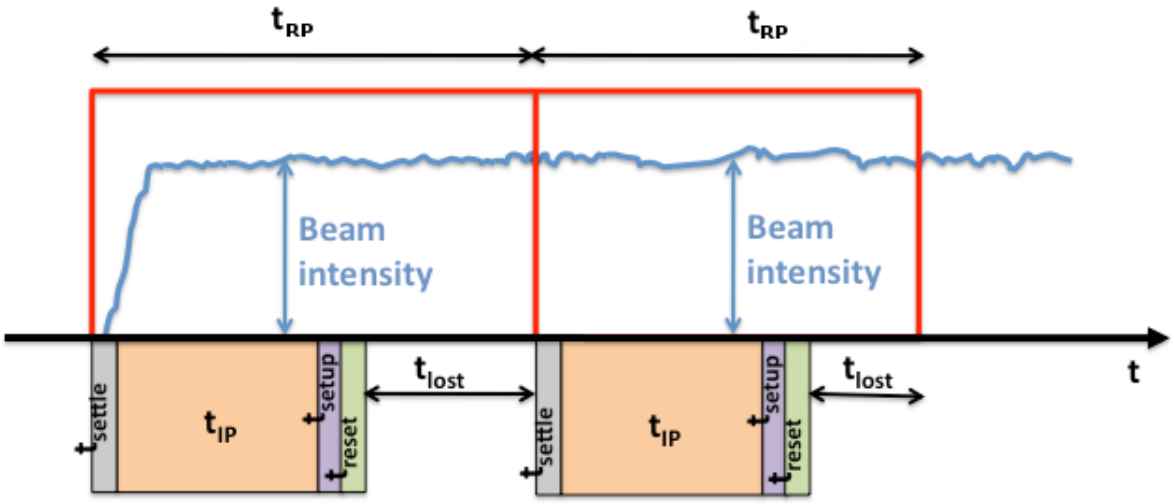

Figure 5.10.: Sketch of the different time intervals of the electronics relative to the beam delivery.

---

field of monoenergetic ^{12}C ions at the same beam intensity thus depends on the variance of the time differences between subsequent beam positions. This is an intrinsic feature of the beam delivery and accelerator system which cannot be optimized by the present HICT set-up.

Concluding, the various timing parameters of the electronics have to be minimized (except t_{IP} that has to be optimized), as well as the number of beam particles per raster point and the fluctuations of the beam intensities. On the other hand, the loss of signal quality must be maintained at a tolerable level to allow the Bragg peak to be detected from the measured ICs current profile.

The scope of the radiographic and tomographic measurements performed in this work was to demonstrate the potential and feasibility of the HICT imaging technique. Since the experiments had to be performed within the limited available beam time, reliable acquisition of data for all raster positions prescribed by the irradiation plan was crucial. To guarantee this, combinations of numbers of beam particles and intensities were chosen to result in typical delivery times per raster point considerably larger than the electronics cycle period and the miminal temporal resolution of the trigger which is available. Moreover, in most of the cases, the smallest available foci at each energy were used to give maximum spatial resolution, and the energies were set to have the Bragg peak fall inside the range telescope. Nevertheless, the main conclusions obtained for the chosen experimental setting would not change when making a choice of parameters more suitable for clinical applications with an improved electronic set-up.

5.3. Experimental characterization

Several measurements have been performed with the HICT set-up depicted in figure 5.7, as presented in the following. Investigations of the dependence of the acquired ICs signal on beam intensity and number of particles per raster point are presented in section 5.3.1. A qualitative assessment of the independence of acquired images on the lateral beam position relative to the ICs stack is summarized in section 5.3.2. Finally, results of calibration measurements to parametrize the dependence of the Bragg peak position on beam energy and target thickness are given in sections 5.3.3 and 5.3.4.

5.3.1. Dependence of ICs stack response on beam intensity and number of particles per raster point

As outlined in section 5.2.5, it is desirable to lower the number of particles per raster point, i.e., the dose given to the patient (cf. equation 5.2), in view of possible future clinical applications. To this regard, the dependence of the ICs stacks signal on beam intensity and number of particles per raster point was studied.

A laterally extended field ($206 \times 10\,\mathrm{mm}^2$) of monoenergetic ^{12}C ion beam of 270.55 MeV/u and beam spot with FWHM of 4.1 mm with a lateral step of the raster scanning system Δx and Δy of 1 mm was used without any imaged object in front of the ICs stack. Figure 5.11 shows the ICs current for subsequent raster points plotted over time for different numbers of beam particles, varying from $7 \cdot 10^3$ to 10^5, at fixed intensity of $I = 2 \cdot 10^6\ s^{-1}$. With $t_{\mathrm{IP}} = 10^{-4}$ s, the integration period was shorter than the typical time of delivery per raster point, given as $t_{\mathrm{RP}} = {}^{N_{\mathrm{RP}}}/_{I} = 3.5 \cdot 10^{-3} - 2.5 \cdot 10^{-1}$ s. Therefore, the electronics registered only the portion of the particles hitting the ICs stack during the integration period.

In the figure it is seen that for 7000 and 10000 particles per raster point, the plan is completed within one spill, while for 50000 and 500000 particles, several spills are necessary. It should be noted that for the latter two plans only a portion of the plan corresponding to 30 s from a total irradiation time of about 50 s and 600 s is shown and that the number of raster points per spill diminishes with the increase of delivered particles per raster point. Within the typical intensity fluctuations, the mean IC current at the Bragg curve plateau and peak is almost equal for all numbers of particles per raster point.

In other words, while the dose delivered to the patient depends on the beam particles per raster point, the number of particles contributing to the signal measured by the ICs stack/electronics depends on the intensity and integration period, as long as the latter is smaller than the typical delivery time per raster point (cf. figure 5.10). On the contrary, only once the delivery time per raster point gets shorter than the integration period, the ICs signal will change with the number of beam particles. Since this acquisition scenario causes image distortions due to omitted data points, as it will be explained in section 5.4.2, parameters should be usually set in such a way to prevent this situation.

To test the ICs signal quality as a function of the measured number of beam particles, the integration period and the number of beam particles per raster point were kept fixed at $t_{\mathrm{IP}} = 10^{-4}$ s and 500000, respectively, while the intensity was varied between 10^6 and 10^8 particles per second, resulting in $N_{measured} = I \cdot t_{\mathrm{IP}} = 10^2 - 10^4$ particles "seen" by the electronics. A laterally extended field ($30 \times 30\,\mathrm{mm}^2$) of monoenergetic ^{12}C ion beam

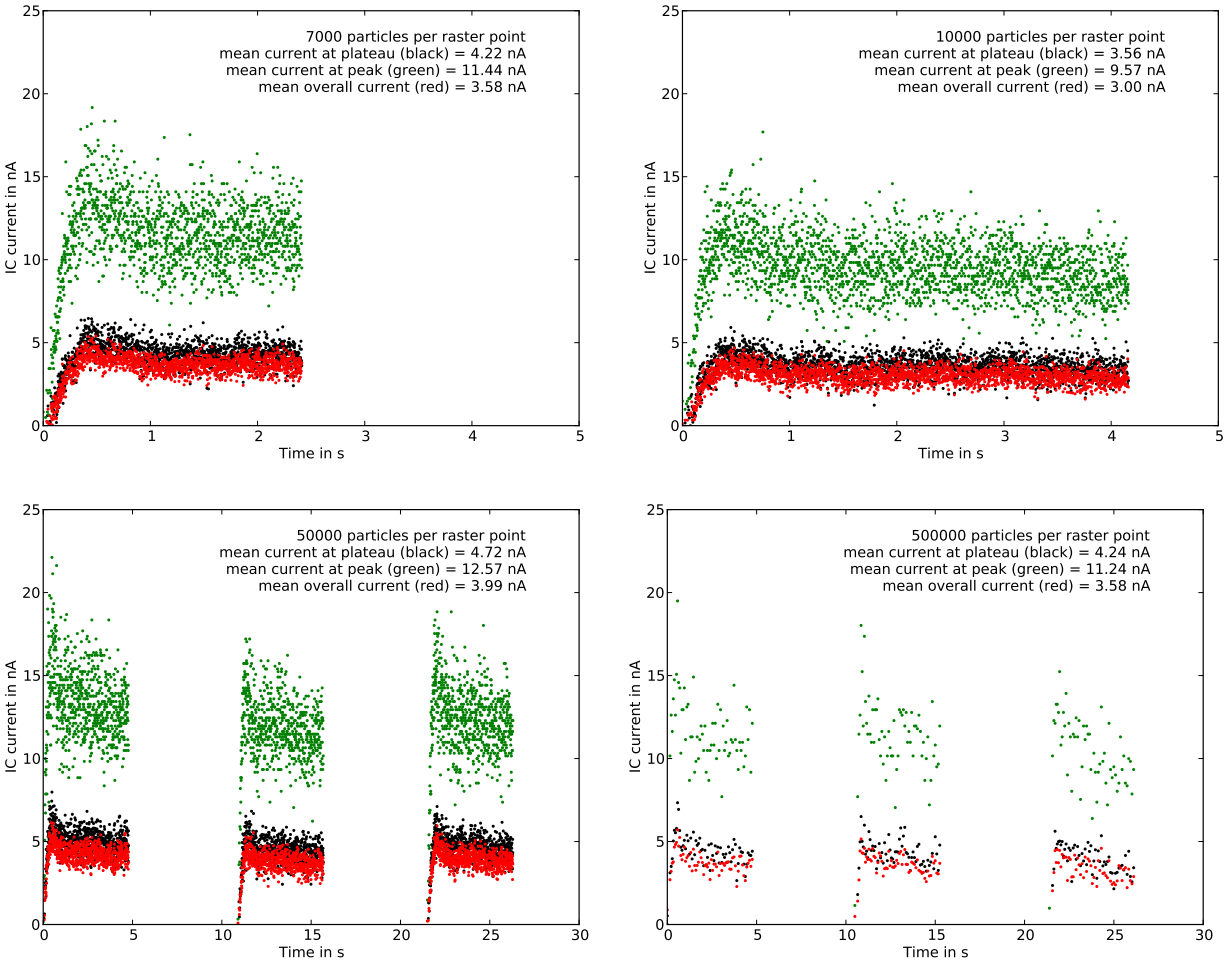

Figure 5.11.: ICs current at the Bragg curve plateau (black), at the peak (green), and the overall mean (red) plotted over a portion of the time of the irradiation plan for different numbers of beam particles, varying from $7 \cdot 10^3$ to 10^5, at fixed intensity of $2 \cdot 10^6\, s^{-1}$. Since the electronics registers only the portion of the particles hitting the ICs stack during the integration period, the signal depends principally on the beam intensity.

---

of 270.55 MeV/u and beam spot with FWHM of 4.1 mm with a lateral step of the raster scanning system Δx and Δy of 1 mm was used without any imaged object in front of the ICs stack.

Figure 5.12 shows the obtained ICs currents plotted over the ICs channel number. While the intensity, i.e., effective number of particles, increases by two orders of magnitude, the mean current measured by the ICs grows only by a factor of ten, or in other words, the ICs current increases roughly with the square root of the intensity. This can be explained by the fact that the ICs charge collection efficiency depends on the high voltage applied to the electrode foils and on recombination effects. For higher beam intensities, more charged particles are created within the gas volume. Those further away from the electrode experience only an effective shielded electric field and thus more likely recombine before reaching the electrode. Therefore, it seems plausible that the measured charge grows less

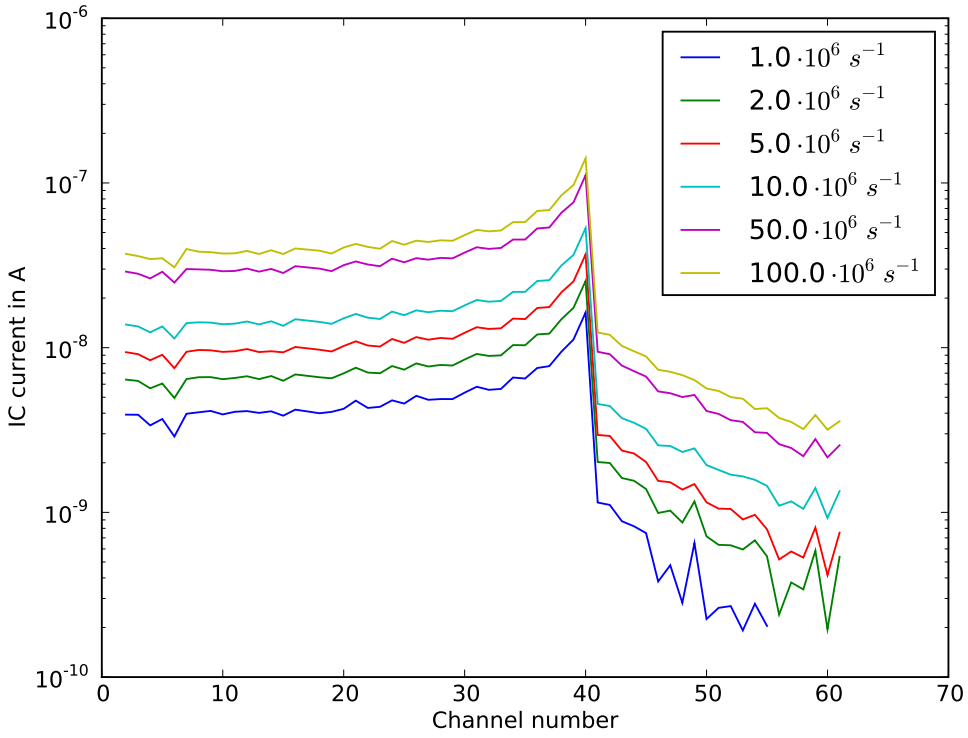

Figure 5.12.: ICs current plotted over channel number for different beam intensities, varying from 10^6 and 10^8 particles per second, at fixed integration period $t_{\mathrm{IP}} = 10^{-4}$ s and $N_{RP} = 500000$.

than linearly with increasing beam intensity.

5.3.2. Dependence of ICs stack response on relative lateral beam position

It is known that the efficiency of PPICs drops in the regions close to the edges. This is of peculiar importance in the case of absolute dosimetry as explained in Brusasco (1999). For HICT, the image information is encoded in the Bragg peak position and not in the absolute IC signal. It is, therefore, sufficient to check, whether the set-up reproduces correctly supposedly flat images. To this scope, the ICs stack was irradiated with a laterally extended field of $200 \times 200\,\mathrm{mm}^2$ and Δx and Δy step sizes of 5 mm of ^{12}C ion at a series of energies (each at smallest available spot size) to obtain information from all the depths of the stack. From the data, both the detected peak position as well as the mean IC current per raster point were determined and separate images were created correlating these values to the x and y position of the raster point. Two examples are shown in figure 5.13 and figure 5.14, respectively. The former qualitatively confirms that the acquired image does not depend on the lateral position of the beam. More interestingly, in the latter images,

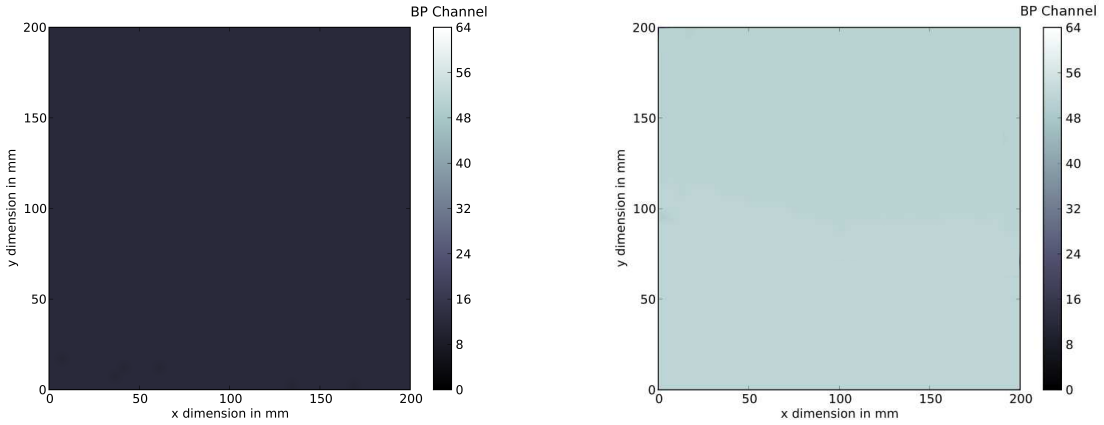

Figure 5.13.: Constructed images obtained from the Bragg peak position for a ^{12}C field of $200 \times 200\,\mathrm{mm}^2$ and Δx and Δy step sizes of 5 mm at two different energies of 136.92 MeV/u (spot size of 7.1 mm FWHM) on the left and 313.76 MeV/u (spot size of 3.8 mm FWHM) on the right.

containing the IC current signal, the start of a beam spill can be recognized by small black streaks. This is because at the beginning of a spill, the beam intensity gradually reaches its maximum following an initial ramp that stretches in time over several subsequent raster points which results in the streaks that gradually fade out. Also, the ICs signal fluctuates in time, partially due to electronic noise and the fluctuating beam intensity. As long as this does not interfere with a correct detection of the Bragg peaks (cf. figure 5.13), this is of no relevance for HICT applications.

5.3.3. ICs stack energy calibration

The peak in the Bragg curve defines the position in the ICs stack, in which most of the initial energy of the ions has been deposited. It is straightforward that, without any object in between, this position depends exclusively on the ion beam energy with the peak appearing at deeper channels in the ICs stack for larger energies (cf. section 1.2.1). Figure 5.15 illustrates this effect. It shows the IC current at five fixed channels measured for a range of ion energies with the same intensity. As the energy increases, the Bragg curve is shifted from the front to the end of the ICs stack, making the shape of the Bragg peak appear flipped in the figure. The data also show that the ICs current in the region of the plateau does not significantly vary with beam energy while the height of the peak changes, as expected.

For two reasons, it is desirable to have a parametrization of the dependence of the peak position on the beam energy. First, for the preparation of experiments it is necessary to set an energy according to the target longitudinal dimension and density to make the Bragg peak fall within the range of the ICs stack. This can be achieved by setting the beam energy appropriately, or by decreasing the beam energy with absorbers (cf. section 5.3.4). Secondly, when comparing a sequence of images acquired at different beam energies, they

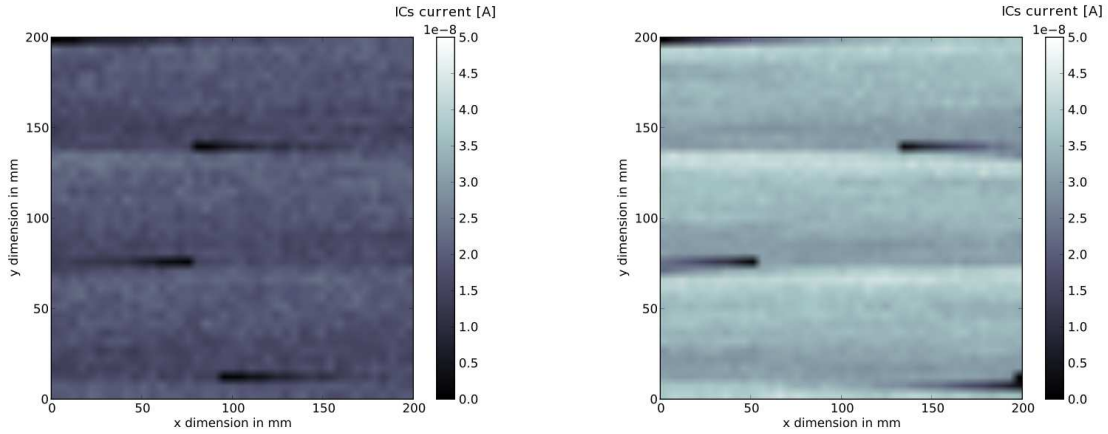

Figure 5.14.: Constructed images obtained from the mean ICs stack signal corresponding to the BP channel position of figure 5.13 for a ^{12}C field of $200 \times 200\,\mathrm{mm}^2$ and Δx and Δy step sizes of 5 mm at two different energies of 136.92 MeV/u (spot size of 7.1 mm FWHM) on the left and 313.76 MeV/u (spot size of 3.8 mm FWHM) on the right.

---

can be re-elaborated based on such a parametrization.

Experimentally, 1681 Bragg curves were registered from a field of $200 \times 200\,\mathrm{mm}^2$ with Δx and Δy steps of 5 mm for a series of beam energies and the smallest available foci. For each curve, the peak position was determined by the criterion of channel identification with the maximum IC signal for each lateral beam position, and the mean channel position from all data for each energy was calculated. The result is shown in figure 5.16. The parametrization was done by fitting the data with the following expression:

$$BP^{\mathrm{pos}} = a \cdot E^{1.75} + b \tag{5.4}$$

as a numerical fit to describe the dependence of the Bragg peak position (BP^{pos}) on the energy (E) from a semi-empirical formula, according to Leo (1987).

In particular, the so obtained parametrization will be used to express radiographies of different phantoms in WE thickness in section 5.4.4.

5.3.4. Dependence of Bragg peak position on target thickness

In analogy to the beam energy calibration in section 5.3.3, a parametrization of the Bragg peak position as a function of target thickness was performed. Again, this is useful to a priori choose parameters in experiments when an absorber in front of the ICs stack is used to attenuate the beam as well as to a posteriori compare images acquired with different absorber thicknesses.

To directly express the Bragg peak position in terms of WE thickness, in an optimum set-up a water column with variable depth should have been used. Due to practical considerations and limited beam time, a double PMMA wedge was instead used in this work. Its geometry is depicted in figure 5.17. This way, a single scan of a lateral field ($206 \times 10\,\mathrm{mm}^2$)

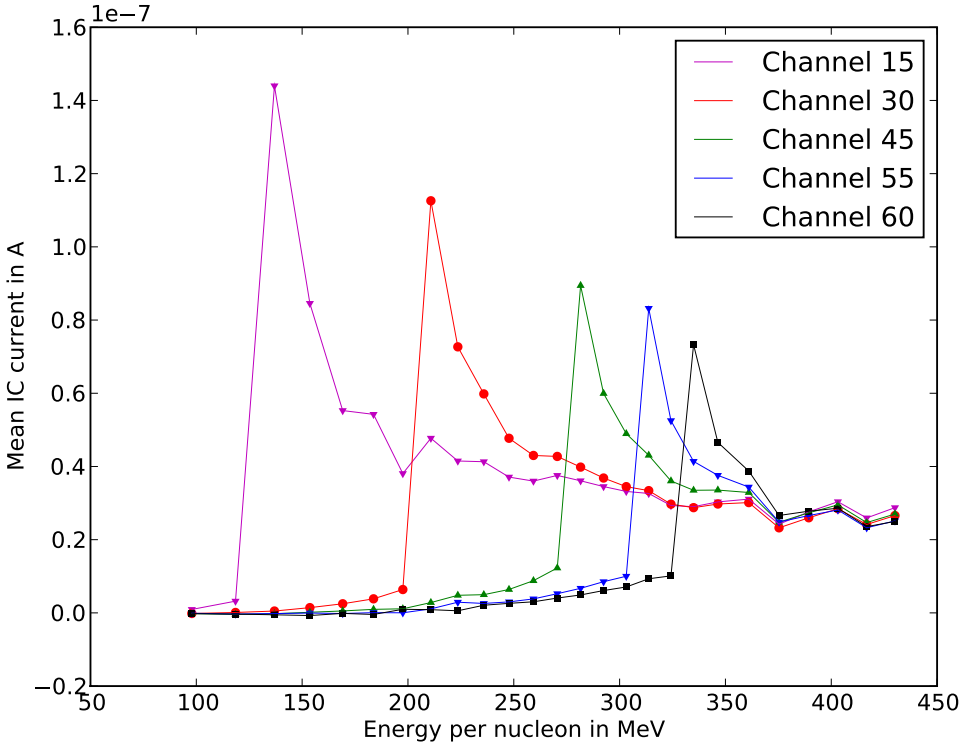

Figure 5.15.: ICs current at fixed channels as a function of energy. The shape of the Bragg peak can be recognized going from right to left.

of ^{12}C ions of 334.94 MeV/u and focus of 3.7 mm FWHM with Δx and Δy steps of 1 mm was sufficient to obtain data across the different PMMA thicknesses given by the wedge.

For each lateral position corresponding to the same wedge thickness, the mean Bragg peak position was determined from 11 Bragg curves (i.e., 11 horizontal rows in the irradiation plan). The result is shown in figure 5.18. The measured wedge profile clearly shows a step-like structure due to the finite nominal resolution of the ICs stack, as described in section 5.2.1. Figure 5.19 reveals the expected linear dependence of the Bragg peak position on PMMA thickness, which was determined from the lateral position in the wedge based on its known geometry. The parametrization was obtained as a linear fit to the data.

This parametrization allows to express radiographic images in terms of equivalent thickness in any homogeneous material, in particular in water, since the measured WEPL value of PMMA at HIT for both, proton and carbon ion beams is known to be $\mathrm{WEPL}_{\mathrm{PMMA}} = 1.165$.

5.4. Radiographic measurements

Radiographic images are the basis for a tomographic reconstruction. In sections 5.4.1 and 5.4.2, it is described how images are obtained from the ICs data and how this relates

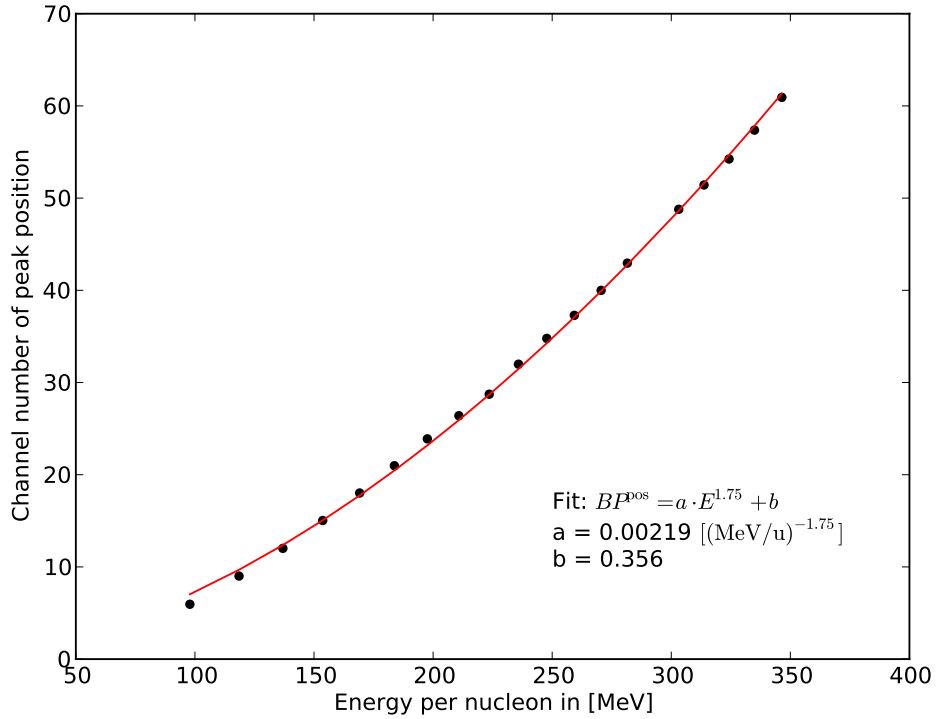

Figure 5.16.: Bragg peak position in the ICs stack as a function of energy. The red line indicate the parametric fit, given by equation 5.4.

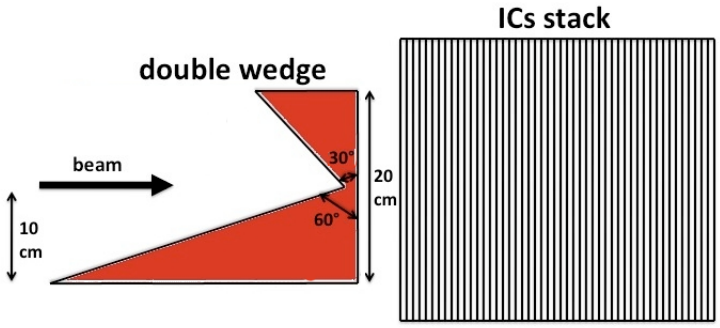

Figure 5.17.: Geometry of the double PMMA wedge and the experimental set-up.

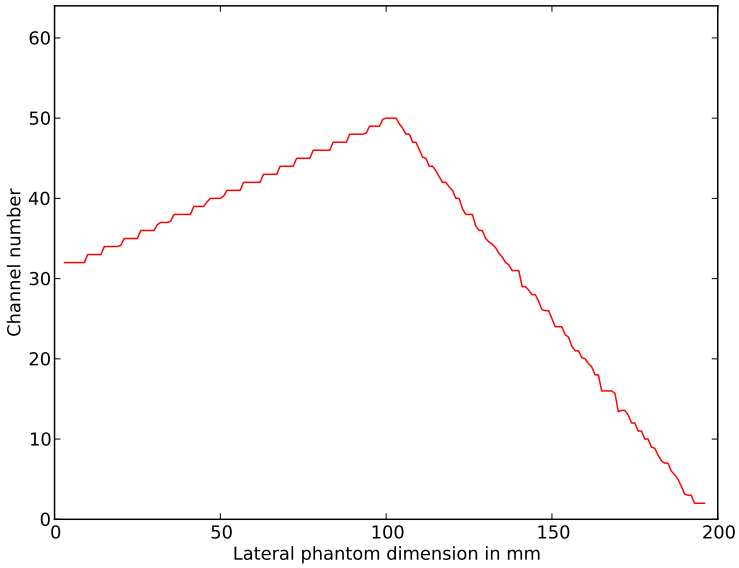

Figure 5.18.: Projection of a radiography of the double PMMA wedge along the lateral dimension used to relate the Bragg peak position in the ICs stack to the PMMA thickness.

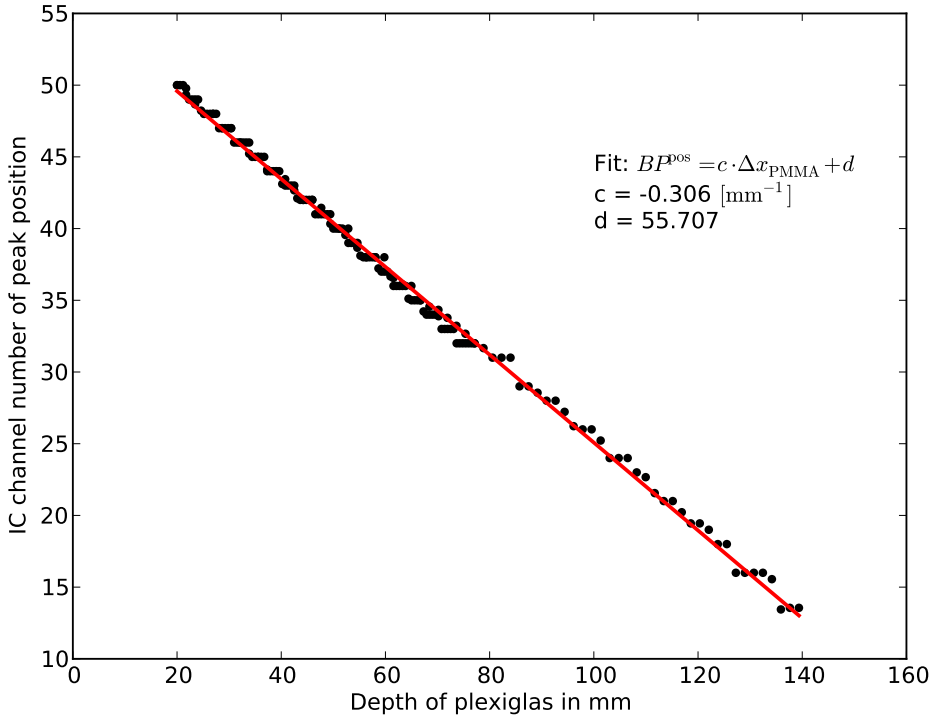

Figure 5.19.: Dependence of the Bragg peak position on PMMA thickness. The red line is given by a linear fit to the data.

to correct triggering with respect to the scanned ion beam delivery system. An analysis of image artifacts at high density contrast interfaces is given in section 5.4.3. Section 5.4.4 describes how images measured with the range telescope can be converted to WE thicknesses and section 5.4.5 shows an experimental verification of the implemented approach. Finally, section 5.4.6 presents results of several experiments and analyses performed with an anthropomorphic Alderson head phantom.

5.4.1. Image formation from ICs stack data

In the scope of using heavy ions to reconstruct tomographic images, 2D integral WE maps are needed for several projection angles. The lateral coordinates in each of these images is given by the beam position while the WE of the material along the traversed path is obtained from the position of the Bragg peak in the ICs stack. In general, the exact line of passage through the irradiated medium has to be known to build up an image. This could be obtained by combining the lateral beam position information given by the BAMS in the beam line and the one determined by an additional position sensitive multi wire proportional chamber between the target and the ICs stack. In case of high energy carbon ion beams, this is not necessarily needed as their trajectories can be assumed to be fairly straight (cf. section 2.4). Thus, a straightforward way to obtain radiographic projections is an irradiation plan that scans the field row-wise, alternating from left to right. The electronics produce a time series of data points where each of them contains the current of the 61 IC channels. These are then spatially distributed according to the irradiation plan to give a radiographic image. The most simple and most effective criterion to establish the Bragg peak position is to search for the channel with the maximum current signal. As long as electronic noise is small with respect to the peak height, this method gives satisfactory results. Compared to alternative methods that might involve fitting theoretical curves to the measured data, the minimal computational effort needed for the criterion of the maximum identification is also promising having in mind a possible future on-the-fly analysis. In all of the images obtained so far with the current set-up, the simplicity of the peak finding criterion was proven not to pose any relevant limiting factor in terms of image precision. An alternative approach proposed in this work will consider the derivative of the measured Bragg curve and identify the peak position by its minimum. This is investigated in some detail and applied in sections 5.4.3 and 5.4.6.1. Furthermore, a method to increase the nominal resolution of the ICs stack is proposed in section 5.5.

5.4.2. Image distortions due to omitted data points

As described in the previous section, formation of a radiographic image from the ICs stack data involves casting a time series into a geometric grid. This requires a one-to-one correspondence between the measured data points and the beam positions given by the irradiation plan. Omitted data points lead to image distortions.

Figure 5.20 shows the very first radiography obtained with the current ICs stack set-up. As phantom, a set of PMMA cubicles of increasing thickness attached to a 1 mm thick PMMA layer was used and it is shown in figure 5.21. A laterally extended ^{12}C ion field ($100 \times 100\,\mathrm{mm}^2$) of 240.65 MeV/u and 4.4 mm FWHM focus was scanned through in Δx

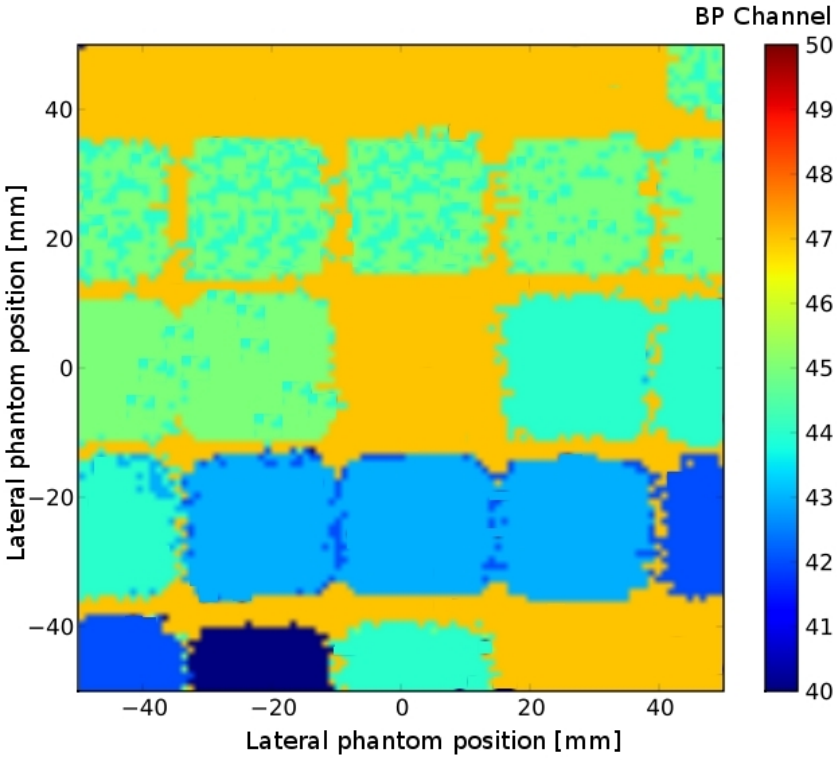

Figure 5.20.: Radiography of the "downtown" stairs phantom consisting of PMMA cubicles of different thicknesses attached to a thin PMMA base. Note the zig-zag shaped borders caused by omitted data points and artifacts occurring at interfaces of high density contrast (cf. section 5.4.3).

---

and Δy steps of 1 mm. The constructed image demonstrates that the cubicles of different thicknesses can indeed be identified based on the peak position in the ICs stack and, in this sense, already provides a first proof of principle. Further, the zig-zag shaped structures along the borders of the squares should be noted. They arise from missing data points where the trigger, which was not fully optimized to work with the ICs stack set-up at that early stage of this first experimental investigation, failed to recognize a new beam position and to initiate a new integration process in the electronics. Moreover, these fuzzy edges can be to some extent caused by an effect occurring at interfaces of high density contrast as will be outlined in section 5.4.3.

To correct for incomplete datasets, the following method was adopted: From the series of time stamps recorded by the electronics, a list of time differences was built. Figure 5.22 shows a series of such intervals plotted over the measurement index. The missed beam positions can be identified by their time difference which is roughly twice the mean over the entire series. The figure also shows some regular peaks which are to be attributed to the beginning of a new spill in the accelerator. To refurbish the image, those points are individuated as omitted positions, whose time difference lies at least 3σ above the average, and which, on the other hand, appear as isolated peaks, in order not to detect points at

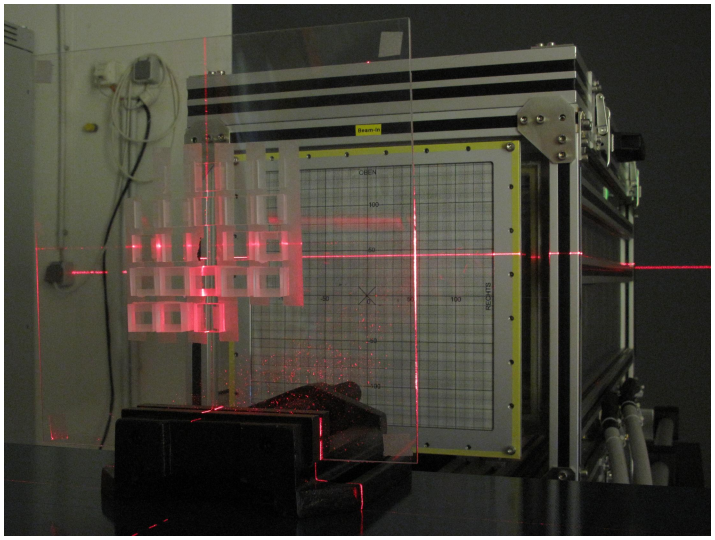

Figure 5.21.: Photography of the "downtown" stairs phantom consisting of PMMA cubicles of different thicknesses attached to a thin PMMA base just in front of the ICs stack.

the beginning of the spill. In the constructed image (cf. figure 5.20), the according pixels are obtained from a linear interpolation to the neighboring pixels.

Although in the subsequently improved experimental setting, a reliable data acquisition has been achieved, the correction method presented in this section proved to be effective and might become useful again if the data acquisition speed should be increased in the future to the edge of its performances, maybe provoking incomplete datasets.

5.4.3. Image artifacts at interfaces of high density contrast

Contrary to an ideal pencil beam, a real particle beam has a finite Gaussian-like spatial profile described by its focus, as explained in section 5.2.2. This means that depending on the lateral position within in the beam, the particles traverse materials of different density, unless the target is completely homogeneous. The ICs stack, on the other hand, only registers the total charge created per raster point in each IC by all ionizing particles within the beam distribution.

This is especially important near interfaces of high density contrast in the target, present also in patients. Considering, for example, a step-shaped density profile, a beam impinging on the interface would produce a superposition of two Bragg curves in the ICs stack. To investigate this effect experimentally, the edge of an 80 mm thick PMMA block in air was irradiated with a 301 MeV/u ^{12}C field of $30 \times 30\,\mathrm{mm}^2$ lateral extension with different beam foci and a lateral Δx and Δy step of 1 mm. Figure 5.23 shows a collection of Bragg curves for two foci of 3.9 mm (smallest available at the given energy) and 10.0 mm (largest clinically available) FWHM at different distances of the beam to the interface.

As expected, two Bragg peaks are visible in the ICs stack current profile. In case of the smaller focus, one of the peaks decreases in height rapidly with growing distance of the beam from the interface. For the larger focus, both peaks are still appreciable even at

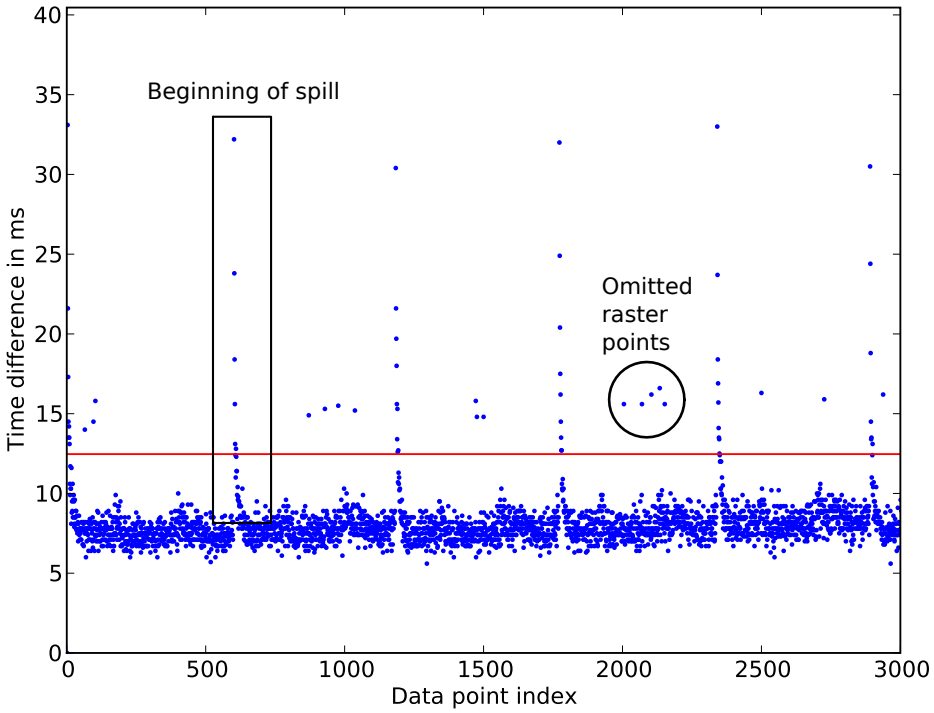

Figure 5.22.: Series of time differences of subsequent data points registered by the electronics. The red line indicates a threshold given by $(\Delta T)_{\text{mean}} + 3\sigma_{\Delta T}$. Several dots, roughly twice the mean, can be attributed to omitted data points. Note the intrinsic fluctuations, mentioned in section 5.2.5, and the peaks due to spill beginning.

greater distance. This is also easily seen from figure 5.24, where the two peak heights are plotted as a function of beam distance to the interface.

At present, images are elaborated from the ICs stack data by assigning to each raster point a unique peak position. For this it is presumed that each raster point consists of locally homogeneous material. Especially in the case of a high contrast interface (i.e., air/bone interfaces), this is not true any more.

Figure 5.25 reveals a problem related to image formation caused by that: If two peaks are present in the IC current profile, both contain information on the target densities in the region around the beam axis defined by the beam width. Together, they provide information on the mean projected density across the beam profile. If only one of them is considered for the construction of the image, the density information encoded in the other is ignored. This results in a sort of digital noise yielding the zig-zag shaped interface seen in the figure.

Another correlated problem is given by the method by which the peaks are located in the measured Bragg curve. In this work two methods are considered. In the first one, the peak position is determined by the maximum criterion, while in the second one, the derivative method, outlined in section 5.4.1, is used. In general, the minimum of the derivative of

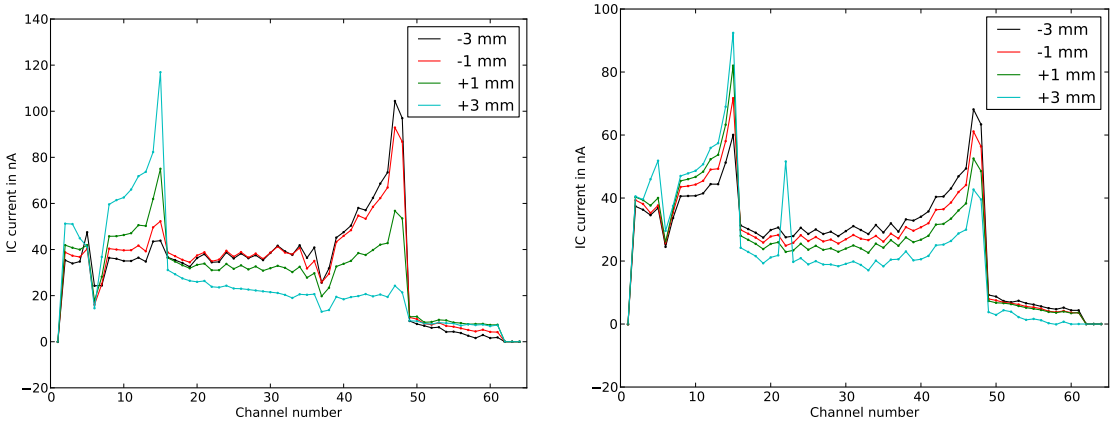

Figure 5.23.: Collection of Bragg curves of 301 MeV/u ^{12}C ion beam for two foci of 3.9 mm (smallest available at the given energy) and 10.0 mm (largest clinically available) FWHM and different distances of the beam to the interface.

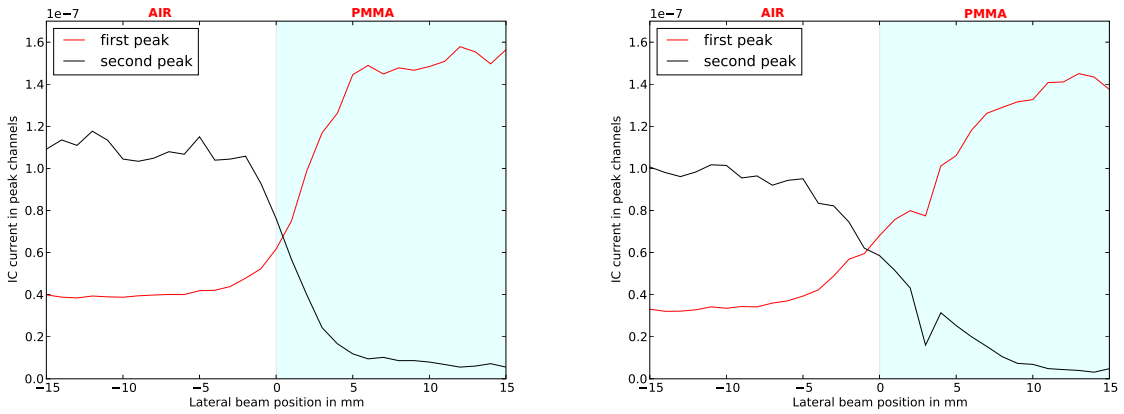

Figure 5.24.: Heights of the two Bragg peaks corresponding to the materials at the interface as a function of beam distance to the interface for irradiation of 301 MeV/u ^{12}C ion beam with the smallest (3.9 mm FWHM, left) and largest (10 mm FWHM, right) focus.

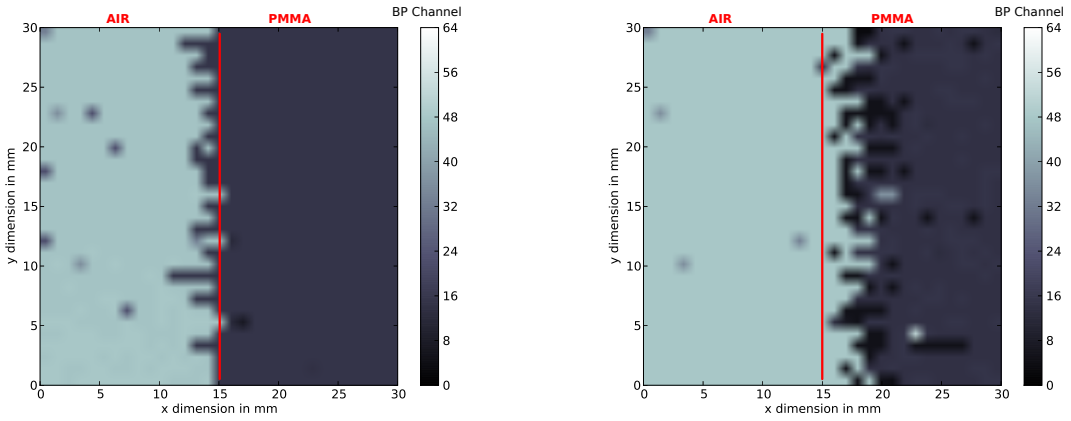

Figure 5.25.: Images of the PMMA-air interface obtained from the Bragg peak positions based on two different approaches. The red line indicates the position of the high contrast interface. For the left image, the channel of maximum signal was chosen. For the right one, the channel of minimim discrete derivative was selected. The bright zone on the latter appears larger. Both exhibit a characteristic zig-zag shape.

a Bragg curve lies further to the right of the maximum position, i.e., the Bragg peak. In particular, the derivative approach might deliver (e.g., in the presence of large straggling effects) slightly varying results for more or less sharp fall-offs behind the peak.

Figure 5.25 shows, however, an effect that cannot be explained by these deviations. In fact, by the derivative approach (on the right), preferably the peak corresponding to the less dense component is chosen. As a result, the bright region at the interface appears larger. The reason probably is that the tail of the first of the two Bragg peaks in figure 5.23 is overlaid by the plateau of the second one. This yields a shallower drop compared to the derivative after the second peak.

Both effects have also been observed in radiographies of the anthropomorphic Alderson head form, as will be presented in section 5.4.6.1. In any case, more detailed investigations will be necessary to optimize image formation methods especially in regard to high density contrast interfaces and multiple maxima.

5.4.4. Re-elaboration of radiographies in WE thickness

The raw images obtained from the ICs stack data contain the channel of the peak position for each pixel. A relevant information would be, though, the projected thickness of the imaged object, e.g. expressed in WE thickness. To this end, calibration of the IC stack based on PMMA was performed as described in section 5.3.4. Since the resulting parametrization was obtained at the beam energy chosen for the calibration, any image acquired at a different energy must first be converted by means of the calibration explained in section 5.3.3. Recalling equation 5.4 therein, a raw image containing Bragg peak positions (BP^{pos}) depends on the energy (E) at which it has been acquired (measured) as:

$$BP^{\text{pos}}_{\text{measured}} = a \cdot E^{1.75}_{\text{measured}} + b$$

The parameters a and b have been experimentally determined (cf. section 5.3.3 and figure 5.16). The same raw image at some reference (ref) energy would be given as:

$$BP^{\text{pos}}_{\text{ref}} = a \cdot E^{1.75}_{\text{ref}} + b$$

Therefore, a measured image can be converted to any desired reference energy by:

$$BP^{\text{pos}}_{\text{ref}} = (BP^{\text{pos}}_{\text{measured}} - b) \cdot \left(\frac{E_{\text{ref}}}{E_{\text{measured}}}\right)^{1.75} + b$$

The relation of PMMA equivalent thickness and the Bragg peak position in the ICs stack is given by a linear fit (cf. section 5.3.4 and figure 5.19) at the reference energy (^{12}C ion beam of 334.94 MeV/u) as:

$$BP^{\text{pos}} = c \cdot \Delta x_{\text{PMMA}} + d$$

therefore combining the following equations Δx_{PMMA} is obtain as:

$$\Delta x_{\text{PMMA}} = \frac{1}{c} \cdot \left[(BP^{\text{pos}}_{\text{measured}} - b) \cdot \left(\frac{E_{\text{ref}}}{E_{\text{measured}}}\right)^{1.75} + b\right] - \frac{d}{c} \tag{5.5}$$

From this, the WE thickness is obtained simply by multiplication with the known WEPL of PMMA ($\text{WEPL}_{\text{PMMA}} = 1.165$): $\Delta x_{\text{WE}} \approx \text{WEPL}_{\text{PMMA}} \cdot \Delta x_{\text{PMMA}}$. Summarizing, a raw image of peak positions is converted into WE by:

$$\Delta x_{\text{WE}} = WEPL_{\text{PMMA}} \cdot \left\{\frac{1}{c} \cdot \left[(BP^{\text{pos}}_{\text{measured}} - b) \cdot \left(\frac{E_{\text{ref}}}{E_{\text{measured}}}\right)^{1.75} + b\right] - \frac{d}{c}\right\} \tag{5.6}$$

5.4.5. Homogeneous cylindric phantom

As a verification, a homogeneous PMMA cylinder with a radius of 8 cm was irradiated with a laterally extended field (200 × 10 mm^2) of monoenergetic ^{12}C ions with an initial energy of 396.29 MeV/u and beam spot with a FWHM of 3.5 mm delivered with a lateral and vertical step of 1 mm. The acquired raw image was converted to PMMA equivalent thickness according to equation 5.5. Figure 5.26 shows the calculated path length as a function of lateral dimension. The values have been plotted half above and half below the zero axis to make the graph resemble the cylinder contour. Evidently, the y dimension of the phantom is correctly reconstructed from the image data suggesting the correctness of the conversion to PMMA, which can be then generalized to WE using equation 5.6 .

It should be noted that zero thickness is not exactly reproduced. In fact, due to the finite size of the ICs stack, there is a minimum material thickness which would result in a Bragg peak still stopping inside the detector for the chosen initial beam energy. Projections of thicknesses below this minimum resulting in a beam not stopped in the detector will cause a false peak identification, mostly yielding the last ICs channel. In the case of the homogeneous PMMA cylinder in figure 5.26, the two non-zero horizontal lines correspond to this minimum measurable thickness.

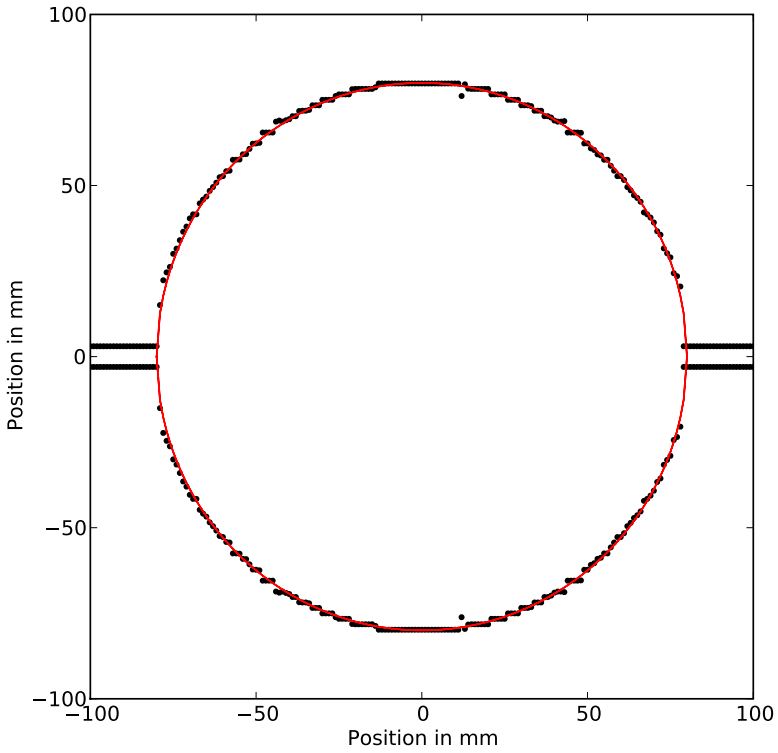

Figure 5.26.: Contour of the homogeneous cylindric PMMA phantom reconstructed from a radiographic projection.

5.4.6. Anthropomorphic Alderson full head phantom

To test the capabilities of the current ICs stack set-up on a more complex phantom and to consider a more realistic case for a clinical application, an Alderson full head form was used. A photograph of the experimental set-up is shown in figure 5.27. The head was irradiated with a lateral field of $250 \times 130\,\mathrm{mm}^2$ and a Δx and Δy step of 1 mm at different energies and the smallest available foci. The radiographic images were built as explained in section 5.4.1. Figure 5.28 shows two radiographies taken at 324.26 MeV/u (3.8 mm FWHM spot size) and 416.73 MeV/u (3.4 mm FWHM spot size). The channel of the Bragg peak is given as gray value, ranging from 1 to 61. The trachea, nasal cavity, and the jaw can be easily identified. The limited nominal resolution of the ICs stack caused step-like changes in the gray value of the image. It can also be seen that at the higher energy, the image appears overexposed where the WE thickness is small and the Bragg peak falls beyond the ICs stack.

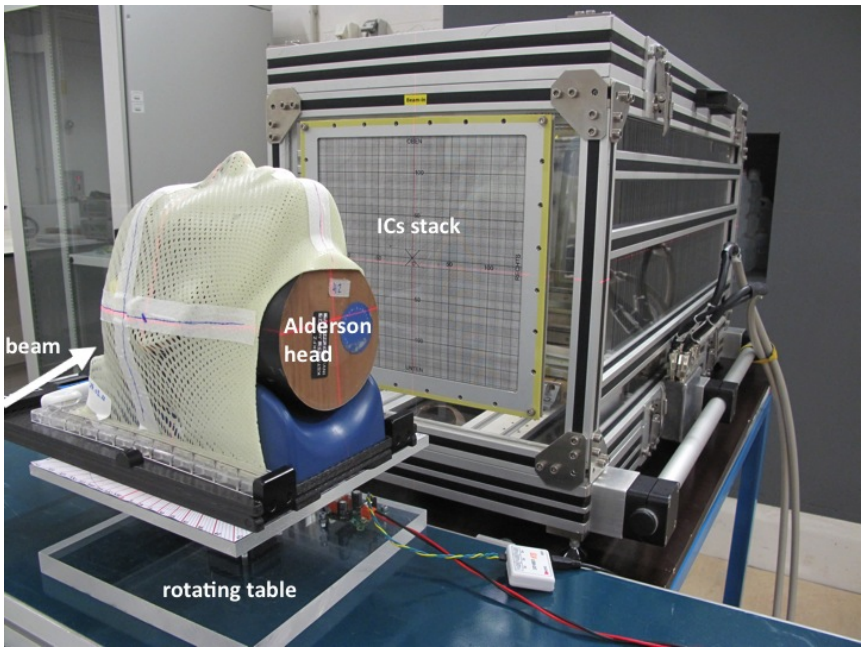

Figure 5.27.: Photograph of the anthropomorphic Alderson head phantom and the experimental set-up, used also for tomographic measurements.

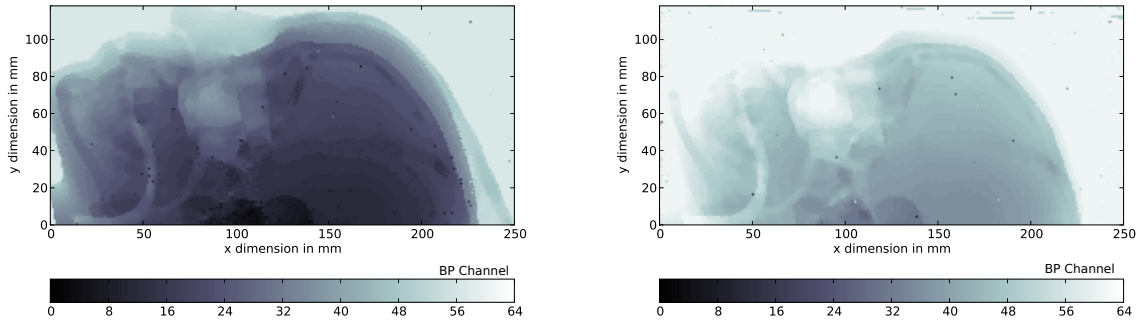

Figure 5.28.: Radiographic images of the Alderson head obtained at 324.26 MeV/u, 3.8 mm FWHM spot size (left) and 416.73 MeV/u, 3.4 mm FWHM spot size (right) using the criterion of maximum identification method to locate the Bragg peak position. The right image shows burned-out regions where the peak fell beyond the ICs stack due to the higher beam energy.

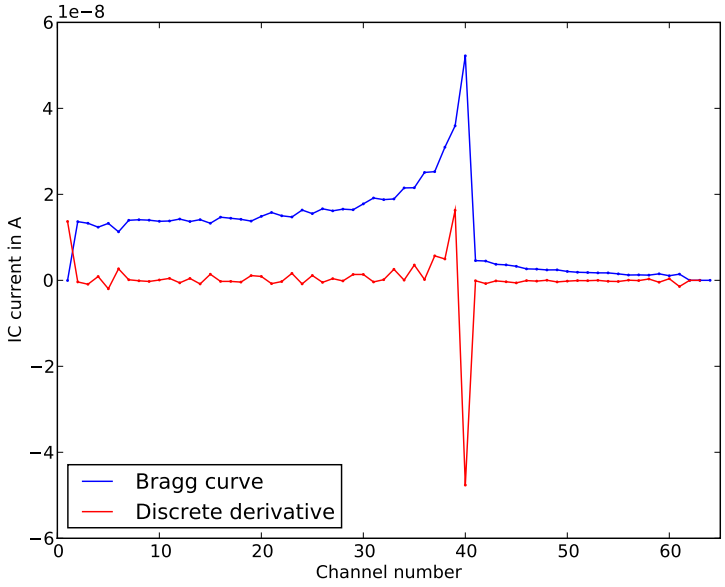

Figure 5.29.: Bragg curve measured with the ICs stack and the discrete derivative thereof.

5.4.6.1. Comparison of methods to locate the Bragg peak

As discussed in section 5.4.1, the simplest criterion to determine the Bragg peak position is to find the channel of maximum signal. This proved to be very reliable. As for any other detection method, the problem of incorrect peak identification arises at interfaces of high density contrast (cf. section 5.4.3) but it is minimized using the smallest foci available at HIT. Nevertheless, alternative criteria could be possibly adopted, yet they should prefereably not require significant computational effort to possibly allow for on-the-fly analysis. Another similarly simple approach would be to consider the derivative of the Bragg curve, i.e., in a discrete dataset the difference of the signals in two subsequent channels. The Bragg peak can then be localized at the point of most negative slope, as illustrated in figure 5.29, although it should be kept in mind that the minimum of the derivative curve systematically yields a position slightly right of the actual peak. In any case, this deviation is taken into account by a calibration based on a PMMA or water phantom and thus the derivative could nonetheless provide a criterion to coherently determine the Bragg peak position. In figure 5.30, this method has been applied to the two radiographies of the Alderson head of figure 5.28.

At first sight, no great difference between the methods can be identified when comparing the images in the two figures. Looking closer, the derivative approach seems to be affected by more wrongly detected points, which seems reasonable, as the difference of two signals is more sensitive to noise. Also, at higher beam energy (in figures 5.28 and 5.30 on the right), the over-exposed regions around the head are filled with a noisy pattern as opposed to the homogeneous white in figure 5.28. The reason is that for a Bragg peak falling just beyond the ICs stack the last channels still carry the highest signal as they lie in the ramp

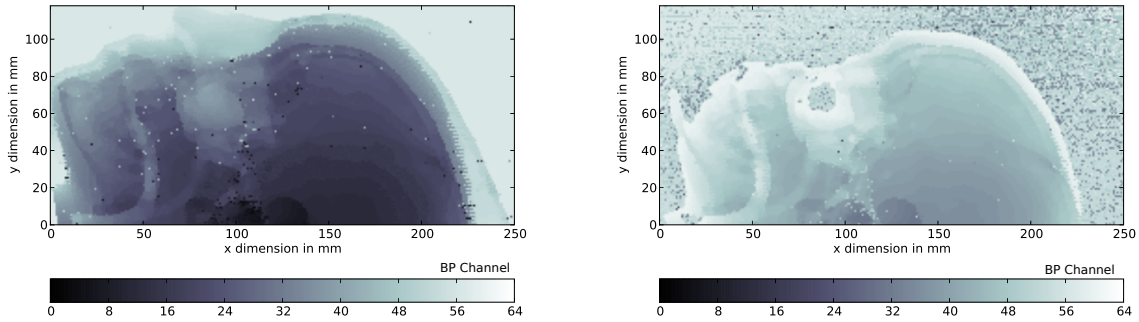

Figure 5.30.: Radiographic images of the Alderson head obtained at 324.26 MeV/u, 3.8 mm FWHM spot size (left) and 416.73 MeV/u, 3.4 mm FWHM spot size (right) using the derivative method to locate the Bragg peak position. The right image shows burned-out regions where the peak fell beyond the ICs stack due to the higher beam energy.

of the Bragg peak. The maximum criterion therefore detects high channel number. As evident from figure 5.29, the discrete derivative of the Bragg curve, on the other hand, has a less pronounced ramp. Its minimum in the region before the peak will therefore mostly be determined by noise.

Slight deviations can also be recognized around lines of strong contrast. In particular, the derivative method tends to yield more fuzzy edges and to emphasize the brighter component in the image as can be seen comparing the regions around the jaw bone and the trachea in figures 5.28 and 5.30. This is in accordance to the findings of section 5.4.3. More investigations will be necessary to optimize the technique to locate the peak in a measured Bragg curve and to understand the influence on the produced image. For the analysis in this work, the criterion of the maximum was preferred because of its simplicity and comparably good and even better results.

5.4.6.2. Radiographies converted to WE thickness

In section 5.4.4, it was explained how raw images containing Bragg peak positions could be converted into WE thickness based on the PMMA calibration described in section 5.3.4. The correctness of this conversion principle has been assessed using a massive PMMA cylinder as target (cf. section 5.4.5). The last step relies on the experimentally validated PMMA-WE conversion, as described in equation 5.6.

For a more realistic application, this conversion was performed on radiographies of the Alderson head. As a basis for a rough comparison, X-ray CT images of the anthropomorphic Alderson phantom were acquired and also re-elaborated in units of WE thickness based on the HU-WEPL calibration curve (cf. section 5.1.1). So obtained calibrated images are shown in figure 5.31.

Since for the two images different head masks were used causing different inclination angles, a quantitative comparison, e.g., by a difference image or sectional profiles, is difficult.

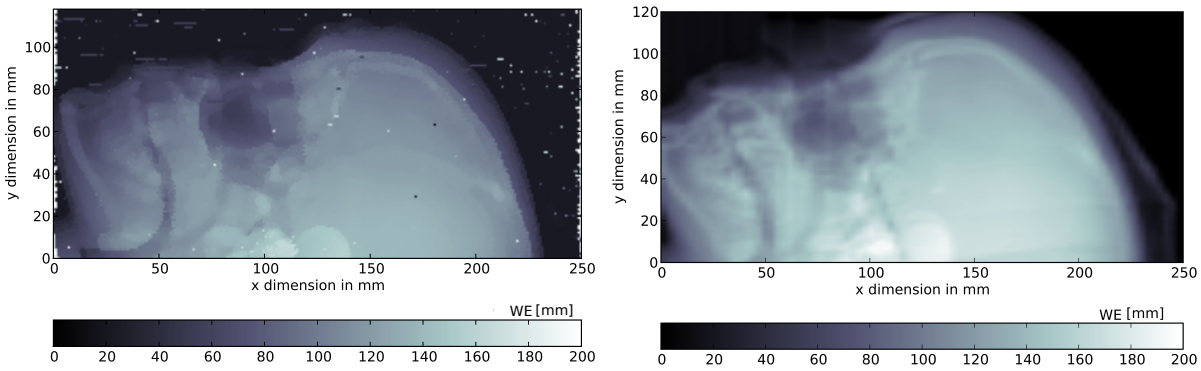

Figure 5.31.: Radiographic image obtained with the ICs stack at 375.32 MeV/u, 3.5 mm FWHM spot size (left) and CT image (right) of the Alderson head phantom, both converted to WE. The colorbar indicates WE thickness in mm. It should be noted that the pixel resolution in the image obtained from X-ray CT data ($3 \times 0.6\,\mathrm{mm}^2$) is lower than in ion-based radiography ($1 \times 1\,\mathrm{mm}^2$).

Qualitatively, the details of the two images do not differ significantly and apart from some mis-detected pixels (i.e., white and black dots) in the ion-based radiography the correspondence is satisfying. Nevertheless, more detailed investigations are still necessary to understand how realistically the WEPL of the tissue is revealed (cf. section 5.6).

5.4.6.3. Dynamic range of the radiographies

The right image of figure 5.28 demonstrated the effect of over-exposure caused by Bragg peaks falling beyond the ICs stack at the chosen beam energy. This raises the question of the necessary range of the IC stack to image a typical target, e.g., a human head. An answer is provided by a histogram plot of the channels in which the Bragg peaks in an image fall. This is shown in figure 5.32 for two cases of beam energies of 375.32 MeV/u (3.5 mm FWHM focus) and 416.73 MeV/u (3.4 mm FWHM focus) delivered to the Alderson head phantom, respectively. In the left panel, the distribution is concentrated around the center of the ICs stack channels indicating a properly exposed radiography, while the right panel corresponds to an over-exposure, as is seen by the distribution cut-off on the right. The high peak in channel 61 is responsible for the bright background. From the histograms it is learnt that the range of the current ICs stack is sufficient for radiographies of a human head, although it is clear that already slight changes in the beam energy will shift the brightness spectrum outside the range. This is of particular importance for tomographic applications, as will be outlined in section 5.6. In any case, a thorough study of the optimal parameters is needed when an improved version of the current ICs stack will likely be designed and built in the future for clinical use.

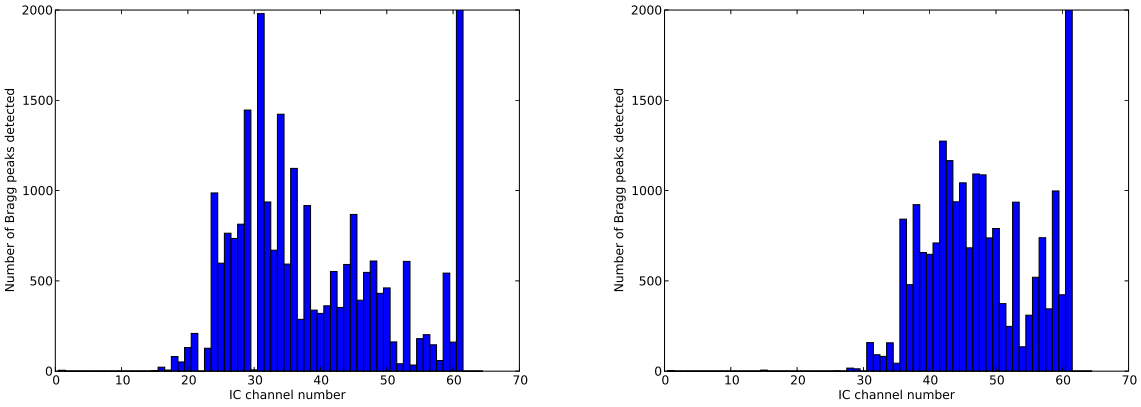

Figure 5.32.: Histogram of the channels in which the Bragg peaks in an image fall for two cases of beam energies, 375.32 MeV/u (3.5 mm FWHM spot size) and 416.73 MeV/u (3.4 mm FWHM spot size) delivered to the Alderson head phantom, respectively. The zero counts in channels 22 and 30 are due to improperly working ICs in this measurement.

5.5. Method to virtually increase the nominal resolution of the ICs stack

For the quality of images obtained with the HICT technique, two features are particularly important. One is the spatial resolution in the image plane, determined by the Δx and Δy steps of the irradiaton plan and the focus of the beam. The second aspect regards the resolution of material thickness levels contained in an image, e.g., expressed in WE thickness. This is given by the nominal resolution of the ICs stack. As seen in section 5.4.6.3, for a radiography of a human head, about 30 channels of the ICs stack are used, corresponding to a range of about 110 mm WE in steps of about 3.5 mm WE. In terms of image depth, this corresponds to a 5-bit image. Consequently, this limits the systems ability to resolve fine nuances in thickness in the scanned object.

By improving the nominal resolution of the ICs stack, one could increase the image depth. One approach would be to utilize thinner slabs of PMMA in the construction of the ICs. Using sheets of 1 mm instead of the currently employed 3 mm, e.g., would increase the resolution by a factor of 3. On the other hand, the range of the 61 ICs in the stack would diminish accordingly from 21 cm WE to about 7 cm WE. This is of particular importance for tomographic applications, as explained in section 5.6.3, where the typical thickness of the irradiated object, and thus the necessary range, depends on the angle of projection. This problem could be overcome either by increasing the total number of ICs/electronic channels, or by compensating for the range shift by dynamically introducing suitable absorbers (Brusasco et al. 2000) during a tomographic scan.

Both of these approaches require considerable hardware and financial effort. These considerations gave the motivation to think about alternative ways to enhance the nominal resolution of the ICs stack. A straightforward approach could consist of parametrizing the expected Bragg curve or peak, which would then be fitted to the ICs signal. In the

following, an alternative method is proposed based on the precise shape of the Bragg peak and the way it is measured by the ICs stack.

As described in section 5.2.1, the ICs stack consists of interleaved layers of air and PMMA (disregarding the foil electrodes). Since the density of PMMA is much larger than that of air, almost all energy deposit occurs in the PMMA slabs. The actual Bragg peak will therefore always be situated in a PMMA sheet. The ICs, in turn, measure the charge created by the ionizing particles in air, which depends on the number of particles and their energy loss (cf. equation 5.1). As the particles deposit energy when passing through the PMMA, their stopping power changes and so does the charge counted in the subsequent IC. In this sense, the measured charge in each IC corresponds to the energy loss and number of particles after the previous PMMA slab. The dataset of IC currents, therefore, corresponds to a discretization of the real Bragg curve. At the position of the Bragg peak, the number of primary particles, in this case ^{12}C ions, quickly drops to zero, leaving behind only lighter secondary fragments. Consequently, the charge created in the IC after the Bragg peak is much lower and it is from this steep drop that the registered ICs stack signal allows to deduce in which PMMA slab the Bragg peak is situated. However, the exact position within the PMMA sheet remains uncertain resulting in the finite nominal resolution of 3 mm.

While at first glance, the Bragg curve seems to drop to zero instantaneously, a closer look shows that it actually decreases gradually over a distance of about 2-3 mm in PMMA. Figure 5.33 shows four zoomed-in Bragg peaks, obtained from a FLUKA MC simulation of a ^{12}C beam at 334.94 MeV/u in PMMA (dominated in the peak by straggling effects). The four panels give different relative positions of the ICs with respect to the physical Bragg curve. The idea is to compare the signal of the two ICs before and after the PMMA slab in which the Bragg peak resides. The ratio of these two signals depends on the peak position in the slab.

In the figure, the green curves quantify the signal ratio of two neighboring channels at 3 mm distance. The value of each such channel pair is attributed to the location of the left channel. A ratio of one is found when the PMMA slab is situated as indicated in figure 5.33(a). In that case, the peak lies close to the right edge of the slab. For the channel of maximum signal situated more to the right (i.e., closer to the theoretical Bragg peak), the ratio drops below one (cf. figures 5.33(b), 5.33(c), and 5.33(d)). This way, the ratio of the two signals provides a way to infer more precisely the position of the Bragg peak within a PMMA slab, effectively increasing the nominal resolution of the range telescope. It has to be noted, that if the position of the maximum channel moves by one slab width (as it is almost the case in figure 5.33(d)), it will be positioned in the adjacent PMMA sheet at the same relative location reproducing again the case of ratio = 1, shown in figure 5.33(a). With respect to a reference point fixed on the Bragg curve, the measured ratio of signals will therefore be periodic.

To assess the proposed method, data obtained from measurements with the double wedge (cf. section 5.3.4) were used. As the beam moves across the wedge, the thickness of traversed PMMA changes continuously, shifting the Bragg curve slowly through several PMMA slabs in the ICs stack. From the measured Bragg curve at each lateral wedge position, the ratio of the signals between the channel behind and at the maximum were calculated. The result is shown in figure 5.34. As the thickness of the wedge decreases

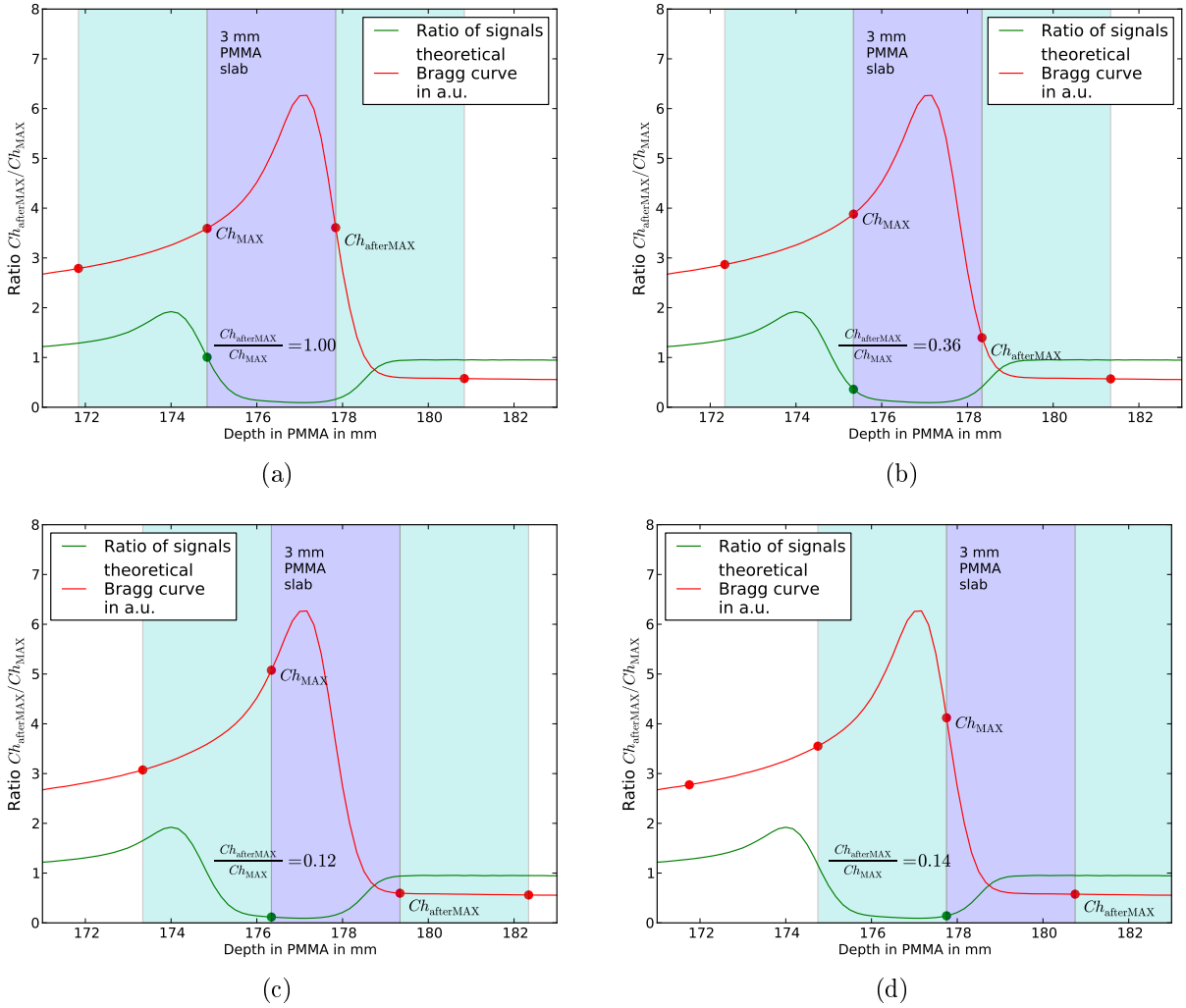

Figure 5.33.: Zoomed-in Bragg peak obtained from a FLUKA MC simulation (red line) of a ^{12}C beam at 334.94 MeV/u and 3.7 mm FWHM spot size in PMMA for four different relative positions of the Bragg peak with respect to the surrounding ICs. The red dots indicate discrete points at 3 mm distance corresponding to the measured signal in the ICs stack channels. The green line is obtained as the ratio of subsequent discrete points at 3 mm distance on the curve. The green dot gives the inverse ratio of the maximum signal measured by the ICs and the signal in the subsequent channel.

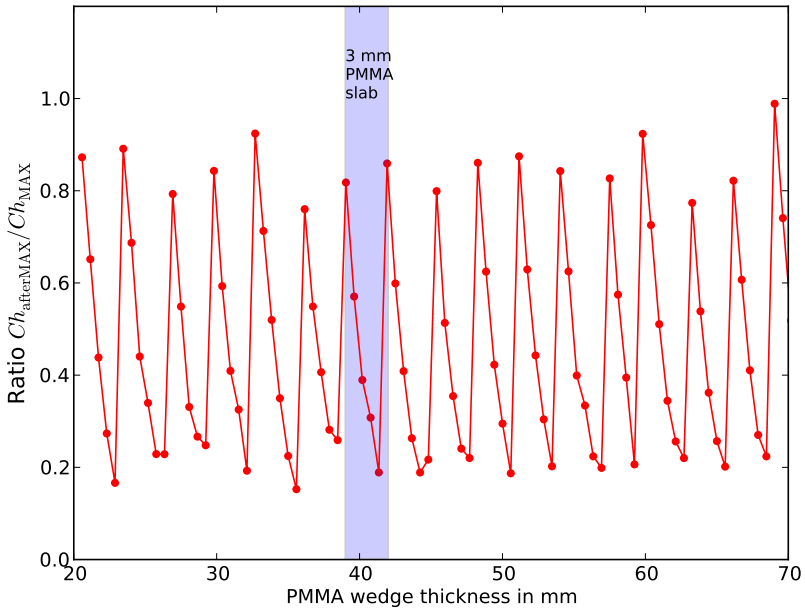

Figure 5.34.: Signal ratio of the channel behind and at the maximum current depending on the thickness of the traversed double PMMA wedge (cf. figure 5.17). The blue bar indicates the width of a PMMA slab in the ICs stack.

during a scan and the Bragg peak moves gradually through a PMMA sheet of the ICs stack, this ratio continuously increases until the peak reaches the next slab. There, it drops back to a minimum and starts to rise again, resulting in the expected oscillation about every 3 mm. This proves the concept of the proposed method.

Returning to the simulated Bragg curve in figure 5.33, all those possible pairs of channels (i.e., pairs of points on the curve 3 mm apart from each other), of which the left channel carries the maximum signal of the entire measured Bragg curve, are limited to the blue shaded region in figure 5.33(a) by periodicity[2].

Therefore, with this applied criterion, only a point on the part of the green curve within the dark blue area in figure 5.33(a) can be seen in the data. Turning this around, one obtains a theoretical curve relating the ratio of signals to the relative position of the Bragg inside the PMMA slab. This is shown in figure 5.35. For the slab width of 3 mm in the current ICs stack, there is no perfect one-to-one correspondence for relative distances to the Bragg peak around zero. This relationship becomes unique for smaller slab thicknesses (< 2 mm).

The accuracy of the correction obtained from the ratio of signals depends, firstly, on the accuracy of the measured signals themselves and, secondly, on the functional correspondence between ratio and relative peak position (cf. figure 5.35). The gained nominal resolution is therefore limited by these two factors. For the current set-up, the improved nominal resolution is estimated to be around 1 mm in PMMA.

[2]In fact, if the position of the channel lay outside this region to the left, the corresponding signal ratio would be larger than one. In other words the signal in the right channel would be higher, violating the assumption of the left channel being the maximum.

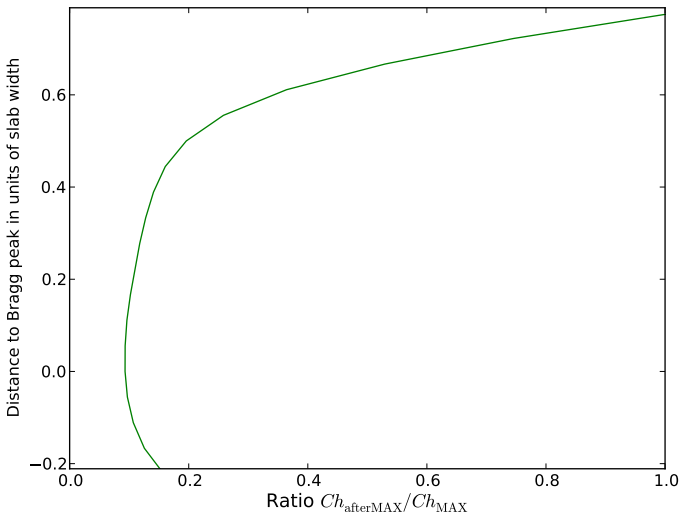

Figure 5.35.: Relationship of the ratio of signals at the channel of maximum current and the relative position of the Bragg peak with respect to the maximum channel. The plot is obtained by inverting the dark blue region in figure 5.33(a).

5.5.1. Applications of the increased nominal resolution

Following the above method, some radiographic data have been recalculated. To this end, from the ratio of signals at the channel of maximum current, the correction for the Bragg peak position was calculated by a simple linear interpolation of the curve in figure 5.35. For the double wedge (cf. section 5.3.4) and the massive cylindric PMMA phantom (cf. section 5.4.5), a comparison of the projections obtained by the simple maximum criterion with and without the additional correction is shown in figure 5.36. It is clear that this method really permits to increase the nominal resolution of the ICs stack, since the ≈ 3 mm step-like structures in the projections are strongly suppressed. It should be noticed, that the kinks in the profile at channel 14, and 22 are due to malfunctioning channels of the ICs stack.

Figures 5.37(a) and 5.37(b) show a comparison of radiographies of the anthropomorphic Alderson head phantom obtained by the simple maximum criterion with and without the additional correction. The difference image in figure 5.37(c) reveals a step-like structure due to the limited nominal resolution if no improvement is done. In fact, it can be seen, that in the refined image, the gray values change more gradually. This can also be seen from the horizontal and vertical sections in the lower four panels of the figure (cf. figures 5.37(d), 5.37(e), 5.37(f), and 5.37(g)). Without the increased nominal resolution (cf. panels on the left), the edgy structure is evident. To obtain still better results, the dependence of the ratio of signals to the peak position would have to be parametrized more precisely. Certainly, it will be interesting to investigate how far such a technique could provide higher nominal resolution images without the need of thinner absorbers between the PPICs. A thorough study of the influence of signal noise on the functioning of the method would also be necessary, but all these investigations are meant for future improvements outside the scope of this work.

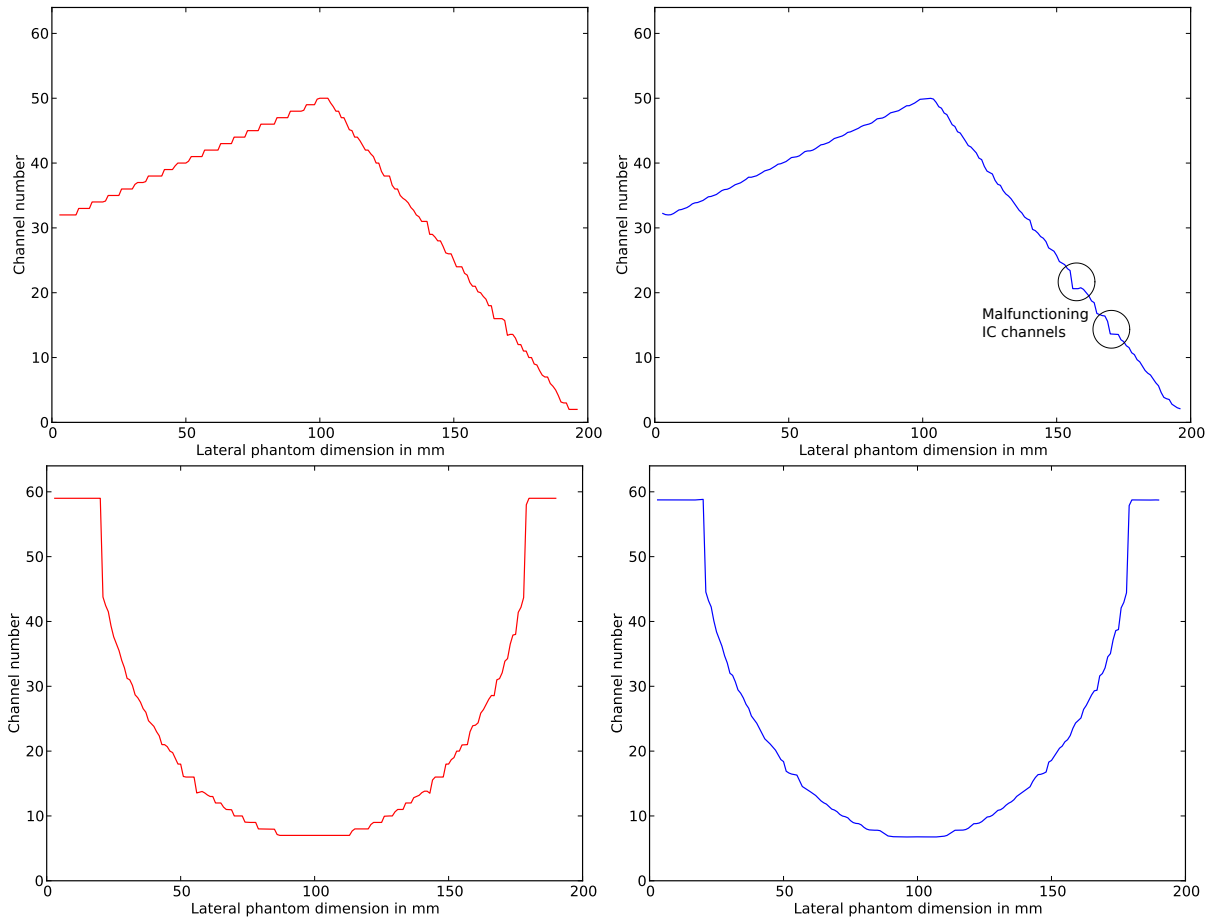

Figure 5.36.: Comparison of radiographic projections obtained by the criterion of maximum identification without (left) and with (right) the additional resolution correction for the irradiation of the double wedge (top, cf. figure 5.17) and the massive cylindric PMMA phantom (bottom, cf. section 5.4.5).

5.6. Tomographic measurements

5.6.1. Principle of image acquisition and reconstruction

The basic dataset for a tomography is given by a series of radiographies acquired at different angles (cf. section 5.4.1). To these projected images, a standard analytical backprojection algorithm based on Fourier transforms (Deans 1983) was applied. For best results, the method requires angles to be equidistant and to cover the entire range necessary for reconstruction (i.e. at least $0° - 180°$). In the backprojection approach, images are usually filtered in Fourier space to produce a correct reconstruction of the WEPL distribution in the projected object. Without such a filter, the inner part of the reconstructed image would be overestimated and contours would be blurred. Although various filters with specific advantages exist in the literature, in this work, a simple ramp filter was employed. A more detailed study of the mathematical reconstruction techniques is out of the scope of

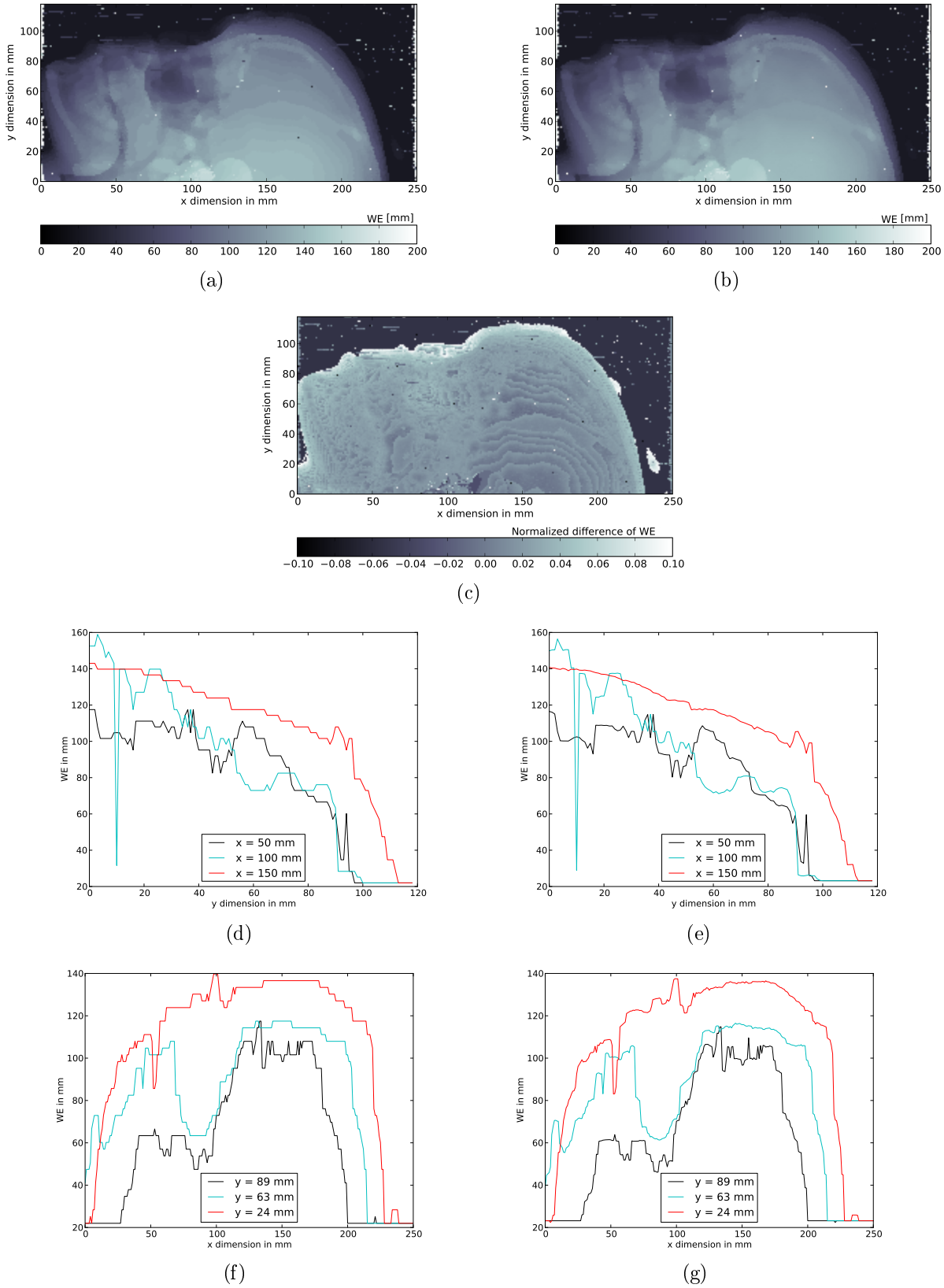

Figure 5.37.: Comparisons of radiographies of the anthropomorphic Alderson head phantom obtained by the criterion of maximum identification without (left) and with (right) the additional correction for improving the nominal depth resolution. In the difference image (c), the step-like structures due to limited resolution can be seen. The lower four panels show several sections in x and y direction through the radiographies for both methods.

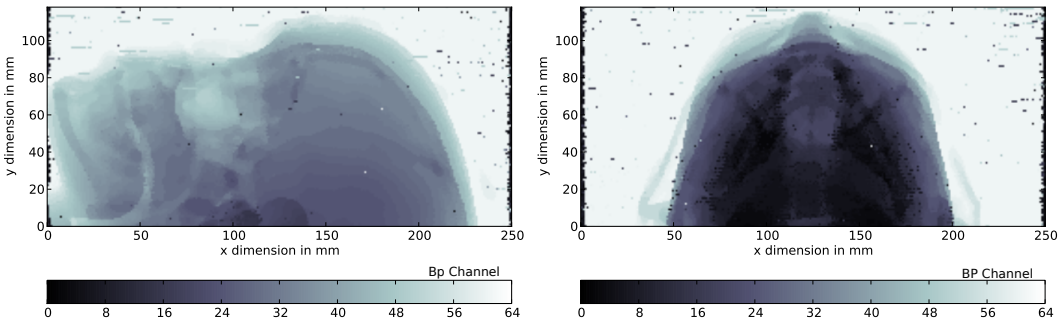

Figure 5.38.: Two radiographies of the anthropomorphic Alderson head form obtained at the same carbon ion beam energy of 375.32 MeV/u and 3.5 mm FWHM spot size for two angles of 0° (left) and 90° (right).

this thesis.

In figure 5.27, the set-up used for tomographic measurements in the experimental room at HIT was shown. A rotating table, remotely controllable, was built to speed up the measurement and to guarantee that the center of rotation was not shifted during data acquisition. Two of the already described phantoms of different complexity were used: The PMMA cylinder ($R = 8$ cm), shown in figure 5.3, with five tissue equivalent rods and the anthropomorphic Alderson head phantom.

5.6.2. Adaptation of the range in dependence of the projection angle

An important consideration for the acquisition of radiographies used for tomographic reconstruction of a non-symmetric object is that the thickness varies with the angle of projection. This can easily be seen from the two radiographies of the anthropomorphic Alderson head phantom in figure 5.38, obtained at the same carbon ion beam energy of 375.32 MeV/u and 3.5 mm FWHM spot size for 0° and 90°. These two angles constitute the extreme positions in a head-like case, as can be seen from figure 5.39. For this plot, the mean Bragg peak position (expressed in channel number) and the standard deviation were calculated for all measured angles ($0° - 360°$ in steps of 2.25°).

Therefore, it might be necessary to adjust the range of the ICs stack depending on the angle of projection. This could be achieved either by changing the beam energy or by inserting absorbers of different thickness during a tomographic scan. Afterwards, the Bragg peak positions contained in the single images would have to be shifted appropriately to compensate for the additional absorber or beam energy. For a tomographic reconstruction to work properly, this re-elaboration must not introduce any mismatches in gray level between images.

In a heuristic approach, this was checked by taking radiographies at a fixed energy (416.73 MeV/u and 3.4 mm FWHM spot size) with PMMA sheets of different thickness in front of the ICs stack. The images, acquired with 20 mm and 80 mm PMMA absorber plates, respectively, and converted to a common reference thickness of 45 mm PMMA absorber, are shown in figure 5.40. To make discrepancies more visible, each image was

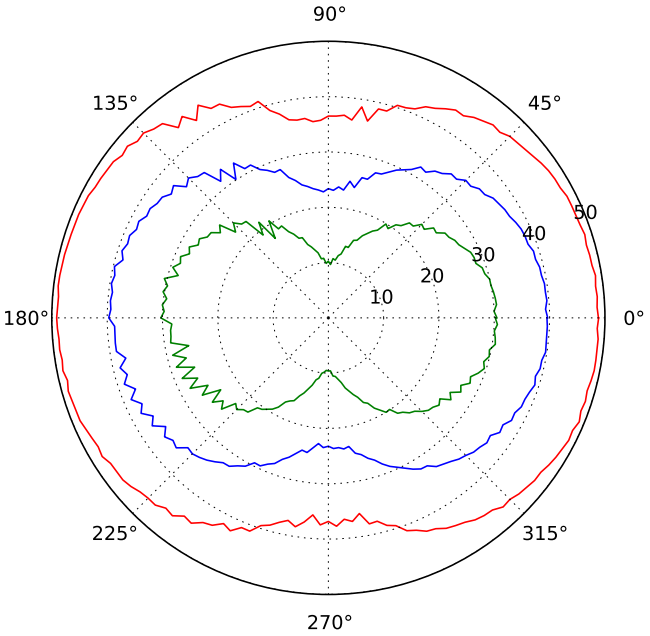

Figure 5.39.: The mean Bragg peak position (expressed in channel number in steps of ten) and the standard deviation calculated for all measured angles ($0° - 360°$ in steps of $2.25°$) for the anthropomorphic Alderson head phantom. The blue line refers to the mean Bragg peak position, while the red and green line represents the mean value plus and minus one standard deviation, respectively.

subtracted from a reference image, acquired with a 45 mm PMMA absorber plate, and normalized by its mean value. The results are presented in the lower two panels.

In principle, the method of correcting the radiographic projections for the amount of inserted energy degraders seems to yield satisfactory results, although a more precise calibration is needed and some additional technical effort would have to be done, which is outside the scope of this work.

5.6.3. Tomographic reconstruction of cylindrical PMMA and Alderson head phantoms

As first proof of principle, tomographic reconstructions of two phantoms have been performed. In figure 5.41, two reconstructions of the cylindric PMMA phantom with five tissue equivalent rods are shown, without (cf. figure 5.41(a)) and with (cf. figure 5.41(b)) a ramp filter in Fourier space. The radiographies were obtained with a ^{12}C beam of 396.29 MeV/u and 3.5 mm FWHM spot size scanned through a laterally extended field ($200 \times 10\,\mathrm{mm}^2$, $\Delta x = \Delta y = 1$ mm) for 36 equi-spaced angles between 0° and 180°, and the method to virtually increase the nominal resolution of the ICs stack was adopted (cf. section 5.5). The Bragg peak position in each pixel of the projected radiographies was converted to WE thickness, according to equation 5.6.

As expected, the reconstruction without filter is artificially bright in the center and

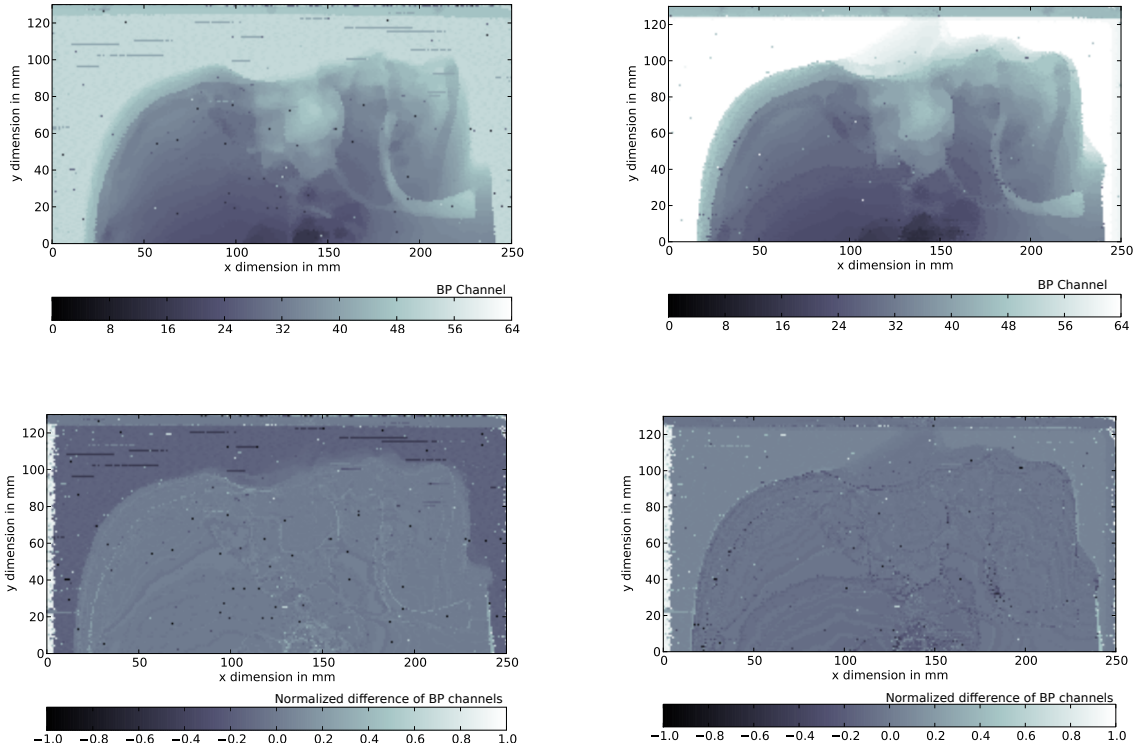

Figure 5.40.: The top panels show images, converted to a common reference thickness of 45 mm PMMA absorber, of two different radiographies obtained at fixed carbon ion beam energy of 375.32 MeV/u, 3.5 mm FWHM spot size and with different PMMA thickness (20 mm, left, and 80 mm, right) in front of the ICs stack. The lower panels show images of the difference of the two radiographies above obtained by subtracting each of them from a reference image obtained with 45 mm absorber and normalizing them by the mean value.

becomes gradually darker outside. On the other hand, the more technically correct reconstruction with ramp filter reproduces the right phantom and rod dimensions and allows to unambiguously identify the structures. It is in the nature of the filter to emphasize image noise. The stripe-shaped artifacts are due to the finite number of angles. In this respect, the influence of the used filters will still have to be investigated in more detail, but it is outside the scope of this work.

The reconstruction produces WEPL slightly above one, coherent with the measured reference value of ($\mathrm{WEPL_{PMMA}} = 1.165$) (cf. section 5.3.4). For the inserted rods, the tomographic image roughly reproduces the expected WEPL of the different materials ($\mathrm{WEPL_{air}} \approx \rho_{\mathrm{air}} = 0.0012\ \mathrm{g/cm^3}$, $\mathrm{WEPL_{lung}} = 0.455$, and $\mathrm{WEPL_{bone}} = 1.618$), as can best be seen in the two lower panels of figure 5.41 showing the horizontal (cf. figure 5.41(c)) and vertical (cf. figure 5.41(d)) sections through the center of the phantom.

As the most complex phantom investigated so far, a reconstruction of the anthropomorphic Alderson head form was performed. The radiographies were obtained with a ^{12}C ion beam of 389.36 MeV/u and 3.5 mm FWHM spot size for 160 equi-spaced angles between 0° and 360° and a field of $250 \times 80\,\mathrm{mm^2}$ with a Δx step of 1 mm and a Δy step of 10 mm,

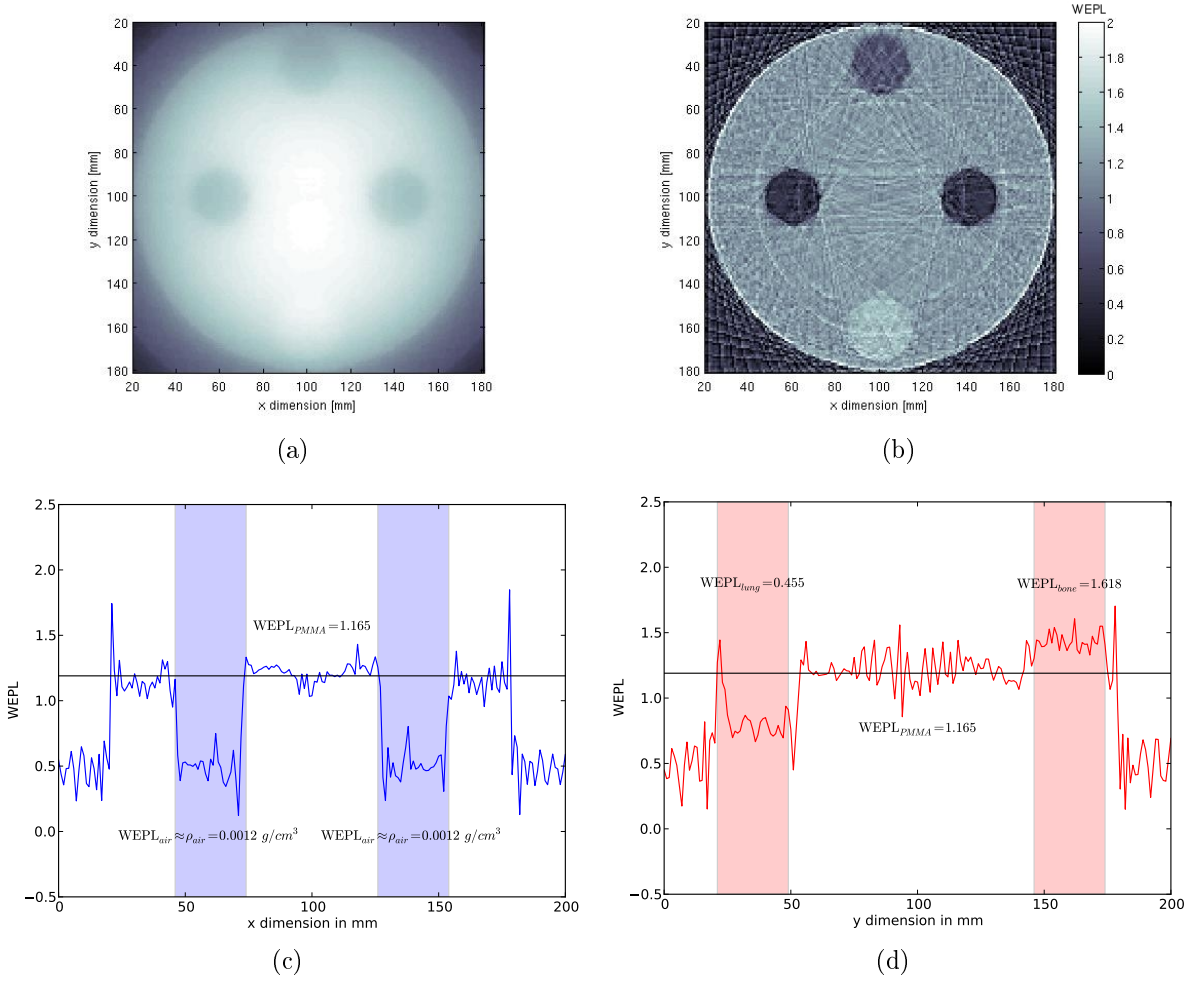

Figure 5.41.: Reconstructions of the cylindric PMMA phantom with five tissue equivalent rods, without (a) and with (b) a ramp filter in Fourier space. The colorbar indicates WEPL. The lower two panels show central sections in the horizontal (c) and vertical (d) direction. The expected WEPL of the materials are indicated for the respective regions.

and then converted to WE tickness according to equation 5.6. In figure 5.42, the seven reconstructed slices are presented. For qualitative comparison, a set of similar seven slices, obtained from an X-ray CT, are presented in figure 5.43. It should be noted, that in both cases the head had a slightly different inclination with respect to the reference table. The sections are therefore not expected to be identical.

Although image noise from the carbon ion radiographies shows up as high contrast streaks, some characteristic features of the human head can be recognized such as the trachea, the nasal and auditory cavities, as well as some bone structures of the skull and the jaw. The outer dimensions of the head are reproduced correctly. As in the case of the cylindric phantom, the WEPL of the reconstructed head is roughly correct. In fact, the supposedly bone-like tissues have a WEPL larger than 1, while the cavities, being filled with air, show a WEPL close to zero.

5.7. Remarks and suggestions for future improvements

The results presented in this chapter have strongly demonstrated the experimental feasibility of the HICT at HIT using a gaseous based detector consisting of 61 PPICs interleaved with 3 mm PMMA absorbers. The promising results achieved so far motivate future work regarding the improvement of the experimental set-up, data analysis and image formation in order to achieve better image quality and to make finer details visible in the reconstructed images. In this respect, a brief collection of ideas to improve future set-ups is listed in the following:

- Optimization of the absorber slabs used in the ICs stack in terms of thickness and material, bearing in mind the proposed method to enhance its nominal resolution.
- Design and implementation of a suitable system to dynamically and remotely adapt the range, e.g., by inserting different absorber sheets, to keep the set-up rather compact and yet cover a sufficiently large range.
- Minimization of the dose delivered to the patient during a HICT scan by lowering the number of particles per raster point while maintaining a sustainable signal quality and guaranteeing reliable data acquisition in time.
- Maximization of the time of integration with respect to the time of delivery per raster point to optimize the ratio of detected to delivered beam particles. To this end, two independent sets of electronics could be triggered to alternately (e.g., odd and even channels) record the ICs stacks data.
- Allowance for shorter recording cycles by the trigger to pose a higher upper limit to the possible scan speed.
- Establishment of optimal corresponding settings of Δx and Δy step sizes and foci to possibly minimize the number of data points necessary for a reconstruction with acceptable spatial resolution.

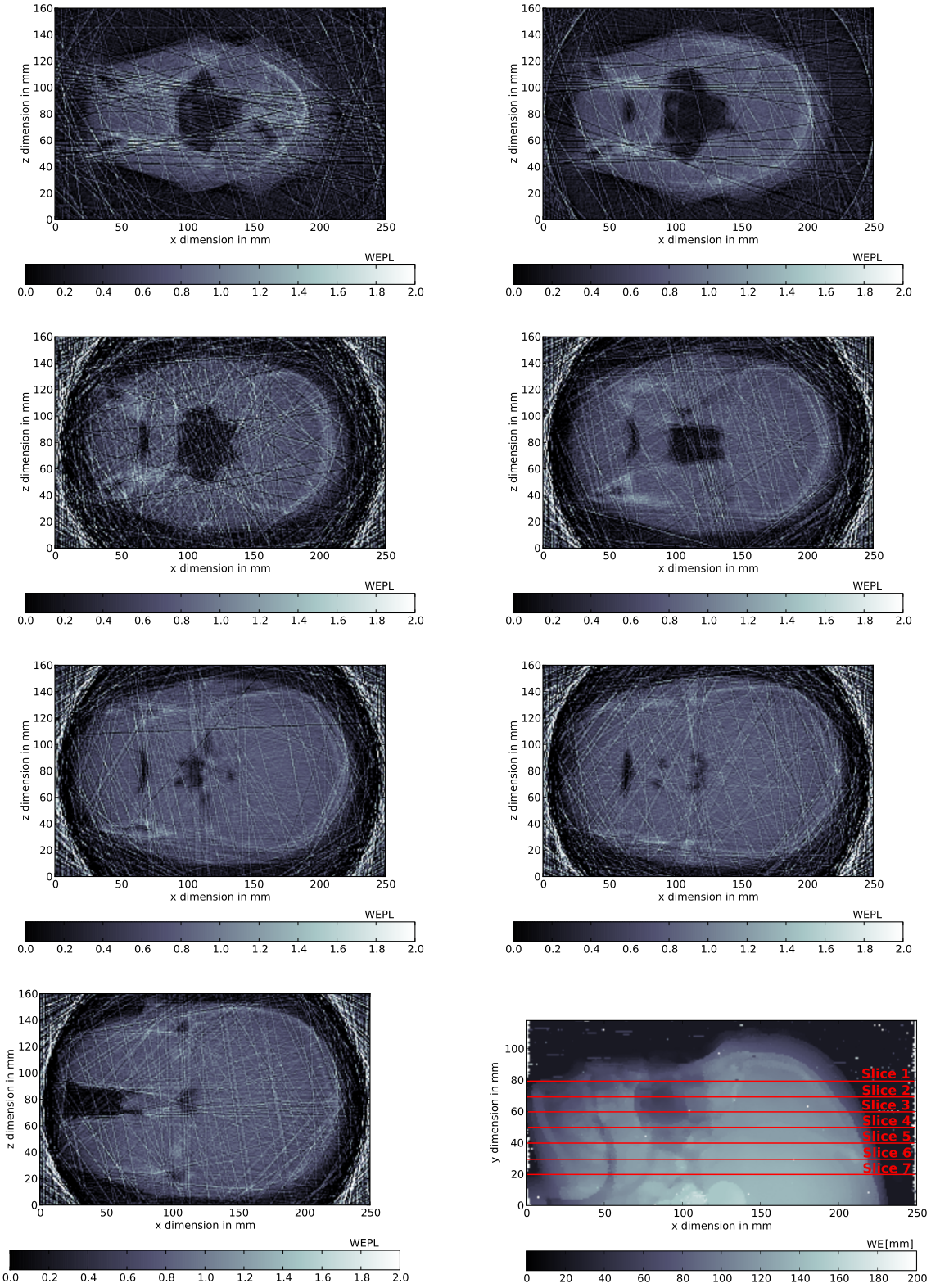

Figure 5.42.: Seven reconstructed slices at 10 mm distance, as shown in the bottom right panel, of the anthropomorphic Alderson head phantom obtained with a ^{12}C beam of 389.36 MeV/u and 3.5 mm FWHM spot size for 160 equi-spaced angles between 0° and 360°. The colorbar indicates WEPL.

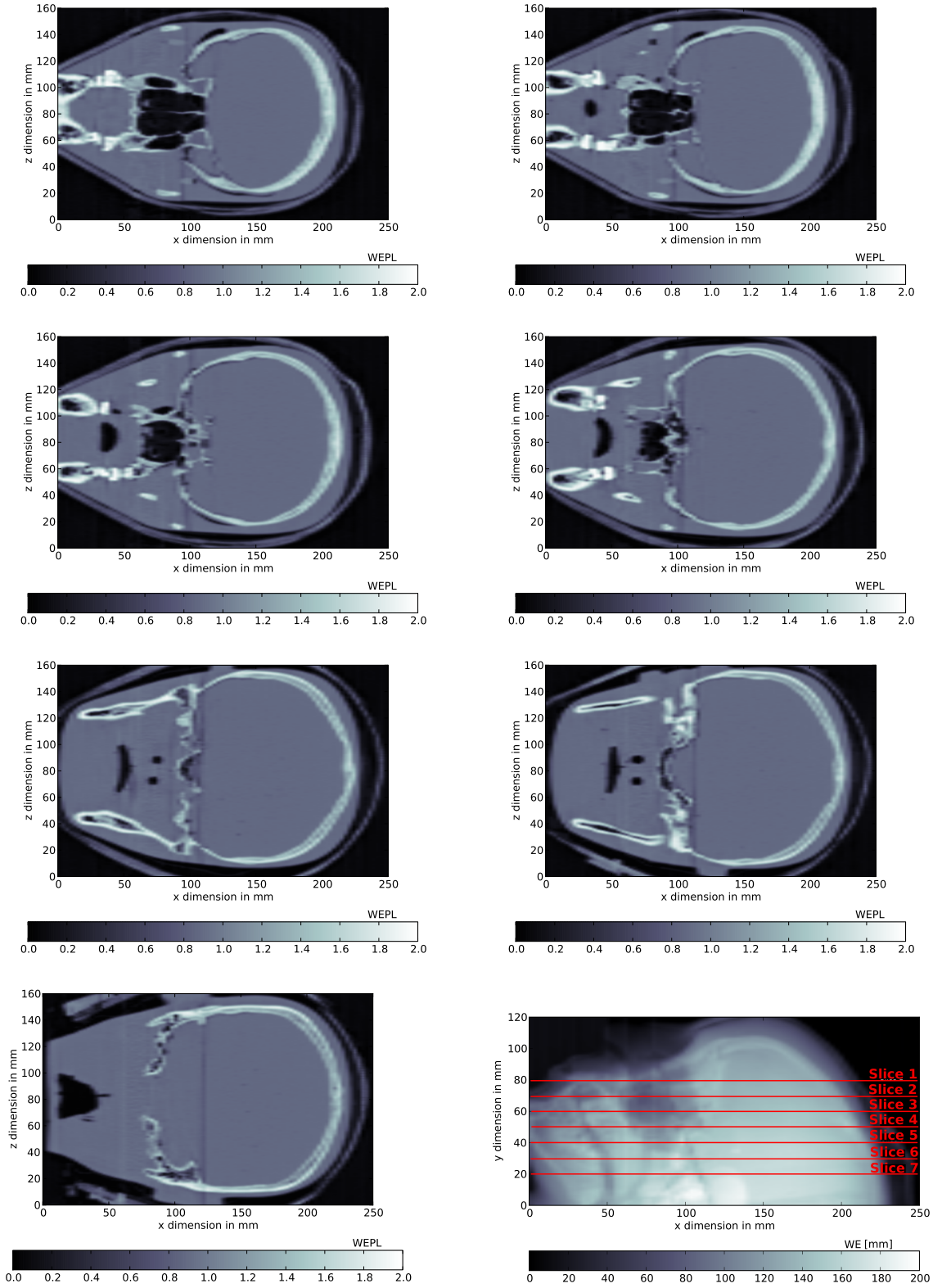

Figure 5.43.: Seven reconstructed slices at 10 mm distance, as shown in the bottom right panel, of the anthropomorphic Alderson head form obtained with an X-ray CT. The colorbar indicates WEPL.

- Implementation of a faster and more automated system of data acquisition.
- Engagement into more detailed studies to find reliable methods for correctly relating the data measured by the ICs stack to the actual target WEPL. This has been shown to be of particular importance at interfaces of high density contrast and involves not only image reconstruction techniques but also more robust methods to precisely detect the Bragg peak position.

Chapter 6

CONCLUSIONS & OUTLOOK

Imaging techniques play an increasingly emerging role for treatment planning and range verification in ion beam therapy. In this thesis, two novel approaches were studied.

The first technique is based on the detection of prompt gammas emerging from the patient, created in the course of nuclear reactions of the beam particles with the target nuclei. After an initial validation of the FLUKA Monte Carlo code for proton beams in Multi Layer Faraday Cups to complement previous extensive validation for carbon ion beams, this technique was investigated especially for protons. In fact, they are expected to be more favorable due to the reduced neutron background. Theoretical studies were performed with the help of the FLUKA code in the framework of the FLUKA collaboration, using a dedicated development version, kindly provided by the FLUKA developer team.

Initially, simulations were done of experiments with carbon ions carried out by groups of Lyon (IPNL and CNDRI-INSA) at the beam facilities at GANIL and GSI, assessing once again the reliability of the FLUKA code and supporting its further use in this thesis. Subsequent theoretical studies focused on the detectability of the prompt gammas in idealized as well as more clinically realistic scenarios. In particular, simulations of an ideal detector response were performed for proton beams impinging on phantoms of different complexity. A correspondence of the gamma depth profile and the Bragg curve was found for sufficient collimation around a detection angle of 90° relative to the beam axis. The gamma profiles could be shown to be sensitive to slight overall density changes as well as local density variations.

In the framework of a scientific international (German, Portugal and Holland) collaboration aiming to develop possible methods for improving the signal-to-noise ratio in future experimental measurements, the time of flight (TOF) spectra of the gammas and of the neutron background were analyzed. The TOF of the gammas was observed to fall in a peak whose width increases with beam energy, i.e., total path length of the beam in the phantom. For phantoms of various complexity, the peak was separable from the neutron continuum, hence encouraging detection methods based on TOF discrimination. Local density variations in the phantom were visible in the TOF spectra as characteristic struc-

tures within the gamma peak due to the varying propagation speed of the gammas in materials of different densities.

As a more clinically relevant case, prompt gammas, revealed in an ideal detector, were simulated for a real treatment plan of a patient head. Two subsets of the plan were considered, one at fixed lateral beam position and varying beam energy, the other at fixed energy and varying the lateral beam position in one dimension. The shape of the gamma depth profiles was found to be correlated to the Bragg curve also in this case of an highly heterogeneous medium. The gamma peak in the TOF spectra was observed to be isolated from the neutron continuum, as in the case of simpler phantoms. It could be demonstrated that the influence of a real beam delivery in comparison to an idealized monoenergetic set-up had an influence on the position of the gamma peak, yet only marginal on the shape. It could be shown that the lateral beam position had almost no impact on the TOF spectrum of the gammas. Finally, a first attempt was made to relate the shape of the gamma depth profile emerging from the patient head to the Bragg peak position based on the gradient of the profile and its minimum. The statistical noise due to the low gamma yield made the use of smoothing algorithms necessary, which might in turn systematically compromise the inferred Bragg peak position. Further studies will be necessary to this regard.

In general, the potential of prompt gammas for localizing the ion range in a target volume could be demonstrated in this thesis. Experimental challenges are mainly related to the low counting statistics of the prompt gamma yield and the related necessity for effective methods to isolate the weak signal from the background radiation. Technical advancements will still be necessary to develop a suitable detector system and bring the prompt gamma approach closer to a clinical stage.

As a second novel imaging technique for low dose 2D and 3D transmission imaging, the Heavy Ion Computed Tomography (HICT) was investigated from an experimental point of view. This was specifically done for carbon ion beams, since their trajectories through a target can be assumed to be in first approximation straight due to their rather small lateral scattering, thus simplifying a lot the reconstruction of their most probable path compared to, e.g., proton based approaches.

An initial study showed that the beam energies available at HIT are sufficiently high to make the Bragg peak fall beyond a typical target volume, such as a patient head, when irradiated with a carbon ion beam. This is required for HICT to minimize the dose delivered to the patient during a scan and to make the detection of the Bragg peak behind the target possible. The promising results of a first proof of principle experiment, for which radiographic film as well as FLUKA MC simulations came to use, motivated the set-up of a new dedicated detector system.

Advantages of revealing the range rather than the residual energy as the earlier is determined only by primary ions while the latter depends on both, primaries and fragmented secondaries, led to the choice of a range telescope as detector. In particular, an Ionization Chambers (IC) stack with 61 chambers was assembled in collaboration with colleagues at GSI and equipped with a fast multi channel electronics module, which was acquired to read-out the ICs stack analog signal. The results of detailed characterization studies underlined the importance of fast data acquisition and triggering to minimize the total scan duration. It was seen that the ICs signal was sufficient for the purpose of image con-

struction even for low count rates underlining the potential of HICT as a low dose imaging technique. On the other hand, the ratio of the number of beam particles seen by the ICs stack and the total number of beam particles delivered to the patient should be optimized by minimizing idle times of the electronics. Since 2D radiographic images are constructed from time series of data points, the reliability of the trigger system even at high scan rates was found to be crucial, as omitted data points will lead to distortions in the composed image.

Two calibrations were done with the dedicated set-up, one to obtain the beam energy dependence of the Bragg peak position revealed in the ICs stack, and the other to relate the detected peak position to the physical target thickness. For the latter, a PMMA wedge was used for the sake of simplicity and since the Water Equivalent Path Length (WEPL) of PMMA is well known from measurements at HIT. Both calibrations can be used to express heavy ion radiographies obtained at any beam energy in terms of water equivalent (WE) target thickness. For future applications, a more precise calibration should be done preferably using a water phantom.

To assess the applicability of the detector system, radiographies were produced for phantoms of different complexity, ranging from a simple massive PMMA cylinder to the Alderson head phantom, and expressed in WE thickness yielding realistic and consistent results. Particular attention was paid to interfaces of high density contrast within the irradiated target. It was shown that they can lead to the superposition of multiple Bragg peaks in the ICs stack and, ultimately, to image defects. More sophisticated methods will be necessary to translate the ICs signal into image information in order to avoid such artifacts.

The thickness of the absorber sheets in the ICs stack determines the nominal resolution of the detector. In the current dedicated set-up, 3 mm PMMA slabs are used. For a single radiography of the Alderson head phantom, the necessary range was measured to be about 90 mm in PMMA, corresponding to 30 channels, while for an entire tomographic scan, up to 50 channels were needed, thus requiring a minimum overall depth of the ICs stack. On the other hand, a fine spatial resolution is desirable for high quality tomographic images calling for thinner absorber sheets. To address this issue, a method was proposed to virtually increase the nominal resolution. In this approach, the position of the real Bragg peak relative to the discrete ICs positions is deduced from the ratio of signals in neighboring channels around the Bragg peak. For the current ICs stack layout, the method is well applicable although future set-ups could intrinsically be improved by optimizing the thickness of the absorber slabs. For simple phantoms, such as a PMMA cylinder and a PMMA wedge, as well as for the more complex Alderson head phantom, the proposed method was shown to deliver radiographies of considerably finer gray value resolution. Nevertheless, the implementation of the method shows still potential for improvement.

As a final proof of principle of HICT, tomographic images were reconstructed based on radiographies (converted to WE thickness) of a cylindric PMMA phantom with small cylindric inserts of different composition and densities, as well as of the Alderson head phantom. This way, the tomographic images directly provided WEPL maps of the target. The latter were also compared to images obtained with a commercial X-ray CT scanner. Although still affected by image noise, the tomographic ion-based images allowed to identify anatomical structures characteristic for the human head.

A detailed list of possible technical improvements has already been presented in sec-

tion 5.7. Generally, the research activities proposed for the future can be divided in 3 directions: Firstly, the data acquisition system, including the electronics and the trigger system, can be improved concerning in particular its speed and reliability. Secondly, the ICs stack should be optimized in terms of total range, compactness, and spatial resolution, also bearing in mind the method proposed in this work to virtually increase the nominal resolution limited by the absorber thickness. The optimized design might imply also the use of more dedicated materials in the composition of the ICs. The outer dimensions of the detector are of peculiar importance if a HICT system shall eventually be integrated in the gantry treatment set-up at HIT. Finally, effort has to be put forward to develop robust algorithms for constructing images out of raw data and for reconstructing adequate tomographic images therefrom.

Summarizing, the results of this thesis strongly support prompt gamma imaging and HICT as very promising imaging modalities with interesting potentialities for future clinical applications to in-vivo range verification on different time scales (i.e., prior to, during, and in-between treatment), thus encouraging further investigations and developments at HIT for proton and ion beams, respectively.

It is expected that eventually the two novel imaging techniques investigated within this thesis will provide valuable information complementary to that from further modalities being currently clinically evaluated (i.e., Positron Emission Tomography, PET) or experimentally investigated (i.e., Interaction Vertex Imaging, IVI), with the final goal to integrate several imaging modalities to reduce range uncertainties and thus provide full clinical exploitation of the physical advantages of ion beams for high precision radiation therapy.

In such a scenario, HICT could be employed to replace or supplement the use of X-ray CT and Hounsfield Unit-WEPL calibration curve in the treatment planning as well as to evaluate the correct patient positioning and to verify the ion range prior to and in-between treatment. Prompt gamma imaging and IVI could serve for real-time in-vivo range monitoring of single pencil beams or isoenergy slices during a treatment. PET could be adopted for tomographic confirmation of the irradiated volume and for dose reconstruction.

BIBLIOGRAPHY

J. Adler Jr., S. Chang, M. Murphy, J. Doty, P. Geis, and S. Hancock. The Cyberknife: A Frameless Robotic System for Radiosurgery. *Stereotact Funct Neurosurg*, 69(1-4): 124–128, 1997. ISSN 1011-6125.

S. Agostinelli et al. G4–a simulation toolkit. *Nuclear Instruments and Methods in Physics Research Section A: Accelerators, Spectrometers, Detectors and Associated Equipment*, 506(3):250–303, July 2003. ISSN 0168-9002.

S. P. Ahlen. Theoretical and experimental aspects of the energy loss of relativistic heavily ionizing particles. *Rev. Mod. Phys.*, 52(1):121–173, Jan 1980.

J. Allison et al. Geant4 developments and applications. *Nuclear Science, IEEE Transactions on*, 53(1):270 –278, feb. 2006. ISSN 0018-9499.

D. Barkas, W.H. & Evans. *Nuclear research emulsions.* 1963.

G. Battistoni, F. Cerutti, A. Fasso, A. Ferrari, S. Muraro, J. Ranft, S. Roesler, and P. R. Sala. The FLUKA code: description and benchmarking. *AIP Conference Proceedings*, 896(1):31–49, 2007.

G. Battistoni et al. The FLUKA code and its use in hadron therapy. *Nuovo Cimento C Geophysics Space Physics C*, 31:69–75, Jan. 2008.

H. A. Bethe, M. E. Rose, and L. P. Smith. The Multiple Scattering of Electrons. *Proceedings of the American Philosophical Society*, 78(4):pp. 573–585, 1938. ISSN 0003049X.

A. Biegun, P. Cambraia Lopes, P. Dendooven, D. Oxley, M. Parodi, K. Pinto, I. Rinaldi, F. Verhaegen, E. Seravalli, D. Schaart, and P. Crespo. Prompt gammas - physics capabilities for monitoring range and density variations during proton therapy. *to be submitted*, 2011.

F. Bloch. Bremsvermögen von Atomen mit mehreren Elektronen. *Zeitschrift für Physik A Hadrons and Nuclei*, 81:363–376, 1933. ISSN 0939-7922. 10.1007/BF01344553.

T. Böhlen, F. Cerutti, M. Dosanjh, A. Ferrari, I. Gudowska, A. Mairani, and J. Quesada. Benchmarking nuclear models of FLUKA and GEANT4 for carbon ion therapy. *Physics in Medicine and Biology*, 55(19):5833, 2010.

N. Bohr. On the Constitution of Atoms and Molecules. *Phil. Mag.*, 26, 1913.

T. Bortfeld. The number of beams in IMRT - theoretical investigations and implications for single-arc IMRT. *Physics in Medicine and Biology*, 55(1):83, 2010.

T. Bortfeld and S. Webb. Single-Arc IMRT? *Physics in Medicine and Biology*, 54(1):N9, 2009.

W. Bragg and R. Kleeman. On the alpha particles of radium and their loss of range in passing through various atoms and molecules. *Philos. Mag*, 10:318, 1905.

B. Braunn, M. Labalme, G. Ban, D. Cussol, J. Fontbonne, F. Lecolley, C. Pautard, F. Haas, D. Lebhertz, M. Rousseau, L. Stuttge, M. Chevallier, D. Dauvergne, F. Le Foulher, C. Ray, E. Testa, M. Testa, and M. Salsac. ^{12}C nuclear reaction measurements for hadrontherapy. In A. F. F. Cerutti, editor, *Proceedings of the 12th International Conference on Nuclear Reaction Mechanisms 12th International Conference on Nuclear Reaction Mechanisms*, volume Vol. 2, pages 531–537, Varenna Italy, 2010. Cern.

C. Brusasco. *A detector system for the verification of three-dimensional dose distributions in the tumor therapy with heavy ions*. PhD thesis, Universität Kassel, 1999.

C. Brusasco, B. Voss, D. Schardt, M. Krämer, and G. Kraft. A dosimetry system for fast measurement of 3D depth-dose profiles in charged-particle tumor therapy with scanning techniques. *Nuclear Instruments and Methods in Physics Research Section B: Beam Interactions with Materials and Atoms*, 168(4):578–592, Aug. 2000. ISSN 0168-583X.

S. V. Bulanov, H. Daido, T. Z. Esirkepov, V. S. Khoroshkov, J. Koga, K. Nishihara, F. Pegoraro, T. Tajima, and M. Yamagiwa. Feasibility of Using Laser Ion Accelerators in Proton Therapy. *AIP Conference Proceedings*, 740(1):414–429, 2004.

S. Cameron, I. Grant, W. Lutz, and J. Pearson. The early effect of irradiation on ventilatory function in bronchial carcinoma, Jan. 1969. ISSN 0009-9260.

A. K. Carlsson, P. Andreo, and A. Brahme. Monte Carlo and analytical calculation of proton pencil beams for computerized treatment plan optimization. *Phys Med Biol*, 42 (6):1033–53–, June 1997.

M. Cavinato, E. Fabrici, E. Gadioli, E. Gadioli Erba, and E. Risi. Boltzmann master equation theory of angular distributions in heavy-ion reactions. *Nuclear Physics A*, 643 (1):15 – 29, 1998. ISSN 0375-9474.

M. Cavinato, E. Fabrici, G. E., E. Gadioli Erba, and G. Riva. Monte Carlo calculations of heavy ion cross-sections based on the Boltzmann Master equation theory. *Nuclear Physics A*, 679(3-4):753 – 764, 2001. ISSN 0375-9474.

F. Cerutti, G. Battistoni, G. Capezzali, P. Colleoni, A. Ferrari, E. Gadioli, A. Mairani, and A. Pepe. Low Energy Nucleus-Nucleus Reactions: The BME Approach and its Interface with FLUKA. *Ric. Sci. Educ. Perm., Suppl.*, 126:507–514, 2006.

A. M. Cormack and A. M. Koehler. Quantitative proton tomography: preliminary experiments. *Physics in Medicine and Biology*, 21(4):560, 1976.

P. Crespo, G. Shakirin, and W. Enghardt. On the detector arrangement for in-beam PET for hadron therapy monitoring. *Physics in Medicine and Biology*, 51(9):2143, 2006.

P. Crespo, G. Shakirin, F. Fiedler, W. Enghardt, and A. Wagner. Direct time-of-flight for quantitative, real-time in-beam PET: a concept and feasibility study. *Physics in Medicine and Biology*, 52(23):6795, 2007.

D. Dauvergne, M. Battaglia, G. Montarou, and E. Testa. New methods of real-time control imaging for ion therapy. 2009.

S. R. Deans. *The Radon Transform and Some of Its Applications.* Krieger Publishing Company, 1983.

A. V. Dementyev and N. M. Sobolevsky. SHIELD - universal Monte Carlo hadron transport code: scope and applications. *Radiat. Meas.*, 30(5):553–557, 1999.

J. W. Denham and M. Hauer-Jensen. The radiotherapeutic injury - a complex "wound". *Radiother Oncol*, 63(2):129–145, May 2002. ISSN 0167-8140.

M. Durante and J. S. Löffler. Charged particles in radiation oncology. *Nat Rev Clin Oncol*, 7(1):37–43, Jan. 2010. ISSN 1759-4774.

W. Enghardt. *In-beam PET for ion therapy monitoring (Positronen-Emissions-Tomographie für die Qualitätssicherung der Ionenstrahl-Therapie von Tumoren).* PhD thesis, Habilitation Thesis, Dresden, University of Technology, 2005.

W. Enghardt, W. D. Fromm, H. Geissel, H. Heller, G. Kraft, A. Magel, P. Manfrass, G. Munzenberg, F. Nickel, J. Pawelke, D. Schardt, C. Scheidenberger, and M. Sobiella. The spatial distribution of positron-emitting nuclei generated by relativistic light ion beams in organic matter. *Physics in Medicine and Biology*, 37(11):2127, 1992.

W. Enghardt, J. Debus, T. Haberer, B. Hasch, R. Hinz, O. Jäkel, M. Krämer, K. Lauckner, J. Pawelke, and F. Pönisch. Positron emission tomography for quality assurance of cancer therapy with light ion beams. *Nuclear Physics A*, 654(1, Supplement 1):1047c – 1050c, 1999. ISSN 0375-9474.

W. Enghardt, P. Crespo, F. Fiedler, R. Hinz, K. Parodi, J. Pawelke, and F. Pönisch. Charged hadron tumour therapy monitoring by means of PET. *Nuclear Instruments and Methods in Physics Research, Section A: Accelerators, Spectrometers, Detectors and Associated Equipment*, 525(1-2):284–288, 2004a.

W. Enghardt, K. Parodi, P. Crespo, F. Fiedler, J. Pawelke, and F. Pönisch. Dose quantification from in-beam positron emission tomography. *Radiotherapy and Oncology*, 73 (Supplement 2):S96 – S98, 2004b. ISSN 0167-8140. Carbon-Ion Theraphy.

M. Epherre and E. Gradsztajn. *J. de Phys.*, 28:48, 1967.

A. Fassò, A. Ferrari, J. Ranft, and P. Sala. New developments in FLUKA modelling of hadronic and EM interactions. In *Proceedings of 3rd Workshop on Simulating Accelerator Radiation Environment, KEK, Tsukuba, Japan*, 1997.

E. Fermi. High Energy. *Nuclear Events Prog. Theor. Phys.*, 5:1570, 1950.

A. Ferrari and P. R. Sala. The Physics of High Energy Reactions. Technical Report ATL-PHYS-97-113. ATL-GE-PN-113, CERN, Geneva, Sep 1997.

A. Ferrari, P. Sala, R. Guaraldi, and F. Padoani. An improved multiple scattering model for charged particle transport. *Nuclear Instruments and Methods in Physics Research Section B: Beam Interactions with Materials and Atoms*, 71(4):412 – 426, 1992. ISSN 0168-583X.

A. Ferrari, J. Ranft, S. Roesler, and P. Sala. Cascade particles, nuclear evaporation, and residual nuclei in high energy hadron-nucleus interactions. *Zeitschrift für Physik C Particles and Fields*, 70:413–426, 1996a.

A. Ferrari, J. Ranft, S. Roesler, and P. Sala. The production of residual nuclei in peripheral high energy nucleus-nucleus interactions. *Zeitschrift für Physik C Particles and Fields*, 71:75–86, 1996b. ISSN 0170-9739. 10.1007/s002880050149.

A. Ferrari, P. R. Sala, A. Fassò, and J. Ranft. *FLUKA: A multi-particle transport code (program version 2005).* CERN, Geneva, 2005.

F. Fiedler, G. Shakirin, J. Skowron, H. Braess, P. Crespo, D. Kunath, J. Pawelke, F. Pönisch, and W. Enghardt. On the effectiveness of ion range determination from in-beam PET data. *Physics in Medicine and Biology*, 55(7):1989, 2010.

E. Fokas, G. Kraft, H. An, and R. Engenhart-Cabillic. Ion beam radiobiology and cancer: Time to update ourselves. *Biochimica et Biophysica Acta (BBA) - Reviews on Cancer*, 1796(2):216–229, Dec. 2009. ISSN 0304-419X.

E. Gadioli and P. Hodgson. *Pre-equilibrium Nuclear Reactions.* 1992.

O. Geiß, D. Schardt, B. Voss, M. Krämer, and G. Kraft. Correlation between CT number and water equivalent thickness. *GSI Scientific Report*, Hrsg.: GSI, Darmstadt; 1998: 133, 1997.

B. Gottschalk, R. Platais, and H. Paganetti. Nuclear interactions of 160 MeV protons stopping in copper: A test of Monte Carlo nuclear models. *Medical Physics*, 26(12): 2597–2601, 1999.

J. J. Griffin. Statistical Model of Intermediate Structure. *Phys. Rev. Lett.*, 19(1):57, Jul 1967.

I. Gudowska, N. Sobolevsky, P. Andreo, D. Belkic, and A. Brahme. Ion beam transport in tissue-like media using the Monte Carlo code SHIELD-HIT. *Physics in Medicine and Biology*, 49(10):1933, 2004.

K. Gunzert-Marx, D. Schardt, R. Simon, F. Gutermuth, T. Radon, V. Dangendorf, and R. Nolte. Response of a BaF_2 scintillation detector to quasi-monoenergetic fast neutrons in the range of 45 to 198 MeV. *Nuclear Instruments and Methods in Physics Research Section A: Accelerators, Spectrometers, Detectors and Associated Equipment*, 536(1-2): 146–153, Jan. 2005. ISSN 0168-9002.

K. Gunzert-Marx, H. Iwase, D. Schardt, and R. S. Simon. Secondary beam fragments produced by 200 MeV/u ^{12}C ions in water and their dose contributions in carbon ion radiotherapy. *New Journal of Physics*, 10(7):075003, 2008.

T. Haberer, W. Becher, D. Schardt, and G. Kraft. Magnetic scanning system for heavy ion therapy. *Nuclear Instruments and Methods in Physics Research Section A: Accelerators, Spectrometers, Detectors and Associated Equipment*, 330(1-2):296–305, June 1993. ISSN 0168-9002.

T. Haberer, J. Debus, H. Eickhoff, O. Jäkel, D. Schulz-Ertner, and U. Weber. The Heidelberg Ion Therapy Center. *Radiother Oncol*, 73:S186–S190, Dec. 2004. ISSN 0167-8140.

E. Haettner, H. Iwase, and D. Schardt. Experimental fragmentation studies with ^{12}C therapy beams. *Radiation Protection Dosimetry*, 122(1-4):485–487, December 2006.

K. Hanson, J. Bradbury, T. Cannon, R. Hutson, D. Laubacher, R. Macek, M. Paciotti, , and C. Taylor. Computed tomography using proton energy loss. *Phys. Med. Biol.*, 26: 965–983, 1981.

K. Hanson, J. Bradbury, R. Koeppe, R. Macek, D. Machen, R. Morgado, M. Paciotti, S. Sandford, and V. Steward. Proton computed tomography of human specimens. *Phys. Med. Biol.*, 27:25–36, 1982.

K. Henkner, N. Sobolevsky, O. Jäkel, and H. Paganetti. Test of the nuclear interaction model in SHIELD-HIT and comparison to energy distributions from GEANT4. *Physics in Medicine and Biology*, 54(22):N509, 2009.

P. Henriquet. *Etude de l'emission de particules chragées secondaires dans l'optique d'une dosimetrie en ligne en hadrontherapie*. PhD thesis, Institut de physique nucléaire de Lyon Université Claude Bernard Lyon 1, 2010.

V. Highland. Some practical remarks on multiple scattering. *Nuclear Instruments and Methods*, 129(2):497–499, 1975.

Y. Hirao. Results from HIMAC and other therapy facilities in Japan. *AIP Conference Proceedings*, 600(1):8–12, 2001.

J. Hüfner. Heavy fragments produced in proton-nucleus and nucleus-nucleus collisions at relativistic energies. *Physics Reports*, 125:129–185, Aug. 1985.

G. Hughes, K. J. Adams, M. B. Chadwick, J. C. Comly, S. C. Frankle, J. S. Hendricks, R. C. Little, R. E. Prael, L. S. Waters, and P. G. J. Young. MCNPXTM - The LAHETTM/MCNPTM code merger. *Proc. 3rd Workshop on Simulating Accelerator Radiation Environments (SARE 3) (Tsukuba, Japan, 7-9 May): KEK Proceedings (June 1997)*, pages 44–51, 1997.

ICRU. *Nuclear Data for Neutron and Proton Radiotherapy and for Radiation Protection.* ICRU Report N. 63, 2000.

O. Jäkel and P. Reiss. The influence of metal artefacts on the range of ion beams. *Physics in Medicine and Biology*, 52(3):635, 2007.

O. Jäkel, C. Jacob, D. Schardt, C. P. Karger, and G. H. Hartmann. Relation between carbon ion ranges and x-ray CT numbers. *Medical Physics*, 28:701–703, Apr. 2001.

T. H. James and C. E. K. Mees. *The Theory of the photographic process.* Macmillan (New York), 1977.

C. Jarlskog and H. Paganetti. Physics Settings for Using the Geant4 Toolkit in Proton Therapy. In *Nuclear Science, IEEE Transactions on, vol.55, no.3, pp.1018-1025*, 2008.

C. Kleffner, D. Ondreka, and U. Weinrich. The Heidelberg Ion Therapy (HIT) Accelerator Coming into Operation. In *Conference. AIP Conference Proceedings, Volume 1099, pp. 426-428*, 2009.

A.-C. Knopf, K. Parodi, H. Paganetti, T. Bortfeld, J. Daartz, M. Engelsman, N. Liebsch, and H. Shih. Accuracy of Proton Beam Range Verification Using Post-Treatment Positron Emission Tomography/Computed Tomography as Function of Treatment Site. *International Journal of Radiation Oncology*Biology*Physics*, 79(1):297–304, Jan. 2011. ISSN 0360-3016.

A. Koehler and V. Steward. Proton radiographic detection of strokes. *Nature*, 245:38–40, 1974.

A. M. Koehler. Proton Radiography. *Science*, 160:303–304, 1968.

G. Kraft. Tumor therapy with heavy charged particles. *Progress in Particle and Nuclear Physics*, 45(Supplement 2):S473 – S544, 2000. ISSN 0146-6410.

M. Krämer and G. Kraft. Calculations of heavy-ion track structure. *Radiation and Environmental Biophysics*, 33(2):91–109, 1994. ISSN 0301-634X.

M. Krämer and M. Scholz. Treatment planning for heavy-ion radiotherapy: calculation and optimization of biologically effective dose. *Physics in Medicine and Biology*, 45(11): 3319, 2000.

M. Krämer, O. Jäkel, T. Haberer, G. Kraft, D. Schardt, and U. Weber. Treatment planning for heavy-ion radiotherapy: physical beam model and dose optimization. *Physics in Medicine and Biology*, 45(11):3299, 2000.

M. Krämer, W. K. Weyrather, and M. Scholz. The increased biological effectiveness of heavy charged particles: from radiobiology to treatment planning. *Technol Cancer Res Treat*, 2(5):427–36, Oct. 2003. ISSN 1533-0346.

LANL. MCNPX User's Manual. *Version 2.4.0*, 2002.

F. Le Foulher, M. Bajard, M. Chevallier, D. Dauvergne, N. Freud, P. Henriquet, S. Karkar, J. Letang, L. Lestand, R. Plescak, C. Ray, D. Schardt, E. Testa, and M. Testa. Monte Carlo Simulations of Prompt-Gamma Emission During Carbon Ion Irradiation. *Nuclear Science, IEEE Transactions on*, 57(5):2768 –2772, oct. 2010. ISSN 0018-9499.

W. Leo. *Techniques for Nuclear and Particle Physics Experiments*. 1987.

X. A. Li, C. Stepaniak, and E. Gore. Technical and dosimetric aspects of respiratory gating using a pressure-sensor motion monitoring system. *Medical Physics*, 33(1):145–154, 2006.

T. R. Mackie, J. Balog, K. Ruchala, D. Shepard, S. Aldridge, E. Fitchard, P. Reckwerdt, G. Olivera, T. McNutt, and M. Mehta. Tomotherapy. *Semin Radiat Oncol*, 9(1):108–117, Jan. 1999. ISSN 1053-4296.

M. Maggiore, L. Calabretta, D. Campo, L. Piazza, and D. Rifuggiato. Design studies of the 300 AMeV superconducting cyclotron for hadrontherapy. In *Particle Accelerator Conference, 2007. PAC. IEEE*, pages 2748 –2750, 2007.

A. Mairani. *Nucleus-Nucleus Interaction Modelling and its Impact on Treatment Planning in Ion Therapy-Physical and Biological Aspects*. PhD thesis, University of Pavia, 2008.

A. Mairani, K. Parodi, S. Brons, F. Cerutti, A. Ferrari, E. Gadioli, M. Scholz, and F. Sommerer. Clinical calculations of physical and biological effective dose distributions in proton and carbon ion therapy using the FLUKA Monte Carlo code. In *Nuclear Science Symposium Conference Record, 2008. NSS '08. IEEE*, 2008.

A. Mairani, S. Brons, F. Cerutti, A. Fassó, A. Ferrari, M. Krämer, K. Parodi, M. Scholz, and F. Sommerer. The FLUKA Monte Carlo code coupled with the local effect model for biological calculations in carbon ion therapy. *Physics in Medicine and Biology*, 55 (15):4273, 2010.

A. Mascia, J. DeMarco, P. Chow, and T. Solberg. Benchmarking the MCNPX nuclear interaction models for use in the proton therapy energy range. In *XIVth ICCR*, 2004.

J. Medin and P. Andreo. Monte Carlo calculated stopping-power ratios, water/air, for clinical proton dosimetry (50 - 250 MeV). *Physics in Medicine and Biology*, 42(1):89, 1997.

C.-H. Min, C. H. Kim, M.-Y. Youn, and J.-W. Kim. Prompt gamma measurements for locating the dose falloff region in the proton therapy. *Applied Physics Letters*, 89(18): 183517, 2006.

K. Niita, T. Sato, H. Iwase, H. Nose, H. Nakashima, and L. Sihver. PHITS–a particle and heavy ion transport code system. *Radiation Measurements*, 41(9-10):1080–1090, Oct. 2006. ISSN 1350-4487.

Y. Ohno, T. Kohno, N. Matsufuji, and T. Kanai. Measurement of electron density distribution using heavy ion CT. *Nuclear Instruments and Methods in Physics Research Section A: Accelerators, Spectrometers, Detectors and Associated Equipment*, 525(1-2): 279 – 283, 2004. ISSN 0168-9002. Proceedings of the International Conference on Imaging Techniques in Subatomic Physics, Astrophysics, Medicine, Biology and Industry.

H. Paganetti. Nuclear interactions in proton therapy: dose and relative biological effect distributions originating from primary and secondary particles. *Physics in Medicine and Biology*, 47(5):747, 2002.

H. Paganetti and B. Gottschalk. Test of GEANT3 and GEANT4 nuclear models for 160 MeV protons stopping in CH_2. *Med Phys*, 30(7):1926–31–, July 2003.

H. Paganetti, A. Niemierko, M. Ancukiewicz, L. E. Gerweck, M. Goitein, J. S. Loeffler, and H. D. Suit. Relative biological effectiveness (RBE) values for proton beam therapy. *Int J Radiat Oncol Biol Phys*, 53(2):407–421, June 2002. ISSN 0360-3016.

K. Parodi. *On the feasibility of dose quantification with in-beam PET data in radiotherapy with ^{12}C and proton beams*. PhD thesis, Technische Universität Dresden, Germany, 2004.

K. Parodi. *Positron-Emission-Tomography for in-vivo verification of ion beam therapy - Modelling, experimental studies and clinical implementation*. PhD thesis, Habilitationsschrift zur Erlangung der Venia legendi für das Fach Physik der Ruprecht-Karls Universität Heidelberg, 2008.

K. Parodi and W. Enghardt. Potential application of PET in quality assurance of proton therapy. *Physics in Medicine and Biology*, 45(11):N151, 2000.

K. Parodi, W. Enghardt, and T. Haberer. In-beam PET measurements of $\beta+$ radioactivity induced by proton beams. *Physics in Medicine and Biology*, 47(1):21, 2002.

K. Parodi, P. Crespo, H. Eickhoff, T. Haberer, J. Pawelke, D. Schardt, and W. Enghardt. Random coincidences during in-beam PET measurements at microbunched therapeutic ion beams. *Nuclear Instruments and Methods in Physics Research Section A: Accelerators, Spectrometers, Detectors and Associated Equipment*, 545(1-2):446 – 458, 2005. ISSN 0168-9002.

K. Parodi, A. Ferrari, F. Sommerer, and H. Paganetti. Clinical CT-based calculations of dose and positron emitter distributions in proton therapy using the FLUKA Monte Carlo code. *Phys Med Biol*, 52(12):3369–87–, June 2007.

K. Parodi, T. Bortfeld, W. Enghardt, F. Fiedler, A. Knopf, H. Paganetti, J. Pawelke, G. Shakirin, and H. Shih. PET imaging for treatment verification of ion therapy: Implementation and experience at GSI Darmstadt and MGH Boston. *Nuclear Instruments and Methods in Physics Research Section A: Accelerators, Spectrometers, Detectors and Associated Equipment*, 591(1):282 – 286, 2008. ISSN 0168-9002. Radiation Imaging Detectors 2007 - Proceedings of the 9th International Workshop on Radiation Imaging Detectors.

K. Parodi, S. Brons, F. Cerutti, A. Ferrari, A. Mairani, H. Paganetti, and F. Sommerer. The FLUKA code for application of Monte Carlo methods to promote high precision ion beam therapy. In *Proceeding 12th International Conference on Nuclear Reaction Mechanisms, Varenna, Italy*, 2009.

K. Parodi, A. Mairani, S. Brons, J. Naumann, M. Krämer, F. Sommerer, and T. Haberer. The influence of lateral beam profile modifications in scanned proton and carbon ion therapy: a Monte Carlo study. *Physics in Medicine and Biology*, 55(17):5169, 2010.

E. Pedroni, R. Bacher, H. Blattmann, T. Böhringer, A. Coray, A. Lomax, S. Lin, G. Munkel, S. Scheib, U. Schneider, and A. Tourovsky. The 200-MeV proton therapy project at the Paul Scherrer Institute: Conceptual design and practical realization. *Medical Physics*, 22:37–53, Jan. 1995.

P. Pemler, J. Besserer, J. de Boer, M. Dellert, C. Gahn, M. Moosburger, U. Schneider, E. Pedroni, and H. Stäuble. A detector system for proton radiography on the gantry of the Paul-Scherrer-Institute. *Nuclear Instruments and Methods in Physics Research Section A: Accelerators, Spectrometers, Detectors and Associated Equipment*, 432(2-3): 483 – 495, 1999. ISSN 0168-9002.

J. C. Polf, S. Peterson, G. Ciangaru, M. Gillin, and S. Beddar. Measurement and calculation of characteristic prompt gamma ray spectra emitted during proton irradiation. *Physics in Medicine and Biology*, 54(22):N519, 2009a.

J. C. Polf, S. Peterson, G. Ciangaru, M. Gillin, and S. Beddar. Prompt gamma-ray emission from biological tissues during proton irradiation: a preliminary study. *Physics in Medicine and Biology*, 54(3):731, 2009b.

B. Poole, D. Blackfield, and S. Nelson. Particle simulations of a linear dielectric wall proton accelerator. In *Particle Accelerator Conference, 2007. PAC. IEEE*, pages 1790 –1792, 2007.

S. Reinhard W., B. Vladimir, K. Márgio, C. Loss, L. Tianfang, W. Andrew J., E. Ivan, W. David C., and S. Todd. Density resolution of proton computed tomography. 32(4): 1035–1046, 2005. ISSN 00942405.

T. Renner and W. Chu. Wobbler facility for biomedical experiments. *Medical Physics*, 14 (5):825–834, 1987.

T. R. Renner, W. Chu, J. Halliwell, B. Ludewigt, M. Nyman, R. P. Singh, G. D. Stover, and R. Stradtner. Preliminary Results of a Raster Scanning Beam Delivery System. In *1989 IEEE Particle Accelerator Conference*, 1989.

E. Rietzel, D. Schardt, and T. Haberer. Range accuracy in carbon ion treatment planning based on CT-calibration with real tissue samples. *Radiation Oncology*, 2(1):14, 2007. ISSN 1748-717X.

I. Rinaldi, A. Ferrari, O. Jäkel, A. Mairani, and K. Parodi. Novel imaging and quality assurance techniques for ion beam therapy: a Monte Carlo study. *Proceedings 12th International Conference on Nuclear Reaction Mechanisms, Villa Monastero, Varenna, Italy, 15 - 19 Jun 2009*, pages 575–580, 2010.

I. Rinaldi, A. Ferrari, A. Mairani, H. Paganetti, K. Parodi, and P. Sala. An integral test of FLUKA nuclear models with 160 MeV proton beams in multi-layer Faraday cups. *Physics in Medicine and Biology*, 56(13):4001, 2011.

B. Schaffner and E. Pedroni. The precision of proton range calculations in proton radiotherapy treatment planning: experimental verification of the relation between CT-HU and proton stopping power. *Physics in Medicine and Biology*, 43(6):1579, 1998.

D. Schardt, P. Steidl, M. Krämer, U. Weber, K. Parodi, and S. Brons. Precision Bragg-curve measurements for light-ion beams in wate. *GSI-Report 2008-1 (GSI Scientific Report 2007)*, page 373, 2007.

D. Schardt, T. Elsässer, and D. Schulz-Ertner. Heavy-ion tumor therapy: Physical and radiobiological benefits. *Rev. Mod. Phys.*, 82(1):383–425, Feb 2010.

U. Schneider and E. Pedroni. Proton radiography as a tool for quality control in proton therapy. *Medical Physics*, 22(4):353–363, 1995.

U. Schneider, E. Pedroni, and A. Lomax. The calibration of CT Hounsfield units for radiotherapy treatment planning. *Physics in Medicine and Biology*, 41(1):111, 1996.

U. Schneider, J. Besserer, P. Pemler, M. Dellert, M. Moosburger, E. Pedroni, and B. Kaser-Hotz. First proton radiography of an animal patient. *Medical Physics*, 31(5):1046–1051, 2004.

U. Schneider, P. Pemler, J. Besserer, E. Pedroni, A. Lomax, and B. Kaser-Hotz. Patient specific optimization of the relation between CT-Hounsfield units and proton stopping power with proton radiography. *Medical Physics*, 32(1):195–199, 2005.

M. Scholz and T. Elsässer. Biophysical models in ion beam radiotherapy. *Advances in Space Research*, 40(9):1381 – 1391, 2007. ISSN 0273-1177.

M. Scholz and G. Kraft. Calculation of Heavy Ion Inactivation Probabilities Based on Track Structure, X Ray Sensitivity and Target Size. *Radiation Protection Dosimetry*, 52(1-4):29–33, Apr. 1994.

R. Schulte, V. Bashkirov, T. Li, Z. Liang, K. Mueller, J. Heimann, L. Johnson, B. Keeney, H.-W. Sadrozinski, A. Seiden, D. Williams, L. Zhang, Z. Li, S. Peggs, T. Satogata, and C. Woody. Conceptual design of a proton computed tomography system for applications in proton radiation therapy. *IEEE Trans. Nucl. Sci.*, 51:866–872, 2004.

D. Schulz-Ertner, C. P. Karger, A. Feuerhake, A. Nikoghosyan, S. E. Combs, O. Jäkel, L. Edler, M. Scholz, and J. Debus. Effectiveness of Carbon Ion Radiotherapy in the Treatment of Skull-Base Chordomas. *International Journal of Radiation Oncology*Biology*Physics*, 68(2):449 – 457, 2007. ISSN 0360-3016.

H. Schwoerer, S. Pfotenhauer, O. Jackel, K.-U. Amthor, B. Liesfeld, W. Ziegler, R. Sauerbrey, K. W. D. Ledingham, and T. Esirkepov. Laser-plasma acceleration of quasi-monoenergetic protons from microstructured targets. *Nature*, 439(7075):445–448, Jan. 2006. ISSN 0028-0836.

R. Serber. Nuclear Reactions at High Energies. *Phys. Rev.*, 72(11):1114–1115, Dec 1947.

H. Shinoda, T. Kanai, and T. Kohno. Application of heavy-ion CT. *Physics in Medicine and Biology*, 51(16):4073, 2006.

F. Sommerer, K. Parodi, A. Ferrari, K. Poljanc, W. Enghardt, and H. Aiginger. Investigating the accuracy of the FLUKA code for transport of therapeutic ion beams in matter. *Physics in Medicine and Biology*, 51(17):4385, 2006.

F. Sommerer, F. Cerutti, K. Parodi, A. Ferrari, W. Enghardt, and H. Aiginger. In-beam PET monitoring of mono-energetic ^{16}O and ^{12}C beams: experiments and FLUKA simulations for homogeneous targets. *Physics in Medicine and Biology*, 54(13):3979, 2009.

B. Spielberger, M. Scholz, M. Krämer, and G. Kraft. Experimental investigations of the response of films to heavy-ion irradiation. *Physics in Medicine and Biology*, 46(11):2889, 2001.

B. Spielberger, M. Scholz, M. Krämer, and G. Kraft. Calculation of the x-ray film response to heavy charged particle irradiation. *Physics in Medicine and Biology*, 47(22):4107, 2002.

E. Testa, M. Bajard, M. Chevallier, D. Dauvergne, F. L. Foulher, N. Freud, J.-M. Letang, J.-C. Poizat, C. Ray, and M. Testa. Monitoring the Bragg peak location of 73 MeV/u carbon ions by means of prompt gamma-ray measurements. *Applied Physics Letters*, 93 (9):093506, 2008.

E. Testa, M. Bajard, M. Chevallier, D. Dauvergne, F. L. Foulher, N. Freud, J. Létang, J. Poizat, C. Ray, and M. Testa. Dose profile monitoring with carbon ions by means of prompt-gamma measurements. *Nuclear Instruments and Methods in Physics Research Section B: Beam Interactions with Materials and Atoms*, 267(6):993 – 996, 2009. ISSN 0168-583X. Proceedings of the Seventh International Symposium on Swift Heavy Ions in Matter.

M. Testa, M. Bajard, M. Chevallier, D. Dauvergne, N. Freud, P. Henriquet, S. Karkar, F. Le Foulher, J. Létang, R. Plescak, C. Ray, M.-H. Richard, D. Schardt, and E. Testa. Real-time monitoring of the Bragg-peak position in ion therapy by means of single photon detection. *Radiation and Environmental Biophysics*, 49:337–343, 2010. ISSN 0301-634X. 10.1007/s00411-010-0276-2.

C. Tobias. Pituitary Irradiation with High-Energy Proton Beams A Prelimanry report. *Cancer Research*, 18(2):121, 1958.

B. Voss, A. Heinz, and H. Risch. Beam Monitors for the High-Energy Beam Line of HIT. *GSI Scientific Report 2005*, GSI Report 2006-1:402, 2005.

B. Voss, M. Henske, A. Heinz, H. Junk, and H. Risch. Fast measurements of single Bragg peaks with an active multi-plane phantom. *GSI Scientific Report*, GSI Report 2007-1: 379, 2006.

B. Voss, L. Doignie, A. Heinz, and H. Risch. First measurements with a homogeneous GEM-foil detector with therapeutic beams. *GSI Scientific report 2006*, Volume GSI 2007-1:380, 2007.

B. Voss, I. Rinaldi, S. Brons, O. Jäkel, R. Panse, and K. Parodi. Heavy-Ion Computed Tomography applying a stack of ionization chambers. *GSI Scientific Report 2010*, Volume 2011-1:484, 2010.

C. Wang, S. Luan, G. Tang, D. Z. Chen, M. A. Earl, and C. X. Yu. Arc-modulated radiation therapy (AMRT): a single-arc form of intensity-modulated arc therapy. *Physics in Medicine and Biology*, 53(22):6291, 2008.

S. Webb. The physical basis of IMRT and inverse planning. *Br J Radiol*, 76(910):678–689, Oct. 2003.

U. Weber and G. Kraft. Design and construction of a ripple filter for a smoothed depth dose distribution in conformal particle therapy. *Physics in Medicine and Biology*, 44 (11):2765, 1999.

V. F. Weisskopf and D. H. Ewing. Erratum: On the Yield of Nuclear Reactions with Heavy Elements. *Phys. Rev.*, 57(10):935, May 1940.

W. K. Weyrather, S. Ritter, M. Scholz, and G. Kraft. RBE for carbon track-segment irradiation in cell lines of differing repair capacity. *Int J Radiat Biol*, 75(11):1357–64, Nov. 1999. ISSN 0955-3002.

R. R. Wilson. Radiological Use of Fast Protons. *Radiology*, 47:487–491, 1946.

J. F. Ziegler. SRIM-2003. *Nuclear Instruments and Methods in Physics Research Section B: Beam Interactions with Materials and Atoms*, 219-220:1027 – 1036, 2004. ISSN 0168-583X. Proceedings of the Sixteenth International Conference on Ion Beam Analysis.

ACKNOWLEDGMENTS

My acknowledgment is first of all addressed to my supervisors PD Dr. Katia Parodi and Prof. Dr. Oliver Jäkel to have accepted and warmly welcomed me in their groups. Thanks for your valuable and enthusiastic scientific guiding with the constant freedom in the development of my work, for your continuous motivation and support and for the numerous opportunities and responsibilities I was granted in these years.

I thank Prof. Dr. Wolfgang Schlegel, Head of the Department of Medical Physics in Radio-Oncology at the German Cancer Research Center (DKFZ), for giving me the possibility to carry out the PhD research activities in his department and for granting me financial support through the fundings of the Helmholtz Association of German Research Centres (HGF) in the "Virtual Institute" under the contract number VH-VI 303.

I am particularly thankful to Prof. Dr. rer.nat. Dr. med. Jürgen P. Debus and Prof. Dr. Thomas Haberer since they give me the possibility to spend these years at the Heidelberg Ion Therapy center (HIT) in an ideal scientific environment for a PhD. Moreover, I thank you for the beam time granted to carry out the experimental part of my work and also for the financial support of the electronics.

I thank all the colleagues at HIT for the daily discussions and advices. In particular all the members of the medical physicist team for their constant helpfulness to answer my questions and for introducing and guiding me into the clinical world of an ion therapy center. Moreover, I thank also all the members of the accelerator team for their ever-present support especially during the nightly measurements.

A special thank is due to Dr. Stephan Brons for his polyvalent scientific support and to Dr. Peter Heeg for his suggestions on every kind of hardware and, both of you, for your kindness and delicacy in human relationships.

I also thank Dr. Andreas Peter for his support with the electronics and for carrying the detector components back and forth between the GSI Helmholtz Center for Heavy Ion Research and HIT, Dr. Ralf Panse for his help with the trigger related issues and Timo Strecker for the fast and cheap set-up of the experimental rotating table and for your friendly corrections of my errors speaking German.

A few words more are due to my officemates Andrea, Christopher, Daniel, Florian, and Julia for the friendly and productive atmosphere of our office. Moreover, I am happy to thank Antoni, Christian, Marion, and Martin, because sharing the PhD time with you has

always been a pleasure both from the scientific and unscientific point of view.

A special acknowledgment is addressed to Dr. Bernd Voss, who takes care of all the technical developments connected to the construction of the ICs stack. He offered me the possibility to work in the technical environment of the detector laboratory at GSI and to improve my knowledge of detectors as well as my mechanical abilities. I would like to thank him also for his friendly availability, and his always positive way of thinking and of doing. His enthusiastic support and his essential suggestions were a constant reference for my work.

I thank all the members of the FLUKA collaboration, especially Dr. Alfredo Ferrari and Dr. Paola Sala, for sharing common research activities, useful hints, and for providing me with confidential FLUKA related material used in this work. A personal thanks is due also to Dr. Andrea Mairani in particular for the initial support and for answering my several FLUKA-related questions, and to Dr. Francesco Cerutti for the fruitful chats.

I would also thank all the members of the Research Group Heavy Ion Therapy and Research Group Applied Medical Radiation Physics at DKFZ for the fruitful discussions in our meetings and seminars.

I am also thankful to all the members of the Lyon groups (Institut de Physique Nucléaire de Lyon and CNDRI-INSA, France) working on the Regional Research Program for Hadrontherapy (ETOILE) for our common scientific activities on prompt gamma imaging techniques and for having given me the possibilty to take part of the measurements at GANIL. In particular, Dr. Denis Dauvergne, Dr. Etienne Testa, Dr. Mauro Testa, Dr. Fabrice Le Foulher, and Dr. George Dedes.

Moreover, I thank all the members of the scientific collaboration related to prompt gamma imaging techniques between the RD&M, Delft University of Technology (The Netherlands), the Maastro Clinic in Maastricht (The Netherlands), the LIP-Laboratório de Instrumentação e Física Experimental de Partículas of Coimbra (Portugal), the ISEC-Instituto Superior de Engenharia de Coimbra (Portugal) and HIT. In particular, Dr. Paulo Crespo, Dr. Dennis R. Schaart, Dr. Aleksandra Biegun and Patricia Cambraia Lopes.

Un grazie veramente speciale e di cuore alla mia mami e al mio papi per essermi sempre stati vicini, nonostante la lontananza geografica, per le vostre mille attenzioni e consigli in questi anni. Alla mia sorellina Laura per essere sempre presente. Ai miei teneri nonnini perché pensano sempre alla loro nipotina.

Ein spezieller Dank geht an Birgit und Klaus für ein offenes Ohr und den einen oder anderen objektiven und bemerkenswerten Rat und an Tim, mich vor drei Jahren mit einem Lachen in Heidelberg empfangen zu haben.

Then, I thank also all my friends for the beautiful moments spent together.

E alla fine un altro grandissimo GRAZIE che però non va scritto qui ma detto altrove.